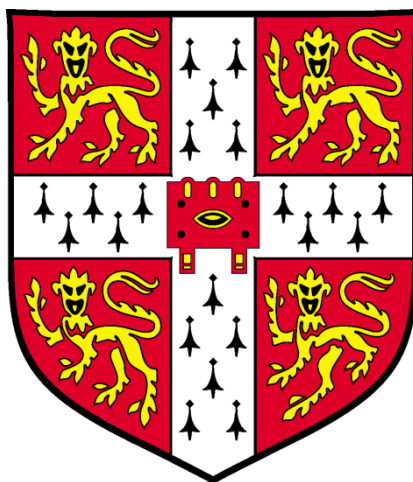# Fundamental Studies of Heap Leaching Hydrology Using Magnetic Resonance Imaging

Marijke Antonia Fagan

Trinity College

This dissertation is submitted for the degree of

Doctor of Philosophy

April 2013

Magnetic Resonance Research Centre

Department of Chemical Engineering and Biotechnology

University of Cambridge

Declaration

The work presented in this dissertation was carried out in the Department of Chemical Engineering and Biotechnology at the University of Cambridge during the period between October 2009 and March 2013. This thesis is the result of my own work and includes nothing which is the outcome of work done in collaboration except where specifically indicated in the text. This dissertation has not been submitted previously in part or in whole to any other universities for degrees, diplomas or other qualifications. Finally, this thesis contains 88 figures and 54,512 words including appendices, bibliography, footnotes, tables and equations.

_____   _____

Marijke Antonia Fagan   Date

Acknowledgements

I would like to begin by thanking the two people who have supervised me while at Cambridge, W/Prof. Mike Johns and Dr Andy Sederman. Their support, guidance and encouragement has given me a solid framework in which to work and learn while simultaneously allowing me the freedom to grow as a researcher to the point where I feel confident in driving my own research. Their time and expertise has been invaluable in the development of my journal papers and conference presentations. They have also been incredibly supportive in the planning of my next steps, for which I am grateful. I very much hope that I will have the opportunity to work with them again in the future.

I would also like to thank Prof. Sue Harrison at the University of Cape Town for her assistance in my original application to study at the University of Cambridge thereby allowing me the opportunity to maintain links to my alma mater while experiencing life and research in Cambridge. She has since been a continued source of heap leaching knowledge and her constant support of my research has been much appreciated.

Thanks are due to a number of people who assisted me with my experiments. I am deeply grateful to (now Dr) Makis Parasoglou who taught me the SPI ropes when I first arrived, all in the days just before his viva. I would like to express my gratitude to Dr Jon Mitchell for his support in smoothing the supervisor transition when Mike moved to Australia and whose assistance at the Schlumberger Gould Research Centre with the low field imaging presented in Chapter 4 is much appreciated. Emmanuel Ngoma at the University of Cape Town has been always helpful when it came to organising ore shipments from South Africa and providing me with information regarding UCT's standard protocols and experiment information. None of the X-ray CT imaging of my samples in Chapter 4 would have been possible without the assistance of Alan Heaver at the Department of Engineering at the University of Cambridge. I also appreciate having been given the opportunity to work with the group at the Department of Materials at Imperial College London on the analysis of their leaching column (Chapter 7), with specific recognition going to Áine Ní Bhreasail and Prof. Peter Lee.

I have had a wonderful time working at the Magnetic Resonance Research Centre and am grateful to everyone there for their company and insights throughout the course of my degree. Thusara Chandrasekera, Dr Mick Mantle and Dr Daniel Holland specifically have helped me countless times with issues ranging from programming problems to figuring out how to get my pulse programs to work on the often perplexing magnets. Thank you for being so generous with your time and expertise.

Finally I would like thank my family and friends, both in Cambridge and abroad, for their unconditional love and support without which I would never have made it this far. Thank you specifically to Chris, Mamma, Pappa, Francois, Emma, Oupa and Nan for showing so much enthusiasm for my work and various milestones, despite often not understanding what I was going on about. Everything is made so much more worthwhile when you can share it. But most importantly I must thank Chris who followed me to the UK without question or hesitation and has been my constant partner in this adventure.

Summary

The recovery of mineral from ore in the heap leaching process requires the mineral to come into contact with the leaching solution. However, heap hydrology is prone to non-uniform behaviour due to the inhomogeneity of the ore particles and the heap structure. The primary aim of this thesis was therefore to develop a magnetic resonance imaging (MRI) technique which would allow for the novel non-invasive imaging of the liquid hold-up in representative laboratory-scale heap leaching systems.

The ferro- and paramagnetic species in the ore were found to cause significant distortions in frequency encoded MRI acquisitions. These distortions were mitigated through the application of single point imaging techniques. Comparison with equivalent X-ray CT acquisitions, which are immune to magnetic susceptibility distortions, confirmed the accuracy of the single point acquisitions. Spin echo single point imaging (SESPI) was demonstrated to be more robust than the simple single point imaging (SPI) technique because the effect of T_2 weighting on the MRI signal was less significant than that of T_2^*.

Mapping of the gas, liquid and solid distributions in unsaturated leaching columns using SESPI allowed for the quantification of the hold-up and voidage values. These compared favourably to gravimetric measurements and literature values, thereby confirming their validity. Novel measurement of the liquid film thickness and the interfacial areas between the three phases was achieved and insight into the liquid behaviour was obtained through different flow rate experiments as well as MRI tracer experiments. Drip irrigation of the ore was considered for beds of large, fine and agglomerated ore. Liquid distribution in the fine ore closely resembled that of irrigation of clay soils whereas flow through the large ore was gravity dominated. Slumping of the agglomerated ore caused permanent limitation of the liquid distribution and the effect of flow rate changes was observed to be limited to the region below the irrigation point. In both the column and drip irrigation experiments, increases in the liquid flow rate caused small increases in the liquid hold-up in the form of new, relatively thicker rivulets, thereby improving the liquid-solid interfacial area. However it did not affect capillary held liquid volume so the effect of flow rate changes decreased as the lateral distance from the irrigation point increased.

Finally, X-ray CT images of a long term ferric leach were analysed to assess the factors affecting the mineral leaching. Proximity of the mineral to the ore surface was found to be the critical factor, as only mineral located within 2 mm of the surface was recovered, though liquid distribution effects were also observed.

Outputs of this Work

The work in this thesis has resulted in the following **refereed publications**:

Fagan, M. A., Sederman, A. J., Harrison, S. T. L. and Johns, M. L. (2012) 'Phase distribution identification in the column leaching of low grade ores using MRI', *Minerals Engineering*, in press, doi: 10.1016/j.mineng.2012.10.005.

Fagan, M. A., Sederman, A. J. and Johns, M. L. (2012) 'MR imaging of ore for heap bioleaching studies using pure phase encode acquisition methods', *Journal of Magnetic Resonance*, 216(1), 121-127.

The following **conference contributions** have also come out of this work:

Fagan, M. A., Ngoma, I. E., Chuime, R. A., Minnaar, S., Sederman, A. J., Johns, M. L. and Harrison S. T. L., 'The impact of drip irrigation on heap hydrology and microbial colonies in bioleaching', *20th International Biohydrometallurgy Symposium*, Antofagasta, Chile. 8-11 October 2013, Oral presentation.

Fagan, M. A. and Sederman A. J., 'Fundamental studies of heap bioleaching hydrology using magnetic resonance imaging', *SET for Britain 2013*, London, United Kingdom. 18 March 2013, Poster presentation.

Fagan, M. A., Johns, M. L., Mitchell, J. and Sederman, A. J., 'Application of single point imaging techniques to the study of liquid distribution in low grade copper ore systems', *11th International Bologna Conference on Magnetic Resonance in Porous Media*, Guildford, United Kingdom. 9-13 September 2012, Poster presentation.

Fagan, M. A., Sederman, A. J., Johns, M. L. and Harrison, S. T. L., 'Phase distribution identification in the column leaching of low grade ores using MRI', *Biohydrometallurgy 2012*, Falmouth, Cornwall, UK. 18-20 June 2012, Oral presentation.

Fagan, M. A., Sederman, A. J. and Johns, M. L., 'Fundamental studies of heap bioleaching hydrology using magnetic resonance imaging', *Trinity Engineers Association Spring Gathering*, Cambridge, United Kingdom. 26 April 2012, Poster presentation (awarded prize for Best Poster Presentation).

Fagan, M. A. and Johns, M. L., 'Hydrology studies of heap leaching columns using magnetic resonance imaging', *10th International Bologna Conference on Magnetic Resonance in Porous Media*, Leipzig, Germany. 12-16 September 2010, Poster presentation (awarded prize for Best Poster Presentation by a young scientist).

Table of Contents

Chapter 1 – Introduction

In recent decades depletion of the more readily accessible high grade ores at the earth's surface and the increasing complexity of the available ores have made conventional mining technologies less economically feasible and so has motivated the search for alternatives (O'Kane Consultants Inc. 2000, Rawlings et al. 2003). One such option is heap leaching which allows for the recovery of valuable metals from low grade ores, aided by the activity of iron- and sulfur-oxidising microorganisms. Heap leaching has many other advantages over conventional mining processes including relatively low capital and operating costs, rapid start-up and the fact that it is more environmentally friendly as it requires substantially less energy and does not produce sulfur dioxide and other harmful gaseous emissions. The process may also be used to remediate mine tailings and waste ore to prevent pollution that results from acid mine drainage from the leaching of the ore occurring naturally.

These factors have led to a significant growth in the heap leaching industry and hence to a greatly improved understanding of the processes and microorganisms involved. Heap leaching has been commercially applied in two main areas: the leaching of secondary copper ores that contain copper sulfides such as chalcocite (Cu_2S) and covellite (CuS) and the pre-treatment of gold bearing ores where the gold is occluded in sulfide minerals (Brierley 2008, Watling 2006). In 2008, heap leaching was found to account for approximately 7% of the total global annual copper production (1.7×10^7 tons), with this figure increasing to 20-25% with the inclusion of dump leaching, a more crude form of heap leaching (Brierley 2008).

One of the main challenges in the optimisation of heap leaching is the heap hydrology. Solution flow needs to be fast enough to ensure that the heap is leached in an economically feasible period, while the flow through the heap must be sufficiently uniform that areas of the heap are not left unleached. However, heaps are unsaturated systems of often highly inhomogeneous nature which makes the hydrology of the leaching systems very complex and spatially variable, leading to issues such as flooding and preferential flow (Bouffard and Dixon 2001, de Andrade Lima 2006, Decker and Tyler 1999, O'Kane Consultants Inc. 2000). Despite its importance, relatively few studies have been done on heap hydrology until recently (Mousavi et al. 2006) and so there is still much scope for investigation. Most of these studies have focused on the application of unsaturated zone soil hydrology theory to preferential flow in heaps (Decker and Tyler 1999, O'Kane Consultants Inc. 2000, Wu et al. 2007, Wu et al. 2009) and on the development of models to predict the heap hydrodynamics and hence the overall heap efficacy (Bouffard and Dixon 2001, Bouffard and West-Sells 2009, Mousavi et al. 2006).

1.1   Objective of this Thesis

The objective of this thesis is to investigate the application of Magnetic Resonance Imaging (MRI) to heap leaching systems. This will allow for the liquid phase inside of a heap leaching ore column to be imaged in a non-invasive manner. MRI would not typically be thought of as a viable technology for use with such systems because the ferro- and paramagnetic species in the ore and leach solution have the potential to cause significant magnetic susceptibility distortions in images acquired with conventional frequency encode methods. However, these distortions can be minimised through the use of pure phase encode MRI pulse sequences. The first aim of this thesis is consequently to identify and optimise the best MRI acquisition method for application to packed ore systems.

Following this, it is desired to use MRI to identify the liquid, solid and gas phase positions in unsaturated leaching systems so that the effect of flow rate, particle size and irrigation method on the liquid distribution may be studied. It is hoped that the results will give further insight into issues such as preferential flow, solution application methods, bed structure and solution flow evolution as a column heap leach progresses.

In the last section of this thesis X-ray computed tomography (CT) is used to image a long term ferric leach with the objective of monitoring the leaching of the mineral grains in the ore.

1.2   Outline of Thesis Chapters

Chapter 1 introduces the concept of heap leaching and details the main objectives of this dissertation.

Chapter 2 presents the heap leaching process theory as well as typical operation practices and describes the challenges associated with the heap hydrology.

Chapter 3 describes the basic principles of nuclear magnetic resonance (NMR) and MRI, summarises the MRI acquisition methods that are used in this thesis and presents the theory of X-ray CT.

Chapter 4 considers what the best MRI acquisition method is for the imaging of ore samples, the aim being to identify the method that produces distortion free images with the best signal to noise ratio.

Chapter 5 presents a study of how MRI acquisitions of column leaches while flowing and saturated are used to develop 3D phase maps which identify the position of the gas, liquid and solid phases. These phase maps are used to determine the pore-occupancy of the liquid and

gas phases and to provide novel measurement of the interfacial area between air, leach solution and ore. Preliminary MRI tracer studies are compared to traditional methods as well.

Chapter 6 shows how MRI is applied to monitor the solution infiltration from a single drip point into a packed bed of ore as a function of flow rate and the ore particle size distribution and preparation.

Chapter 7 describes how X-ray CT imaging is used to quantify the mineral content present in ore samples at different stages in the leaching process and to identify the position of the mineral relative to its distance from the edge of the ore particles.

Chapter 8 presents the main conclusions that can be drawn from this work and details those aspects of the work that may be of interest for future research.

1.3 Nomenclature

Abbreviations

CT   -   computed tomography

MRI   -   magnetic resonance imaging

NMR   -   nuclear magnetic resonance

1.4 References

Bouffard, S. C. and Dixon, D. G. (2001) 'Investigative study into the hydrodynamics of heap leaching processes', *Metallurgical and Materials Transactions B-Process Metallurgy and Materials Processing Science,* 32(5), 763-776.

Bouffard, S. C. and West-Sells, P. G. (2009) 'Hydrodynamic behavior of heap leach piles: Influence of testing scale and material properties', *Hydrometallurgy,* 98(1-2), 136-142.

Brierley, C. L. (2008) 'How will biomining be applied in future?', *Transactions of Nonferrous Metals Society of China,* 18(6), 1302-1310.

de Andrade Lima, L. R. P. (2006) 'Liquid axial dispersion and holdup in column leaching', *Minerals Engineering,* 19(1), 37-47.

Decker, D. L. and Tyler, S. W. (1999) 'Hydrodynamics and solute transport in heap leach mining' in Kosich, D. and Miller, G., eds., *Closure, Remediation & Management of Precious Metals Heap Leach Facilities*, Reno, Nevada: University of Nevada.

Mousavi, S. M., Jafari, A., Yaghmaei, S., Vossoughi, M. and Sarkomaa, P. (2006) 'Computer simulation of fluid motion in a porous bed using a volume of fluid method: Application in heap leaching', *Minerals Engineering,* 19(10), 1077-1083.

O'Kane Consultants Inc. (2000) 'Demonstration of the application of unsaturated zone hydrology for heap leaching optimization', *Industrial Research Assistance Program Contract # 332407,* (628-1).

Rawlings, D. E., Dew, D. and du Plessis, C. (2003) 'Biomineralization of metal-containing ores and concentrates', *Trends in Biotechnology,* 21(1), 38-44.

Watling, H. R. (2006) 'The bioleaching of sulphide minerals with emphasis on copper sulphides - A review', *Hydrometallurgy,* 84(1-2), 81-108.

Wu, A. X., Yin, S. H., Qin, W. Q., Liu, J. S. and Qiu, G. Z. (2009) 'The effect of preferential flow on extraction and surface morphology of copper sulphides during heap leaching', *Hydrometallurgy,* 95(1-2), 76-81.

Wu, A. X., Yin, S. H., Yang, B. H., Wang, J. and Qiu, G. Z. (2007) 'Study on preferential flow in dump leaching of low-grade ores', *Hydrometallurgy,* 87(3-4), 124-132.

Chapter 2 – Heap Leaching Theory

This chapter describes the heap leaching process, with an emphasis on the structure of the heaps as well as the gas and solution flows. As described in the Introduction chapter, the heap hydrology is one of the key heap leaching process optimisation challenges due to the unsaturated nature of the heaps and is the ultimate focus of this thesis. The pivotal current theories and issues regarding heap hydrology as well as the techniques that have been used to assess these in the literature are summarised.

2.1   Heap Leaching Flow Sheet

Heaps are highly inhomogeneous, unsaturated systems with gas occupying the spaces that are not taken up by solids or liquid. A typical heap leaching circuit is shown in Figure 2.1. The heap is aerated from a network of pipes buried at the base of the heap into which air is pumped. The leach solution is distributed across the top of the heap by either sprinklers or drip emitters and then flows downwards through the heap under gravity. The leaching reactions occur when this leach solution comes into contact with the metal sulphides in the ore. The liberated metal ions then diffuse into the liquid whereby they are transported out of the heap. The pregnant leach solution (PLS) that exits the heap is collected at the base of the heap and is stored in the PLS pond. It is then sent to solvent extraction unit where the metal of interest (usually copper) is removed into the electrolyte solution and sent to an electrowinning stage for metal recovery. The leach solution that leaves the solvent extraction stage is known as the raffinate and is recycled back to the heap via the raffinate (barren) pond. An acidic make-up stream which may contain microorganisms and nutrients is combined with the raffinate in order to get the feed solution to specification.
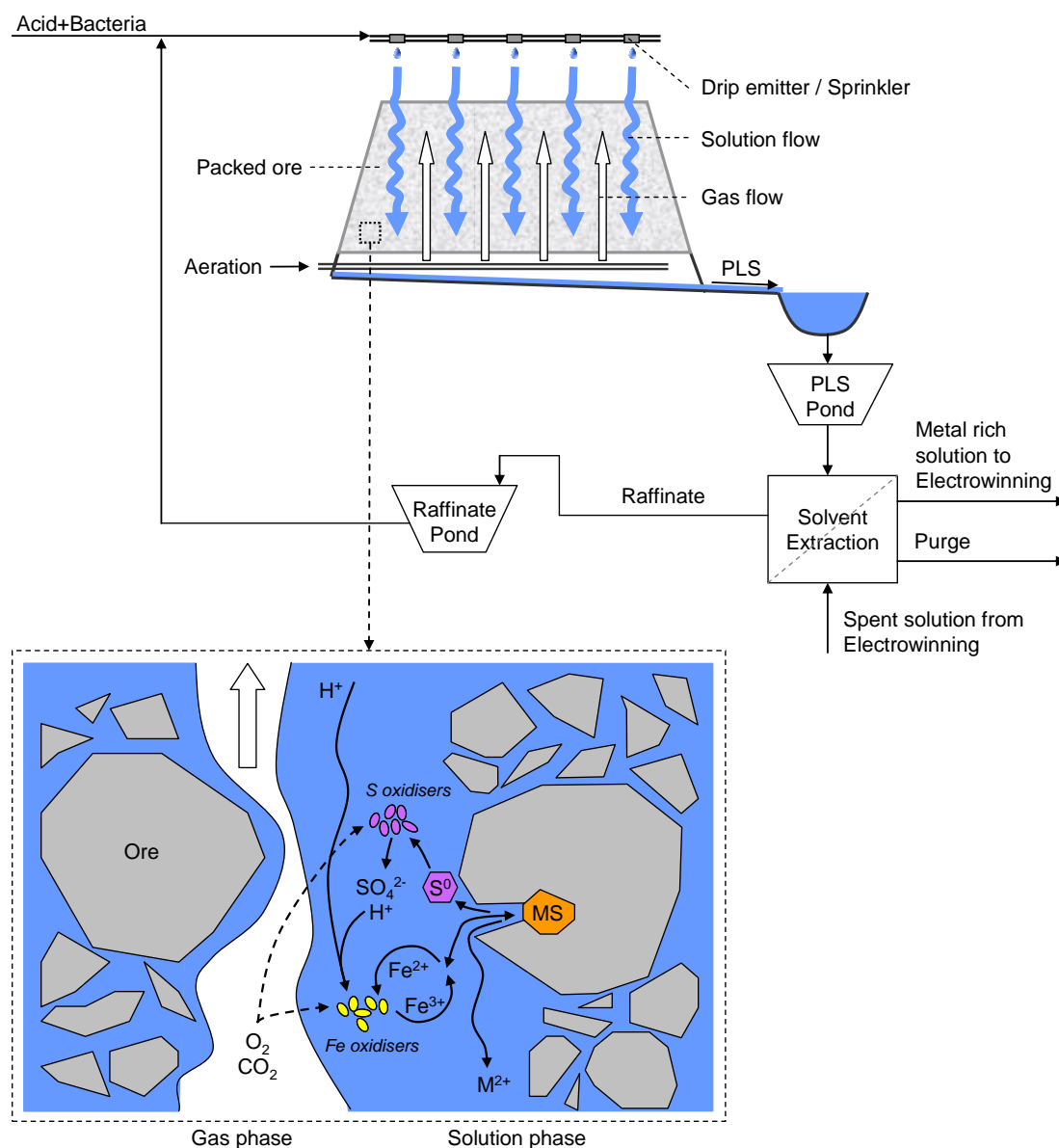
Figure 2.1. Flow sheet of a typical heap leaching process as described in the text. A micro-scale representation of the leaching reactions is inset which illustrates the interactions between the gas, liquid and solid phases and the main roles of the sulfur (purple) and iron (yellow) oxidising microorganisms in the metal sulfide leaching reactions. Based on Petersen and Dixon (2007).

2.2 Heap Leaching Reactions

The leaching reactions occur in the liquid phase with the pathway of leaching determined by the acid-solubility of the metal sulfides. Acid-soluble metal sulfides are leached via the polysulfide pathway while acid-insoluble metal sulfide dissolution is achieved through the thiosulfate pathway. A non-stoichiometric schematic of the two pathways is shown in Figure

2.2. In both pathways Fe^{3+} ions react with the metal sulfides (MS) in the ore to produce M^{2+} ions and water soluble intermediary sulfur compounds – elemental sulfur in the polysulfide pathway and thiosulfate in the thiosulfate pathway. The polysulfide pathway involves an additional proton attack which binds the MS valance band electrons. The reduced iron (Fe^{2+}) that results from this reaction is then oxidised by bacteria back to Fe^{3+} and thereby recycled. The intermediary sulfur compounds are further oxidised either abiotically or by bacteria.

Two classes of microorganisms are involved in these reactions, namely iron- and sulfur-oxidising chemolithotrophs. These microorganisms grow autotrophically by fixing carbon dioxide from the atmosphere and gain their energy not from the sun, but from using ferrous iron and/or reduced inorganic sulfur compounds as electron donors and oxygen as the electron acceptor (Rawlings et al. 2003). Sulfuric acid is a product of the inorganic sulfur oxidisation and so the bacteria have adapted to be acidophilic (Olson et al. 2003, Watling 2006). Any other nutrients required by the bacteria, such as nitrate, phosphate and potassium, are provided through heap aeration or irrigation (Rawlings et al. 2003). Some of the most commonly used and competitive microorganisms are the iron- and sulfur-oxidising *Acidithiobacillus thiooxidans (At)*, the sulfur-oxidising *At. ferrooxidans (Af)*, *At. caldus (Ac)*, and the iron-oxidising *Leptospirillum ferrooxidans* and *L. ferriphilum (Lf)*, though many other microbes do exist (Olson et al. 2003, Rawlings 2002, Rawlings et al. 2003, Watling 2006).
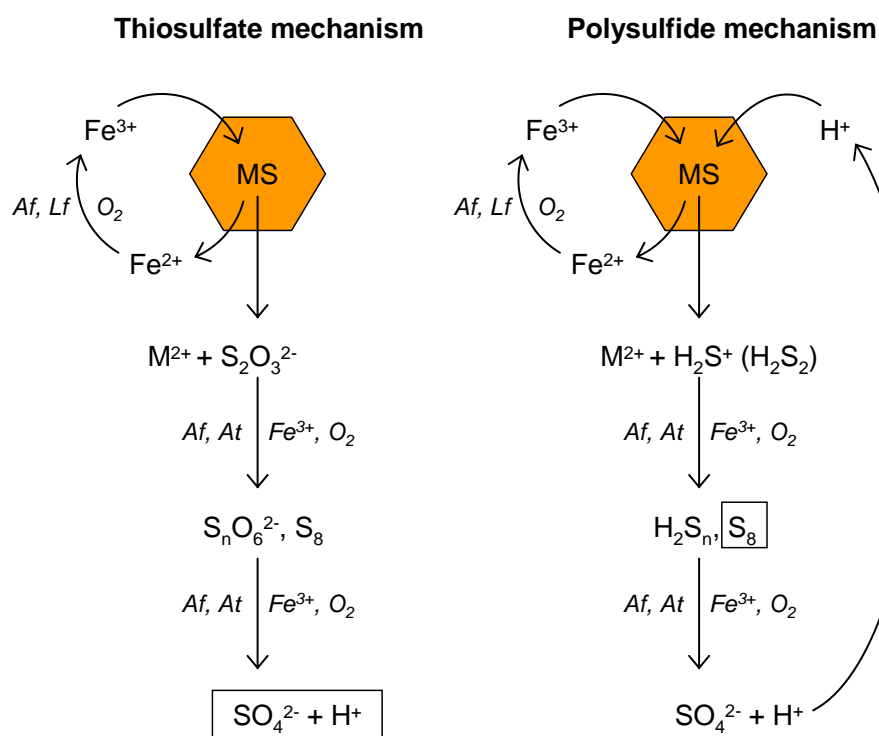
Figure 2.2. A schematic comparison of the thiosulfate and polysulfide mechanisms in bioleaching of metal sulfides, based on Rohwerder et al. (2003).

2.3   Heap Structure

2.3.1   Ore Preparation

Heap leaching ores typically have a very broad particle size distribution (PSD), encompassing particles in the micrometre to the centimetre ranges. Miller et al. (2003) demonstrated that a smaller crush size results in a higher percentage of the mineral being exposed on the ore surface and therefore allows for higher potential recoveries. However, fine-grained particles and clays in an ore may cause areas of low permeability to develop in heaps, resulting in restricted solution and gas flow. This has the potential to cause parts of the heap to remain unleached or for the bacteria to become oxygen and carbon dioxide deprived. This problem is especially apparent in the segregation that occurs during the stacking of ore into heaps, where larger rocks roll to the bottom of the heap while fines predominate in the top, resulting in layers of differing permeability and hence non-uniform flow through the heap (Bartlett 1998, O'Kane Consultants Inc. 2000). The crush size of the ore is consequently one of the key factors in the design of a heap leach.

In order to improve the homogeneity of the heap, the ore is commonly agglomerated prior to heap construction. In this process liquid and sometimes binder are added to the ore sample which is then agitated, for example, in a rotary drum. This causes the fines and clays in the ore to become attached to larger particles to form agglomerates, thereby producing more uniformly sized particles. Agglomeration leads to an improvement in heap homogeneity, with less segregation and movement of fines occurring. The more uniform heap permeability ultimately leads to more uniform flow through the heaps and so aids in the optimisation of metal recovery. Agglomeration is also advantageous as it allows for the leaching solution to be applied to the whole ore sample prior to normal heap operation being commenced and it can be used as the first heap bacterial inoculation step.

One of the main concerns in the agglomeration process is the final structural integrity and strength of the agglomerates. Three critical parameters that ensure stable and permeable agglomerates with adequate handling strength have been identified by the U.S. Bureau of Mines: amount of binder, moisture content and curing period (Bartlett 1998). These three parameters have major effects on the flow through the heaps, specifically the flow rate at which flooding of the heap occurs.

2.3.2 Scale-up

Different stages exist during the development of a heap leaching operations design. The systems generally increase in size with time and the most common design testing stages (in order) are column tests, cribs and demonstration heaps, after which full heap operation is begun.

Column tests are used at the start of process development in order to find the approximate optimum leaching conditions (Bouffard and West-Sells 2009). Aspects that will be considered at this stage will include: crush size, heap stability, permeability versus heap height, the need for agglomeration, leach time, leaching agent consumption and maximum possible recovery (de Andrade Lima 2006, Kappes 2002). Recoveries at the column test stage are often much higher and faster than would be found in full scale practice. This is largely because:

- ore is packed more uniformly in columns than it would be in a heap,

- the small diameter of the columns result in inadequate inlet solution distribution not being identified

- and the solution to ore ratio is generally higher in columns (Kappes 2002).

Differences can also be seen in the ore's structural behaviour, for example, where the walls of columns limit the degree of slumping that is seen compared to cribs. Cribs are large silos whose heights are equal to the anticipated heap lift heights. They are often employed at the end of successful column tests. (Bouffard and West-Sells 2009)

Finally, demonstration heaps are used to confirm the behaviour and efficiency of an ore leaching design before full scale operation is commenced. Demonstration heaps can be isolated or embedded piles that can range from 1000 to 100000 tonnes (Bouffard and West-Sells 2009).

2.3.3 Heap Construction

Heaps are laid on impermeable base pads made with high density polyethylene or plastic sheeting in order to prevent the loss of solution, which is both a production loss and an environmental hazard (Rawlings 2002, Rawlings et al. 2003). The surface on which the pad is placed is sloped to allow for lateral drainage to a point where the PLS is collected (Bartlett 1998). A layer of coarse rock is commonly placed immediately on top of the pad to improve drainage and occasionally on the heap surface too in order to improve the solution infiltration into the heaps (O'Kane Consultants Inc. 2000).

The heaps are constructed by dumping from haul trucks, stacking with a front-end loader or mechanical stacking with conveyer belts (Bartlett 1998, Kappes 2002, O'Kane Consultants Inc. 2000). The major disadvantage of truck dumping is the compaction of the ore due to the weight of the trucks and their loads. This is more of a concern with softer ore (Kappes 2002). Consequently the heap surfaces are often ripped before leaching is commenced in order to break up the compacted zone, thereby improving the permeability of the top of the heap and avoiding preferential flow development as a result of plugging (Bartlett 1998, Kappes 2002). Conveyer stacking allows for the gentle placement of ore which can help to minimise compaction and segregation of the ore (O'Kane Consultants Inc. 2000). In some cases where the heap height is significant, the base of the heap can become compacted due to the large drop from the conveyer to the ground. This problem can be overcome largely by leaving the stacker at the full height of the pile and then allowing the ore to slide down the existing heap (O'Kane Consultants Inc. 2000).

2.3.4   Heap Height

Typical heap heights are between 4 m and 10 m though in cases where insulation is an issue, heaps may be as high 18 m (du Plessis et al. 2007). The height of a heap is a critical design parameter as it:

- can exaggerate the gradients in microbial inoculation migration and colonisation, pH and carbon dioxide and oxygen supply (du Plessis et al. 2007),

- affects the insulation of the heap which is especially important in cold climates and with thermophile bioleaching (du Plessis et al. 2007), and

- affects the porosity (compaction) and segregation of the ore which in turn affects the gas and solution flow in the heap (Bartlett 1998, Kappes 2002, O'Kane Consultants Inc. 2000).

Heap heights do not remain constant after leaching is started due to collapsing or slumping of the beds. This slumping causes a decrease in the bed voidage and permeability (increase in bulk density) which can affect the gas and liquid flows. Slumping will generally occur as soon as the freshly stacked ore is wetted. Bouffard and Dixon (2001) found that the slump experienced by agglomerated ore was two to five times more than that experienced by non-agglomerated ore. They attributed this behaviour to the fact that agglomerates tend to be more spherical and uniform in size which led to the agglomerate bed having a higher void fraction before wetting. Further slumping tends to occur during heap operation as ore, especially fines,

shifts in the bed and as material is dissolved and/or leached from the ore which compromises the original structural integrity of the ore and agglomerates causing them to disintegrate.

2.4 Gas Flow

Heaps are unsaturated systems where the gas occupies the spaces that are not taken up by solids or liquid. Sufficient aeration of heaps is a key factor in bioleaching, as carbon dioxide is required as a carbon source and oxygen is required as an electron acceptor in the sulfur and iron oxidising reactions facilitated by the acidophilic bacteria that colonise the ore (Acevedo 2000, Lizama 2001). It has been found in previous ore leaching studies (through oxygen solubility and mass transfer coefficient measurement followed by modelling) that the rate limiting step in heap leaching is gas-liquid mass transfer (Petersen 2010a, Petersen 2010b) with the supply of oxygen to the liquid phase reaction systems being mass-transfer limited. This issue has been largely overcome by the forced aeration of heaps which was first implemented in the mid-1990s in both Australia and Chile (Watling 2006). Aeration pipes are laid at the base of the heap during construction and low pressure blowers are then used to force air into the heap. The significant improvements in copper recovery as a result of the implementation of forced aeration that were observed at Girilambone, NSW prompted many poorly performing heaps to be re-mined and then aerated (Watling 2006).

After heap construction has been completed, the air flow rate is one of the main operational controls, with typical air flow rates being 0.02 to 0.08 $m^3 \: t^{-1} \: h^{-1}$ (STP) (du Plessis et al. 2007). High air flow rates generally favourably affect microbial activity and hence heat generation, while lower rates have the benefit of improving heat conservation (du Plessis et al. 2007). A balance between these effects needs to be found, especially in the case of thermophilic bioleaching. Another important consideration is that the air flow rate needs to be high enough to prevent oxygen and carbon dioxide limitation at the top of the heap, as these gases are consumed as the air passes upwards.

Poor permeability of ore beds can make aeration difficult and hence more expensive. Higher permeabilities tend to be found at the base of heaps due to the ore segregation that occurs during construction, so good air penetration, both vertically and laterally, results from aeration at the bottom of the heaps. Typically, the higher the heap, the larger the allowable distances between the aeration points (Bartlett 1998).

Heap aeration can also be passive, in which case air is drawn into the heap with the flowing liquid (Rawlings et al. 2003), though forced aeration tends to be more common as it allows for more operational control.

2.5 Heap Hydrology

2.5.1 Solution Application

The two most common devices used to apply leach solution to heaps are sprinklers and pressure drip emitters.

Sprinklers are usually arranged in set patterns which are then separated by 7 to 10 metres (Bartlett 1998). The exact spacing will depend on the individual sprinkler arc overlap that is required to ensure that there is uniform supply of solution across the heap surface; too little overlap will lead to some areas of the heap receiving too little solution, while too much overlap will lead to the over wetting of some areas. The high impact from some sprinkler droplets can cause fine particles on the surface of the heap to become dislodged from agglomerates (O'Kane Consultants Inc. 2000). These fines are then washed into the heap and can lead to the formation of flow barriers either inside the heap or on the heap surface, the effect of which is that affected areas of the heap can remain unleached. Another disadvantage is that evaporation losses tend to be quite high with sprinklers, up to 35%, in hot dry climates (Bartlett 1998) which decreases the efficiency and hence increases the cost of irrigation.

Drip emitters do not have these disadvantages associated with them (Bartlett 1998, O'Kane Consultants Inc. 2000). In each emitter a small volume of solution flows through a torturous path of grooves between the core and the envelope of the emitter, all the while losing pressure, before being discharged. The eventual drip flow rate that comes from the emitter depends on the line pressure which is typically in the range of 35 to 140 kPa, significantly less than for sprinklers (Bartlett 1998). Another advantage of drip emitters is that they permit a much wider range of solution application rates. Drip emitters have to be placed closer together than sprinklers, with an emitter every 0.5 to 1.5 metres (Kappes 2002). They are designed to cover an area of between 0.25 and 1 m^2 (Bartlett 1998, Afewu and Dixon 2008). The pipes and emitters are typically covered with a thin layer of ore, which allows for operation in very cold climates (prevents freezing) as well as very hot climates (minimises evaporation).

2.5.2 Solution Application Rate

The solution flow rate that is applied to a heap needs to be selected carefully in order to maximise metal recovery whilst ensuring that the heap operation is cost effective and not too long. Typical solution volumetric fluxes range between 4 and 18 L m^{-2} h^{-1} (Rawlings and Johnson 2007).

Irrigation rates that are too high have a number of major disadvantages. High solution application rates can lead to flooding, depriving those areas of the bed of air. This will cause the bacteria to become deprived of oxygen and carbon dioxide, resulting in a decrease in microbial activity and hence metal recovery. Furthermore, each heap will have a zone of minimum permeability, often located at the top of the heap, which determines the maximum allowable solution application rate. If this rate is exceeded, short-circuiting and channelling of solution occurs, leaving areas of the heap not penetrated by the solution and hence unleached (O'Kane Consultants Inc. 2000). A third disadvantage of an excessively high flow rate is that the PLS that leaves the heap will be very dilute which makes metal recovery more difficult and expensive. If the solution flow rate is too low, leaching times may become too long which in turn could make a heap economically unfeasible (O'Kane Consultants Inc. 2000).

Variations in the leach solution application rate can sometimes be advantageous. An example of this is with gold leaching, where decreasing the solution feed can offset the decrease in metal leaching that tends to happen over time (Bartlett 1998). Furthermore, changes in solution feed rates may be called for due to the evolution of the heap permeability (Watling 2006). Leach/rest cycles can also improve the economics of leaching, especially in the case of older heaps. During the periods of no irrigation, stagnant solution remains in a fraction of the void spaces and the dissolution of valuable metal species will continue in this liquid. When irrigation is recommenced the liberated metal ions that have built up in the stagnant solution are washed out of the heap. This cyclical approach can dramatically reduce the operating costs for irrigation (pumping) and metal recovery from the PLS, as its grade will be higher (O'Kane Consultants Inc. 2000).

2.5.3   Solution Flow

The liquid in heaps is affected by gravitational forces, surface tension and atmospheric pressure (Bartlett 1998). As heaps are unsaturated systems with highly inhomogeneous solid structures, the degree of wetness and hydraulic conductivity of the ore vary thought the bed. This makes heap leaching hydrology spatially variable, highly complex and difficult to model. Chemical engineering models that have been developed for trickle beds are often not suitable for heap leaching systems as they describe uniform particle size systems operated at comparatively higher flow rates (Bartlett 1998). A more suitable description of heap hydrology is the unsaturated zone hydrology theory, a theory that was originally developed for soils (Decker and Tyler 1999, O'Kane Consultants Inc. 2000). It predicts the solution flow paths based on an ore's hydraulic conductivity which in turn is highly dependent on the pore size distribution and therefore on the aggregate or ore particles' size distribution and

placement, the solution application rates and methods and the degree of saturation (O'Kane Consultants Inc. 2000).

The total moisture potential of a system is defined as the sum of the capillary potential, gravitational potential, electrochemical potential and osmotic suction. In an unsaturated system the solid's pore-water pressure is less than that of the atmosphere due to the capillary and adsorptive forces present binding the solution in the solid matrix, which then causes solution to be drawn up into the pores. This phenomenon is appropriately called capillary potential or matric suction and is defined as the negative pore-water pressure referenced to the pore-air pressure ($u_a - u_w$). The matric suction is a function of the nature of the solid as well as the moisture content of the porous medium, with lower moisture contents leading to higher matric potential magnitudes (Freeze and Cherry 1979, O'Kane Consultants Inc. 2000). The electrical potential and osmotic suction make relatively insignificant contributions to the total moisture potential (Freeze and Cherry 1979). Therefore the total moisture potential may be approximated as:

$$\Phi = \varphi_m(\theta) + \varphi_z \qquad\qquad 2.1$$

where Φ = total moisture potential (Pa)

φ_m = matric suction (Pa)

θ = volumetric moisture content (m^3 liquid m^{-3})

φ_z = gravitational potential (Pa)

An alternative way of expressing this equation is in terms of head (Freeze and Cherry 1979):

$$h = \frac{\Phi}{\rho_l g} = h_c(\theta) + z \qquad\qquad 2.2$$

where h = total pressure head (m)

ρ_l = liquid density (kg m^{-3})

g = gravitational acceleration (9.81 m s^{-2})

h_c = capillary head (m)

z = height above a certain datum (m)

The steady state rate of flow through saturated soil is described by Darcy's law:

$$v = \frac{Q}{A} = -K\left(\frac{dh}{dl}\right) \qquad\qquad 2.3$$

where v = specific discharge or superficial velocity (m s^{-1} but actually (m^3 s^{-1}) m^{-2})

Q = volumetric flow rate (m^3 s^{-1})

A = area cross sectional to flow (m^2)

K = hydraulic conductivity (m s^{-1})

dh/dl = hydraulic gradient

The negative sign indicates that the solution flows from a high to a low head. In the case of unsaturated systems the hydraulic conductivity is a function of moisture content and the properties of the fluid and porous medium (Bartlett 1998, O'Kane Consultants Inc. 2000). Therefore, the original Darcy equation is modified to:

$$v = -K(\theta)\left(\frac{dh}{dl}\right)$$
2.4

with:

$$K(\theta) = \frac{k_i(\theta)\rho_l g}{\mu_l}$$
2.5

where k_i = intrinsic permeability (m^2)

μ_l = liquid dynamic viscosity (kg m^{-1} s^{-1})

The solid media's hydraulic properties are highly dependent on the pore size distribution and therefore on the aggregate or ore particles' size distribution and placement, the solution application rates and methods and the degree of saturation. Hence, in order to determine the solution retention and distribution in an unsaturated system, the effect of the solid media on the matric suction and the hydraulic conductivity must be understood.

The hydraulic conductivity is at a maximum at low matric suction, which occurs at 100% saturation, and is known as the saturated hydraulic conductivity, K_{sat} (Freeze and Cherry 1979). This value is the same as the hydraulic conductivity term in Darcy's law for saturated systems (Equation 2.3). The K_{sat} for a coarse textured material is higher than that for a fine textured material due to the larger pore size of the coarse material. However, as matric suction increases, the coarse material drains faster than the fine material, so that at a given point the hydraulic conductivity of the fine material will become higher than that for the coarse ore. This is because the smaller pores present in the fine material still have the ability to conduct solution at the higher suction values. At even higher matric suction values, the solution will start to drain from the fine material too, thereby decreasing the hydraulic conductivity from K_{sat}.

Practically, this means that solution will flow preferentially through the coarse ore if a high solution flux is applied such that the moisture content is near saturation, as the coarse material hydraulic conductivity will be higher than the fine material's. The preferred flow path may be through the fine material if a low solution flux is applied, so that the hydraulic conductivity of the fine material is higher than the coarse material. Therefore the preferred path will depend on the solution application rate.

The non-homogenous flow that results from variations within the heap is known as preferential flow. These variations commonly develop due to segregation and compaction of ore during heap construction as well as the movement of fines in the heap. The effect of preferential flow is to reduce the solution-ore contact in the areas that the solution flows away from, thereby reducing the overall metal recovery and hence the viability of the heap.

Macro-pore preferential flow, also known as short-circuiting (O'Kane Consultants Inc. 2000) occurs when solution flows preferentially through the larger pores (channels) in a heap. As flow rates are increased, even higher fractions of the total liquid volume flow through these channels, thereby decreasing the percentage liquid contact with the ore particles. Because of this, care must be taken to not make solution application rates too high, as mentioned in Section 2.5.2.

Fingering is a further form of preferential flow. It is found when an interface develops between two or more solutions of different density or viscosity and one fluid displaces another, leading to the formation of 'fingers' of fluid. It tends to occur when the fresh or recycled leach solution enters the bed and beneath the interface of a coarse material overlain with fine material, where solution retention or ponding exists above the fine material. Factors that promote fingering include gravitational forces, heap heterogeneity and the existence of areas with low hydraulic conductivity. Capillary forces, on the other hand, tend to have a stabilising effect. (O'Kane Consultants Inc. 2000)

2.5.4   Liquid Phases – Stagnant and Flowing

In descriptions of heap hydrodynamics, the solution in a bed may be simplified by dividing into two parts or phases, namely stagnant and flowing liquid. The understanding of the roles of these two phases as well as how solution is distributed between them is essential to improving leaching efficiencies.

Stagnant liquid is found in crevices between and in the pores of the ore particles, replacing the air when the ore is wetted. It is also believed to exist as a film on the external surfaces of the ore. The dissolution reactions all occur in the stagnant liquid from whence the various species

diffuse to the flowing liquid (Sheikhzadeh et al. 2005). The stagnant solution hold-up in a bed can be affected by physical properties of the solution and the ore, including shape, agglomeration, size and wettability (contact angle) (Bouffard and Dixon 2001). Typically it accounts for 17 to 32% of the bed void volume or 7 to 13% of total bed volume (assuming a bed porosity of 40%) as measured in copper dumps and columns containing rocks ranging in size from 5 to 152 mm (Bouffard and Dixon 2001). Bouffard and Dixon (2001) found that the stagnant solution hold-up increased as the ore crush size was made smaller.

The flowing liquid phase moves down through the bed under gravity (Sheikhzadeh et al. 2005). This liquid starts to flow when small channels (such as pores) are flooded, after which it drains through the bed as rivulets and films across the ore particles' surfaces. The flowing liquid volume is primarily influenced by the packing characteristics of the bed as well as the physical properties of the fluid, the liquid flow rate and the gas flow rate (Bouffard and Dixon 2001). It may be approximately measured as the drainage from the heap. Should the liquid flow rate be high enough to cause air-filled voids to pinch off, the voids will rapidly fill and 'flood'. Flooding can cause substantial increases in the flowing liquid volume and can also impact gas flow patterns, sometimes causing gas mass transfer limitations (Bartlett 1998, Bouffard and Dixon 2001).

2.5.5   Previous Heap Hydrology Studies

This review of previous heap hydrology studies serves as an introduction to the literature and identifies some of the key approaches that have been used in the past. Further studies which are concerned with specific aspects of heap hydrodynamics will be discussed in each of the experimental chapters as the work becomes relevant.

Preferential flow due to variations in particle size distribution has been one of the main areas focussed on in the literature. O'Kane et al. (1999), O'Kane Consultants (2000), Wu et al. (2007) and Wu et al. (2009) all performed experiments where they packed a column so that there were distinct zones of fine and coarse material on either side of the column, as illustrated in Figure 2.3. They then applied a range of solution fluxes to the column and collected the solution that left the coarse and fine regions separately. In all four studies it was found that the solution flowed preferentially through the coarse material when the applied flux was greater than the saturated hydraulic conductivity of the fine material. O'Kane et al. (1999) found this effect to be very strong, with 95% of the solution leaving on the coarse side at an applied flux only slightly higher than the saturated hydraulic conductivity of the fine material. However, at fluxes less than the saturated hydraulic conductivity, K_{sat}, the solution was found to flow preferentially through the fine material.
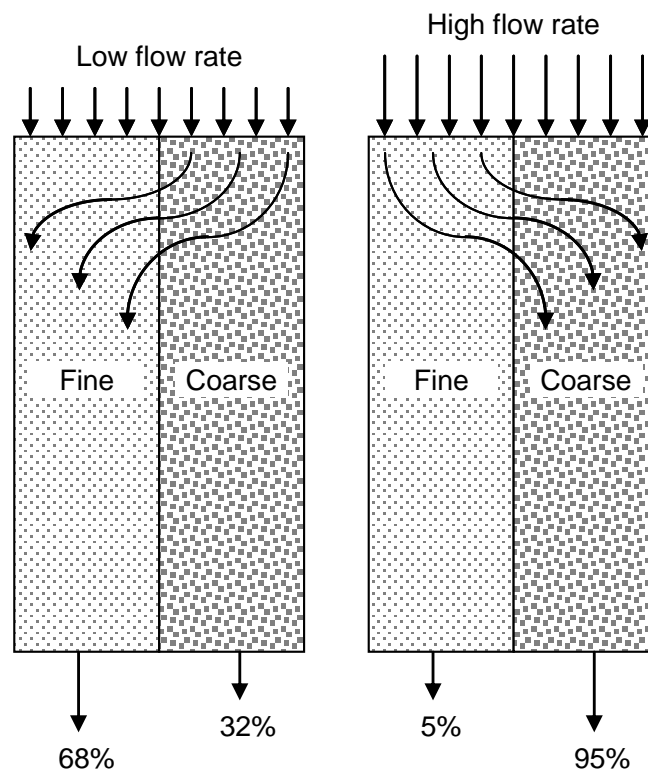
Figure 2.3. Example results from a preferential flow experiment where segregated particle size distribution columns were irrigated at different flow rates, based on O'Kane et al. (1999).

Tracer tests can provide valuable insight into the residence time distribution (RTD) of heaps. This information is often used in conjunction with flow models to extract time-dependant hydrodynamic parameters such as axial dispersion, plug flow velocity and the rate of exchange of solutes between the stagnant and flowing liquid phases (Bouffard and West-Sells 2009, de Andrade Lima 2006). Tracer studies have been performed by O'Kane Consultants (2000), Decker and Tyler (1999), Wu et al. (2007), Bartlett (1998) and Bouffard and West-Sells (2009) using NaCl, NaBr, NaCl, Cl⁻ and water, respectively, as tracers. Most of these studies were performed in columns, though Bouffard and West-Sells (2009) did column, crib and heap tests.

The two most extensive tracer studies were performed by Bouffard and Dixon (2001) and de Andrade Lima (2006). Bouffard and Dixon (2001) used a $NaNO_3$ tracer, whose concentration was measured by electrical conductivity, to evaluate hydrodynamic parameters and the effect that flow rate, agglomeration, binder addition, bed height and particle size distribution had on them. The RTD results showed that higher application flow rates produced narrow asymmetric peaks, as had previously been described by Bartlett (1998), and slower application rates had much wider spreads. All of the data sets had long tails, resulting from the slow diffusion in and out of the stagnant pore liquid. They proceeded to use the RTD data

to confirm the validity of their profile side-pore diffusion and mixed side-pore diffusion models, which they found to be successful. They concluded that the stagnant solution volume was affected by the crush size, agglomeration and solution application rates. de Andrade Lima (2006) performed similar experiments, but used HCl as a tracer and measured pH to determine the effluent concentrations. They used the piston-dispersion exchange model which describes a column as a trickle bed reactor having piston flow with axial dispersion and mass transfer with dead-water areas. They investigated the effect of different flow rates on axial dispersion and saturation and found that both of these factors played important roles and should therefore both be considered in heap modelling. Furthermore, they linked the Reynolds number to the stagnant solution volume and the mass transfer coefficient.

X-ray computed tomography (CT) has been used to study the porosity, moisture hold-up and air volume in a column leach experiment (Bouffard and West-Sells 2009). A major disadvantage of using X-ray CT is that the leaching system may be sterilised during the scan, therefore making it a non-ideal for taking images during a leach. Lin et al. (2005) and Yang et al. (2008) both used CT scans to evaluate the evolution of the pore structure along the length of a column. Yang et al. (2008) did not agglomerate their ore and only acid washed the ore while Lin et al. (2005) did agglomerate and performed a biotic leach. The CT scans were conducted before and after leaching. In order to allow for analysis of the pore geometry, the original greyscale 2D sections were transformed to binary images with the same threshold value. The porosity was calculated as the pore voxel volume divided by the total voxel volume of the stacked 3D data set. Lin et al. (2005) observed differences between the porosities at the top and base of the column before leaching, significant slumping of the bed during leaching and a corresponding reduction in the column porosities. Analysis of the final images indicated that finer particles had accumulated as a cone at the base of the column with the porosity analysis accordingly showing an increase in the difference between the porosities at the top and bottom of the column. They used their results to analyse further the saturated flow through the column based on lattice-Boltzmann simulations. Their simulation results suggested that most of the flow occurred in a small portion of the available pore space. However, to develop a more accurate model of the leaching system the lattice-Boltzmann simulations should be based on unsaturated flow conditions. Yang et al. (2008) claimed to observe similar trends to Lin et al. (2005), though they were far less pronounced. They had significant variations in the porosity values along the bed height, such that their data sets from before and after leaching overlapped considerably and so did not show much change in the bed structure as a result of the leaching.

Bouffard and West-Sells (2009) make note of a further method to study heap hydrology: electrical resistivity tomography (ERT). ERT was used to measure the moisture hold-up in test cells that had been embedded in a heap. This study's results indicated that some areas were partially saturated, while others were completely filled with solution and therefore were gas limited. ERT has been used by Water Management Consultants at Minera Escondida in Northern Chile, Cripple Creek heap in Colorado and at Phelps Dodge's Tyron property in New Mexico (Bouffard and West-Sells 2009). A possible disadvantage of ERT is that it requires there to be electrical contact between the electrode and solution, so isolated pockets of solution may not be detected. ERT resolution is also much coarser than that of other tomographic techniques such as X-ray CT and magnetic resonance imaging (MRI) (Stevenson et al. 2010).

2.6 Nomenclature

Abbreviations

CT	-	computed tomography
ERT	-	electrical resistivity tomography
MRI	-	magnetic resonance imaging
MS	-	metal sulfides
PLS	-	pregnant leach solution
PSD	-	particle size distribution
RTD	-	residence time distribution
STP	-	standard temperature and pressure

Symbols

A	-	area cross sectional to flow [m^2]
dh/dl	-	hydraulic gradient
g	-	gravitational acceleration [9.81 m s^{-2}]
h	-	total pressure head [m]
h_c	-	capillary head [m]
K	-	hydraulic conductivity [m s^{-1}]
K_{sat}	-	saturated hydraulic conductivity [m s^{-1}]
k_i	-	intrinsic permeability [m^2]
u_a	-	pore-air pressure [Pa]
u_w	-	pore-water pressure [Pa]
v	-	specific discharge or superficial velocity [m s^{-1}]
Q	-	volumetric flow rate [m^3 s^{-1}]
z	-	height above a certain datum [m]

Greek letters

θ	-	volumetric moisture content [m^3 liquid m^{-3}]
μ_l	-	liquid dynamic viscosity [kg m^{-1} s^{-1}]
ρ_l	-	liquid density [kg m^{-3}]
Φ	-	total moisture potential [Pa]
φ_m	-	matric suction [Pa]
φ_z	-	gravitational potential [Pa]

2.7 References

Acevedo, F. (2000) 'The use of reactors in biomining processes', *EJB Electronic Journal of Biotechnology,* 3(3), 1-9.

Afewu, K. I. and Dixon, D. G. (2008) 'Calibrating a 3D axisymmetric water and solute transport model for heap leaching' in Young, C.A., Taylor, P.R., Anderson, C.G. and Choi, Y., eds., *Hydrometallurgy 2008, Proceedings of the Sixth International Symposium*, Littleton, Colorado: Society for Mining, Metallurgy, and Exploration, Inc., 955-966.

Bartlett, R. W. (1998) *Solution Mining: Leaching and Fluid Recovery of Materials,* 2nd ed.*,* Gordon and Breach Science Publishers.

Bouffard, S. C. and Dixon, D. G. (2001) 'Investigative study into the hydrodynamics of heap leaching processes', *Metallurgical and Materials Transactions B-Process Metallurgy and Materials Processing Science,* 32(5), 763-776.

Bouffard, S. C. and West-Sells, P. G. (2009) 'Hydrodynamic behavior of heap leach piles: Influence of testing scale and material properties', *Hydrometallurgy,* 98(1-2), 136-142.

de Andrade Lima, L. R. P. (2006) 'Liquid axial dispersion and holdup in column leaching', *Minerals Engineering,* 19(1), 37-47.

Decker, D. L. and Tyler, S. W. (1999) 'Hydrodynamics and solute transport in heap leach mining' in Kosich, D. and Miller, G., eds., *Closure, Remediation & Management of Precious Metals Heap Leach Facilities*, Reno, Nevada: University of Nevada.

du Plessis, C. A., Batty, J. D. and Dew, D. W. (2007) 'Commercial applications of thermophile bioleaching' in Rawlings, D. E. and Johnson, B. D., eds., *Biomining*, illustrated ed., Springer-Verlag, 57-80.

Freeze, R. A. and Cherry, J. A. (1979) *Groundwater,* illustrated ed.*,* Prentice Hall.

Kappes, D. W. (2002) *Precious Metal Heap Leach Design and Practice,* Reno, Nevada: Kappes, Cassiday & Associates.

Lin, C. L., Miller, J. D. and Garcia, C. (2005) 'Saturated flow characteristics in column leaching as described by LB simulation', *Minerals Engineering,* 18(10), 1045-1051.

Lizama, H. M. (2001) 'Copper bioleaching behaviour in an aerated heap', *International Journal of Mineral Processing,* 62(1-4), 257-269.

Miller, J. D., Lin, C. L., Garcia, C. and Arias, H. (2003) 'Ultimate recovery in heap leaching operations as established from mineral exposure analysis by X-ray microtomography', *International Journal of Mineral Processing,* 72(1–4), 331-340.

O'Kane, M., Barbour, S. L. and Haug, M. D. (1999) *A Framework for improving the ability to understand and predict the performance of heap leach piles,* Phoenix, Arizona: Copper 99 Conference, 409-419.

O'Kane Consultants Inc. (2000) 'Demonstration of the application of unsaturated zone hydrology for heap leaching optimization', *Industrial Research Assistance Program Contract # 332407,* (628-1).

Olson, G. J., Brierley, J. A. and Brierley, C. L. (2003) 'Bioleaching review part B: Progress in bioleaching: Applications of microbial processes by the minerals industries', *Applied Microbiology and Biotechnology,* 63(3), 249-257.

Petersen, J. and Dixon, D.G. (2007) 'Modelling zinc heap bioleaching', *Hydrometallurgy*, 85(1), 127-143.

Petersen, J. (2010a) 'Determination of oxygen gas-liquid mass transfer rates in heap bioleach reactors', *Minerals Engineering,* 23(6), 504-510.

Petersen, J. (2010b) 'Modelling of bioleach processes: Connection between science and engineering', *Hydrometallurgy,* 104(3-4), 404-409.

Rawlings, D. E. (2002) 'Heavy metal mining using microbes', *Annual Review of Microbiology,* 56, 65-91.

Rawlings, D. E., Dew, D. and du Plessis, C. (2003) 'Biomineralization of metal-containing ores and concentrates', *Trends in Biotechnology,* 21(1), 38-44.

Rawlings, D. E. and Johnson, D. B. (2007) 'The microbiology of biomining: development and optimization of mineral-oxidizing microbial consortia', *Microbiology,* 153, 315-324.

Rohwerder, T., Gehrke, T., Kinzler, K. and Sand, W. (2003) 'Bioleaching review part A: Progress in bioleaching: Fundamentals and mechanisms of bacterial metal sulfide oxidation', *Applied Microbiology and Biotechnology,* 63(3), 239-248.

Sheikhzadeh, G. A., Mehrabian, M. A., Mansouri, S. H. and Sarrafi, A. (2005) 'Computational modelling of unsaturated flow of liquid in heap leaching - using the results of column tests to calibrate the model', *International Journal of Heat and Mass Transfer,* 48(2), 279-292.

Stevenson, R., Harrison, S. T. L., Mantle, M. D., Sederman, A. J., Moraczewski, T. L. and Johns, M. L. (2010) 'Analysis of partial suspension in stirred mixing cells using both MRI and ERT', *Chemical Engineering Science,* 65(4), 1385-1393.

Watling, H. R. (2006) 'The bioleaching of sulphide minerals with emphasis on copper sulphides - A review', *Hydrometallurgy,* 84(1-2), 81-108.

Wu, A. X., Yin, S. H., Qin, W. Q., Liu, J. S. and Qiu, G. Z. (2009) 'The effect of preferential flow on extraction and surface morphology of copper sulphides during heap leaching', *Hydrometallurgy,* 95(1-2), 76-81.

Wu, A. X., Yin, S. H., Yang, B. H., Wang, J. and Qiu, G. Z. (2007) 'Study on preferential flow in dump leaching of low-grade ores', *Hydrometallurgy,* 87(3-4), 124-132.

Yang, B. H., Ai-Xiang, W., Jiang, H. C. and Chen, X. S. (2008) 'Evolvement of permeability of ore granular media during heap leaching based on image analysis', *Transactions of Nonferrous Metals Society of China,* 18(2), 426-431.

Chapter 3 – Imaging Theory

This chapter presents the theory behind the two imaging methods that are used in this thesis – Magnetic Resonance Imaging (MRI) and X-ray computed tomography (CT).

The discovery of Nuclear Magnetic Resonance (NMR) is attributed to Felix Bloch and Edward Purcell who in 1946 independently discovered the phenomenon and in 1952 shared the Nobel Prize. Their method was principally used for structural analysis in chemistry. Almost 30 years later Paul Lauterbur (1973) and Mansfield and Grannell (1973, 1975) extended the science to reconstruct the first proton density map and so develop Magnetic Resonance Imaging (MRI). Since its inception MRI has a proven to be a powerful technique for the non-invasive study of the spatial structure and dynamics of a huge variety of optically opaque systems. The fundamentals of NMR and MRI are presented in the first part of this chapter. This is followed by a description of the MRI acquisition methods used in this thesis.

The final section of this chapter is concerned with the basic principles of X-ray CT, a well established technique for the imaging of opaque samples. Though primarily developed and used as a non-destructive medical imaging technique, X-ray CT can also be a useful tool for the study of chemical engineering systems. Already in the field of heap bioleaching it has been used on a macro scale to study the slumping of ore beds (Lin et al. 2005, Yang et al. 2008) as well as on a micro scale to monitor the structure of ore particles as a leach progresses (Ghorbani et al. 2011).

3.1   Basics of NMR

3.1.1   Introduction

Protons, neutrons and electrons in an atom all possess a fundamental quantum mechanical property called spin. It is quantified by the spin quantum number, I, with each individual nucleon constituent having $I=\frac{1}{2}$. Atomic nuclei have a nuclear spin number, which is dependent on how many unpaired protons and neutrons it contains. Nuclei that contain even numbers of protons and neutrons (hence even mass numbers) have no net spin and are NMR inactive. Nuclei with odd mass numbers have $\frac{1}{2}$ integer spin numbers, whilst nuclei with even mass numbers and odd atomic numbers have whole integer spin numbers. Table 3.1 summarises some of the most important atoms in NMR and their corresponding nuclear spin numbers. This thesis considers the spin of the ^1H atom in H_2O and in some instances exploits the NMR inactivity of ^2H (or D) in D_2O.

Table 3.1. Unpaired nucleons and net spin number for a selection of atoms.

Nuclei	Unpaired Protons	Unpaired Neutrons	Net Spin
^{1}H	1	0	1/2
^{2}H	1	1	1
^{31}P	1	0	1/2
^{23}Na	1	2	3/2
^{14}N	1	1	1
^{13}C	0	1	1/2
^{19}F	1	0	1/2

The net spin of NMR active nuclei gives rise to a magnetic dipole along the spin axis. The angular momentum, $\mathbf{P}$, of a nucleus may be determined based on the spin quantum number:

$$\mathbf{P} = \hbar\left[I(I+1)\right]^{\frac{1}{2}} \qquad 3.1$$

where $\hbar$ is the reduced Planck's constant. The magnetic moment, $\mathbf{m}$, of the nucleus is the intrinsic magnitude of the dipole and is related to the angular momentum by a proportionality constant called the gyromagnetic ratio, γ, which is characteristic for each nucleus:

$$\mathbf{m} = \gamma\mathbf{P} \qquad 3.2$$

In the absence of an external magnetic field, the magnetic moments of the individual nuclei are randomly orientated and so the net magnetic moment, $\mathbf{M}$, is zero. When placed in a static external magnetic field, $\mathbf{B}_0$, orientated along the z direction, the nuclear magnetic moments align with the field, a phenomenon known as the Zeeman interaction. This can occur in $2I+1$ ways corresponding to different possible energy levels, where the individual moments either reinforce or oppose $\mathbf{B}_0$. These possible energy states are separated by:

$$\Delta E = \hbar\gamma B_0 \qquad 3.3$$

In the case of the ^{1}H nucleus, two possible energy states exist, as depicted in Figure 3.1.
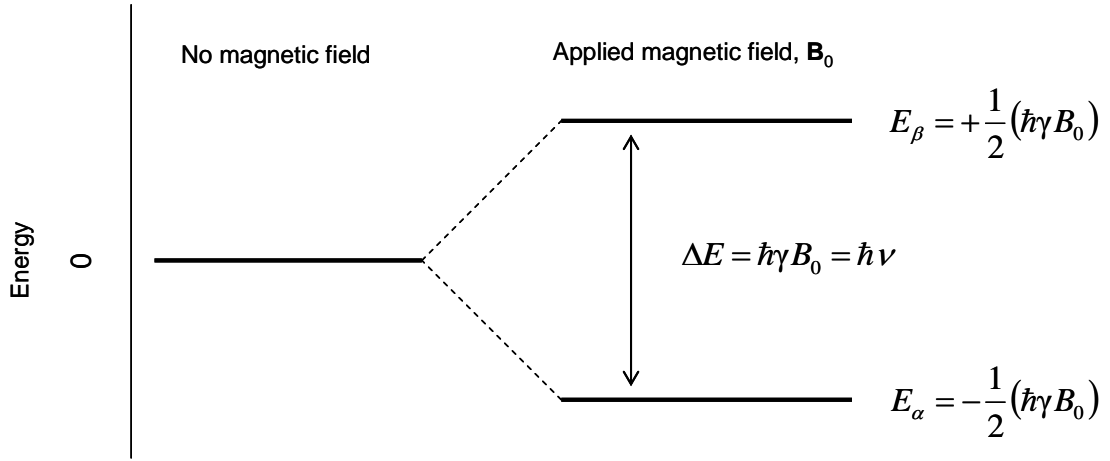
Figure 3.1. An energy level diagram for ^{1}H nucleus in the presence of an external magnetic field, $\mathbf{B_0}$.

Transitions between the energy states may be induced by using electromagnetic radiation of frequency v such that:

$$\Delta E = \hbar \gamma B_0 = \hbar v \qquad 3.4$$

It is this principle that is the basis of NMR. Knowledge of the gyromagnetic ratio of the atom in question and the applied magnetic field therefore allows for the determination of the required frequency. This resonance frequency is known as the Larmor frequency and is given by:

$$\omega_0 = \gamma B_0 \qquad 3.5$$

The Larmor frequency describes the frequency at which the magnetic moments of the nuclei precess around $\mathbf{B_0}$. The difference between the populations of the two energy states will determine the magnitude of the observable net magnetisation, $\mathbf{M}$, and is given by the Boltzmann distribution:

$$\frac{N_\beta}{N_a} = \exp(-\frac{\Delta E}{k_B T}) \qquad 3.6$$

where N_β and N_α are the populations of the higher and lower energy levels respectively, k_B is Boltzmann's constant and T is absolute temperature.

3.1.2   Spin Excitation, the Rotating Frame and Signal Detection

The net magnetisation vector, $\mathbf{M}$, can only be observed in the plane transverse to $\mathbf{B_0}$, known as the x-y plane. Orientation of $\mathbf{M}$ to this plane is achieved by applying a transverse magnetic field, $\mathbf{B_1}$, oscillating at ω_0 to the system thereby causing $\mathbf{M}$ to precess simultaneously around

both $\mathbf{B}_0$ and $\mathbf{B}_1$. This is known as the resonance phenomenon. The transverse magnetic pulse is induced by a sinusoidal current in a coil surrounding the sample at a frequency typically in the radio frequency (RF) range. The angle of rotation, α, of $\mathbf{M}$ depends on the length of time the field is on, τ, and its magnitude B_1 according to:

$$\alpha = \gamma \, \tau \, B_1 \qquad\qquad 3.7$$

A pulse of suitable magnitude and duration can tip $\mathbf{M}$ by 90°, transferring all of the magnetisation into the transverse plane. By doubling the time for the 90° pulse an 180° pulse may be achieved where $\mathbf{M}$ is completely inverted from its equilibrium state.

After the application of $\mathbf{B}_1$, the magnetisation vector will continue to rotate around $\mathbf{B}_0$ at the Larmor frequency. In order to simplify the motion of $\mathbf{M}$, a rotating frame of reference is introduced. In this case the frame rotates around $\mathbf{B}_0$ at the Larmor frequency and so $\mathbf{B}_1$ appears to remain static and $\mathbf{M}$ simply rotates about $\mathbf{B}_1$. This is illustrated in Figure 3.2.
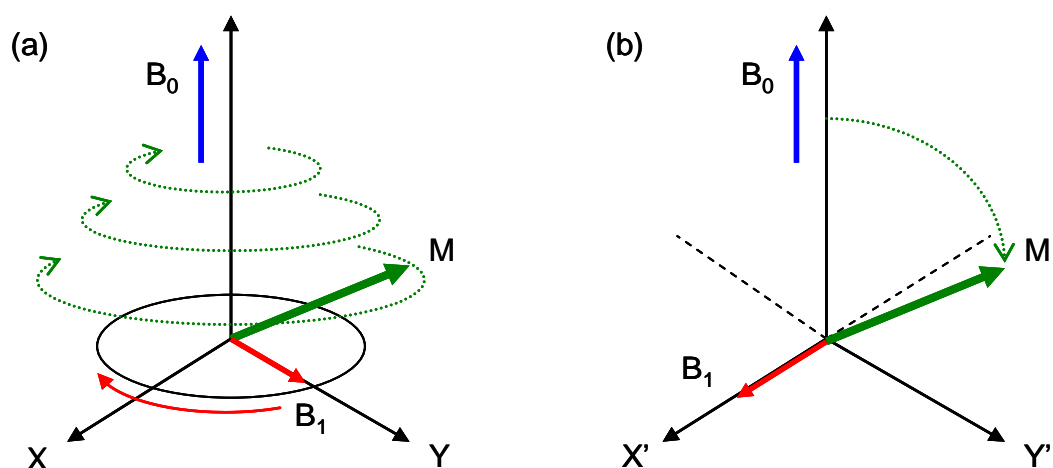
Figure 3.2. (a) The laboratory frame of reference and (b) the rotating frame of reference.

As $\mathbf{M}$ rotates about $\mathbf{B}_0$ it will induce a voltage in the same coil that is used to apply the RF pulse. This voltage is converted into a signal, S. Expressed in the time domain, the signal is an oscillating function known as the free induction decay (FID) shown in Figure 3.3 that decays in an exponential manner due to the relaxation effects that will be explained in the next section.
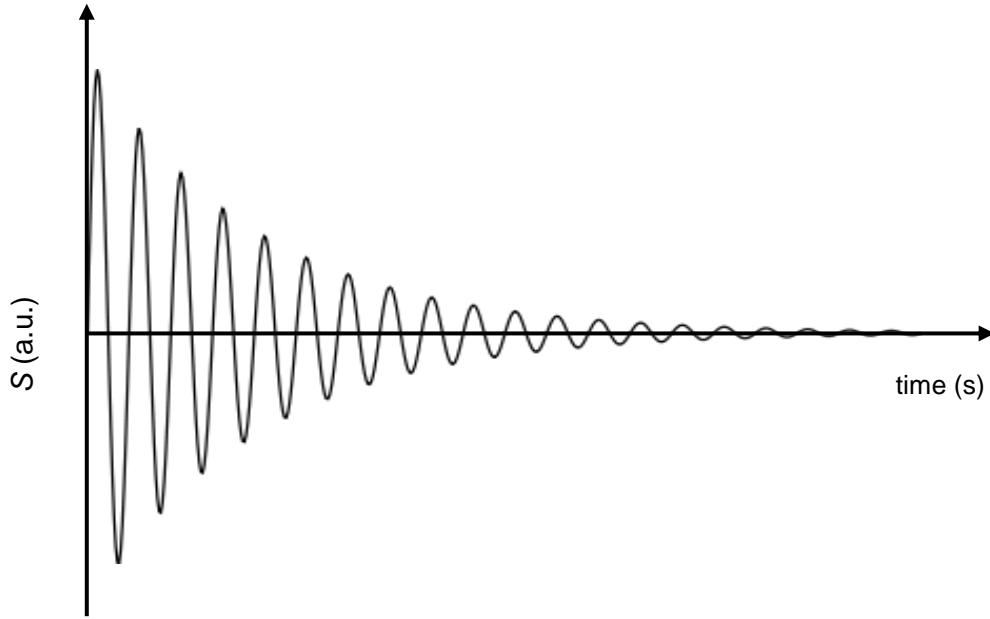
Figure 3.3. Example of a FID.

3.1.3 Spin Relaxation

When a RF pulse is applied to a sample, the result is to remove the spin system from its equilibrium state. The process whereby the spins return to equilibrium is known as relaxation.

3.1.3.1 Spin-Lattice Relaxation

Spin-lattice relaxation describes the return to equilibrium of the longitudinal magnetisation component through the exchange of energy between the spin system and the thermal reservoir surrounding it (the 'lattice'). This recovery process may be expressed as:

$$\frac{dM_z}{dt} = -\frac{(M_z - M_0)}{T_1}$$

3.8

where M_z is the z-component of magnetisation, M_0 is the equilibrium z-component of magnetisation and T_1 is the spin-lattice relaxation time constant. The most common way to measure the T_1 of a sample is by using the inversion recovery pulse sequence. In this sequence the magnetisation is first inverted using an 180° pulse, followed by a 90° pulse after time t_d to flip the magnetisation into the transverse plane and so allow for its detection. The relaxation from $-M_0$ back to M_0 at thermal equilibrium can be ascertained by varying t_d. The solution to Equation 3.8 may then be used to estimate T_1 and is given by:

$$M_z(t_d) = M_0 \left(1 - 2\exp\left(-\frac{t_d}{T_1}\right)\right)$$

3.9

A second way to measure T_1 is to use the saturated recovery method. This method uses a series of 90° pulses to destroy the magnetisation to the centre from whence the signal is measured as before. It takes about $5{\times}T_1$ for equilibrium to be reached almost fully.

3.1.3.2 Spin-Spin Relaxation

The second relaxation process is known as spin-spin relaxation and it describes the return to equilibrium of the transverse magnetisation through the interaction with the other nuclear spins. The result of this process is that the individual spins dephase thereby assuming random orientations and so increasing the entropy of the system. It is often modelled as:

$$\frac{dM_{xy}}{dt} = -\frac{M_{xy}}{T_2}$$

3.10

the solution to which is:

$$M_{xy}(t) = M_{xy}(0)\exp\left(-\frac{t}{T_2}\right)$$

3.11

where T_2 is the spin-spin relaxation time constant and M_{xy} is the transverse component of magnetisation. T_2 will always be less than or equal to T_1.

The irreversible loss in transverse magnetisation, T_2, is a result of interaction between molecules. It is determined using the CPMG pulse sequence. This method exploits the spin-echo pulse sequence which consists of a 90° pulse followed by multiple 180° pulses and will be described in further detail later in this chapter. The amplitude of the echo can then be fitted to Equation 3.11 to estimate T_2.

The second factor that contributes to transverse relaxation decay, $T_{2,inhomogeneous}$, is inhomogeneities in B_0, the effect of which is almost reversible through echo formation as described above. The combined time constant that describes the transverse relaxation is T_2^*, also known as the effective spin-spin relaxation constant. Assuming an exponential decay, it is given as:

$$\frac{1}{T_2^*} = \frac{1}{T_2} + \frac{1}{T_{2,inhomogenous}}$$

3.12

T_2^* may be calculated following a pulse-acquire sequence from the full width at half the maximum height (FWHM) of the resonance line shape in the frequency domain according to:

$$T_2^* = \frac{1}{\pi\,FWHM}$$

3.13

3.2   Basics of MRI

3.2.1   Magnetic Field Gradients

For NMR spectroscopy experiments it is desired to obtain information regarding the chemical environment of the spins; hence it is important to have as homogeneous an applied magnetic field as possible. However, in order to obtain information about the position of the nuclei in a sample (perform an imaging experiment) it is necessary to apply magnetic gradients to the system. These gradients are constant across the sample and may be applied in all three dimensions. The Larmor frequency of a nucleus within the sample thus becomes a function of its position according to the equation:

$$\omega(\mathbf{r}) = \gamma\left(B_0 + \mathbf{G}\cdot\mathbf{r}\right) \qquad\qquad 3.14$$

where $\mathbf{G}$ is the magnetic gradient and $\mathbf{r}$ refers to the position within the sample.

3.2.2   Spin Density and k-space

If the effects of relaxation are ignored, the transverse magnetisation and so the signal dS from an element of volume dV at position $\mathbf{r}$ with spin density $\rho(\mathbf{r})$ may be expressed in complex notation as:

$$dS\left(\mathbf{G},t\right) \propto \rho(\mathbf{r})dV \exp\left[i\,\omega(\mathbf{r})t\right] \qquad\qquad 3.15$$

Ignoring the constant of proportionality and substituting Equation 3.14 this becomes:

$$dS\left(\mathbf{G},t\right) = \rho(\mathbf{r})\exp\left[i\,\gamma\left(B_0 + \mathbf{G}\cdot\mathbf{r}\right)t\right]dV \qquad\qquad 3.16$$

By recording the signal in the rotating frame the γB_0 term may be neglected. This is achieved through a process known as 'heterodyne mixing' where the RF signal is mixed with a reference oscillation at frequency γB_0, the 'on-resonance' condition. The integrated signal may then be written as:

$$S(t) = \iiint \rho(\mathbf{r})\exp\left[i\,\gamma\,\mathbf{G}\cdot\mathbf{r}\,t\right]d\mathbf{r} \qquad\qquad 3.17$$

In order to simplify this relationship, the concept of $\mathbf{k}$-space is introduced, where:

$$\mathbf{k} = \frac{\gamma\,\mathbf{G}\,t}{2\pi} \qquad\qquad 3.18$$

The $\mathbf{k}$-space vector has units of reciprocal space [m^{-1}] and may be traversed either by moving in time or by changing $\mathbf{G}$. Hence Equation 3.17 may be rewritten as:

$$S(\mathbf{k}) = \iiint \rho(\mathbf{r}) \exp[i\, 2\pi \mathbf{k} \cdot \mathbf{r}] d\mathbf{r} \qquad\qquad 3.19$$

The spatial distribution of the spins can be found by applying a Fourier transform to Equation 3.19 to obtain:

$$\rho(\mathbf{r}) = \iiint S(\mathbf{k}) \exp[-i\, 2\pi \mathbf{k} \cdot \mathbf{r}] d\mathbf{k} \qquad\qquad 3.20$$

Thus it may be seen that $\rho(\mathbf{r})$ and $S(\mathbf{k})$ are a mutually conjugate Fourier transform pair. In order to acquire a fully resolved image, all of the points in **k**-space need to be traversed and acquired. This is generally done using frequency and/or phase encoding.

3.2.3 Frequency Encoding

Frequency encoding is where a line of **k**-space is acquired using a constant field gradient, called the read gradient, G_R. This acquisition process is shown schematically in Figure 3.4, where section (a) describes the pulse sequence and section (b) illustrates what happens in **k**-space. The applied gradient is comprised of two parts. The first application of the gradient, label 1 in Figure 3.4 (a), is known as the dephasing gradient. It serves to take the spins to the positive edge of **k**-space following generation of the transverse magnetisation by the application of the 90° excitation pulse. The 180° pulse (step label 2 in Figure 3.4 (a)) that is applied after half the echo time, TE, then inverts the spins to the negative edge of **k**-space. The second read gradient, label 3 in Figure 3.4 (a), carries the spins back to the positive edge of **k**-space. The echo signal is acquired at intervals t_{dw}, the dwell time, while the second, rephasing read gradient is applied so that an entire line of **k**-space is sampled. Due to the effect of the gradient, different parts of the signal will have different Larmor frequencies.

Fourier transformation of the data (as acquired using the 1D sequence in Figure 3.4) will produce a 1D projection of the spins along the axis of the applied gradient, in this case x. From Fourier transform theory, the field of view (FOV), Δx, of the projection is the inverse of the spacing between the points in **k**-space, dk, and so:

$$\Delta x = \frac{1}{dk} = \frac{2\pi}{\gamma G_R t_{dw}} \qquad\qquad 3.21$$
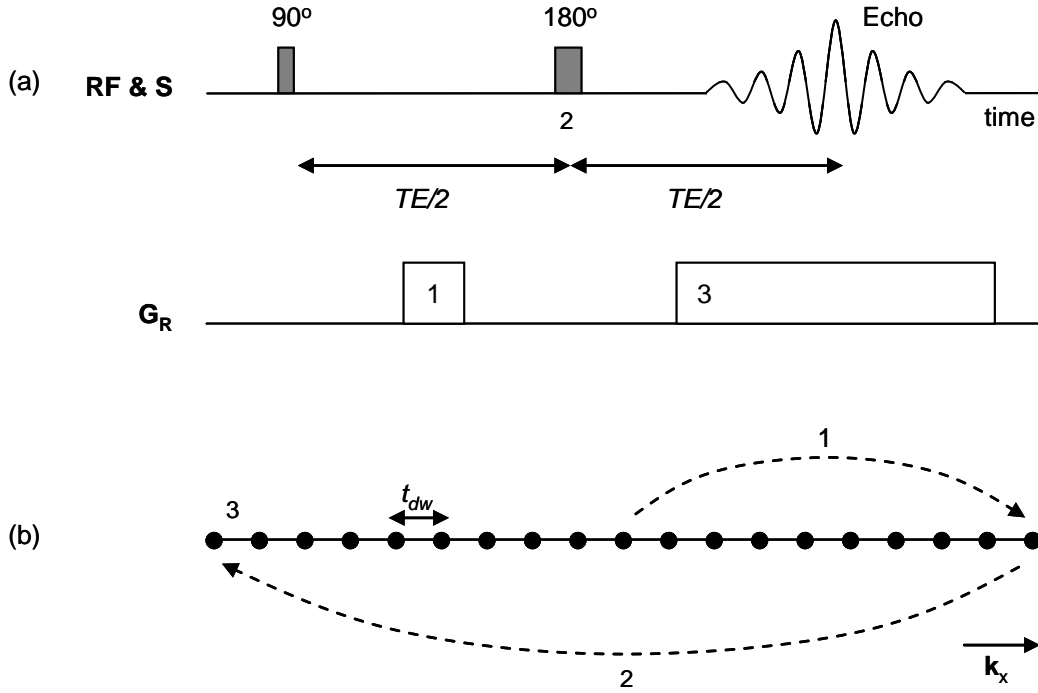
Figure 3.4. Schematic representation of acquisition of a single line of **k**-space by frequency encoding where (a) describes the 1D pulse sequence and (b) shows what correspondingly happens in **k**-space.

3.2.4   Phase Encoding

The second method for traversing **k**-space is phase encoding. Here an additional field gradient, G_P, is applied between the 90° and 180° pulses. It serves to encode the phase of the spins depending on their position in the sample. The resulting phase shift of an individual spin is given as:

$$\varphi = \gamma \mathbf{G}_P \cdot \mathbf{r}\, t \qquad\qquad 3.22$$

The time for which the gradient is applied, t_p, is fixed, so in order for successive phase encoded points in **k**-space to be acquired, the strength of the phase encode gradient is ramped. It is conventionally ramped from the negative to the positive edge of **k**-space. The phase encoding process is shown schematically in Figure 3.5. In this case the FOV is:

$$\Delta x = \frac{1}{dk} = \frac{2\pi}{\gamma G_P t_p} \qquad\qquad 3.23$$
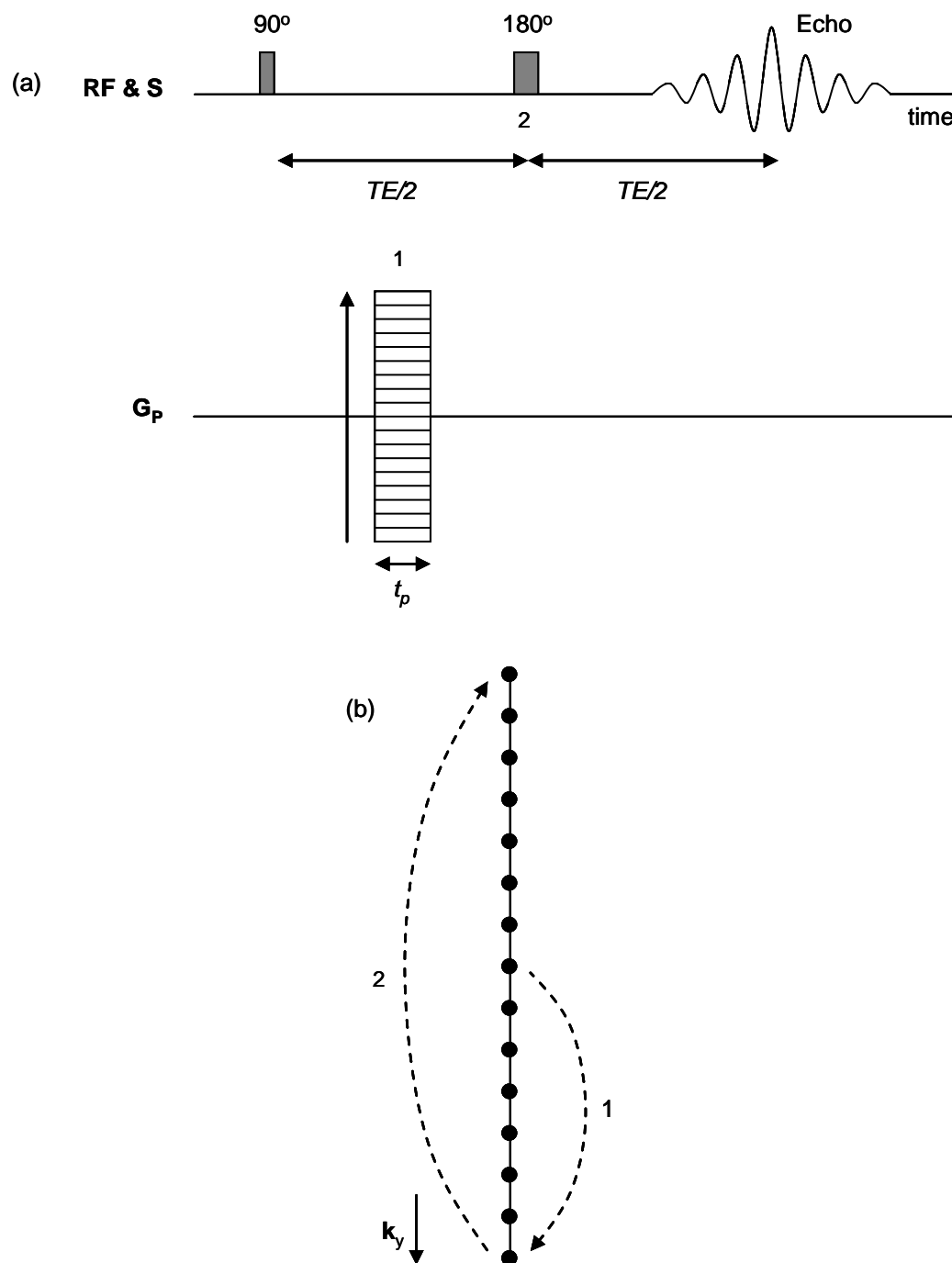
Figure 3.5. Schematic of phase encoding where (a) describes the 1D pulse sequence applied in the y direction and (b) shows what correspondingly happens in **k**-space.

3.2.5   Slice Selection

Slice selection is obtained when only a specific region of the NMR frequency spectrum is excited during the application of a slice gradient, the result of which is an MRI acquisition of a select region of the sample, a 'slice'. This is achieved through the simultaneous application of a soft RF pulse (frequency selective) and a slice selective gradient, G_S, as is illustrated in Figure 3.6. The gradient causes the spins along its direction of application to have different Larmor frequencies as determined by Equation 3.14. A soft RF pulse will excite only a select bandwidth of frequencies, therefore only those spins that have a Larmor frequency that falls into the RF bandwidth will be excited. The width of the slice may be adjusted by altering either the RF bandwidth or G_S.
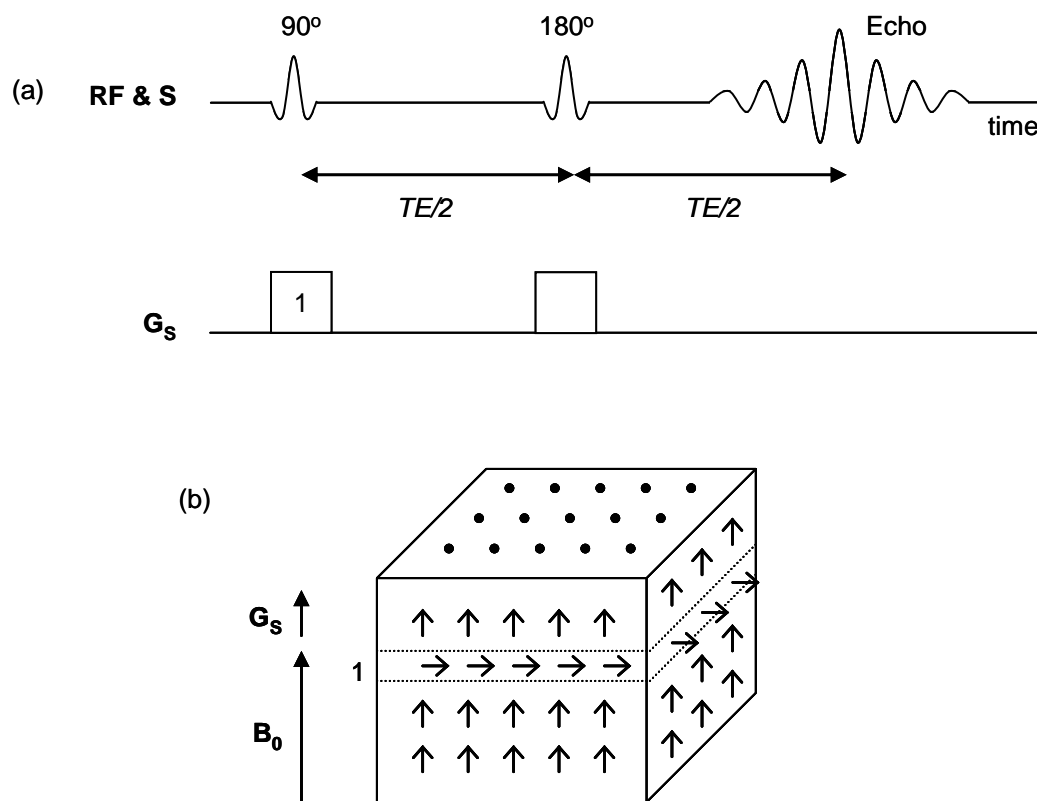
Figure 3.6. Schematic of slice selection where (a) shows the simultaneous application of the soft RF pulse and the slice selection gradient and (b) demonstrates the effect on a cube of magnetised vectors.

3.2.6   Signal to Noise Ratio (SNR)

The SNR of an image is a common measure of the image's quality and relates the signal received to the noise in the background of the image. One method of improving SNR is to

employ signal averaging where multiple scans are performed and then co-added. True signal will add coherently; conversely, noise adds in random phase. The SNR will improve by $N^{1/2}$, where N is the number of scans. The recovery time, TR, also has a strong influence on the SNR. As previously described, full recovery of the transverse magnetisation occurs after approximately $5 \times T_1$. A TR less than this will result in only a fraction of the original magnetisation being recovered, so the acquired signal decreases. The pulse angle can too be optimised for SNR, with the optimal angle for a pulse acquire known as the Ernst angle, θ_E (Callaghan 1995). It may be calculated as:

$$\cos \theta_E = \exp\left[-\frac{TR}{T_1} \right]$$

3.24

The Ernst angle is only truly optimal for a single pulse acquisition, but is near optimal for a single spin echo. In the case of a 90° tip angle, as commonly used in MRI acquisition sequences, the optimal SNR is acquired when the repetition time, TR, is equal to 1.256 times T_1 (Sankey 2008).

Further factors that influence SNR will be discussed on a case by case basis later in this and subsequent chapters. SNR can be calculated by taking the mean of a homogeneous area of signal by the standard deviation of the image background (noise) (Haacke et al. 1999). Care must be taken to not include any artefacts in the background noise value.

3.2.7   Magnetic Susceptibility Artefacts

The magnetic susceptibility of a material describes the degree to which it is magnetised in the presence of a magnetic field. Ferro- and paramagnetic materials contain unpaired valence electrons which will line up with an external magnetic field, thereby reinforcing it. This effect is much stronger for ferromagnetic materials as the electrons tend to align themselves in a parallel fashion so as to maintain a lower energy state. Diamagnetic materials oppose the magnetic field, but their effect is much weaker than that of ferro- and paramagnetic materials. The electrons in a diamagnetic material are paired so there is no permanent net magnetic moment of the atom. The effect of the magnetic susceptibility of a material is to create local distortions in the static magnetic field, $\mathbf{B}_0$, as illustrated in Figure 3.7.

Magnetic susceptibility will always affect the signal in an MRI acquisition, but it is only when there are large and abrupt susceptibility differences between adjacent substances that significant artefacts will result (Farahani et al. 1990, Lüdeke et al. 1985). The field inhomogeneities cause local shortening of the T_2^* which can result in poor SNR due to a loss of signal. A further effect is to induce local variations in the Larmor frequencies of the spins

(according to Equations 3.5 and 3.14). This can result in the absence of spin excitation during slice selection and so a loss of signal. Spatial misregistration of the signal may also occur during the application of the read gradient which may cause the appearance of areas of (misregistered) intense signal and signal voids next to the ferro- or paramagnetic material. As a result, distortions in the images that are frequency encoded tend to be observed in the read direction (Schenck 1996). This issue does not occur with phase encoding so the appearance of such artefacts can be minimised by the application of certain pulse sequences, such as pure phase encoding imaging techniques.
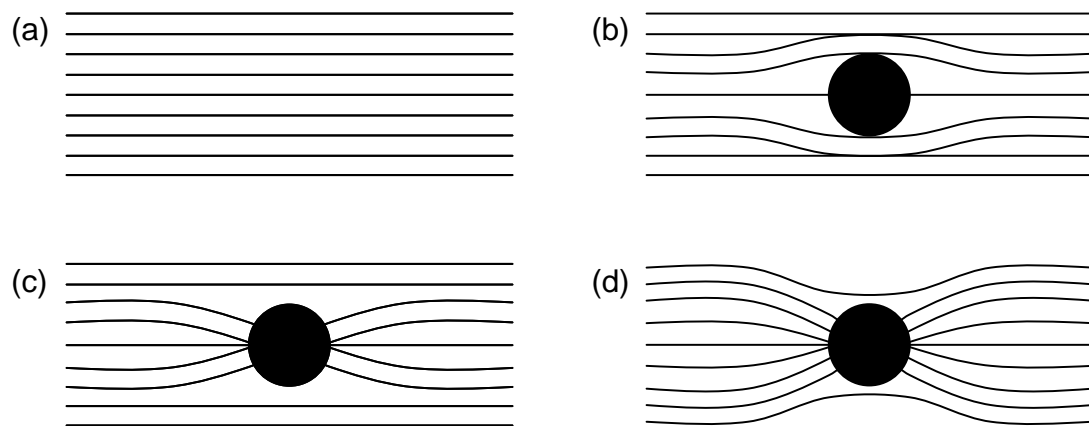
Figure 3.7. The effect of magnetic materials on a (a) uniform magnetic field. Diamagnetic materials (b) have a slight negative magnetic susceptibility and so repel the magnetic lines of force. Paramagnetic materials (c) have a positive magnetic susceptibility and therefore attract the magnetic lines of force. Ferromagnetic materials (d) have a stronger attractive effect and can result in substantial distortion in the uniformity of the magnetic field. Adapted from Patton (1994).

3.3   MRI Acquisition Methods

3.3.1   Spin Echo Imaging

Spin echo imaging is the most common imaging method. It consists of a 90° pulse followed by an 180° pulse after a time $TE/2$ where TE is the echo time. The 180° pulse serves to refocus the spins that have dephased due to inhomogeneities in the magnetic field thereby forming an echo with the spins coming back into phase at time TE after the 90° pulse. Spin echo imaging makes use of both changes in gradient strengths and time to traverse **k**-space. The slice selective gradient, G_S, along the z-axis is applied simultaneously with the RF pulse and ensures that only a slice of the spins in a sample are tipped and hence imaged. A reversed

slice gradient is applied directly after this to rephase the spins. The gradients in the frequency and phase (or x and y) directions that are applied between the 90° and 180° pulses are used to move to different positions in **k**-space. Time is then used to traverse the length of **k**-space during the echo formation. A second frequency encode gradient, called the read gradient, is applied at this time such that the resonance frequency of the spins are given positional dependence. Figure 3.8 is a schematic of the basic pulse sequence.
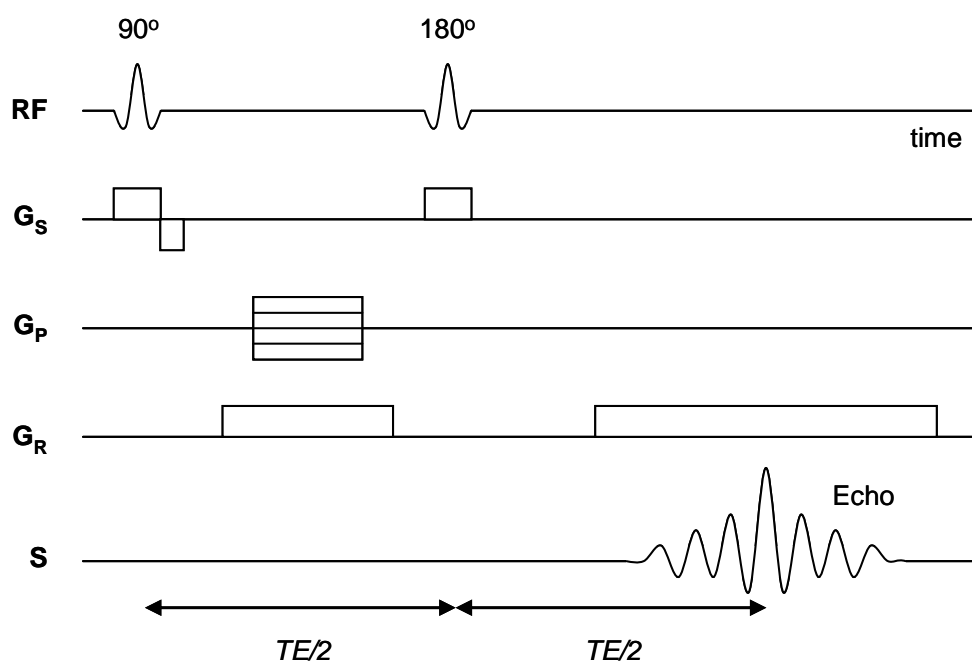
Figure 3.8. Simple spin-echo pulse sequence.

3.3.2   Single Point Imaging (SPI)

SPI, also known as constant time imaging, is a pure phase encoding technique that was developed by S. Emid and J.H.N. Creyghton (Emid and Creyghton 1985, Emid 1985). Pure phase encoding means that the time evolution of the signal is not measured during the acquisition sequence and as a result the extent to which magnetic susceptibility, chemical shift and dipolar and quadrupolar distortions are observed is significantly reduced (Gravina and Cory 1994). Magnetic susceptibility artefacts have been discussed already in Section 3.2.7. Chemical shift artefacts occur when there are species of different chemical composition in a sample, such as fat and water in medical MRI, which have slightly different Larmor frequencies because of the magnetic shielding of the nucleus by the electron cloud (Callaghan 1995). Dipolar interactions are due to the influence of the small magnetic field associated with each nuclear spin dipole on the dipole moments of neighbouring spins (Callaghan 1995). Finally, quadrupolar interactions occur when the electric quadrupole moment, which exists in

atoms with $I > ½$ which have an asymmetric distribution of the nucleons, interacts with the electric field gradient thereby affecting the Zeeman interaction (Callaghan 1995, Fukushima and Roeder 1981).

A typical 3D SPI pulse sequence is shown in Figure 3.9. Gradients are applied in all three Cartesian directions, after which a RF excitation pulse is applied that tips the magnetisation vector by a small angle, α. A single point in **k**-space is acquired at a set time, t_p, after each RF excitation pulse, unlike in conventional frequency encoded methods where an entire line of **k**-space is recorded per pulse. Therefore the time evolution of the signal is not measured and so only the interaction of the applied gradients contributes to the signal distribution. The basic SPI pulse sequence in Figure 3.9 is repeated after a time *TR*. With each repetition, the value of the applied gradient, *G*, is changed, thereby allowing for a three dimensional map of **k**-space to be traversed, according to Equation 3.18.
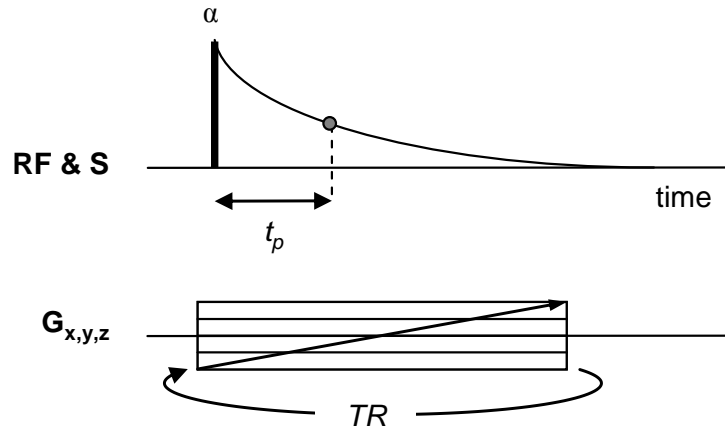
Figure 3.9. SPI pulse sequence in three dimensions.

The Nyquist theorem requires that the product of the FOV, Δx, and the increments between each **k**-space measurement, dk, is one:

$$dk\,\Delta x = 1 \qquad\qquad 3.25$$

Violation of the Nyquist condition causes image artefacts to develop, such as wrap around. If this theorem is combined with the definition of **k** (Equation 3.18) then the gradient increment, dG, is defined as a function of the FOV and the phase encoding time:

$$dG = \frac{2\pi}{\gamma t_p \Delta x} \qquad\qquad 3.26$$

Hence if *n* points in **k**-space are measured along one dimension, the maximum gradient needed is:

$$G_{max} = \frac{\pi n}{\gamma t_p \Delta x}$$

3.27

The missing factor of 2 in Equation 3.27 is because both positive and negative gradient values are used (Gravina and Cory 1994).

SPI makes use of hard RF pulses and therefore is not slice selective. This is a potential disadvantage of the method, especially if a sample extends beyond the RF probe or if only a particular region of the sample is of interest. Balcom et al. (1996) presented a crude slice selection technique where they used a movable internal RF shield to restrict the excitation to a specific region of the sample.

As the pulses are applied in the presence of the gradients, they need to be sufficiently short in order to excite all of the frequencies introduced by the applied gradients. Gravina and Cory (1994) have determined limits on the pulse duration, t_{pul}, and the filter width, FW, for a rectangular pulse to fulfil this requirement. If the spatial extent of the object is Δx and the maximum gradient strength is applied, the frequency bandwidth of the pulse, Δv, needs to be:

$$\Delta v \geq \frac{\gamma G_{max} \Delta x}{2\pi} = \frac{n}{2t_p}$$

3.28

The pulse duration may be approximated as the inverse of the bandwidth and so:

$$t_{pul} = \frac{1}{\Delta v} \leq \frac{2t_p}{n}$$

3.29

The receiver bandwidth also needs to be large enough to accommodate the entire frequency spread. The frequency measured at the maximum gradient will be $\Delta v/2$, assuming that the spectrum is on resonance in the absence of the gradient. Therefore:

$$FW \geq \frac{n}{4t_p}$$

3.30

If these limits are not adhered to, the magnetisation measurements near the maximum gradients (large **k**-space values) will be attenuated. This in turn will result in the blurring of the sharp edges of the image and a lower than expected resolution.

3.3.2.1 Single Point Ramped Imaging with T_1-enhancement (SPRITE)

One of the major disadvantages of SPI is the long acquisition times. Attempting to reduce the time by rapidly switching the gradient pulses can result in excessive gradient vibration due to impulsive Lorentz forces. In response to this problem Balcom et al. (1996) developed a

modified version of SPI: single point ramped imaging with T_1-enhancement (SPRITE). In the SPRITE sequence the gradient in the primary encode direction is ramped in discrete steps, with a RF pulse being applied and a data point collected at each step, thereby avoiding the time wastage incurred through the switching on and off of the gradients. This allows for faster acquisition times with greatly reduced dB/dt, thus minimising gradient vibration. A typical 3D SPRITE pulse sequence is shown in Figure 3.10.
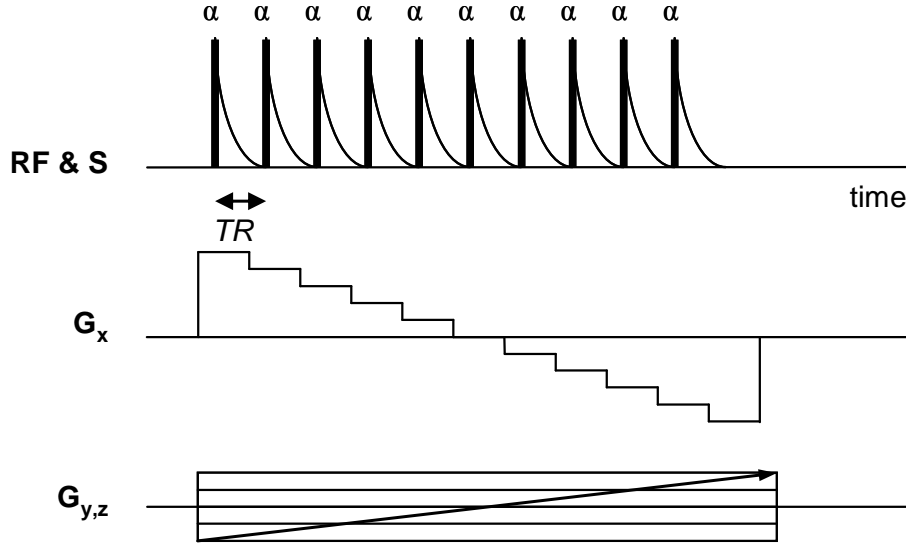
Figure 3.10. SPRITE pulse sequence.

SPRITE is well suited to imaging samples with short T_1 as this enables the use of a short TR. However, the applicability of SPRITE is compromised if the sample's T_1 is very long (in the order of a few seconds) as the magnetisation is not able to recover with the short TR, resulting in extensive blurring. Increasing the TR is undesirable for SPRITE as the gradient duty also increases which may lead to overheating. The tip angle can be made smaller in order to compensate for this, though this decreases the SNR. Therefore it is usually better to use SPI instead of SPRITE for long T_1 samples (Parasoglou et al. 2008).

3.3.2.2 Magnetisation Evolution

SPI is a transient magnetisation imaging technique. The longitudinal magnetisation, M_z, does not remain constant during a SPI experiment, but instead decays exponentially from the equilibrium magnetisation, M_0, to a steady state value as a function of the RF pulse tip angle, α, the spin-lattice relaxation time, T_1, and TR (Halse et al. 2004, Mastikhin et al. 1999, Parasoglou et al. 2008). This means that each point in **k**-space is sampled with a different amount of magnetisation, which results in the broadening of the point spread function (PSF) in real space of $\rho(\mathbf{r})$ (Parasoglou et al. 2008, Halse et al. 2004). Using the notation of

Mastikhin et al. (1999), the available longitudinal magnetisation after n excitation pulses and in the absence of magnetisation preparation is:

$$M_{z,n} = M_0(1-w)C^n D^n + M_0 w \qquad 3.31$$

where

$$D = \exp(-TR/T_1) \qquad 3.32$$

$$C = \cos(\alpha) \qquad 3.33$$

and

$$w = \frac{1-D}{1-CD} \qquad 3.34$$

The first term in Equation 3.31 is dependent on n and is therefore the transient component. It influences the image blurring. The second term, which is independent of n, is the steady-state component and it affects the SNR. The relative significance of these two terms is determined by the value of w (Halse et al. 2004, Mastikhin et al. 1999). An example of the evolution of the magnetisation as the number of pulses is increased is shown in Figure 3.11 for different values of α and TR/T_1. Longer T_1, shorter TR and larger tip angles, α, have the effect of increasing the extent of image blurring.
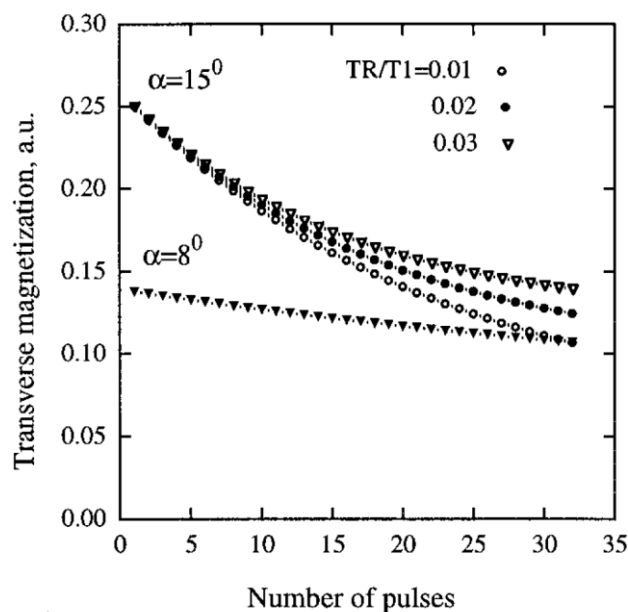

Figure 3.11. Transient behaviour of the observed magnetisation during a pulse train, according to Equation 3.31. (Mastikhin et al. 1999)

While *TR* affects the magnetisation evolution and hence the image resolution, it also influences the acquisition time of the experiment and the length of each gradient step. Practically, *TR* is set with consideration to the acquisition time and the duty cycle and is thus not necessarily optimised with respect to resolution (Halse et al. 2004). As T_1 is fixed for a given sample, the flip angle is the only parameter left that may be adjusted in order to optimise the image resolution. Making the flip angle larger has the effect of increasing the signal magnitude, but at the cost of resolution, as can be seen by comparing the magnetisation decay in Figure 3.11 when α is 8° and 15°. In addition to this, the bandwidth restriction on the RF excitation, as dictated by Equation 3.29, further limits the flip angle size. Hence the ability to vary the flip angle in order to prevent longitudinal magnetisation evolution is also limited (Mastikhin et al. 1999).

As with standard pulse acquire sequences, the transverse magnetisation decays after the application of the RF excitation pulse according to the time constant T_2^*, while the longitudinal magnetisation recovers with T_1. The image signal intensity for SPI is thus affected by both of these relaxation processes and is given by:

$$S(\mathbf{z}) = \rho(\mathbf{z})\exp\left(-\frac{t_p}{T_2^*}\right)\left[\frac{1-\exp(-TR/T_1)}{1-\cos(\alpha)\exp(-TR/T_1)}\sin(\alpha)\right] \qquad 3.35$$

where $\rho(\mathbf{z})$ is the local proton density. If an image is acquired with a small flip angle or long *TR* compared with T_1, the signal intensity simply becomes proportional to the local proton density weighted by the T_2^* value at that point:

$$S(\mathbf{z}) \propto \rho(\mathbf{z})\exp\left(-\frac{t_p}{T_2^*}\right) \qquad 3.36$$

Hence if T_2^* is known or constant at each point in the profile, the image may be used to obtain the relative spatial distribution of the sample. In the case where T_2^* is much longer than t_p the signal intensity becomes approximately proportional to the proton density.

3.3.2.3 Sensitivity

Gravina and Cory (1994) performed a detailed analysis comparing the sensitivity of SPI with conventional spin echo imaging techniques. In general, though SPI will provide distortion free images, it will have a lower sensitivity (SNR) than that of frequency encoded methods. However, they found that SPI had higher sensitivity when a sample's T_2 is shorter than the gradient stabilisation time. This advantage is increased even further when the number of acquired points is decreased.

3.3.2.4   Multiple Point Acquisition (MPA)

The efficiency of SPI experiments is considerably less than that of frequency encoding methods as only a single point in **k**-space is obtained for every RF pulse. In order to improve the efficiency Halse et al. (2004) proposed that multiple FID points are collected following each excitation pulse. This technique was originally applied to SPRITE sequences, though it is equally applicable to SPI (Parasoglou 2009). An example of a multiple point acquisition (MPA) sequence is given in Figure 3.12.
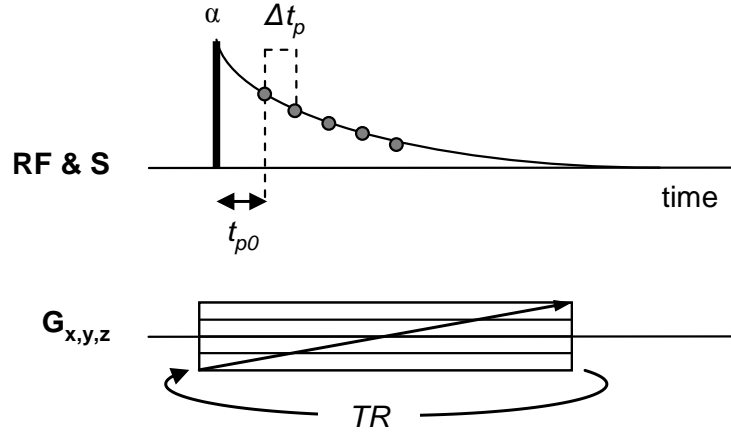
Figure 3.12. A multiple point acquisition with $N_T = 5$.

A total of N_T points are collected, with the first point sampled at a time t_{p0} after the excitation pulse and the remaining points sampled in intervals of Δt_p thereafter. Hence the acquisition time of the jth point will be:

$$t_{p,j} = t_{p0} + (j-1)\Delta t_p \qquad \text{for} \qquad 1 \le j \le N_T \qquad\qquad 3.37$$

Therefore, N_T complete sets of **k**-space data points will be acquired, each corresponding to a unique t_p value. This extra information can then be used to map T_2^* and for signal averaging, where successive images are added in order to improve the SNR. However, the data sets cannot be directly compared or added as each will have different T_2^* weighting and **k**-space encoding according to Equation 3.18. The T_2^* weighting can be minimised through the use of short dwell times in the case of signal averaging and can even be advantageous in T_2^* mapping applications. The **k**-space encoding, though, must be corrected for. The different data sets will all have a unique **k**-space step size and hence a unique FOV, according to the Nyquist theorem (Equation 3.25). The FOV for the jth point is:

$$\Delta x_j = \frac{2\pi}{\gamma \, dG \, t_{p,j}} \qquad\qquad 3.38$$

This relationship indicates that the FOV is inversely proportional to the phase encode time. Hence in order to make the information sets comparable, the individual FOVs need to be scaled to a common value. This is achieved through the implementation of a Chirp z-Transform (CZT) (Rioux et al. 2007, Kaffanke et al. 2006, Halse et al. 2004).

The CZT belongs to the more general family of z-Transforms, which for a defined set of numbers x_n is defined as:

$$X(z_k) = \sum_{n=0}^{N-1} x_n z_k^{-n}$$ 3.39

where there exist N non-zero points in the sequence of numbers. CZTs can be used to evaluate the z-Transform on any spiral or circular contour in the z-plane. The contour is defined by:

$$z_k = AW^{-k}$$ 3.40

where for a unit circle contour in the z-plane:

$$A = \exp(i\theta_0)$$ 3.41

$$W = \exp(i\phi_0)$$ 3.42

and so the CZT is given by:

$$X(z_k) = \sum_{n=0}^{N-1} x_n \exp(-in\theta_0)\exp(ink\phi_0)$$ 3.43

The parameters θ_0 and φ_0 in the above equations refer to the initial angle of the z-plane trajectory and the angular step, respectively. If a single rotation of the unit circle is evaluated using this algorithm where:

$$\theta_0 = 0 \text{ and } \quad \varphi_0 = -\frac{2\pi}{N}$$

the CZT simply becomes the discrete Fourier transform:

$$X(z_k) = \sum_{n=0}^{N-1} x_n \exp\left(-\frac{i2\pi nk}{N}\right)$$ 3.44

This means that the CZT evaluated on a unit circle may be used to transform **k**-space data to the image space. Furthermore, the CZT can be used to transform the **k**-space data to the image space and scale the image FOV simultaneously. The FOV image scaling factor, Z, is given as the ratio of the desired and actual FOV:

$$Z = \frac{\Delta x_{desired}}{\Delta x_{actual}} = \frac{t_{p,actual}}{t_{p,desired}}$$

3.45

Images are generally corrected with the smallest FOV (longest t_p) set as the desired FOV as this maximises the resolution (Rioux et al. 2007). In order to transform the **k**-space data into the image space while including the image scaling factor, the CZT is evaluated over the range of angles corresponding to ½(1-Z) through ½(1+Z). Put differently, the CZT is evaluated in N steps with:

$$\theta_0 = \pi(1 - Z) \quad \text{and} \quad \varphi_0 = -2\pi\frac{Z}{N}$$

In practice, application of this image scaling method requires that the total image intensity stay constant over the FOV correction. Through the scaling process the physical size of each voxel in the image is altered by a factor of Z^n where n is the number of dimensions that have been scaled. For the total signal to remain constant as is required, the signal in each voxel of the scaled image must be corrected by a factor of Z^n. This correction is applied to both the signal and the noise, introducing an inconsistency into the SNR of the FOV-corrected MPA images such that each image will have a different SNR. This effect may be minimised by keeping Z close to one. Halse et al. (2004) limited their Z to values greater than 0.8. Parasoglou (2009) kept their Z closer to 1 with a lower limit of approximately 0.9. He found that ratios below this resulted in blurring.

The number of points that can be sampled on the FID, N_T, is constrained by a few factors. The first is that the interval Δt_p must be large enough to avoid noise correlation between successive images. If points are too close, the noise may become correlated instead of random and so no improvement in the SNR would result from MPA. Secondly, the speed at which the spectrometer is able to take samples limits the minimum time between sample points. Finally, the extent of FOV scaling must be limited so that spatial resolution is maintained, as discussed above.

In order to ensure that the noise between points is not correlated, Halse et al. (2004) advocate that the dwell time between the sampled points on the FID must be greater than the inverse of twice the filter width. Hence, if the optimal filter width is used (equality in Equation 3.30) the constraint on Δt_p to maximise the SNR is:

$$\Delta t_p \geq \frac{2t_p}{n}$$

3.46

At this stage a T_2^* decay curve can be defined for each image voxel. Furthermore, a nuclei density map can be produced by using the relationship given in Equation 3.35 or 3.36, depending on the conditions. It must be noted that the range of t_p values that are required to define a T_2^* decay curve accurately is much greater than a single experiment's acceptable t_p range (Halse et al. 2004). Therefore several repeat experiments must be performed which together define the whole curve. A cluster of FID points is acquired in each experiment, such that all the previously mentioned limits are adhered to. This is shown schematically in Figure 3.13. The multiple FID point images are scaled to the FOV of the longest t_p within that experiment.
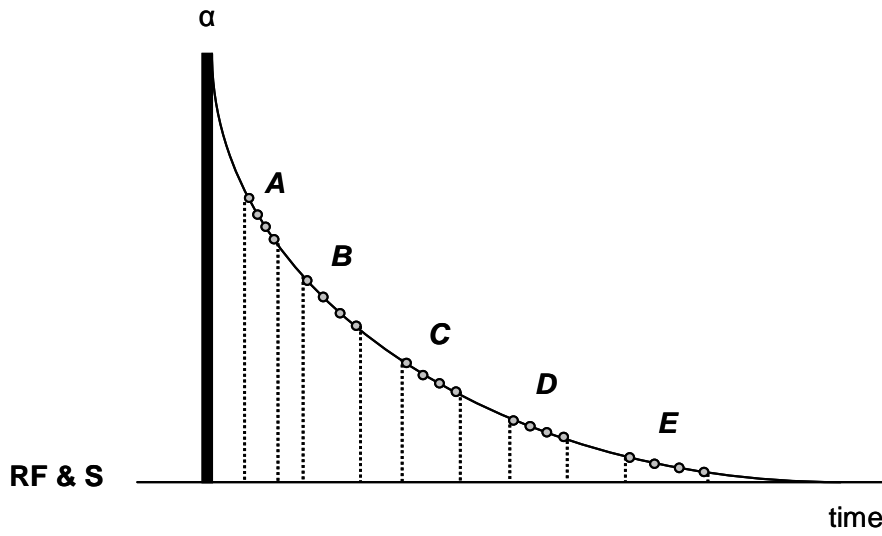
Figure 3.13. A multiple FID point acquisition scheme where experiments A to E sample clusters of points so that a T_2^* decay curve can be fitted.

3.3.3 Spin Echo Single Point Imaging (SESPI)

SESPI combines the principles of the spin echo and SPI acquisition methods in order to obtain images of increased relative SNR. It was first proposed by Prado et al. (2000) and then expanded on by Ouriadov et al. (2004). Like in SPI, **k**-space is traversed by changing the gradient magnitudes, with a single data point being collected per excitation. However in this sequence the collected data point is the signal magnitude at the peak of an echo so that a T_2 weighted image is obtained. Unlike in SPI, the RF pulses are applied in the absence of the gradients. This permits a much reduced filter width compared with SPI and hence an improved SNR as:

$$SNR \propto \frac{1}{\sqrt{FW}}$$
3.47

Ouriadov et al. (2004) proposed a set of standard SESPI pulse sequences. Since their publication, these sequences have been used by Zhang et al. (2008a), Zhang et al. (2008b) and Zhang and Balcom (2010). Figure 3.14 (a) illustrates the simplest form of SESPI. In this case a phase encoding gradient is applied after a 90° excitation pulse, followed by an 180° pulse. This results in the formation of an echo, the amplitude of which is recorded. In the second pulse sequence, Figure 3.14 (b), a second gradient is applied after the 180° pulse and is of opposite polarity to the first. This allows for a decreased encoding time, t_p, which consequently reduces the echo time, TE, by a factor of two relative to the first sequence. This means that there will be less time for T_2 decay and so an image of increased signal may be obtained.

(a)

(b)
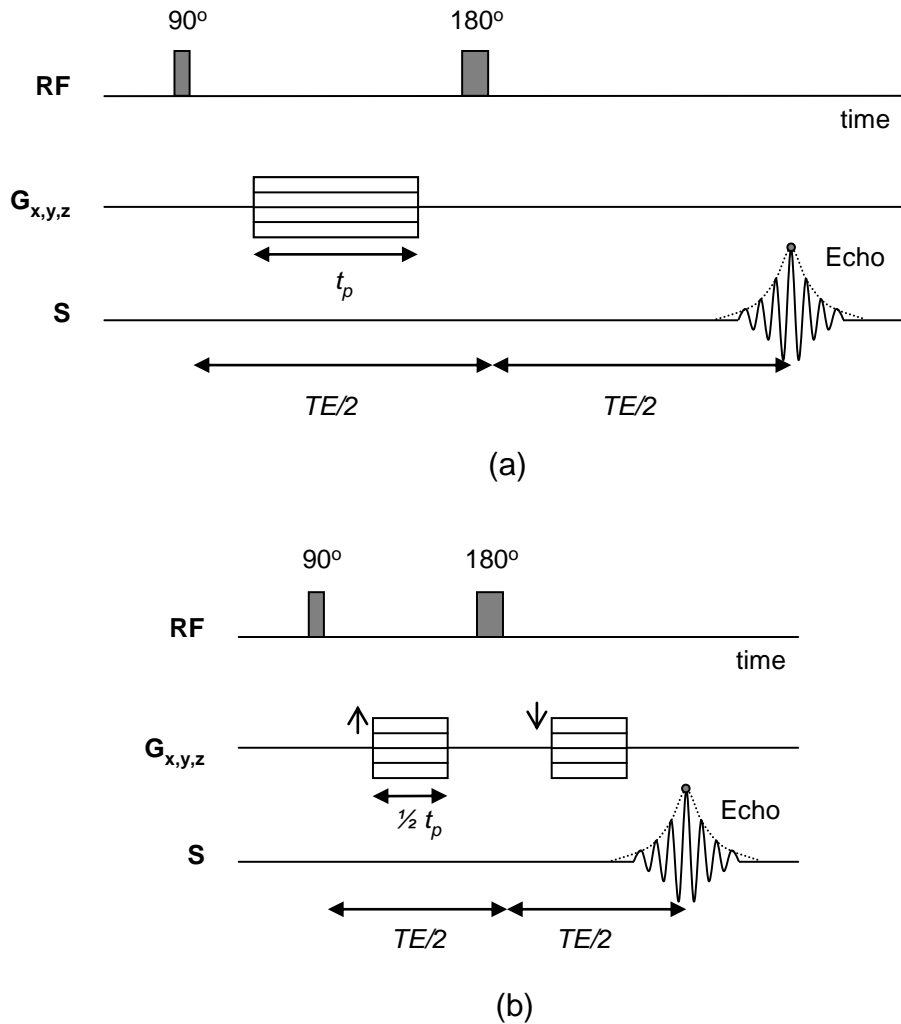
Figure 3.14. (a) Simple and (b) double phase encode SESPI pulse sequence

Multiple echoes can also be employed, thereby allowing for the acquisition of a series of T_2 weighted images. Ouriadov et al. (2004) expected significant inhomogeneities in their B_1

fields and so included spoiling gradients in their pulse sequence as well as an XY-4 phase cycle (Gullion 1993) in order to compensate for pulse length imperfections.

The signal acquired in a SESPI experiment such as that depicted in Figure 3.14 may be described by the following relationship:

$$S(\mathbf{k}) = \int \rho_0 \exp\left(-\frac{TE}{T_2}\right) \exp(i\,2\pi\mathbf{k}\cdot\mathbf{r})\,d\mathbf{r}$$

3.48

and so following Fourier transformation:

$$\rho(\mathbf{r}) = \rho_0 \exp\left(-\frac{TE}{T_2(\mathbf{r})}\right)$$

3.49

which closely resembles the expression for the nuclear spin density from a SPI acquisition.

3.4 X-ray CT

X-ray CT imaging is based on the measurement of the attenuation of the X-rays by the sample. Though X-ray scanners will vary in their individual configuration, all will include three key components, illustrated in Figure 3.15: an X-ray source, a sample through which the X-rays pass and a series of detectors which measure the X-ray intensity attenuation along multiple X-ray beam paths (Ketcham and Carlson 2001).

Figure 3.15. A basic X-ray CT imaging setup.

The most common X-ray source (also the type that is used in this study) is an X-ray tube which emits a fan beam wide enough to encompass the entire width of the sample. The effectiveness of an X-ray source is determined by the size of the focal spot (the area on the X-ray tube anode that is struck by electrons and from which the resulting X-rays are emitted),

the spectrum of X-ray energies that are generated and the X-ray intensity (Ketcham and Carlson 2001). The size of the focal spot is important as it determines the number of source-to-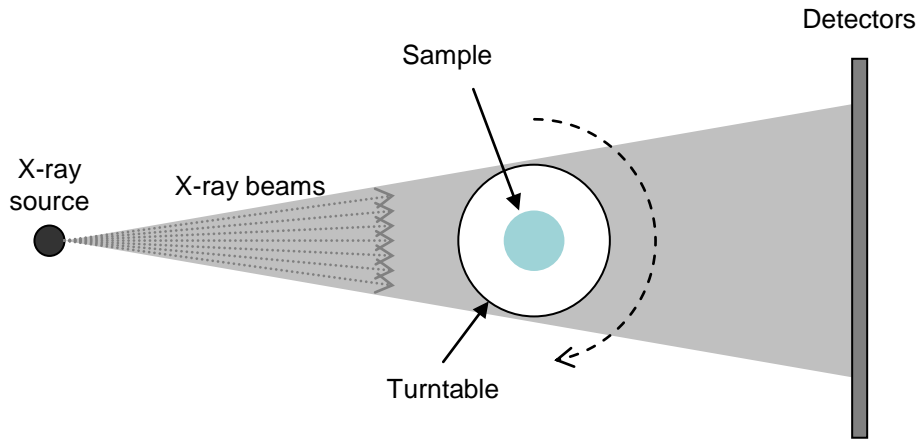detector paths that can intersect a given point in the sample and so it in part defines the spatial resolution obtainable by the system. The energy spectrum determines the penetrative ability of the X-rays, with higher energy X-rays being more effective at penetration than lower energy ones. The energy spectrum also defines the expected relative attenuation of the X-rays as they pass through materials of different densities. In this regard higher energy X-rays may be disadvantageous as they are less sensitive to changes in material density and composition. Finally, the X-ray intensity is set by adjusting the current and it affects the SNR, with higher intensities being effective at improving the SNR. However, this can be at the cost of a larger focal spot requirement to prevent thermal damage.

On the other end of the X-ray beam path, the detectors which measure the attenuated X-ray intensities usually contain scintillating materials in which the incoming X-rays produce flashes of light which are then counted. The size of an individual detector determines the amount of the sample that is averaged into a signal intensity region whilst the number of detectors determines the overall resolution of the image (Ketcham and Carlson 2001).

The relationship between the intensity of the applied and attenuated X-rays (I_0 and I_1) may be described by Beer's law in the case of a monochromatic (monoenergetic) X-ray source, such that:

$$\frac{I_1}{I_0} = \exp(-\mu h) \tag{3.50}$$

where μ is the linear attenuation coefficient and h refers to the length of the X-ray path through the sample (Van Geet et al. 2000). The attenuation of the X-ray signal is dominated by three processes, namely photoelectric absorption, Compton scatter and pair production (Ketcham and Carlson 2001). Photoelectric absorption is when the total energy of an incoming X-ray photon is transferred to an inner electron, thereby causing the ejection of the electron and therefore the ionisation of the atom. The interaction of a photon with an outer electron is known as Compton scatter or incoherent scatter. The result of Compton scatter is for the electron to be ejected while losing only part of its energy after which the photon is deflected in a different direction. Pair production is when the photon interacts with a nucleus thereby causing it to be transformed into a positron-electron pair. In this case any excess energy is transferred into kinetic energy in the particles produced. At energy levels below 200kV, Compton scatter and photoelectric absorption are known to have the predominant effect on μ, the effect of which may be expressed as:

$$\mu = \rho_b \left(a + b \frac{Z_b^{3.8}}{E^{3.2}} \right) \qquad 3.51$$

where ρ_b is the bulk density of the material, Z_b is the bulk atomic number of the material, E is the X-ray energy and a and b are energy dependent coefficients (Han et al. 2009). The first term within the brackets describes the effect of Compton scatter whilst the second term corresponds to the effect of photoelectric absorption (Van Geet et al. 2000). In the case where there is a mixture of atoms present, the effective atomic number Z_e is used:

$$Z_e = \left(\sum f_i Z_i^{3.8} \right)^{1/3.8} \qquad 3.52$$

where f_i is the fraction of the total number of electrons contributed by element i and Z_i is the associated atomic number (Van Geet et al. 2000). The factor $Z^{3.8}$ in Equation 3.51 means that as the atomic number increases, μ and hence the attenuation will become increasingly dominated by photoelectric absorption (Boespflug et al. 1995).

If the sample contains many different materials, the μ and h of each individual material must be considered and so Equation 3.50 becomes:

$$\frac{I_1}{I_0} = \exp\left[\sum_i (-\mu_i h_i) \right] \qquad 3.53$$

where i refers to the different materials. This situation is easily solved for a monochromatic beam, but in the case of a polychromatic X-ray source, the effect of the varying E on μ must be taken into account. To do this Equation 3.53 would need to be solved over the energy spectrum used:

$$I_1 = \int I_0(E) \exp\left[\sum_i (-\mu_i(E) h_i) \right] dE \qquad 3.54$$

The majority of reconstruction strategies solve for a single μ at each spatial position (Ketcham 2012) in which case μ can be calculated as an effective linear attenuation coefficient. This complicates absolute calibration because the effective μ will be a function of both the X-ray energy spectrum as well as the material in the sample. Use of a polychromatic spectrum can also cause beam hardening artefacts to appear in the images, where the edges of the sample appear brighter than the centre even if the material is the same throughout the sample (Ketcham and Carlson 2001). This is due to the fact that low energy X-rays are preferentially attenuated which results in the attenuated beam having a higher average energy than the incident beam despite the overall intensity being less.

In a single 2D X-ray image of a sample, the attenuated X-ray intensity will have been affected by all the material along the X-ray path through the sample. Therefore all the internal features of the object will be superimposed onto the final image, thereby limiting the information about the internal structure. CT was developed to avoid this super-imposition and to improve the final resolution (Van Geet et al. 2000). In a CT scan multiple images are acquired of the sample at different, evenly spaced angles. This may either be achieved by rotating the X-ray source around the sample (as is done in medical imaging) or by rotating the sample itself. It is the latter configuration that was used in this study and is illustrated in Figure 3.15 and Figure 3.16.

A reconstruction algorithm is used to produce a 3D data set following the acquisition of all the 2D images. The most common method for this is filtered back-projection. The simple back-projection method for the acquisition of a 2D image is presented schematically in Figure 3.16. Many individual projections of the sample (in this case a simple cylinder) are acquired at different angles, an effect achieved by rotating the sample on a turntable as was described in the previous paragraph. These projections are then superimposed at angles corresponding to their acquisition angle in order to produce a 3D image. Increasing the number of projections (performing more scans by employing a smaller angle of rotation) will result in a clearer final image, but simple back-projection will always include a blurring artefact around the object of interest (star shape in Figure 3.16). Filtered back-projection allows for the removal of this artefact. This improvement in the method includes application of a mathematical filter to the projection which counteracts the effect of the sudden density changes which result in the blurring. The filter can also be referred to as a convolution kernel or convolution filter. Many different filters exist which have been optimised for different samples. Two of the most common filters are the Ram-Lak filter (Ramachandran and Lakshminarayanan 1971) and the Shepp-Logan filter (Shepp and Logan 1974). The Ram-Lak filter is used primarily when high resolution images are desired whilst the Shepp-Logan filter is used more frequently in medical X-ray imaging to reduce noise at the expense of resolution (Ketcham and Carlson 2001).
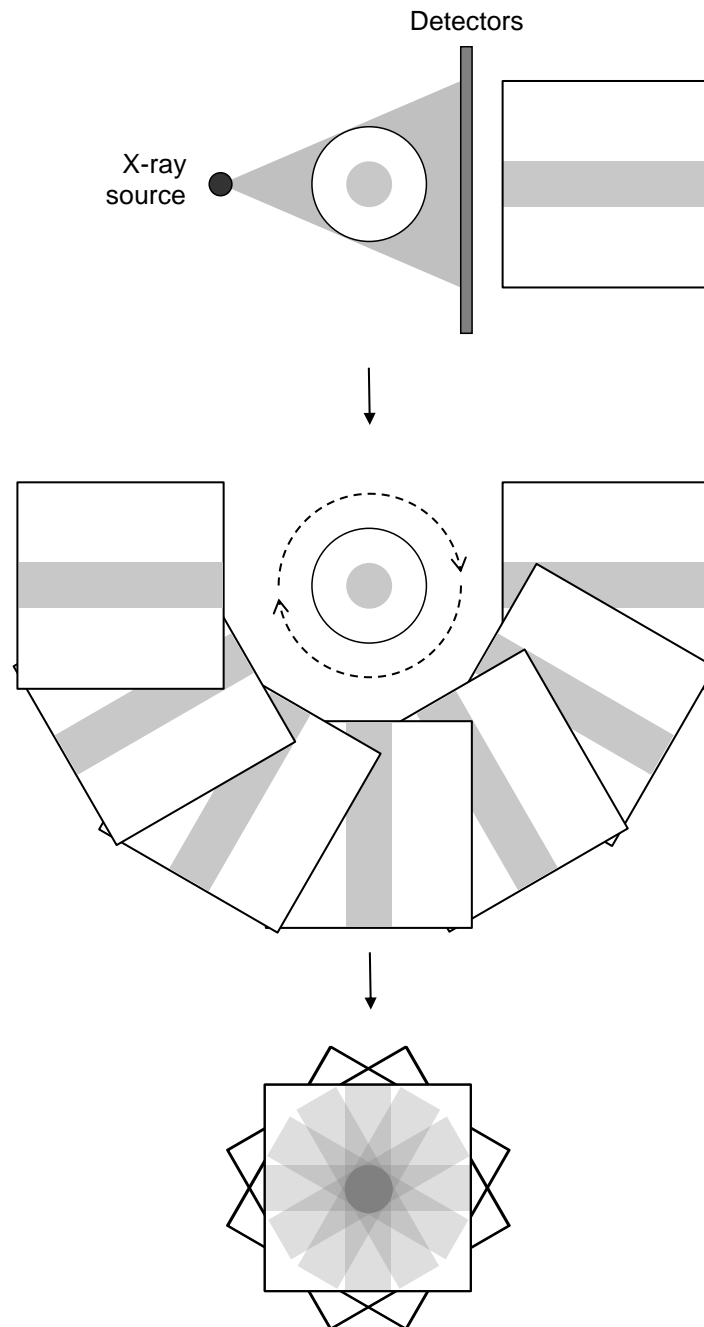
Figure 3.16. Schematic of the back-projection reconstruction method. Individual X-ray projections of a cylindrical sample are obtained at different angles by rotating the sample. The information in the projections is then combined to produce a 2D image.

3.5 Nomenclature

Abbreviations

CT — computed tomography

CZT — chirp z-transform

FID — free induction decay

FOV — field of view

FW — filter width

FWHM — full width at half the maximum height [Hz]

MPA — multiple point acquisition

MRI — magnetic resonance imaging

NMR — nuclear magnetic resonance

PSF — point spread function

RF — radio frequency

SESPI — spin echo single point imaging

SNR — signal to noise ratio

SPI — single point imaging

SPRITE — single point ramped imaging with T_1-enhancement

Symbols

$\mathbf{B}_0$ — external magnetic field [T]

$\mathbf{B}_1$ — transverse magnetic field [T]

dG — gradient increment [T m^{-1} per scan]

dk — increments between each $\mathbf{k}$-space measurement [m^{-1}]

E — Energy [J]

f_i — fraction of total number of electrons contributed by element i

$\mathbf{G}$ — magnetic field gradient [T m^{-1}]

G_{max} — maximum strength of the applied gradient [T m^{-1}]

G_R - read gradient [T m^{-1}]

G_P - phase gradient [T m^{-1}]

G_S - slice selective gradient [T m^{-1}]

h - length of X-ray path through sample [m]

$\hbar$ - reduced Planck's constant [1.055×10^{-34} J s]

I - spin quantum number

I_1 - attenuated X-ray intensity [a.u.]

I_0 - incident X-ray intensity [a.u.]

$\mathbf{k}$ - reciprocal space vector [m^{-1}]

k_B - Boltzmann's constant [1.381×10^{-23} J K^{-1}]

$\mathbf{m}$ - magnetic moment [J T^{-1}]

$\mathbf{M}$ - net magnetic moment [T]

M_0 - equilibrium longitudinal magnetisation [T]

M_{xy} - transverse component of magnetisation [T]

M_z - longitudinal magnetisation [T]

n - number of dimensions

n - number of gradient steps

N - number of scans

N_T - number of points sampled on the FID

N_α - population of the lower energy levels

N_β - population of the higher energy levels

$\mathbf{P}$ - angular momentum [J s]

$\mathbf{r}$ - position vector [m]

S - signal intensity [a.u.]

t - time [s]

t_d - delay between 180° and 90° pulses in the inversion recovery sequence [s]

t_{dw} - dwell time [s]

t_p - phase encode time [s]

t_{p0} - phase encode time [s]

t_{pul} - RF pulse duration [s]

T - absolute temperature [K]

T_1 - spin-lattice relaxation constant [s]

T_2 - spin-spin relaxation constant [s]

T_2^* - effective spin-spin relaxation constant [s]

TE - echo time [s]

TR - repetition time [s]

V - volume [m^3]

Δx - field of view [m]

Z - field of view image scaling factor

Z_b - bulk atomic number [kg kmol^{-1}]

Z_e - effective atomic number [kg kmol^{-1}]

Greek letters

α - RF excitation pulse tip angle [rad]

γ - gyromagnetic ratio [rad s^{-1} T^{-1}]

θ_0 - initial angle of the z-plane trajectory [rad]

θ_E - Ernst angle [rad]

μ - linear intensity coefficient [m^{-1}]

ρ - spin density

ρ_b - bulk density [kg m^{-3}]

τ - length of time the **B**$_1$ field is on [s]

φ - phase shift [rad]

φ_0 - angular step [rad]

v - radiation frequency [s^{-1}]

Δv - RF pulse frequency bandwidth [s^{-1}]

ω _____ Larmor frequency [s^{-1}]

3.6 References

Balcom, B. J., MacGregor, R. P., Beyea, S. D., Green, D. P., Armstrong, R. L. and Bremner, T. W. (1996) 'Single-point ramped imaging with T-1 enhancement (SPRITE)', *Journal of Magnetic Resonance Series A,* 123(1), 131-134.

Boespflug, X., Long, B. F. N. and Occhietti, S. (1995) 'CAT-scan in marine stratigraphy: a quantitative approach', *Marine Geology,* 122(4), 281-301.

Callaghan, P. T. (1995) *Principles of Nuclear Magnetic Resonance Microscopy,* New York: Oxford University Press.

Emid, S. (1985) 'Ultra high-resolution multiple quantum spectroscopy in solids', *Physica B & C,* 128(1), 79-80.

Emid, S. and Creyghton, J. H. N. (1985) 'High-resolution NMR imaging in solids', *Physica B & C,* 128(1), 81-83.

Farahani, K., Sinha, U., Sinha, S., Chiu, L. C. L. and Lufkin, R. B. (1990) 'Effect of field strength on susceptibility artifacts in magnetic resonance imaging', *Computerized Medical Imaging and Graphics,* 14(6), 409-413.

Fukushima, E. and Roeder, S. B. (1981) *Experimental Pulse NMR: A Nuts and Bolts Approach,* Reading, Massachusetts: Addison-Wesley Publishing Company Inc.

Ghorbani, Y., Becker, M., Petersen, J., Morar, S. H., Mainza, A. and Franzidis, J. P. (2011) 'Use of X-ray computed tomography to investigate crack distribution and mineral dissemination in sphalerite ore particles', *Minerals Engineering,* 24(12), 1249-1257.

Gravina, S. and Cory, D. G. (1994) 'Sensitivity and resolution of constant-time imaging', *Journal of Magnetic Resonance Series B,* 104(1), 53-61.

Gullion, T. (1993) 'The Effect of Amplitude Imbalance on Compensated Carr-Purcell Sequences', *Journal of Magnetic Resonance Series A,* 101(3), 320-323.

Haacke, E. M., Brown, R. W., Thompson, M. R. and Venkatesan, R. (1999) *Magnetic Resonance Imaging – Physical Properties and Sequence Design*, Wiley-Liss.

Halse, M., Rioux, J., Romanzetti, S., Kaffanke, J., MacMillan, B., Mastikhin, I., Shah, N. J., Aubanel, E. and Balcom, B. J. (2004) 'Centric scan SPRITE magnetic resonance imaging: optimization of SNR, resolution, and relaxation time mapping', *Journal of Magnetic Resonance,* 169(1), 102-117.

Han, I., Demir, L. and Şahin, M. (2009) 'Determination of mass attenuation coefficients, effective atomic and electron numbers for some natural minerals', *Radiation Physics and Chemistry,* 78(9), 760-764.

Kaffanke, J., Dierkes, T., Romanzetti, S., Halse, M., Rioux, J., Leach, M. O., Balcom, B. and Shah, N. J. (2006) 'Application of the chirp z-transform to MRI data', *Journal of Magnetic Resonance,* 178(1), 121-128.

Ketcham, R. (2012) 'X-ray Computed Tomography (CT)', [online], available: http://serc.carleton.edu/research_education/geochemsheets/techniques/CT.html [accessed 16 February 2012].

Ketcham, R. A. and Carlson, W. D. (2001) 'Acquisition, optimization and interpretation of X-ray computed tomographic imagery: applications to the geosciences', *Computers and Geosciences,* 27(4), 381-400.

Lauterbur, P. C. (1973) 'Image formation by induced local interactions - examples employing Nuclear-Magnetic-Resonance', *Nature,* 242(5394), 190-191.

Lin, C. L., Miller, J. D. and Garcia, C. (2005) 'Saturated flow characteristics in column leaching as described by LB simulation', *Minerals Engineering,* 18(10), 1045-1051.

Lüdeke, K. M., Röschmann, P. and Tischler, R. (1985) 'Susceptibility artefacts in NMR imaging', *Magnetic Resonance Imaging,* 3(4), 329-343.

Mansfield, P. and Grannell, P. K. (1973) 'NMR diffraction in solids', *Journal of Physics C-Solid State Physics,* 6(22), L422-L426.

Mansfield, P. and Grannell, P. K. (1975) 'Diffraction and microscopy in solids and liquids by NMR', *Physical Review B,* 12(9), 3618-3634.

Mastikhin, I. V., Balcom, B. J., Prado, P. J. and Kennedy, C. B. (1999) 'SPRITE MRI with prepared magnetization and centric k-space sampling', *Journal of Magnetic Resonance,* 136(2), 159-168.

Ouriadov, A. V., MacGregor, R. P. and Balcom, B. J. (2004) 'Thin film MRI - high resolution depth imaging with a local surface coil and spin echo SPI', *Journal of Magnetic Resonance,* 169(1), 174-186.

Parasoglou, P. (2009) *Spectroscopic Studies of Moisture Transport in Food Wafer Systems*, unpublished thesis, University of Cambridge.

Parasoglou, P., Sederman, A. J., Rasburn, J., Powell, H. and Johns, M. L. (2008) 'Optimal k-space sampling for single point imaging of transient systems', *Journal of Magnetic Resonance,* 194(1), 99-107.

Patton, J. A. (1994) 'MR imaging instrumentation and image artifacts', *Radiographics,* 14(5), 1083-1096.

Prado, P. J., Blumich, B. and Schmitz, U. (2000) 'One-dimensional imaging with a palm-size probe', *Journal of Magnetic Resonance,* 144(2), 200-206.

Ramachandran, G. N. and Lakshminarayanan, A. V. (1971) 'Three-dimensional reconstruction from radiographs and electron micrographs: Application of convolutions instead of Fourier transforms', *Proceedings of the National Academy of Sciences of the United States of America,* 68(9), 2236-2240.

Rioux, J., Halse, M., Aubanel, E., Balcom, B. J., Kaffanke, J., Romanzetti, S., Dierkes, T. and Shah, N. J. (2007) 'An accurate nonuniform Fourier transform for SPRITE magnetic resonance imaging data', *ACM Transactions on Mathematical Software,* 33(3), 1-21.

Sankey M. H. (2008) *Velocity Mapping in Trickle-Bed Reactors and Multiphase Systems Using MRI*, unpublished thesis, University of Cambridge.

Schenck, J. F. (1996) 'The role of magnetic susceptibility in magnetic resonance imaging: MRI magnetic compatibility of the first and second kinds', *Medical Physics,* 23(6), 815-850.

Shepp, L. A. and Logan, B. F. (1974) 'Reconstructing interior head tissue from X-ray transmissions', *Nuclear Science, IEEE Transactions on,* 21(1), 228-236.

Van Geet, M., Swennen, R. and Wevers, M. (2000) 'Quantitative analysis of reservoir rocks by microfocus X-ray computerised tomography', *Sedimentary Geology,* 132(1–2), 25-36.

Yang, B. H., Ai-Xiang, W., Jiang, H. C. and Chen, X. S. (2008) 'Evolvement of permeability of ore granular media during heap leaching based on image analysis', *Transactions of Nonferrous Metals Society of China,* 18(2), 426-431.

Zhang, J. and Balcom, B. J. (2010) 'Parallel-plate RF resonator imaging of chemical shift resolved capillary flow', *Magnetic Resonance Imaging,* 28(6), 826-833.

Zhang, J., MacGregor, R. P. and Balcom, B. J. (2008a) 'Liquid crystal diffusion in thin films investigated by PFG magnetic resonance and magnetic resonance imaging', *Chemical Physics Letters,* 461(1-3), 106-110.

Zhang, Z., Martin, J., Wu, J., Wang, H., Promislow, K. and Balcom, B. J. (2008b) 'Magnetic resonance imaging of water content across the Nafion membrane in an operational PEM fuel cell', *Journal of Magnetic Resonance,* 193(2), 259-266.

Chapter 4 – Application of MRI Methods to Ore Systems

This chapter begins with a brief description of the difficulties associated with the magnetic resonance imaging (MRI) of ore systems, with a specific focus on magnetic susceptibility artefacts. A study is presented where a saturated ore sample is imaged using three different MRI acquisition techniques, namely spin echo, single point imaging (SPI) and spin echo single point imaging (SESPI). Variations on these techniques, such as multiple point acquisition (MPA) and proton mapping are also considered. The resulting images are compared with respect to image quality and are also assessed for their accuracy against a distortion-free X-ray computed tomography (CT) image of the system. The relaxation constants of saturated ore samples are further investigated, where the effect of particle size distribution and magnetic field strength are considered. A second case study is then presented where the most successful MRI techniques are applied to an unsaturated packed ore column to ascertain their performance in that environment. Finally, the application of under-sampling and compressed sensing (CS) to the most successful imaging technique is explored.

4.1 Introduction

The overall aim of this thesis, as defined in Chapter 1, is to use MRI to image low grade copper ore leaching systems non-invasively and thereby to further the understanding of heap leaching hydrology. MRI has already been extensively applied to a range of chemical engineering systems, of which Gladden (1994) and Mantle and Sederman (2003) provide good reviews. MRI, however, would not typically be thought of as a viable tomographic technology for use with ore systems because the ferro- and paramagnetic species in the ore have the potential to cause significant magnetic susceptibility distortions in images acquired with conventional frequency encode methods. MRI studies of soil samples which contain similar ferro- and paramagnetic components have struggled with this problem in the past (e.g. Fang et al. (2001)). The magnetic materials in the ore and leach solution are also expected to cause shortening of the samples' relaxation times. This is a further problem for frequency encoded methods as a minimum time is required for the formation of an echo.

The pure phase encode techniques such as SPI and SESPI have been reported to be effective at minimising magnetic susceptibility distortions (Fang et al. 2001, Gravina and Cory 1994, Ramos-Cabrer et al. 2003) because they do not measure the time evolution of the signal and so only the interaction of the applied gradients contributes to the signal distribution. Furthermore, single point imaging techniques have been shown to be effective for imaging systems with short T_2^* values, similar to what is expected for the ore systems (Gravina and

Cory 1994, Prado et al. 1999). Pure phase encode imaging is hence postulated to be a viable alternative acquisition technique.

4.2 Imaging of a Saturated Column

Different MRI acquisition techniques are expected to result in varying degrees of magnetic susceptibility distortions, due to the effect of frequency versus phase encoding and the relaxation time weighting of the signal. It is therefore desired to establish which imaging techniques are best suited to the imaging of the low grade copper ore systems. The quality of the images can be assessed and compared using simple signal to noise ratio (SNR) measurements, but it is also important to consider the accuracy of the images – a good quality (high SNR) image can still be subject to magnetic susceptibility distortions. Measurement of the image accuracy can be achieved through comparison of the MRI acquisitions with distortion free X-ray CT acquisitions.

4.2.1 Experimental

4.2.1.1 Sample Preparation

The MRI techniques were compared using a small column of saturated ore which was prepared to be suitable for imaging with X-ray CT and MRI. For this setup low grade Escondida Type B copper ore (average composition 2.95% Fe, 0.69% Cu and 2.02% S by weight) of a select particle size (>9.50 mm) was packed into a Perspex column with an internal diameter 40 mm and height of 50 mm. The column is illustrated in Figure 4.1. The selective particle size was to ensure that the ore did not shift inside of the column while it was transported between experiment locations. The column was saturated with distilled water and then doped with $GdCl_3$ to reduce the T_1 of the system from 208 ms to circa 50 ms so that the repeat time, TR, and hence the SESPI acquisition time could be reduced. This value had also been observed to be a typical mixed particle size saturated ore T_1 in preliminary studies. The column had three water-filled capillary tubes attached to the outside for image registration when comparing the MRI acquisitions and the X-ray CT images.
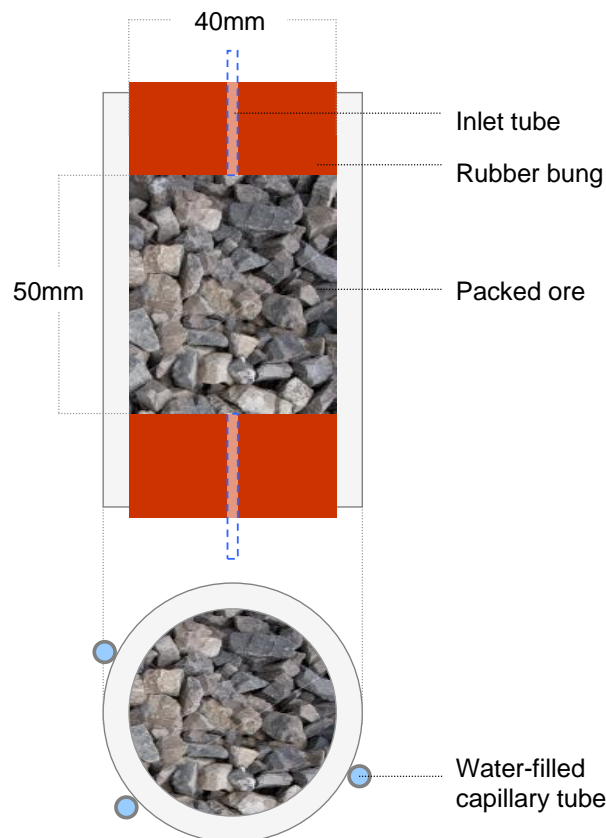
Figure 4.1. Column packed with ore and saturated with water doped with $GdCl_3$ that was imaged using MRI and X-ray CT for method validation.

4.2.1.2 MRI Hardware and Imaging Parameters

The column was imaged on a Bruker AV 85, 2 T horizontal bore spectrometer with a radio frequency (RF) coil which had an inner diameter of 83 mm. The field of view (FOV) was 60 mm × 60 mm in the x and y directions and was 72 mm in the z direction (along the bore length). The acquisition size was 64×64×64, which corresponded to a nominal resolution of 938 μm in the x and y directions and 1125 μm in the z direction. The filter width (FW) of the spectrometer was 125 kHz.

Spin echo, SPI and SESPI 3D acquisition sequences were used as illustrated in Figure 3.8, 3.9 and 3.14(b) respectively. Unless otherwise specified, four repeat scans were done for phase cycling. The spin echo imaging was performed with sweep widths of 100 and 200 kHz. An echo time (*TE*) of 1 ms and a repetition time (*TR*) of 150 ms were used. Repetition times of 5 ms and 50 ms were used in the SPI and SESPI experiments respectively and both pulse sequences used a total gradient encoding time (t_p) of 300 μs. The SPI tip angle was set as 10°, an optimised value based on Ernst angle calculations coupled with the restriction on the RF pulse duration (t_{pul}) (Equation 3.29). A square spiral gradient trajectory where all of the

k-space points were split into four interleaves was used, as implemented by Parasoglou et al. (2008). Four points were acquired along the free induction decay (FID) for the SPI-MPA acquisitions (pulse sequence illustrated in Figure 3.12), spaced at 10 μs intervals from a t_{p0} of 300 μs. In the SESPI acquisitions the gradients were split before and after the 180° pulse and the *TE* was approximately 750 μs. Like for SPI-MPA, eight points were acquired along each SESPI echo for signal averaging.

4.2.1.3   X-ray CT Imaging Parameters

An X-Tek Real Time X-Ray HMX 160 scanner was used to image the saturated ore column. The scanner was operated with a copper filter (to attenuate low energy X-rays) at 90 kV and 85 μA. The angular increment was 0.5°, so a total of 720 images were acquired with 32 image averages per rotation. Image reconstruction was performed on NGI CT Control and CT-Pro Client. The final images had a resolution of 63 μm. The acquisition was thresholded and converted to a uint8 format (unsigned integer) so as to reduce the size of the data files, thereby making them workable on a standard processor.

4.2.2   Spin Echo Imaging

It is important to establish if standard spin echo (frequency encode) methods are not suitable for the imaging of the ore systems as hypothesised before pure phase encode imaging methods are explored. Spin echo slices from the 3D images of the saturated column acquired at two sweep width values, 100 kHz and 200 kHz, are presented in Figure 4.2 (a) and (b). The lower sweep width image shows distortions in the read direction whereas the image should show a round sample. Incrementing the sweep width results in a reduction in these distortions. This is because the effect of reducing the sweep width is to decrease the time evolution of the signal and so minimise any magnetic susceptibility artefacts. Despite this improvement, it is evident that spin echo imaging is prone to the development of magnetic susceptibility artefacts and is therefore not the best choice of imaging method. Figure 4.2 (c) shows a severely distorted spin echo slice of a different sample which illustrates that the degree of distortion varies for each sample.
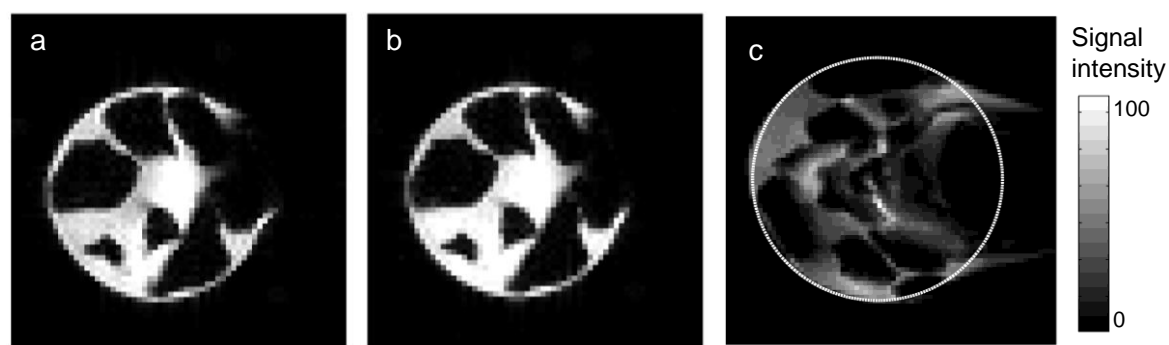
Figure 4.2. Spin echo slices of the saturated column acquired with sweep widths of (a) 100 kHz and (b) 200 kHz and (c) a severely distorted spin echo slice of a similarly prepared sample acquired with a sweep width of 100 kHz. The white line in (c) shows the expected boundary. The read direction is across the page.

4.2.3   Pure Phase Encode Imaging

The pure phase encoded images of the sample do not include any such obvious shape distortions as can be seen in the SPI-MPA and SESPI slices presented in Figure 4.3 (b) and (c). The SNR of the simple SPI 3D acquisition's central slice, calculated as the mean signal divided by the standard deviation of the noise (area outside of region of interest), is the lowest at 28 whereas the SPI-MPA acquisition's SNR is 65. The SNR should increase by a factor of the square root of the number of scans (Callaghan 1995), so the approximate factor of 2 improvement is consistent with expectations. SPI-MPA is therefore employed for all later SPI acquisitions.

The SESPI acquisition with the same t_p and number of scans as the SPI acquisition has a SNR of 189. This is almost three times higher than the SPI-MPA result. However, the total SESPI acquisition time is 13 hours and 31 minutes as opposed to 3 hours and 21 minutes for SPI-MPA. This is a consequence of the long *TR* required for SESPI due to the 90° excitation pulse (compared with 10° for SPI). An acquisition time equivalent SPI-MPA experiment (16 repeat scans and an acquisition time of 13 hours and 23 minutes) is measured to have a SNR of 138. This is approximately double the SNR of the shorter SPI-MPA acquisition as would be expected. It is still lower than the SESPI acquisition though, so the best acquisition method with respect to SNR is SESPI.
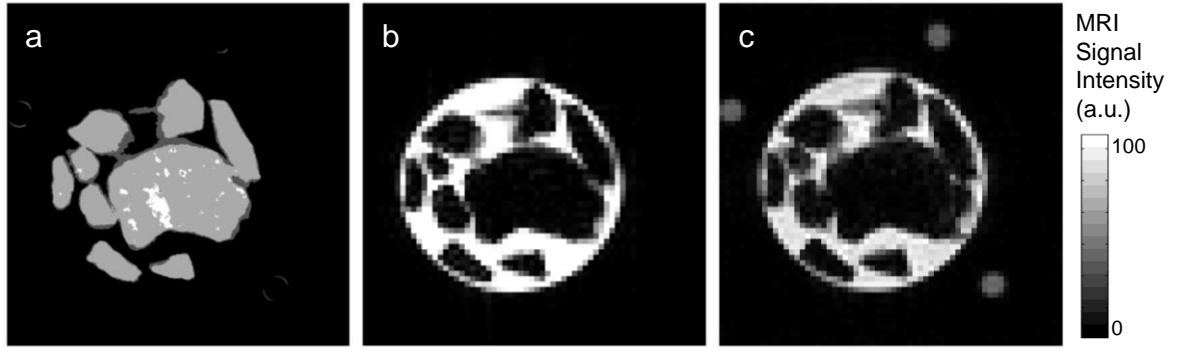
Figure 4.3. Equivalent (a) X-ray CT, (b) SESPI and (c) SPI-MPA slices from the 3D acquisitions of the saturated ore column that are used to assess the accuracy of the MRI images.

The SNR differences may be because of the T_2 and T_2^* relaxation of the signal as SPI signal is T_2^* weighted whereas SESPI signal is T_2 weighted. T_2^* has been measured previously using information from multiple SPI-MPA acquisitions where the acquisition time is changed in each experiment (Halse et al. 2004, Parasoglou et al. 2009). This approach however does not capture the initial signal decay as shorter t_p values are not accessible due to both the requirement of an increased gradient strength in order to maintain the same FOV and the influence of background signal. An alternative method is to use simple pulse acquire data, but this would include signal from water outside the region of interest, specifically the water in the tubes for image registration in this case. The T_2^* decay may also be estimated as (Gladden 1994):

$$T_2^* = \frac{1}{\pi \; FWHM}$$

4.1

where FWHM stands for the full width at half maximum height, as described in the MRI theory chapter. This method gives a value of 225 μs for the saturated ore column. However, a more precise value is desired. It is proposed that this may be done by performing a series of SESPI acquisitions, where multiple points are acquired from the top of the echo along its decay. This method allows for the acquisition of the signal closer to the zero time than can be achieved with SPI-MPA and it avoids the need for reconstruction of the data using the chirp z-transform (CZT) algorithm. It also allows for the exclusion of signal from water outside the region of interest.

A preliminary study was conducted to test that the T_2^* value calculated using the SESPI method gives the same result as the accepted SPI-MPA approach. This was done on another mixed particle size distribution saturated ore sample which did not have the water filled capillary tubes attached to the outside of the column. SPI-MPA gradient encoding times (t_p)

of 200, 350, 500, 650 and 800 μs were used for this and 4 points were acquired along the FID at intervals of 10, 11, 16, 21 and 25 μs respectively. Eight points were acquired along the echo in the SESPI experiments, spaced at intervals of 20, 100, 200, 500 and 1000 μs in each different run. The resulting average decays presented in Figure 4.4 show that there is minimal difference between the two methods' signal magnitude measurements. Therefore measurement of the T_2^* decay using multiple SESPI acquisitions is an acceptable approach.
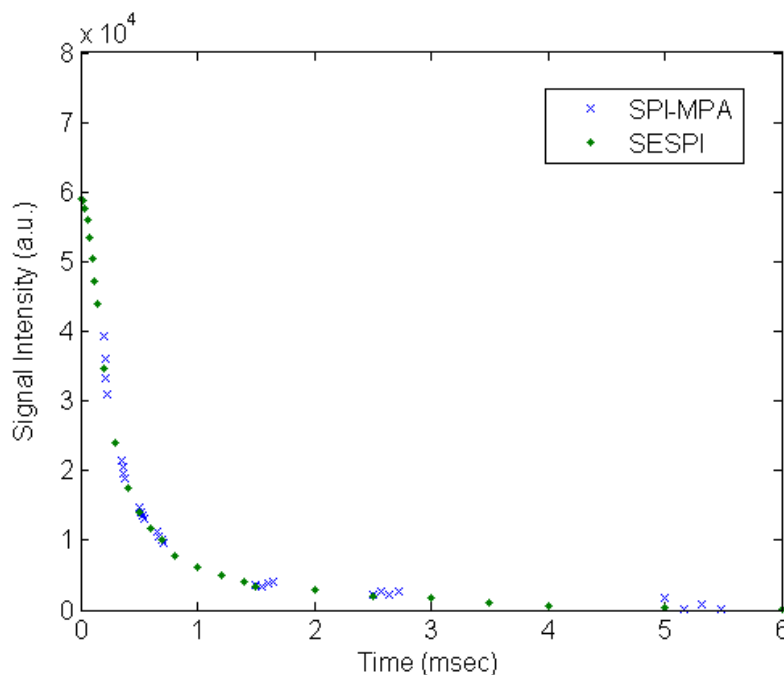
Figure 4.4. The decay of the signal to be used to calculate T_2^*, determined using multiple SPI-MPA experiments as well as multiple SESPI experiments.

When the main saturated ore sample is studied using multiple SESPI acquisitions, the average T_2^* for the system is found to be 380 μs. Therefore only 45% of the refocused signal remains 300 μs after the excitation. By comparison, the T_2 of the system, measured using a standard CPMG approach, is 8.71 ms. Therefore 93% of the original signal remains at the SESPI acquisition time. This will have contributed significantly to the relatively poor performance of SPI-MPA compared with SESPI.

4.2.4   Comparison to X-Ray CT

The MRI images were compared pixel-by-pixel to equivalent X-ray CT images, which are unaffected by magnetic susceptibility artefacts, to determine if the MRI images are accurate, distortion-free representations of the system. An example of the slices compared is given in Figure 4.3 where the SESPI and SPI-MPA images have the same total acquisition time. The X-ray CT images also show the position of the mineral in the ore, as its absorption of the

X-rays is higher than that of the benign rock. It is therefore possible to assess if any distortions in the MRI acquisitions are directly linked to the position of the mineral in the ore. The magnetic resonance (MR) images are thresholded prior to the analysis and the X-ray CT images are adjusted to match their MRI equivalents. This requires matching the FOV, rotating the images so that the signal from the capillary tubes is aligned and reducing the resolution to be the same as the MR images.

Of the SESPI pixels in each slice 89±3% match the X-ray CT image. This is marginally, though not statistically better than the match between the X-ray and SPI-MPA pixels, 86±6%. Of those pixels that do not match, the large majority are found to be adjacent to matched ones for both imaging methods (89±7% for SESPI and 86±11% for SPI-MPA), which suggests that the majority of the error may be attributed to partial volume effects and any slight misalignment of the images. No correlation is found to exist between the mineral location in the ore and local differences between the X-ray CT and MRI data. This exercise hence confirms that both pure phase encoded imaging methods produce accurate images of the saturated ore sample. Visually the SESPI images look to have significantly better contrast than the SPI-MPA acquisitions, as the particle edges are more defined.

4.2.5   Effect of Particle Size Distribution

Heap leaches are characterised by a broad particle size distribution (PSD), ranging from micrometres to centimetres. It is consequently desired to understand if the different particle sizes have a significant effect on the spin relaxation constants of the immediately surrounding liquid. If they do, they could potentially cause local variations in the relaxation constants, which may ultimately affect the images.

The Escondida Type B ore was determined to have a particle distribution by sieving as specified in Table 4.1. Five samples of different PSDs (<0.71, 0.71-2.0, 5.6-9.5, 5.6-9.5 and >9.5) were selected and saturated with distilled water. The gravimetric voidage (equivalent to the liquid uptake) was measured to be circa 40% for all of the samples. The T_1 and T_2 of the samples were measured using the inversion recovery and CPMG (*TE* of 1 ms) pulse sequences on the Bruker AV 85, 2 T horizontal bore spectrometer. The T_2^* was estimated from the FWHM of the resonance line shape using Equation 4.1 as well as by using the decay of the signal after the SESPI induced echo as was done for the saturated column. The latter method was performed by acquiring SESPI 2D projections of the samples and averaging the signal from the ore-containing region only. This was done to avoid inclusion of signal from water that was situated outside the region of interest. Table 4.2 summarises the resulting spin relaxation constants.

Table 4.1. PSD of the Escondida Type B ore.

Size (mm)	Weight (%)
> 13.2	14.0
9.5 - 13.2	18.4
5.6 - 9.5	20.3
2.0 - 5.6	19.8
0.71 - 2.0	9.1
< 0.71	18.5

Table 4.2. Spin relaxation constants of ore in water samples with different PSDs.

Size (mm)	T_1 (ms)	T_2 (ms)	T_2^* echo (µs)	T_2^* FWHM (µs)
> 9.5	100	69	421	159
5.6 - 9.5	44	28	355	369
2.0 - 5.6	35	19	228	189
0.71 - 2.0	22	12	125	238
< 0.71	19	5.8	129	121

The results show that T_1 and T_2 are heavily influenced by the PSD, with their values decreasing with decreasing particle size. A smaller size distribution of ore has a higher surface to volume ratio which results in the water being exposed to more ferro- and paramagnetic centres on the ore surface, thereby causing the reduction in the T_1 and T_2.

The bulk T_2^* values as measured with the FWHM are not observed to change significantly relative to the particle size distribution of the sample whereas the T_2^* values evaluated from the echo decay show that the T_2^* decreases with particle size until the second smallest sample. As the FWHM results are influenced by the shape of the peaks (which tended to be irregular) their results are deemed to be less accurate. The T_2^* decrease with particle size is consistent with a greater influence of susceptibility gradients.

The samples were imaged using SPI-MPA and SESPI in addition to the spin relaxation measurements. The same settings as had been used for the saturated column imaging (Section 4.2.1) were used and the images were acquired with a common receiver gain. Figure 4.5 shows slices of the SPI-MPA and SESPI acquisitions where the images (a) - (e) and (f) - (j) have been produced with common signal intensity scales.

The SPI-MPA acquisitions' signal intensities are shown to be strongly dependent on the PSD. The signal magnitudes in the three larger particle size samples (a - c) are fairly similar, but the smallest two particle size samples (d and e) have significantly less signal. This behaviour is not seen to the same degree in the SESPI images. The smallest particle size sample (j) has a lower average signal magnitude than the larger particle size samples, but it is significantly less attenuated compared with the SPI-MPA image. The SESPI reduction in signal magnitude is due to the decrease in T_2 as just over 10% of the original signal in sample (j) will have decayed by the SESPI acquisition time versus 1% of the original signal in sample (f). The T_2^* values of the smallest two PSD samples is less than a third of the T_2^* of the largest PSD sample, which explains the significant decrease in signal magnitude of the SPI-MPA images. This result indicates that SESPI is a more appropriate imaging technique for the study of the low grade copper ore samples.
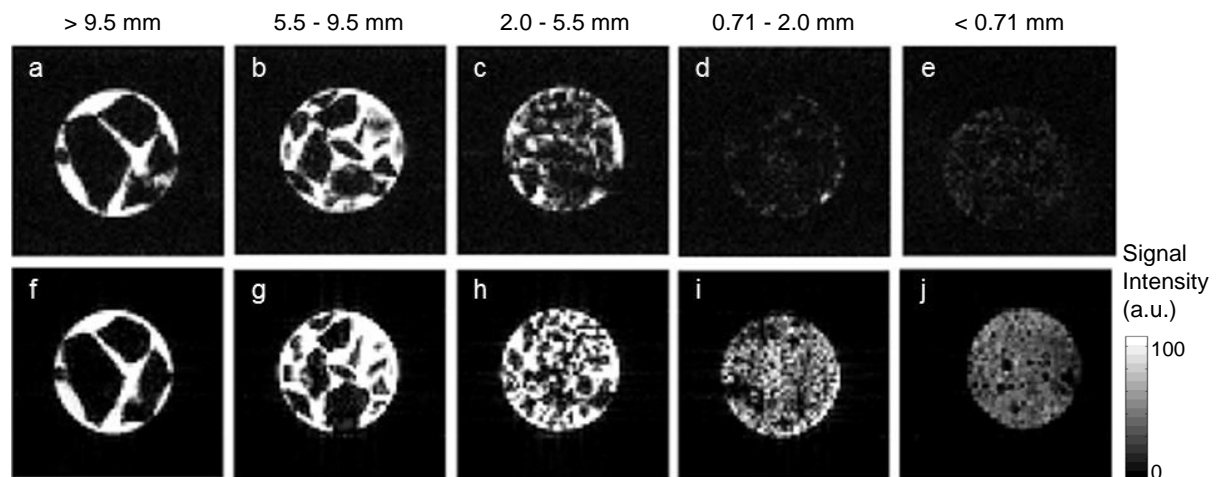
Figure 4.5. Images of saturated ore samples of different PSDs acquired with SPI-MPA (a - e) and SESPI (f - j). The images have been produced with common intensity scales.

4.2.6 T_2^* Mapping

Because significant T_2^* variation is demonstrated between the ore samples of different PSD it is desired to determine if proton density mapping would improve the quality of the SPI-MPA image information. In this process the results of multiple SPI-MPA experiments are fitted with Equation 3.35 or 3.36 to determine voxel specific T_2^* values and the original signal magnitude, prior to any relaxation effects. This signal is proportional to the proton density and so the amount of liquid present.

A water saturated ore sample (full PSD) was prepared for this. A series of SPI-MPA data sets were acquired for the T_2^* mapping at t_{p0} times of 300, 500 and 700 μs with five points

acquired spaced at 10, 16 and 22 µs respectively. Equation 3.36 was used for the fitting as a small tip angle was employed. Figure 4.6 shows a slice from the 300 µs SPI-MPA acquisition and its corresponding proton density map and T_2^* distribution.
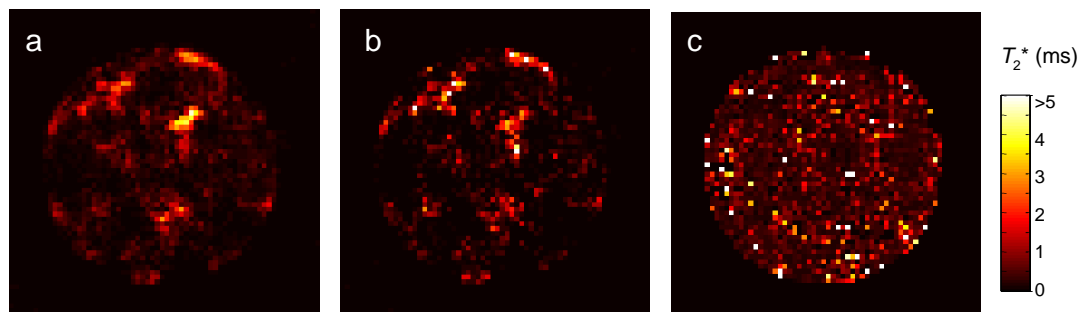

Figure 4.6. 2D slices of a water saturated agglomerated ore sample where (a) is the SPI-MPA image (t_{p0} of 300 µs), (b) is the proton density map and (c) is the corresponding T_2^* data where the scale bar gives the time (ms).

The fits in the liquid containing region have R^2 values consistently above 0.9 so it may be concluded that a single exponential decay fit is appropriate. Using this approach the average T_2^* in the liquid containing region is found to be 412 µs. The proton density maps have marginally better SNR compared with the 300 µs SPI-MPA acquisition (64 versus 59), but the signal location remains unchanged and gating of the SPI-MPA image and proton density map result in the same binary image. T_2^* mapping therefore does not offer a significant improvement on the single SPI-MPA acquisition.

4.2.7 Effect of Magnet Field Strength

A strong magnetic field is traditionally associated with an increase in SNR because an increase in the static magnetic field, $\mathbf{B}_0$, results in a larger energy gap, as explained in the previous chapter. The larger gap results in a higher proportion of the spins aligning with $\mathbf{B}_0$, causing the signal to improve relative to the background noise. However, a higher magnetic field strength can also worsen magnetic susceptibility distortions because the magnetisation of the material scales with $\mathbf{B}_0$. The increase in field inhomogeneity causes shortening of T_2^* which can reduce the acquired signal magnitude, thereby decreasing the SNR and the spin relaxation constants. The ideal magnet strength for the imaging of the ore would therefore require a balance between these effects.

To explore the effect of magnetic field strength on the ore systems a distilled water saturated ore sample in a 30ml bottle was prepared and tested on three different magnets. The first magnet was a low field (1.9 MHz) Oxford Instruments Maran-DRX 42 mT spectrometer with

"Big-2" magnet. The second was a Bruker AV 85, 2 T horizontal bore spectrometer and the final magnet was a Bruker AV 300, 7 T vertical bore spectrometer. T_1 was determined using the inversion recovery pulse sequence and T_2 was measured with a CPMG experiment. The results are summarised in Table 4.3.

Table 4.3. Spin relaxation constants of a water saturated ore sample as measured on magnets of different field strengths.

Spectrometer field strength	T_1 (ms)	T_2 (ms)	$T_2{}^*$ FWHM (µs)
42 mT	14.5	13.8	-
2 T	26.4	16.3	222
7 T	29.2	9.1	150

The T_1 values increase with the magnet strength as is expected. The T_2 initially increases as well, but the 7 T result is shorter than on both the other magnets. The $T_2{}^*$ also decreases as the magnet strength is increased from 2 to 7 T. This shows that higher field strength can have a negative effect on the T_2 and $T_2{}^*$ of the ore samples and that a tipping point does exist. The strength of the magnet therefore should be a consideration in experiment design. However, the T_2 values are all of a length that the quality of any SESPI acquisitions should not be compromised significantly.

4.3   Imaging of a Flowing Column

Following the successful imaging of the saturated ore samples, it is desired to see how SPI-MPA and SESPI perform when imaging a flowing system. A higher field magnet with a vertical bore is used for this to allow for a standard flowing heap leaching experiment configuration. As previously discussed, a higher field typically is advantageous as it results in SNR improvements, however it is also expected to exaggerate any magnetic susceptibility distortions and increase the width of the resonance line shape in the frequency domain (shorten the $T_2{}^*$ decay of the signal).

4.3.1   Experimental

4.3.1.1   Sample Preparation

The full PSD (Table 4.1) of the Escondida Type B ore (400 g) was agglomerated with 20 ml of 0.1 M sulfuric acid and packed into the column shown in Figure 4.7. The external diameter of the column was restricted by the magnet's internal bore, so the inner diameter was 50 mm.

The total height of the ore bed was 135 mm and the gravimetric voidage of the packed ore was found to be 38.5±0.8%. Distilled water was used for the liquid phase. The column was irrigated drip-wise from the top at a rate of 40 ml h^{-1}. The system was allowed two hours to stabilise before any images were taken, at which point the outlet flow rate matched the inlet. The column was saturated by flooding the column with distilled water at the end and imaged.

4.3.1.2   MRI Hardware and Imaging Parameters

The flowing column imaging was carried out on a Bruker DMX 200, 4.7 T vertical bore spectrometer with an internal RF coil which had a 63 mm internal diameter and an imaging region of approximately 70 mm in length. The field of view was 60 mm × 60 mm in the horizontal plane (x and y) and 72 mm in the vertical (z) direction. The acquisition size was 64×64×32, which corresponded to a nominal resolution of 938 μm in the horizontal plane and 2250 μm in the vertical direction. Only SPI-MPA and SESPI imaging were performed. The same settings as for the saturated column were used with the following exceptions. The t_p was increased to 350 μs due to gradient strength restrictions, the FW was 27.2 kHz and five points were acquired along the FID for SPI-MPA.
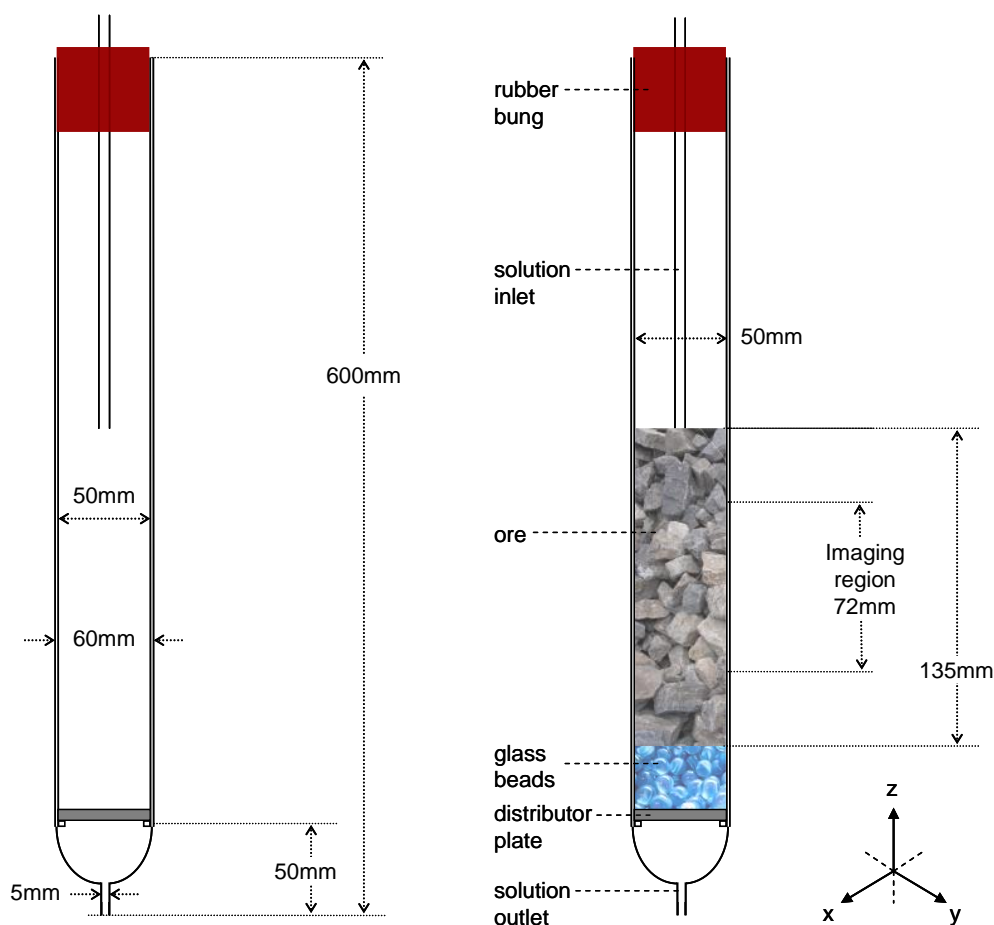

Figure 4.7. Column packed with agglomerated ore that was used for the flowing experiments.

4.3.2   Flowing Column Results

Figure 4.8 shows SESPI and SPI-MPA original and gated slices of the packed ore column when saturated with water. Individual ore particles can be seen clearly in the SESPI slice. This is not true for the SPI-MPA equivalent and it is clear that there are large regions in the image where signal has erroneously disappeared. This may have been due to smaller ore particles being present in these regions of the column, which have been demonstrated to result in a significant loss of signal in SPI acquisitions. Thus SPI-MPA does not perform as well as SESPI for the saturated system.

Figure 4.9 shows original and gated images of the unsaturated flowing system. The SPI-MPA acquisition shows significantly less detail than the SESPI image set, which shows the liquid as having been distributed throughout the whole column. The majority of the signal in the SPI-MPA images appears in the region of the column walls ($71.1\pm11.8\%$ of the total signal is within the outer 3.75 mm of the column). Though it is expected that some of the liquid will preferentially flow down the sides of the column due to wall effects, it is unlikely that the majority of it will. An explanation for this is that there is a smaller distortion in the magnetic field at the glass wall than in the ore filled part of the bed. This will result in a longer local T_2^* in the wall region, limiting the signal attenuation. Meanwhile, the liquid on the ore particle surface will be exposed to a higher degree of distortion, thereby causing an apparent weighting to the wall liquid. The overall T_2^* was determined to be 36 μs from the FWHM, which is short for SPI-MPA considering that the t_p was 350 μs. In comparison, a standard CPMG experiment yielded a T_2 value of 59 ms which is not short enough to be expected to affect the quality of SESPI acquisitions significantly. This confirms that SESPI is the most appropriate imaging method for the study of low grade copper ore heap leaching hydrology.
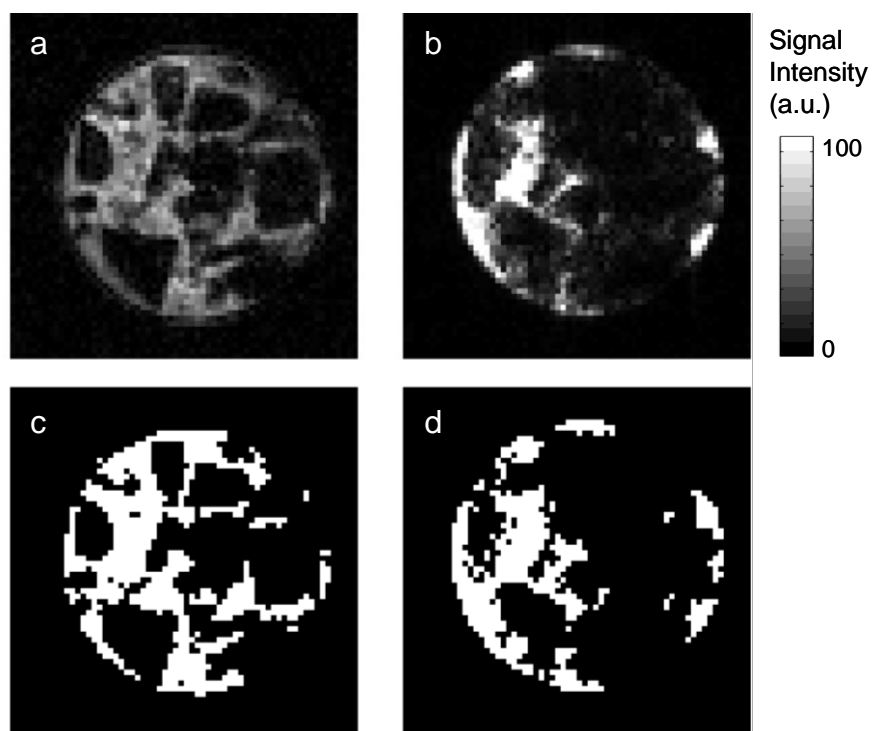
Figure 4.8. Slices of the flowing ore column after saturation acquired with (a) SESPI and (b) SPI-MPA with their gated equivalents (c) and (d).
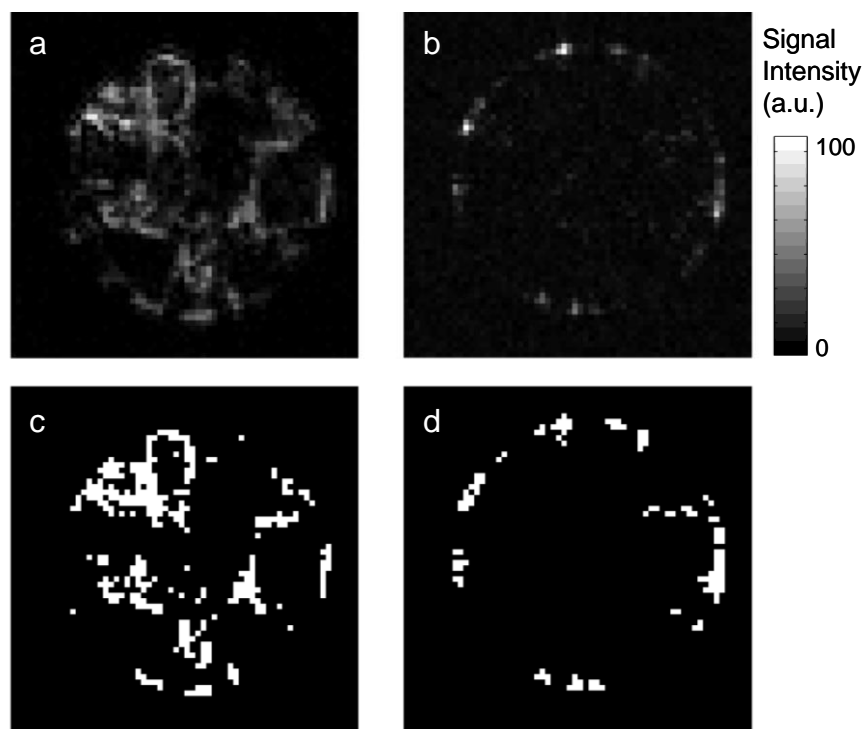

Figure 4.9. Slices of the unsaturated, flowing ore column acquired with (a) SESPI and (b) SPI-MPA with their gated equivalents (c) and (d).

4.3.3   SESPI Acquisition Thresholding

The analysis of the MRI acquisitions requires thresholding of the images to identify the position of the liquid within the ore samples. This requires the choice of an appropriate thresholding level based on the SNR of the acquisition and known characteristics of the system, such as the voidage in the case of a fully saturated system.

Figure 4.10 is a histogram of the signal in the SESPI modulus intensity image of the saturated ore column. Higher frequencies at larger signal magnitude values which account for the water signal are readily distinguishable from the noise at the lower signal magnitudes, as is described by Haacke et al. (1999). Therefore an appropriate thresholding level between these regions (indicated in Figure 4.10 by the bracket) can be chosen without difficulty, despite the fine particles in the system which have the potential to blur these regions together. This is because the finer particles were evenly distributed on the surface of the larger particles during the agglomeration process. The formation of regions of high fine particle content, for example due to accumulation towards the base of the column as they are dislodged by the flowing liquid, may complicate this process and should be taken into account in the design of future experiments.

The effect of the thresholding level choice on the binary image is illustrated in Figure 4.11. Thresholding at the lower bound causes overestimation of the voidage and information regarding the edges of the particles is lost. Thresholding at the higher bound causes for information about the boundaries between adjacent particles to be lost, so that particles become amalgamated. This must be avoided as this is expected to correspond to the flowing liquid path in an unsaturated system, especially at lower flow rates where capillary effects dominate the liquid distribution. The best thresholding level (given by the arrow in Figure 4.10) is determined by balancing the errors that result at the two extremes based on a visual assessment of the thresholding level choice and by comparing the voidage calculated from the thresholded images with the gravimetrically calculated value.

The same choice of thresholding level is used for the analysis of the unsaturated flowing experiments. This is considered to be acceptable as the structure of the ore packing remained the same and because the same liquid that was used to flood the column was used to irrigate it. The effect of partial volumes on the accuracy of the thresholded images will be accounted for as an error measurement in later experiments and will be discussed in the following chapter.
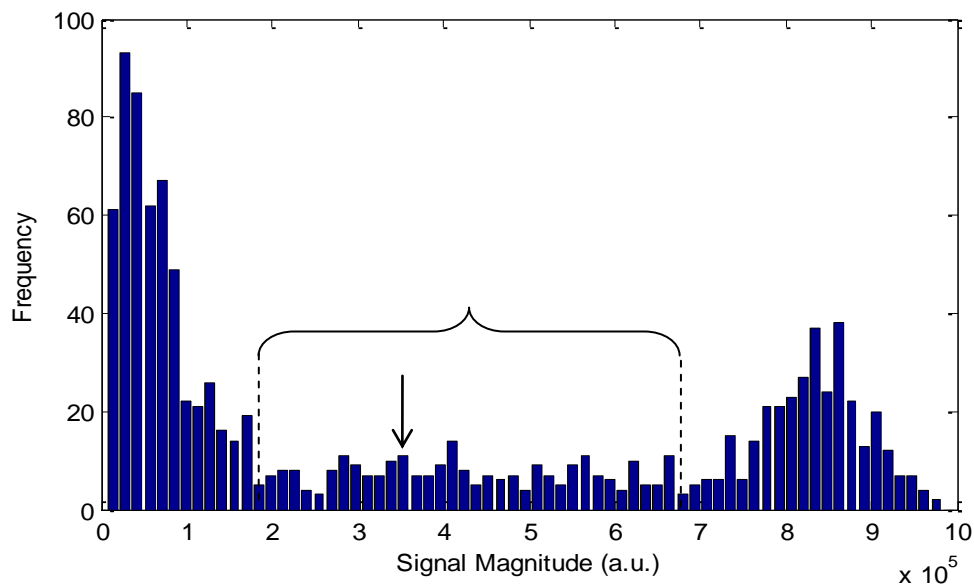
Figure 4.10. Histogram of the saturated ore column which shows the noise (left peak) and the signal from the water (right peak). A possible thresholding range between the two regions is indicated by the bracket, with the eventual thresholding level indicated by the arrow.
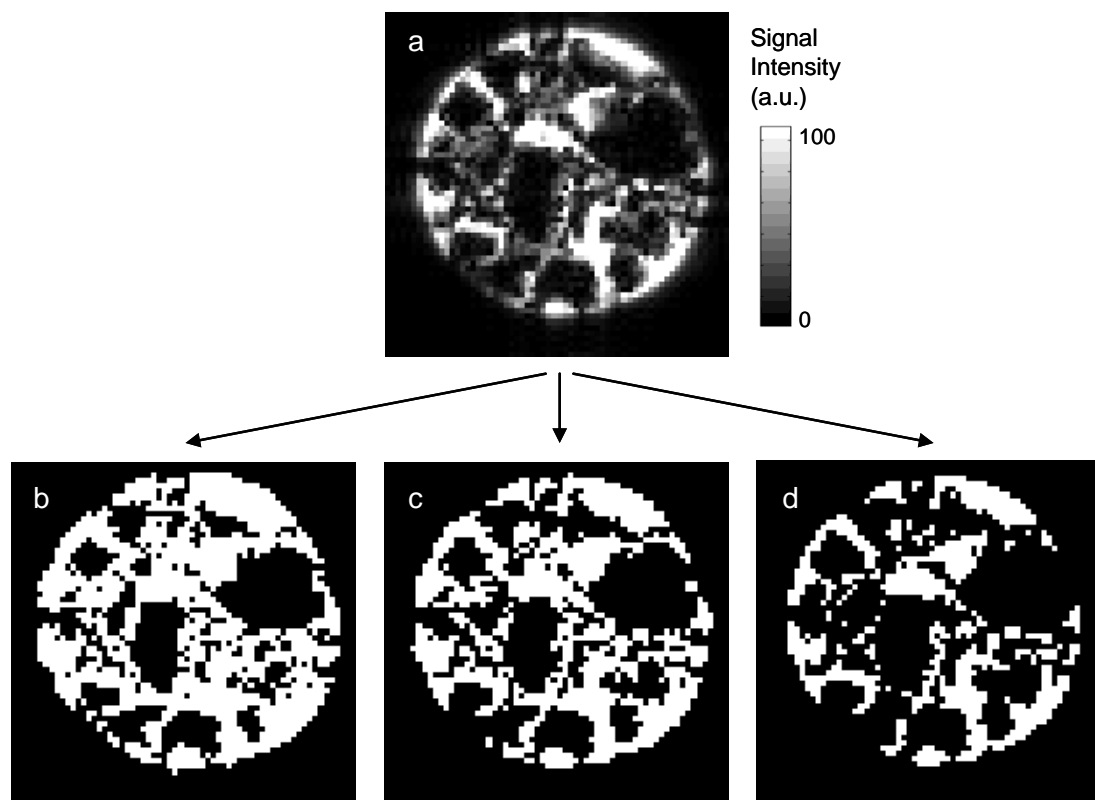
Figure 4.11. Illustration of the different possible thresholding levels where (a) the original image is thresholded at (b) the lower bound of the thresholding range, (d) the higher bound of the thresholding range and (c) the eventual best thresholding level.

4.4 Preliminary Testing of Under-Sampling Techniques

SESPI is an inherently slow acquisition sequence which could prove to be problematic in certain experiments where the observation of short-term behaviour is desired. The long acquisition times could be cut down on by employing under-sampling, possibly in conjunction with compressed sensing (CS) (Parasoglou et al. 2009).

When under-sampling is employed only a selection of the points in **k**-space (as defined in Equation 3.18) is acquired which leads to a shortening of the acquisition time. The unacquired points are then zero-filled before Fourier Transformation. As an alternative to zero-filling, Parasoglou et al. (2008) obtained hybrid images where they first acquired a full **k**-space data set and then used these values to fill the unacquired points in subsequent under-sampled scans. Another time saving technique for centric scans was put forward by Mastikhin et al. (1999) that exploits the inherent symmetry of **k**-space. In a centric scan only one half of **k**-space is acquired during a magnetisation cycle and so the acquisition needs to be repeated to obtain the other half, a time consuming process. Instead, the data from the first half can be used to reconstruct the data for the other half, though this does require knowledge of the exact centre of **k**-space and results in a decrease in the SNR due to the acquisition of fewer independent data points.

Parasoglou et al. (2008) proposed a different way of sampling **k**-space which exploits prior knowledge of the system. Longitudinal magnetisation decays with time, so not all of **k**-space is sampled with the same amount of magnetisation, as described in the section on magnetisation evolution in the previous chapter. This method aims to acquire the points in **k**-space with the highest expected modulus signal with the largest possible magnetisation, thereby improving the SNR. To do this, the points from a conventionally acquired full **k**-space data set are ranked in order of decreasing modulus signal and then sorted into batches called interleaves, as illustrated in Figure 4.12. Subsequent experiments use this ordering to sample **k**-space. For this technique to be used successfully, the geometry of the system should not change significantly during the testing period. In their study, Parasoglou et al. (2008) found that by implementing this sampling method they were able to maintain image quality (low percentage error) while significantly under-sampling **k**-space and hence shortening the acquisition time.

Sorting *k*-space points from maximum to minimum value

| 1 | 2 | 3 | 4 | 5 | 6 | 7 | 8 | 9 | 10 | 11 | 12 | ... |

Reshape points for the case of 4 interleaves

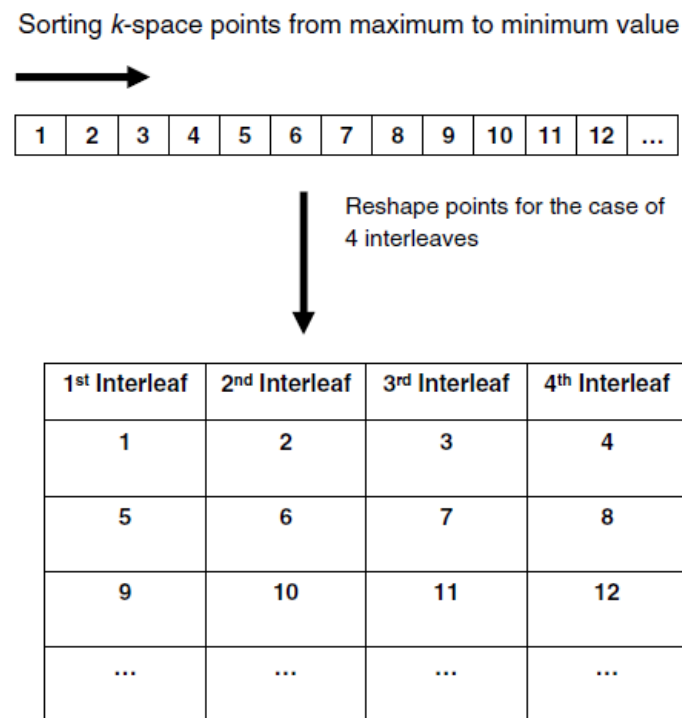| 1st Interleaf	2nd Interleaf	3rd Interleaf	4th Interleaf
1	2	3	4
5	6	7	8
9	10	11	12
...	...	...	...

Figure 4.12. Sorting and reshaping k-space points. First all **k**-space points are sorted according to their modulus value (top), the global maxima will be sampled first at each interleaf (bottom). (Parasoglou et al. 2008)

Reconstruction of the image from under-sampled **k**-space data using linear transforms (such as the Fourier transform) is expected to result in diminished accuracy and artefacts in the images due to the violation of the Nyquist theorem (Equation 3.25) (Parasoglou et al. 2009). An alternative image reconstruction technique that may be applied is CS which aims to reconstruct significantly under-sampled images while avoiding loss of quantification (Lustig et al. 2007, Lustig et al. 2008). This is done by exploiting the inherent sparsity of MR images found in an appropriate known and fixed mathematical transform domain. Examples of these transformations include wavelet and spatial finite-differences (Lustig et al. 2008, Parasoglou et al. 2009). The image domain may also be used as the transform domain if it exhibits sufficient sparsity, in other words, if there are relatively few significant pixels with non-zero values (Lustig et al. 2007). Note that a signal is described as sparse if it contains only a small number of non-zero values or if these values decay rapidly (Parasoglou et al. 2009).

Hence, CS may be used to acquire accurate image reconstructions from only a small subset of **k**-space. For this technique to be applied successfully, Lustig et al. (2008) have outlined three requirements that must be met:

1. The image must have a sparse representation in a known transform domain.

2. Any artefacts in reconstruction that result from the under-sampling of **k**-space should be incoherent (noise-like) in this transform domain.

3. The image needs to be reconstructed by a nonlinear method that enforces both the image representation sparsity and the consistency within the data.

The first requirement is met by MR images, as described in the previous paragraphs. The incoherency of acquisition, mentioned in the second point is determined by the sampling scheme (random, spiral, radial, etc). With regards to the third requirement, the image is generally reconstructed using a method based on solving a convex optimisation problem that involves l_1-norms. If the reconstructed image is represented by a complex vector m, then Ψ is the linear operator that transforms from the pixel representation to the chosen sparse domain. Let F be the under-sampled Fourier Transform (FT) to **k**-space and y be the **k**-space measurements from the MRI scanner. The reconstructions are then obtained by solving the following constrained optimisation problem:

$$\text{minimise} \left\| \Psi m \right\|_1 \qquad\qquad 4.2$$

$$\text{such that } \left\| Fm - y \right\|_2 < \varepsilon \qquad\qquad 4.3$$

where ε is a threshold that can be set to be roughly the expected noise level. The l_1 norm here is defined as:

$$\left\| x \right\|_1 = \sum_i \left| x_i \right| \qquad\qquad 4.4$$

Therefore, minimising the l_1-norm promotes sparsity, so that an image is produced which has the sparsest possible representation in the transform domain, while still remaining consistent with the acquired measurements. The constraint equation enforces this data's consistency.

Parasoglou et al. (2009) have shown that CS may be used with SPI to significantly reduce the loss of accuracy in images reconstructed from under-sampled acquisition data. An advantage of using CS with SPI that they identify is that it allows for unconstrained selection of sampling trajectories, an issue that had been previously identified by Lustig et al. (2008).

Consequently it is desired to establish if standard protocols for under-sampling are viable time-saving options when imaging ore systems. The two extremes of random and sorted (Parasoglou et al. 2008) under-sampling of **k**-space are considered for this. The effect of using a standard CS algorithm (Parasoglou et al. 2009) for the image reconstruction on the accuracy of the image is also tested.

4.4.1   Experimental

The column used for the saturated sample section was used for these experiments (Figure 4.1). Approximately 80 g of ore (full PSD) was agglomerated with 20 ml of 0.1 M sulfuric acid and packed into the column. The ore was saturated with distilled water and the gravimetric voidage was measured to be 39.2%.

The column was imaged on the AV 85 spectrometer using SESPI. The same settings as specified for the saturated column (described in Section 4.2.1.2) were used. The whole of **k**-space was sampled in the actual acquisition. Any reduction in the number of sampled points was done as part of the data processing. The non-sampled **k**-space points were zero-filled. For the sorted under-sampling the voxels from a full acquisition were sorted based on their relative signal importance as was done by Parasoglou et al. (2008). Points in **k**-space were then acquired in subsequent under-sampled scans based on this order. The CS algorithm of Parasoglou et al. (2009) was applied to the sorted under-sampled data only and the image was used as the sparsifying transform.

4.4.2   Application of Under-Sampling and CS to SESPI Acquisition

The error introduced into the images due to **k**-space under-sampling was quantified so that the performance of the different methods could be assessed. This was done by calculating the average (absolute) pixel error of the under-sampled images relative to the fully reconstructed image. The resulting errors are summarised in Table 4.4.

Table 4.4. Percentage error in the reconstructed images that result from the under-sampling of **k**-space. A dash indicates data not acquired.

Method	75% sampled	50% sampled	25% sampled
Random under-sampling	36.6 ± 0.5	-	-
Sorted under-sampling			
Fourier transform	1.29	3.96	6.93
Compressed sensing	1.36	4.04	6.99

Figure 4.13 compares a slice from the fully acquired image with an under-sampled reconstruction where 75% of the **k**-space points were acquired. The average error is 36.6±0.5% and the loss in image quality is readily visible in Figure 4.13. This random under-sampling result is indicative of the worst error that may be expected due to under-sampling as no prior knowledge of the system is used to optimise the selection of **k**-space that is acquired.
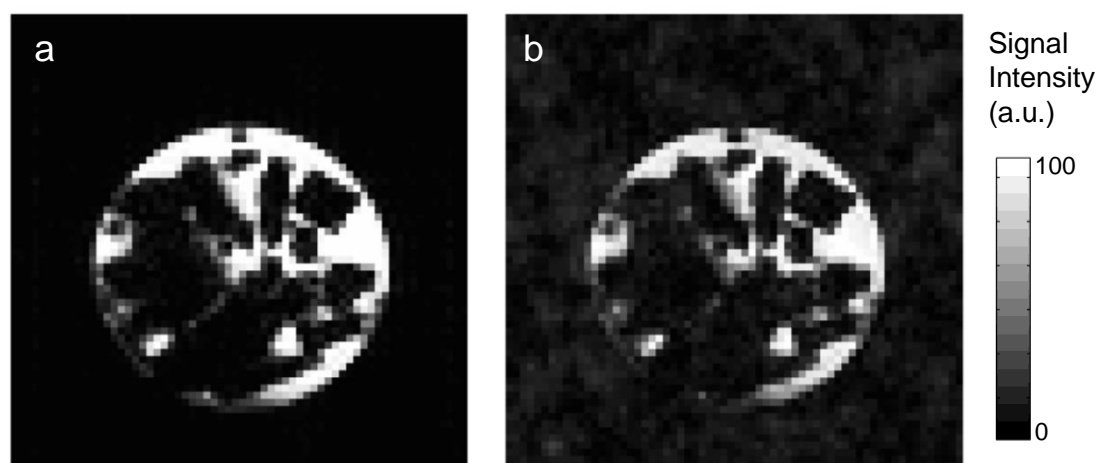
Figure 4.13. Slices of the saturated agglomerated ore sample reconstructed from (a) all of **k**-space and (b) 75% of **k**-space, randomly selected and zero-filled.

When sorted under-sampling is used, a 75% acquisition results in an error of only 1.29%. This is a significant improvement on the random under-sampling. The error in the images increases when smaller fractions of the data are used, with 50% and 25% acquisitions having errors of 3.96% and 6.93% respectively. These errors are much smaller than for the random under-sampling approach and sorted under-sampling therefore would be a viable time saving technique. However, this technique does require prior knowledge of the system which may not always be possible, for example due to a transient system. Therefore other under-sampling approaches, such as putting requirements on the randomly sampled points' distribution, should be considered in the future if the acquisition time of an SESPI experiment needs to be significantly reduced.

The CS error is consistently higher than when the sorted under-sampled data is reconstructed with a simple Fourier transform, contrary to what has been observed by Parasoglou et al. (2008). This suggests that the reconstruction of the image using this CS method is not advantageous. This is possibly because the sample's high degree of inhomogeneity or the SNR results in the image space not being sufficiently sparse for CS to be effective. If this is the case other transform domains (e.g. wavelet) could be considered in future experiments. The small increase in the error could also be because the CS causes an increase in the SNR of the image (Lustig et al. 2008) thereby resulting in an apparent difference from the fully sampled imaged rather than a true error. CS should therefore still be considered in future experiments.

4.5 Conclusions

The spin echo acquisitions confirmed that frequency encode methods are not appropriate for the imaging of ore systems due to the formation of magnetic susceptibility artefacts. The pure phase encode techniques, SPI and SESPI, were found to be effective for obtaining distortion free images of the saturated ore column at a moderate field strength (2 T). This was confirmed through the comparison of the MRI images with a high resolution distortion free X-ray CT acquisition. The SNR and contrast of the SESPI acquisition of the saturated system was better than that of the SPI-MPA ones. Furthermore, the SPI-MPA signal was found to decrease with PSD due to T_2^* decreasing with the particle size of the ore, while it was found to have only a comparatively small effect on SESPI signal. These results support the use of SESPI over SPI-MPA for the imaging of the ore samples.

Flooded and flowing experiments on a higher field magnet confirmed this, where SPI-MPA was found effectively to collapse due to T_2^* being reduced because of the higher field. SESPI still worked well as the T_2 remained suitably long. Hence it was concluded that SESPI was the most robust imaging method for the study of low grade copper ore heap leaching hydrology.

Sorted under-sampling of **k**-space was demonstrated to result in minimal loss of image accuracy relative to random under-sampling and would therefore be an effective technique for the shortening of acquisition times if required in future experiments. It does however have the disadvantage of requiring prior knowledge of the system which may not always be possible, in which case different under-sampling techniques should be investigated. CS was not found to be obviously beneficial with regards to the reconstructed image accuracy, but further testing should be considered in the future.

4.6 Nomenclature

Abbreviations

CS   -   compressed sensing

CT   -   computed tomography

CZT   -   chirp z-transform

FID   -   free induction decay

FOV   -   field of view

FT   -   Fourier transform

FW   -   filter width

FWHM -   full width at half maximum height

MR   -   magnetic resonance

MRI   -   magnetic resonance imaging

PSD   -   particle size distribution

RF   -   radio frequency

SESPI -   spin echo single point imaging

SNR   -   signal to noise ratio

SPI   -   single point imaging

Symbols

$\mathbf{B}_0$ -   static external magnetic field [T]

F -   under-sampled FT to $\mathbf{k}$-space

$\mathbf{k}$ -   reciprocal space vector [m^{-1}]

$\boldsymbol{m}$ -   complex vector that represents the reconstructed image

t_p -   phase encode time [s]

t_{pul} -   RF pulse duration [s]

t_{p0} -   initial phase encode time [s]

T_1 -   spin-lattice relaxation constant [s]

T_2 -   spin-spin relaxation constant [s]

T_2^* -   effective spin-spin relaxation constant [s]

TE   -   echo time [s]

TR   -   repetition time [s]

y   -   **k**-space measurements from the MRI scanner

Greek letters

ε -   threshold parameter

Ψ -   linear operator that transforms from the image to the sparse domain

4.7 References

Callaghan, P. T. (1995) *Principles of Nuclear Magnetic Resonance Microscopy,* New York: Oxford University Press.

Fang, Z. J., Hoepfel, D. and Winter, K. (2001) 'Application of Single Point Imaging (SPI) to solid state materials', *Magnetic Resonance Imaging,* 19(3-4), 501-503.

Gladden, L. F. (1994) 'Nuclear magnetic resonance in chemical engineering - Principles and applications', *Chemical Engineering Science,* 49(20), 3339-3408.

Gravina, S. and Cory, D. G. (1994) 'Sensitivity and resolution of constant-time imaging', *Journal of Magnetic Resonance Series B,* 104(1), 53-61.

Haacke, E. M., Brown, R. W., Thompson, M. R. and Venkatesan, R. (1999) *Magnetic Resonance Imaging – Physical Properties and Sequence Design*, Wiley-Liss.

Halse, M., Rioux, J., Romanzetti, S., Kaffanke, J., MacMillan, B., Mastikhin, I., Shah, N. J., Aubanel, E. and Balcom, B. J. (2004) 'Centric scan SPRITE magnetic resonance imaging: optimization of SNR, resolution, and relaxation time mapping', *Journal of Magnetic Resonance,* 169(1), 102-117.

Lustig, M., Donoho, D. and Pauly, J. M. (2007) 'Sparse MRI: The application of compressed sensing for rapid MR imaging', *Magnetic Resonance in Medicine,* 58(6), 1182-1195.

Lustig, M., Donoho, D. L., Santos, J. M. and Pauly, J. M. (2008) 'Compressed sensing MRI', *IEEE Signal Processing Magazine,* 25(2), 72-82.

Mantle, M. D. and Sederman, A. J. (2003) 'Dynamic MRI in chemical process and reaction engineering', *Progress in Nuclear Magnetic Resonance Spectroscopy,* 43(1-2), 3-60.

Mastikhin, I. V., Balcom, B. J., Prado, P. J. and Kennedy, C. B. (1999) 'SPRITE MRI with prepared magnetization and centric k-space sampling', *Journal of Magnetic Resonance,* 136(2), 159-168.

Parasoglou, P., Malioutov, D., Sederman, A. J., Rasburn, J., Powell, H., Gladden, L. F., Blake, A. and Johns, M. L. (2009) 'Quantitative single point imaging with compressed sensing', *Journal of Magnetic Resonance,* 201(1), 72-80.

Parasoglou, P., Sederman, A. J., Rasburn, J., Powell, H. and Johns, M. L. (2008) 'Optimal k-space sampling for single point imaging of transient systems', *Journal of Magnetic Resonance,* 194(1), 99-107.

Prado, P. J., Balcom, B. J. and Jama, M. (1999) 'Single-point magnetic resonance imaging study of water adsorption in pellets of zeolite 4A', *Journal of Magnetic Resonance,* 137(1), 59-66.

Ramos-Cabrer, P., van Duynhoven, J. P. M., Van der Toorn, A. and Nicolay, K. (2003) 'MRI of hip prostheses using single-point methods: in vitro studies towards the artifact-free imaging of individuals with metal implants', *20th Annual Meeting of the ESMRMB,* 22, 1097-1103.

Chapter 5 – Phase Distribution Identification in Column Leaches

In this chapter magnetic resonance imaging (MRI) is used to develop 3D phase maps which allow for the identification of the position of the gas, liquid and solid phases within agglomerated ore columns. The phase maps are used to quantify the voidage and liquid hold-up, to measure the interfacial area between the phases and to classify the liquid distribution with respect to its proximity to the solid ore surface. A study on the effect of flow rate on these parameters is presented and a set of MRI and traditional tracer experiments are used to examine the stagnant versus flowing liquid distribution within the column. Comparison with traditional chemical engineering measurement techniques are considered throughout this work.

5.1   Introduction

The design of heap leaches and models to describe their performance requires knowledge of certain characteristic parameters of the ore beds such as voidage and liquid hold-up. The low liquid flow rates (typically Reynolds number is < 1), atmospheric pressure operation, the almost stagnant gas phase and the irregular structure and shape of the ore agglomerates mean that heap leaching conditions are very different to typical trickle bed reactors (de Andrade Lima 2006). As a result, standard trickle bed coefficients and correlations are not applicable to heap leaching systems. Therefore accurate analysis of heap leaching hydrodynamics requires the measurement of key ore bed characteristics anew.

The voidage and the liquid hold-up of ore beds are typically measured using gravimetric techniques. The standard method for voidage measurement is to flood the ore bed with liquid so that the pore spaces are filled. This is typically done at the start of column leaching experiments. Ilankoon and Neethling (2012) however reason that this can cause higher steady state liquid hold-ups during subsequent leaching of the ore due to hysteresis effects. This may be a contributing reason for the differences between laboratory and full scale operation. Bouffard and Dixon (2001) presented a method whereby estimates of the flowing and stagnant liquid hold-up can be measured. They proposed that the flowing liquid hold-up corresponded to the liquid drained from the column after 24 hours when the irrigation of the ore was halted. The stagnant liquid hold-up was measured in two ways. In the first method the stagnant liquid hold-up was defined as the liquid that remained in the column after the 24 hours of drainage from an initially saturated state. In the second approach the stagnant liquid hold-up was defined as the difference between the amount of liquid that had been

irrigated onto an initially dry ore column and the solution that had been collected at the base following the onset of steady state (when the inlet and outlet flow rates matched).

Lin et al. (2005) took a microscopic experimental approach to measuring the voidage, using X-ray computed tomography (CT) to image leaching systems before and after leaching. This also allowed for variations along the height of the column to be identified. X-ray CT however provides limited signal contrast between the air and liquid phases in the presence of comparatively high density solids and therefore is not an ideal technique to study the liquid hold-up. Furthermore, in the context of bioleaching X-ray radiation could also sterilise the column.

Other parameters such as mass transfer coefficients, the liquid-gas and liquid-solid contact area, pore length and axial dispersion coefficients have been approximated by fitting a variety of models to experimental results from tracer studies (Bouffard and Dixon 2001, de Andrade Lima 2006). These experiments have also been used to assess the relative importance of gravitational flow, axial dispersion and pore diffusion.

The aim of this study is to develop a method whereby MRI acquisitions of a flowing, partially saturated ore column can be combined with images of the fully saturated column to produce a 3D phase map which illustrates the relative positions of the gas, liquid and solid phases within the column. This map will allow for the quantification of various parameters characterising the system hydrodynamics including hold-up, contact area between the different phases and the distribution of phases with respect to the solid matrix. The effect of flow rate on these parameters is then considered. Tracer studies are also performed to examine the liquid flow at steady state. Comparison with the standard measurement techniques as have been presented in the literature is considered throughout.

5.2 Experimental

5.2.1 Leaching Column

Low grade copper ore was used in the experiments. It had an average composition of 2.95% Fe, 0.69% Cu and 2.02% S on a weight basis. The particle size distribution (PSD), measured by sieving, is given in Table 5.1. The ore was agglomerated with 0.1 M sulfuric acid in a ratio of 1 ml liquid per 20 g solid and packed into the column illustrated in Figure 5.1. The inner diameter of the column was 50 mm which was restricted by the magnet's internal bore. Two packed ore columns were used in the study. The first was for the method development experiments, for which the weight of the dry ore was 400 g and the initial height

of the agglomerated ore bed was 135 mm. The second column was used to assess the effect of liquid flow rate changes and was packed with 600 g of dry ore that had been agglomerated which had an initial height of 230 mm in the column.

Table 5.1. PSD of the Escondida Type B ore used in the leaching column.

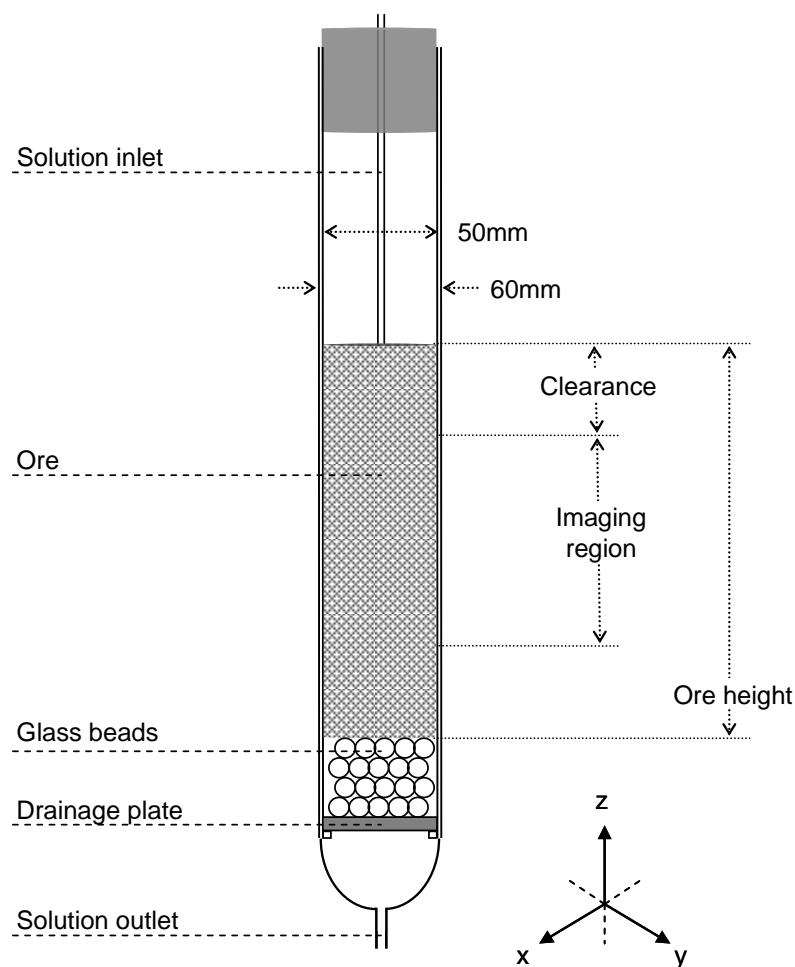| Size (mm)	Weight (%)
> 13.2	14.0
9.5 - 13.2	18.4
5.6 - 9.5	20.3
2.0 - 5.6	19.8
0.71 - 2.0	9.1
< 0.71	18.5

Figure 5.1. Schematic of the leaching column.

The column was irrigated drip-wise from the top using a peristaltic pump at a rate of 40 ml h^{-1}. Flow rates of 10 ml h^{-1}, 20 ml h^{-1} and 60 ml h^{-1} were also used to examine the effect of different flow rates. This is approximately equivalent to 5, 10, 20 and 30 L m^{-2} h^{-1}. The system was allowed to stabilise before any images were acquired so that the outlet flow rate matched the inlet. The column was flooded to allow for the full void space to be imaged and for the gravimetric voidage of the ore to be calculated. For the method development experiments distilled water was used for the liquid while water doped with 0.8 g L^{-1} of GdCl$_3$·6H$_2$O was used in the flow rate experiments to allow for a faster acquisition time.

5.2.2   MRI Parameters

The method development imaging was conducted on a Bruker DMX 200, 4.7 T vertical bore spectrometer with a radio frequency (RF) coil with internal diameter of 63 mm and an imaging region of approximately 70 mm in length. A single echo per excitation spin echo single point imaging (SESPI) pulse sequence with split phase encoding gradients was used. The field of view (FOV) was 60 mm × 60 mm in the horizontal plane (x and y) and 72 mm in the vertical direction (z). The acquisition size was 64×64×32, which corresponded to a resolution of 938 μm in the horizontal plane and 2250 μm in the vertical plane. The resolution was limited by the maximum allowable gradient strengths and time restrictions. The acquisitions had a repeat time (*TR*) of 50 ms, a total gradient encoding time (t_p) of 350 μs and an echo time (*TE*) of 870 μs. Four repeat scans were done for phase cycling and eight points were acquired at 5 μs intervals along the echoes and added together in order to improve the final signal to noise ratio (SNR).

The different flow rate and tracer experiments were performed on a Bruker AV 300, 7 T vertical bore spectrometer with a wide bore RF coil which had an inner diameter of 63 mm. The FOV was approximately 53 mm × 53 mm in the x and y directions and 89 mm in the z (along the bore length). The z FOV was longer than the length of the homogeneous imaging region of the coil, but it was chosen to prevent wrap-around artefacts that would affect the image analysis. The acquisition size was 64×64×64 in the case of a 3D acquisition. This corresponds to a nominal resolution of 830 μm per pixel in the x and y directions and 1390 μm in the z direction. A standard SESPI acquisition sequence was used as before. It utilised a t_p of 300 μs, a *TR* of 50 ms and a *TE* of 750 μs. Four repeat scans were done for phase cycling and eight points were acquired at 5 μs intervals along each echo for signal averaging.

5.2.3 Tracer Experiments

The validity of MRI images as a means to describe the solution flow was tested by comparing an MRI step tracer experiment with a conventional $NaNO_3$ tracer experiment (Bouffard and Dixon 2001, Bouffard and West-Sells 2009). In both cases the column inlet solution was step changed to the tracer following the establishment of steady state flow (when the inlet and outlet flow rates were matched). The flow of the tracer was then monitored for a period of six hours.

The MRI experiments used D_2O (99.9 atom % D) as the tracer. D_2O is MRI inactive and so it does not give off signal during a proton MRI experiment. The ingress of the tracer solution into the column was monitored by recording the signal magnitude in the imaging region every 10 minutes. SESPI profiles of the signal in the x, y and z directions were also acquired.

The traditional tracer experiments used a 1 M $NaNO_3$ solution as the tracer. Conductivity measurements were taken every 15 minutes to monitor the concentration of the tracer in the column effluent. A linear relationship exists between the solution concentration and the conductivity at the concentrations used (Bouffard and Dixon 2001) so no conversion of the readings was required. The column was initially irrigated with a 0.05 M $NaNO_3$ solution until the conductivity of the outlet was stable and matched that of the feed solution. This was then followed by the step change to the tracer solution.

5.3 Method Development

5.3.1 Production of the Phase Map

Since signal in the MRI images is obtained only from the liquid phase, the flooded column images can be used to identify the void space within the column whilst the flowing images only show where the solution is present in the partially saturated system. The positions of the solid, liquid and gas phases can therefore be identified by combining the two acquisitions to produce a 3D phase map as has been done in the past in studies such as that by Sederman and Gladden (2001). Figure 5.2 (a) shows a representative 2D slice (from the 3D acquisition) of the flooded column, binary gated to liquid (white) and solid ore (black) in Figure 5.2 (b). The corresponding slice for the unsaturated 40 ml h^{-1} flowing system is shown in Figure 5.2 (c) with the binary gated image shown in Figure 5.2 (d) (here black indicates solid ore or air). By addition of Figure 5.2 (b) and (d) Figure 5.2 (e) is produced, a phase map where white represents the gas phase, grey is the liquid phase and black is the solid ore phase or outside the sample. Partial volume effects where pixels are occupied by more than one phase need to

be accounted for in the phase map. They are identified as those pixels that were assigned to be non-void (solid) pixels in the flooded image gating, but subsequently identified as being occupied by liquid in the flowing system images. It is not possible to determine what fraction of these pixels is liquid filled, therefore two boundary scenarios are considered for the calculation of the various phase distribution properties. In the one case the partial volume pixels are assumed to be liquid filled, thereby allowing for an upper bound to be calculated. The pixels are assumed to be free of liquid in the lower bound scenario. The final 3D phase map for the ore column is shown in Figure 5.3 with air (white), water (light and dark grey for filled and partially filled pixels) and solid (black) identified. For clarity of presentation the corresponding 2D slices are shown in Figure 5.4, extracted from the 3D image in the axial direction where the separation distance is 2250 μm.

The average voidage of the imaging region as measured from the flooded image is 41.7±2.4%. The error margins, determined according to the variation within the sample, overlap with the gravimetrically determined voidage of 38.5±0.8%. Direct agreement is not expected as the gravimetric measurement is necessarily performed on the whole ore sample. For the unsaturated flowing column, the liquid phase is found to account for 17.4±2.2% and the gas phase accounts for 24.4±2.4% of the total bed space. These overall and phase-specific values are in good agreement with those reported previously in the heap leaching literature. For example in Bouffard and Dixon (2001), their columns had an average total void fraction of 43% and the most similar columns to the one studied here had a liquid content of between 12 and 23% which compares favourably to the circa 17% measured here. They determined these values using standard gravimetric measurements and by measuring effluent flow volumes, as described in the Introduction. These results indicate that the MRI phase maps provide accurate values for the voidage and liquid hold-up of the agglomerated ore bed, despite the ferro- and paramagnetic content of the ore.
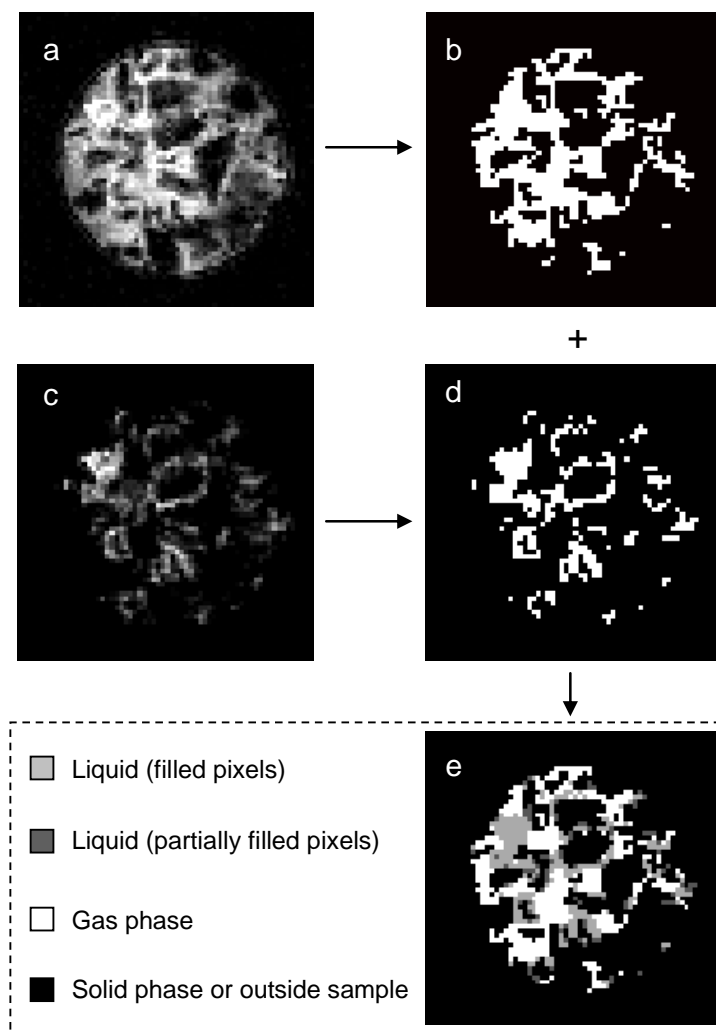
Figure 5.2. Method used to process the MRI data to produce the phase map. The (a) flooded column images are thresholded to (b) binary images. The same is done for the (c) flowing column images to produce (d). The thresholded images (b) and (d) are finally combined to produce the phase map (e).
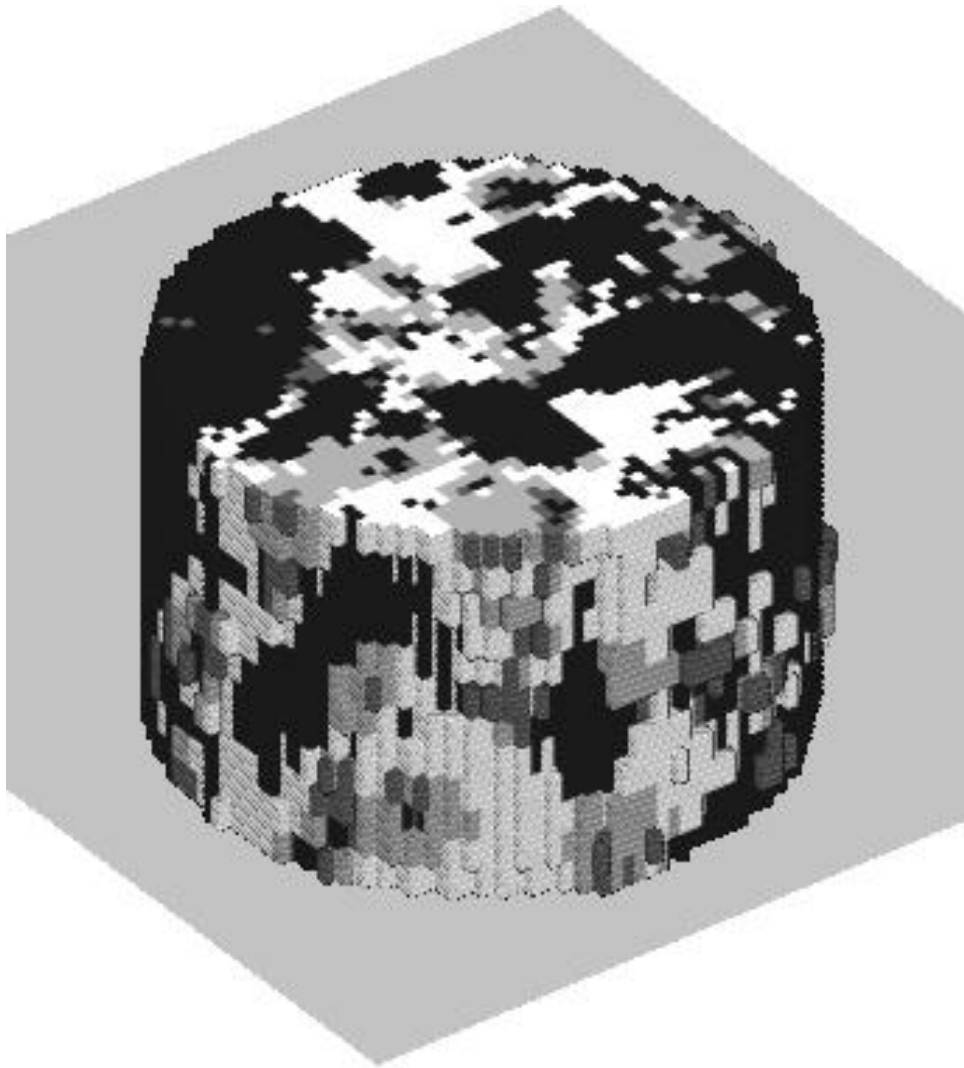
Figure 5.3. Full 3D phase map of the unsaturated column after data analysis as described in the text. Different shades of grey are used to identify the various phases as is detailed in Figure 5.2 (e).
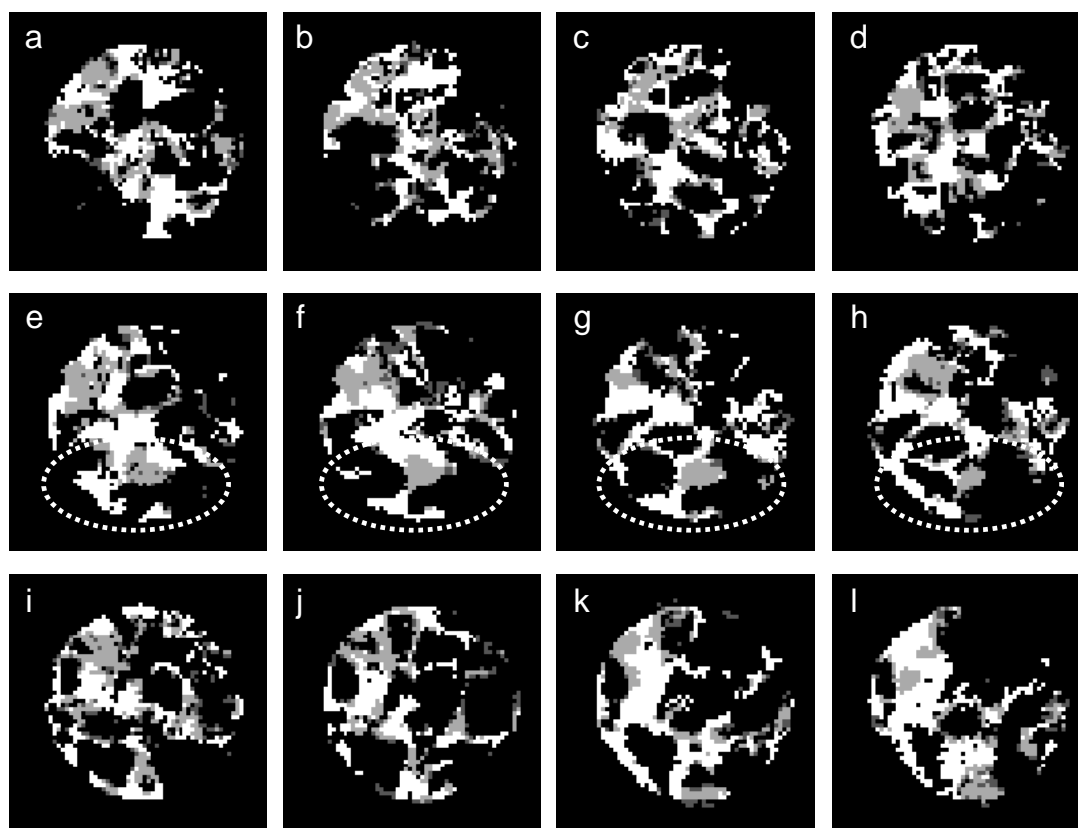
Figure 5.4. 2D phase maps of the unsaturated column extracted from the 3D data shown in Figure 5.3. The slices have an axial separation of 2250 μm where (a) is at the top of the imaging region and (l) is at the bottom. Different shades of grey are used to identify the various phases as shown in Figure 5.2 (e). Inter-linking flow channels are highlighted in slices (e) to (h).

5.3.2   Column Wetting

Different types of flow can be observed from the phase maps. With respect to Figure 5.4, channels of flow are evident linking adjacent slices, such as is highlighted in the bottom half of images (e) to (h). The majority of the solution is seen to flow along the edges of the ore particles in thin films or between adjacent particles as pore flow, where pores refer to an inter-particle phenomenon. This is consistent with the ore being preferentially water-wetting. The phase maps are used to determine the distance of the liquid from a solid edge boundary in order to explore this observation quantitatively. This is done using the pore thinning algorithm of Baldwin et al. (1996) on the total void space after which the liquid pixels are identified. The algorithm works by shrinking the pore space pixel by pixel, during which the local maximum distances are identified. The results of this analysis are given in Table 5.2.

It is found that 57.8±5.4% of the liquid occurs less than 1 mm from the solid while only 2.5±0.4% is located more than 3 mm from a solid boundary. The effect of considering the partial volume pixels to be liquid filled is to increase the number of total void and liquid pixels nearest the surface, resulting in a larger percentage range for those pixels less than 1 mm from the solid. This is expected as the partial volume effect is defined as being at the interface of the liquid and the solid phases. Furthermore, the percentage of the void space occupied by liquid for the larger distance ranges remains approximately constant at around 40%. This indicates that not all flow is dominated by wettability effects and that some liquid flow is in the form of larger channels.

Table 5.2. Position of the liquid in the method development column expressed as its distance from the solid surface and the percentage of the void space at that distance. The error measurements are generated by considering partial volume effects.

Distance from solid ore surface (mm)	Liquid pixels (%)	Pore space occupied by liquid (%)
< 1	57.8 ± 5.4	39.6 ± 6.0
1 - 2	26.1 ± 3.1	38.1 ± 0.9
2 - 3	13.7 ± 1.9	34.5 ± 0.5
3 - 4	1.7 ± 0.3	44.3 ± 0.2
4 - 5	0.7 ± 0.1	41.8 ± 0.0
5 - 6	0.1 ± 0.0	40.0 ± 0.0

An alternative approach to the distance calculation is to generate the distance map from the liquid pixels only and not the total void space. This takes into account that the liquid may not be connected to the nearest solid surface by other liquid pixels. For the majority of the liquid (77%) the distance is unchanged from the distances populated for Table 5.2. For the remaining pixels the liquid film bridges beyond the centre of the pore, whilst not making contact with the other side, resulting in a longer distance to the solid. The maximum liquid film thickness in the bed is found to be 7.3 mm using this method. This measurement of liquid film thickness is important with respect to the mass transfer of oxygen and carbon dioxide from the gas to the leaching sites. The average distance of the liquid from a solid edge is calculated using the second method to be 1.27±0.05 mm, compared with 1.37 mm for the total void space. This confirms that overall the liquid slightly favours high surface flow in the form of small pore rivulets, a behaviour that may be attributed to wettability effects.

5.3.3   Interfacial Area between Phases

The phase maps allow for the measurement of the interfacial area between the different phases. The gas-liquid interfacial area for the column is determined to be 906 ± 57 m^2 m^{-3} of liquid. The volume of column considered excludes the pixels adjacent to the column walls to avoid including wall effects in the analysis. This value also refers to the entire liquid volume as the stagnant and flowing liquid are not individually identified.

Previous ore leaching studies have found that the rate limiting step in heap bioleaching is gas-liquid mass transfer (Petersen 2010a, Petersen 2010b) with the supply of oxygen to the liquid phase reaction systems becoming mass transfer limited. The rate of gas adsorption (r_{GLMT}) is usually modelled as:

$$r_{GLMT} = k_L a \left(c^* - c_b \right)$$

5.1

where $k_L a$ is the lumped area-mass transfer coefficient, c^* is the solubility of the gas at the gas-liquid interface and c_b is the bulk concentration within the liquid.

The mass transfer coefficient has been treated in the literature as this lumped parameter as it can be determined experimentally from exit measurements (Petersen 2010b). Values reported in the bioleaching literature range between 20 and 47 h^{-1} (Bouffard and Dixon 2009, Petersen 2010b, Petersen and Dixon 2007). The coefficient is a combination of k_L, the overall gas-liquid mass transfer coefficient (m h^{-1}), with a, the available gas-liquid contact area per unit volume of stagnant solution (m^2 interfacial area per m^3 liquid). The gas-liquid contact area has not been measured separately for the leaching systems in these studies, though its effect has been indirectly discussed in the literature with respect to the influence of particle size distribution on the magnitude of $k_L a$ (Petersen 2010b). Measurement of a using MRI can allow for the factors which affect a to be examined independently. This will enable the best design and operation of a leach to be identified with respect to the maximisation of the gas-liquid interfacial area and consequently the optimisation gas-liquid mass transfer.

The liquid-solid interfacial area is an indicator how much of the ore's surface is available for leaching. It is found to be 389 ± 42 m^2 m^{-3} solid while the gas-solid interfacial area is 576 ± 91 m^2 m^{-3} solid. Therefore less than half of the ore's exposed surface area is in contact with liquid. This suggests that the majority of the metal would not be recovered if this system is leached with the current flow pattern, a problem that has been reported in the industrial operation of heaps (O'Kane Consultants Inc. 2000).

The relatively coarse spatial resolution of the MRI images and the SNR will have an effect on the accuracy of these results. Finer details in the structure are not accounted for and will cause

an artificial reduction in the surface area, whilst the pixilation of the interface may cause an increase in the measured surface area. Furthermore, very thin films of liquid may have been unaccounted for in the distance measurements and liquid-solid contact area. These sources of error could be minimised in future experiments by using a higher imaging resolution. However, any resolution improvements would depend on the magnet capabilities and the degree to which it is necessary to acquire undistorted images.

5.4 Effect of Liquid Flow Rate

An additional set of experiments was conducted during the method development study where the column was operated with flow rates of 20 ml h^{-1}, 40 ml h^{-1} and 60 ml h^{-1}. The liquid hold-up in the imaging region was calculated from the gated images. It is observed to increase from 15.7% to 16.7% to 17.0% respectively. This result from the thresholded images is supported by the fact that the signal intensity at the centre of **k**-space (MRI signal acquisition domain) increases with flow rate, which is indicative of an increase in liquid hold-up. The flow paths of the liquid are also observed to change in some places in the column, an example of which is shown in Figure 5.5. In particular, new rivulets are seen to form as has been predicted by Ilankoon and Neethling (2012) and has been observed previously in trickle beds at low flow rates (Sederman and Gladden 2001).
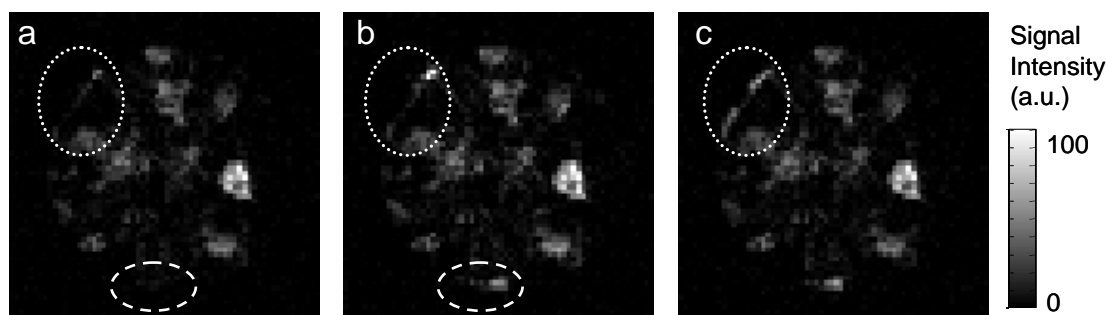

Figure 5.5. 2D slices of the flowing method development column when irrigated at a rate of (a) 20 ml h^{-1}, (b) 40 ml h^{-1} and (c) 60 ml h^{-1}. New rivulets that develop with the flow rate changes are highlighted.

These preliminary experiments were followed by a more in depth study on the effect of flow rate on the liquid distribution. A fresh sample of agglomerated ore was imaged flooded as well as while being irrigated at flow rates of 10, 20 and 40 ml h^{-1} (approximately 5, 10 and 20 L m^{-2} h^{-1}). The gravimetrically determined voidage of this ore column, 38.0±0.8%, agrees with the phase map calculated voidage of 37.9±3.9%, where the error range indicates the variation within the column.

The liquid hold-up of the column under the different flowing conditions is measured in three manners. In the first instance the traditional gravimetric method of Bouffard and Dixon (2001) is used. The liquid hold-up is then assessed in the MRI experiments by considering the total (summed) signal magnitude of the images of the flowing systems as well as by quantifying the liquid filled volume in the phase maps. The results of all of the methods are shown in Table 5.3.

The two MRI liquid quantification methods produce similar relative increases in the liquid hold-up. The MRI total liquid signal values are expected to be a more accurate measurement of the liquid hold-up than the phase map results because it does not require the choice of a thresholding level for the image. The results therefore confirm that the phase map method for the liquid quantification is an acceptable methodology. The MRI results also compare favourably with the traditional gravimetric measurements, as was observed for the previous column. Each doubling of the flow rate results in an absolute increase in the liquid hold-up of between 2% and 3%. The increase in the liquid hold-up when the flow rate increases from 10 to 20 ml h^{-1} was also marginally higher than for the subsequent increase to 40 ml h^{-1}.

Table 5.3. Change in the liquid hold-up of the ore bed as a function of flow rate. The percentage change in the hold-up relative to the lower flow rate value is given in brackets.

Flow rate	Liquid volume (% of column)		MRI total signal magnitude (a.u.)
	Gravimetric	MRI	
10 ml h^{-1}	13.6 ± 1.8	12.8 ± 3.2	1.0
20 ml h^{-1}	17.1 ± 3.4 (26%)	15.8 ± 3.3 (23%)	1.2 (19%)
40 ml h^{-1}	19.2 ± 0.9 (12%)	18.4 ± 3.2 (16%)	1.4 (14%)

The signal magnitude of a pixel is proportional to the amount of liquid held in that region. Therefore the highest intensity pixels will indicate the position of the larger channels of liquid where the pixel is liquid filled. Pixels of lower signal magnitude are indicative of liquid held by capillary forces in small pores or in thin films, unless they fall on the edge of larger channels. Figure 5.6 shows there is an increase in the amount of liquid in all of the pixel magnitude ranges, but the fraction of the total liquid volume held in high magnitude pixels increases while the fraction held in the lowest magnitude pixels decreases. This means that as the flow rate increases the fraction of the liquid that flows in channels increases relative to the liquid volume retained by capillary action in pores. This agrees with the findings of Bouffard and Dixon (2001) who reported that the flowing liquid hold-up increases with increasing flow

rate while the stagnant liquid hold-up remains roughly unchanged. This was done through the use of gravimetric measurements.
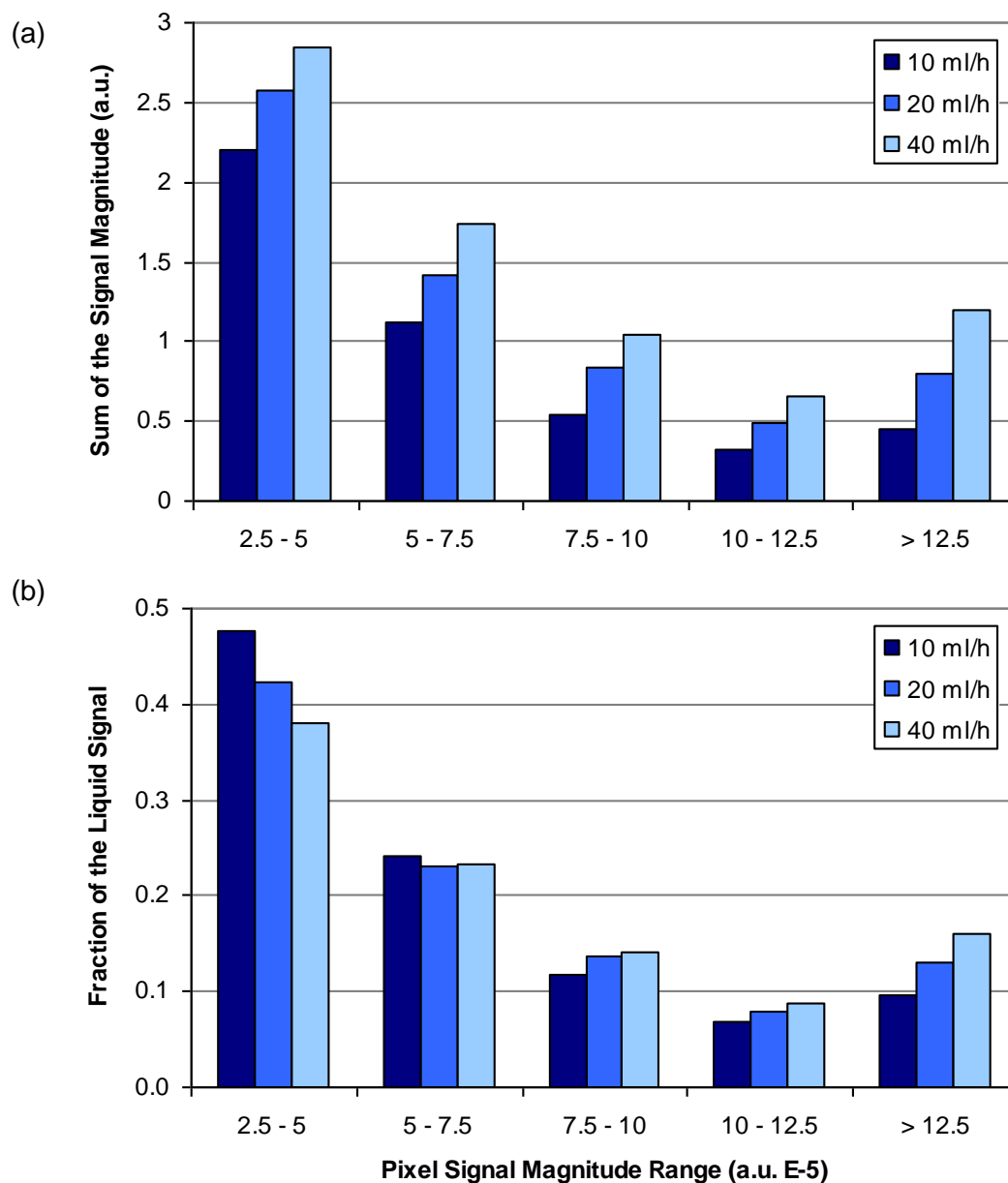
(a)

(b)

Figure 5.6. Distribution of the liquid signal at different flow rates where the signal magnitude is proportional to the volumetric liquid content of the pixel. It is presented as both (a) the sum of the signal magnitude in each range and (b) the fractional contribution of that signal to the overall total.

The MRI results have the advantage of allowing for the spatial resolution of the liquid hold-up, which gravimetric measurements do not. The positions of the liquid and pore space relative to the ore surface are presented in Table 5.4 and the percentages of the different

regions of the pore space occupied by liquid are presented in Table 5.5. Three quarters or more of the liquid is found to be located within less than 1 mm of the ore surface and more than 99% of the liquid is within 2 mm. The average distance of the liquid from the solid ore surface is consequently circa 0.97 mm for all three flow rates. This indicates that there is a stronger preference for surface flow in this ore packing than there is in the column used for the method development experiments, where less than 60% of the liquid is less than 1 mm from the solid and more than 15% is located further than 2 mm from the ore surface. The smaller pore space in this column, where 97% of the pore space is within 2 mm of the ore surface, means that a similar liquid distribution is not possible. This demonstrates that there is a significant degree of variability in the hydrodynamics between different packed ore beds that MRI generated phase maps can identify.

Unlike in the method development experiment, the percentage of the pore space that is liquid filled decreases as the distance from the ore surface increases. This is another indicator of a stronger preference for surface flow in this ore bed. For each increase in flow rate, the liquid occupation of the pore space increases by circa 4% in the 0 to 1 mm and 1 to 2 mm distance ranges. Relatively negligible change occurs in the pore space further from the solid surface, though this is not unexpected as this pore space accounts for less than 3% of the total.

The liquid that is 1 to 2 mm from the solid surface accounts for a larger portion of the total liquid hold-up as the flow rate is increased, while the proportion that is located less than 1 mm from the solid surface decreases. It may therefore be concluded that higher flow rates result in relatively thicker rivulets forming. This is also reflected in the average distance of the liquid from the solid which increases slightly as the flow rate increases. Of the additional liquid retained by the ore bed following the flow rate increases, 92.5±8.2% is not in contact with the existing liquid hold-up (at the lower flow rate). Therefore additional liquid hold-up following an increase in liquid flow rate is in the form of new rivulets rather than due to the growth of existing rivulets. This agrees with and therefore confirms the conjecture of Ilankoon and Neethling (2012) whose gravimetric experiments and models of heap hydrodynamics indicated that additional liquid hold-up in faster flow rate situations was due to the formation of new rivulets.

Table 5.4. Position of the pore (total void) space and the liquid in the column as a function of flow rate expressed as its distance from the solid ore surface. The error measurements are generated by considering partial volume effects.

Distance from solid ore surface (mm)	Pore space (%)	Liquid pixels (%)		
		10 ml h^{-1}	20 ml h^{-1}	40 ml h^{-1}
< 1	64.7 ± 0.5	78.2 ± 5.4	76.2 ± 6.5	74.2 ± 7.4
1 - 2	33.1 ± 0.7	21.7 ± 5.3	23.5 ± 6.5	25.5 ± 7.2
2 - 3	2.2 ± 0.2	0.2 ± 0.1	0.2 ± 0.1	0.3 ± 0.2
3 - 4	0.1 ± 0.0	0.0	0.0	0.0
> 4	0.02 ± 0.00	0.0	0.0	0.0
Average distance (mm)	1.06 ± 0.38	0.95 ± 0.25	0.96 ± 0.26	0.97 ± 0.27
Maximum distance (mm)	4.68	2.90	2.90	2.90

Table 5.5. Percentage of the pore space occupied by the liquid as a function of the flow rate. The error measurements are generated by considering partial volume effects.

Distance from solid ore surface (mm)	Pore space occupied by liquid (%)		
	10 ml h^{-1}	20 ml h^{-1}	40 ml h^{-1}
< 1	25.4 ± 10.3	30.1 ± 11.2	34.0 ± 12.3
1 - 2	14.7 ± 9.5	19.0 ± 12.1	24.0 ± 15.6
2 - 3	2.0 ± 1.6	3.3 ± 2.6	4.4 ± 4.3
3 - 4	0.0	0.0	0.0
> 4	0.0	0.0	0.0

The effect of changing the flow rate on the interfacial areas between the three phases is illustrated in Figure 5.7. The liquid-solid interfacial area increases as the liquid flow rate is increased. This is because of the formation of new rivulets along the ore surface as has been discussed. This shows that increasing the flow rate has the advantage of increasing the amount of liquid-solid contact in a column experiment. This has the potential to improve leaching efficiencies as more of the mineral in the ore will come into contact with the leaching solution, an important finding as less than half of the ore surface is in contact with the liquid films in both of the columns tested. By contrast, the gas-liquid interfacial area decreases as the flow rate is increased because of the increase in the rivulet thickness at the higher flow rate. This will have the effect of increasing the diffusion path for oxygen and carbon dioxide from the gas through the liquid to the bioleaching microorganisms and

reaction sites. This may negatively impact mineral recovery since the liquid mass transfer of oxygen is proposed to be one of the key rate limiting processes (Petersen 2010a, Petersen 2010b). It is likely that an optimal flow rate exists that balances the effect of the liquid-solid and gas-liquid contact areas, though the leaching experiments to determine this point were not considered as part of this study.
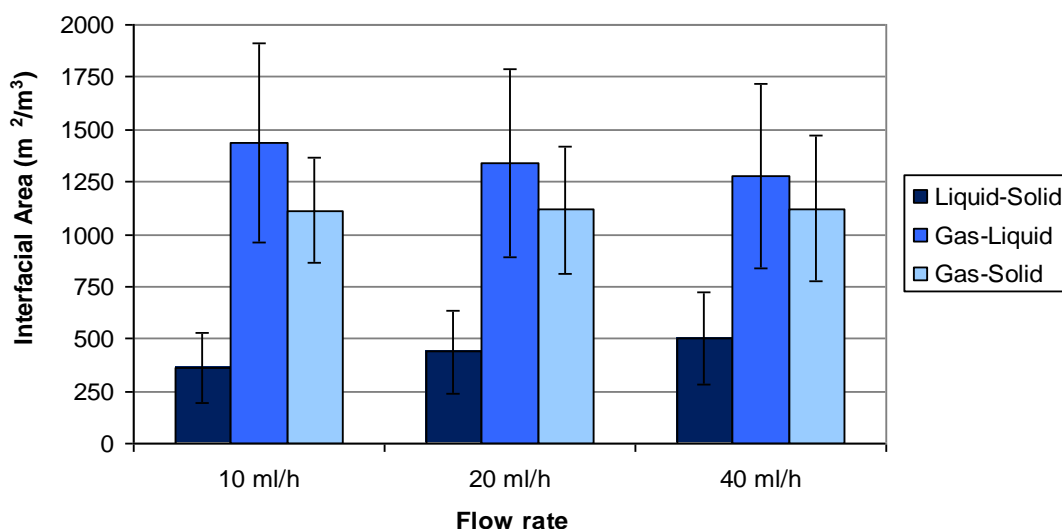

Figure 5.7. Interfacial areas between the gas, liquid and solid phases as a function of flow rate. The error bars indicate the maximum and minimum interfacial areas when partial volume effects are considered.

5.5 Tracer Experiments

Tracer experiments have been used extensively in heap leaching studies to extract the hydrodynamic characteristics of ore beds (de Andrade Lima 2006). Similar MRI experiments may be conducted using D_2O (heavy water), an MRI inactive liquid which will cause the disappearance of MRI signal. Such studies allow for the acquisition of spatially resolved data which may prove useful for the identification of the stagnant and flowing liquid in the ore bed. To establish the validity of the MRI tracer method, a trial D_2O (99.9 atom % D) step tracer experiment is compared to a standard method using $NaNO_3$ as the tracer as was done by Bouffard and Dixon (2001). This was conducted on the column used for the liquid flow rate experiments at a flow rate of 40 ml h^{-1}. The concentration curves that were derived from the two methods are presented in Figure 5.8.

The two curves compare quite closely, though the $NaNO_3$ tracer curve is slightly above the D_2O curve at the 30 and 45 minute readings. Exact agreement between the curves is not

expected as the MRI measurement zone was the imaging region, whereas the NaNO$_3$ experiment was necessarily performed on the exit sample. This may account for slight lag in the NaNO$_3$ tracer relative to the MRI value. The long flat tail common to heap leaching systems (Bouffard and West-Sells 2009) is evident in the results. This result confirms that MRI tracer experiments using D$_2$O are an accurate measure of the ore hydrodynamics.

Figure 5.9 shows a selection of the x, y and z profiles that were acquired of the liquid signal in the column as the experiment progressed. The z profile shows that the D$_2$O has only travelled 60 mm into the imaging region in the first 10 minutes after the step change to the tracer solution. The 20 minute z profile then shows that the D$_2$O has fully penetrated the length of the imaging region. After this time the signal magnitude decreases uniformly along the length of the column. During the first 10 minutes of the tracer flow, signal in the x profile only decreases significantly in the region from 6 to 30 mm. Similarly in the y profile there is no real change in the signal between 15 and 25 mm, while there is in the regions either side of these markers to the column wall. These initial isolated changes show where the main channels of liquid flow are located. The y profiles indicate that preferential flow along the walls of the column may be present in the column. This is a known issue in column studies and is not unexpected considering the relatively small diameter of the column. However the later profiles show that the signal decreases relatively uniformly across the column width. The rate of exchange slows with time, as is clearly illustrated in Figure 5.8, until essentially all of the liquid has exchanged at the end of the six hours. There is thus no evidence of poor liquid exchange within the imaging region of the column.
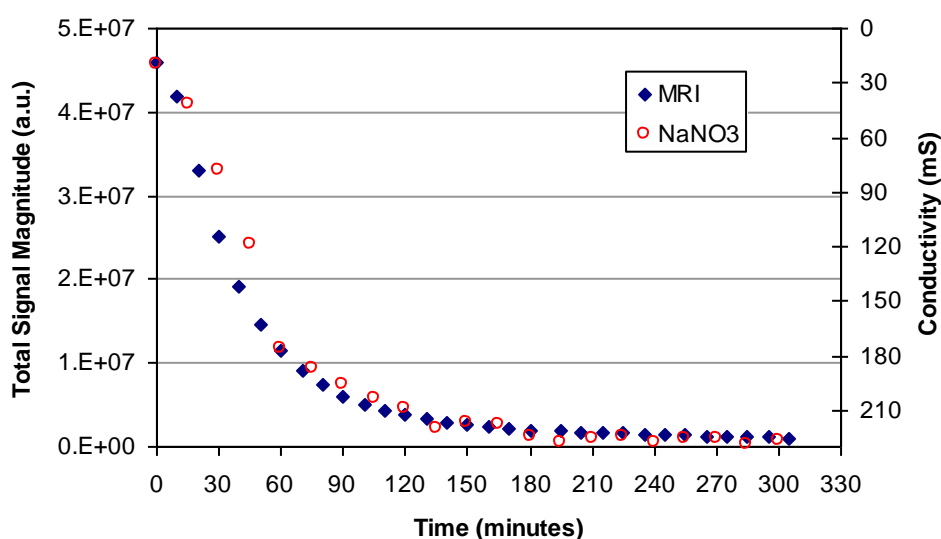

Figure 5.8. Total signal magnitude evolution after the feed solution is swapped from MRI active GdCl$_3$ doped water to MRI inactive D$_2$O.
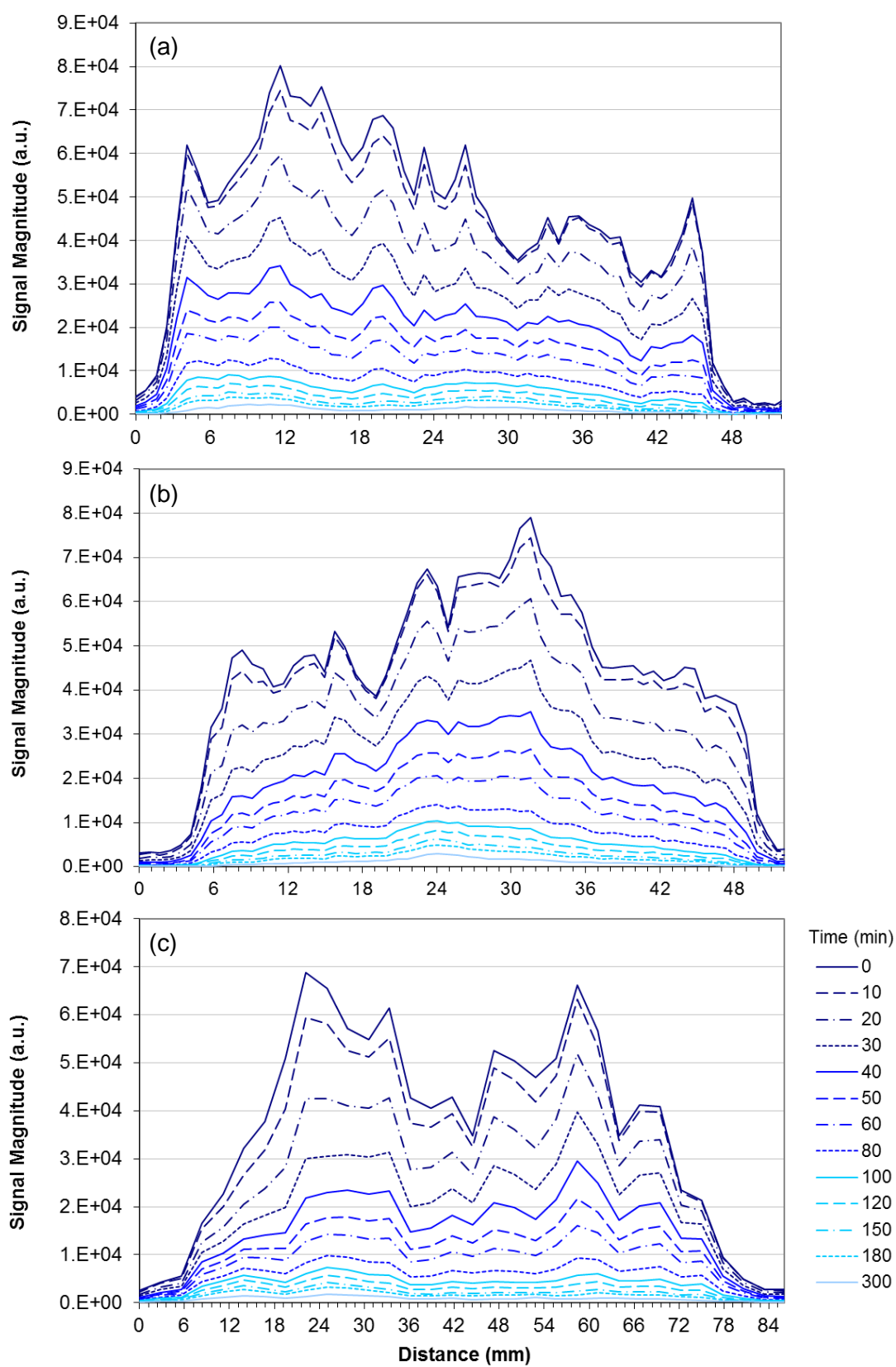
Figure 5.9. The (a) x, (b) y and (c) z MRI signal profiles of the column during the D_2O tracer experiment. The z profile is orientated so that the top of the imaging region is at 0 mm.

5.6 Conclusions

In this study, MRI acquisitions were used to produce 3D maps of the phase distribution within two columns of packed agglomerated ore, from which the solid, liquid and gas phase positions could be identified quantitatively. The voidages of the two columns considered calculated from the phase maps, both around 38%, compared closely with the gravimetrically determined overall voidages. In the first column the liquid and gas phases were found to account for 17.4±2.2% and 24.4±2.4% respectively of the total bed space under flowing conditions at 40 ml h^{-1}. The liquid hold-up of the second column at the same flow rate was very similar at 18.4±3.2%. These values compared favourably with equivalent gravimetric measurements and those values reported in the literature for similar systems.

In the first column it was found that 84% of the liquid occurred less than 2 mm from the solid surface while in the second column there was a stronger preference for surface flow, with 99% of the liquid positioned within 2 mm of the ore surface. The average distance of the liquid from the ore surface was consequently less in the second column, 0.97±0.27 mm versus 1.27±0.04 mm. The stronger preference for surface flow meant that the percentage of the pore space that was liquid occupied decreased as the distance from the ore increased. This was the case in the first column, where circa 40% of the pore space was occupied by liquid in all regions. These results highlight how significant the variation in liquid distribution can be in different ore samples (despite preparing the ore in the same way) and how important it is to acquire data such as this in order to design optimised leaching operations.

Increasing the flow rate increased the liquid hold-up as new rivulets formed in the ore bed while the thickness of the liquid films also increased slightly. This had the effect of improving the liquid-solid interfacial area, an advantageous result as more of the mineral in the ore would be contacted with the leaching solution. This is particularly important as less than half of the ore surface was in contact with the liquid in both columns. The gas-liquid interfacial area decreased as the flow rate increased because the liquid films thickened. This may cause issues with oxygen mass transfer through the liquid to the leaching sites. Hence both these factors need to be considered when determining the best leaching flow rate for a given ore.

Preliminary MRI step tracer tests matched the results of a conventional NaNO$_3$ experiment which confirms the validity of the MRI method. The MRI approach is advantageous as it allows for the spatial resolution of the tracer ingress into the system. MRI tracer profiles enabled the identification of the position of the faster flowing liquid channels. No areas of poor liquid exchange were observed to exist, presumably because the small diameter of the column did not allow them to develop.

5.7 Nomenclature

Abbreviations

CT - computed tomography

FOV - field of view

MRI - magnetic resonance imaging

PSD - particle size distribution

RF - radio frequency

SESPI - spin echo single point imaging

SNR - signal to noise ratio

Symbols

a - available gas-liquid contact area per unit volume of stagnant solution

$[m^2$ interfacial area per m^3 liquid]

c_b - bulk concentration in the liquid [mol m^{-3}]

c^* - solubility of the gas at the gas-liquid interface [mol m^{-3}]

k_L - overall gas-liquid mass transfer coefficient [m h^{-1}]

k_La - lumped area-mass transfer coefficient [h^{-1}]

r_{GLMT} - rate of gas adsorption [mol m^{-2} h^{-1}]

t_p - phase encode time [s]

TE - echo time [s]

TR - repetition time [s]

5.8 References

Baldwin, C. A., Sederman, A. J., Mantle, M. D., Alexander, P. and Gladden, L. F. (1996) 'Determination and characterization of the structure of a pore space from 3D volume images', *Journal of Colloid and Interface Science,* 181(1), 79-92.

Bouffard, S. C. and Dixon, D. G. (2001) 'Investigative study into the hydrodynamics of heap leaching processes', *Metallurgical and Materials Transactions B-Process Metallurgy and Materials Processing Science,* 32(5), 763-776.

Bouffard, S. C. and Dixon, D. G. (2009) 'Modeling pyrite bioleaching in isothermal test columns with the HeapSim model', *Hydrometallurgy,* 95(3-4), 215-226.

Bouffard, S. C. and West-Sells, P. G. (2009) 'Hydrodynamic behavior of heap leach piles: Influence of testing scale and material properties', *Hydrometallurgy,* 98(1-2), 136-142.

de Andrade Lima, L. R. P. (2006) 'Liquid axial dispersion and holdup in column leaching', *Minerals Engineering,* 19(1), 37-47.

Ilankoon, I. M. S. K. and Neethling, S. J. (2012) 'Hysteresis in unsaturated flow in packed beds and heaps', *Minerals Engineering,* 35(1), 1-8.

Lin, C. L., Miller, J. D. and Garcia, C. (2005) 'Saturated flow characteristics in column leaching as described by LB simulation', *Minerals Engineering,* 18(10), 1045-1051.

O'Kane Consultants Inc. (2000) 'Demonstration of the application of unsaturated zone hydrology for heap leaching optimization', *Industrial Research Assistance Program Contract # 332407,* (628-1).

Petersen, J. (2010a) 'Determination of oxygen gas-liquid mass transfer rates in heap bioleach reactors', *Minerals Engineering,* 23(6), 504-510.

Petersen, J. (2010b) 'Modelling of bioleach processes: Connection between science and engineering', *Hydrometallurgy,* 104(3-4), 404-409.

Petersen, J. and Dixon, D. G. (2007) 'Modeling and optimization of heap bioleach processes' in Rawlings, D. E. and Johnson, B. D., eds., *Biomining*, Springer-Verlag, 153-176.

Sederman, A. J. and Gladden, L. F. (2001) 'Magnetic resonance imaging as a quantitative probe of gas–liquid distribution and wetting efficiency in trickle-bed reactors', *Chemical Engineering Science,* 56(8), 2615-2628.

Chapter 6 – Drip Irrigation of Ore

This chapter focuses on the irrigation of ore from a single drip point, studied using magnetic resonance imaging (MRI). The liquid distribution in beds exclusively packed with very large ore particles or fines are presented first. The irrigation of agglomerated ore beds is then described. The effect of varying the flow rate and the repeat irrigation of the ore on the liquid flow path are considered. Finally, tracer-type studies where the liquid feed is stepped between normal water and heavy water (D_2O) are presented. These experiments are used to obtain a measure of the lateral dispersion of the liquid through the ore bed over time as well as how much of the liquid flowed downwards through the bed, dominated by gravitational forces.

6.1 Introduction

Heap leaching hydrology has been the focus of a number of studies, most of which have considered the issue of preferential flow (Decker and Tyler 1999, O'Kane et al. 1999, O'Kane Consultants Inc. 2000, Wu et al. 2007, Wu et al. 2009) or the use of tracer studies to extract hydrodynamic parameters and develop models of the liquid flow (Bouffard and Dixon 2001, Bouffard and West-Sells 2009, de Andrade Lima 2006). Comparatively little work has been done to study the liquid distribution within a heap from a single drip irrigation point, when irrigation of heaps using drip emitters is one of the most common methods of irrigation (Kappes 2002).

van Hille et al. (2010) used the setup shown in Figure 6.1 to study the radial distribution of the leach solution and microbial populations. The depicted vessel was filled with acid agglomerated ore, divided into three concentric regions by 10 mm high Perspex rings attached to the base of the vessel and sheets of permeable geotextile. It was irrigated at a rate of 5 L m^{-2} h^{-1} from a central drip irrigation point and the effluent liquid was collected from nine points at the base of the vessel, corresponding to the annuli.

They found that solution flow occurred preferentially in the central core below the irrigation point. Initially more than 80% of the liquid exited in this region of the column, but radial diffusion was observed to increase with time. A steady state was established after 15 days of operation at which time there was around twice as much liquid that left the column in the central region than did in the outer ring. The effluent flow in the intermediate ring was closer to the volume collected in the outer ring than flowed out of the inner core. The hydraulic residence time was consequently longer further from the centre which affected the pH as acid consumption was higher in longer hydraulic residence time regions. This resulted in more

jarosite precipitation in the outer regions of the column which then limited the copper recovery. The highest recovery of the copper was in the central core of the bed and the recovery decreased as the distance from the irrigation point was increased.

In the thesis of Chiume (2011) a box reactor, illustrated in Figure 6.2, was used to monitor the moisture content of the ore and the microbial population in different regions of an aerated ore bed. The box was packed with 132 kg of acid agglomerated ore and, after an initial acid wash, the ore was irrigated from a single drip point on one side of the bed at a rate of 6 L m^{-2} h^{-1} for a period of 83 days. The moisture content in nine zones of the bed was measured at the start and end of the bioleaching experiment and at 2 points in between from a series of sample ports by drying 20 g samples of the wet ore to find the weight percentage of the wet ore that was liquid. The effluent solution was collected at 13 points at the base of the box.

The moisture content varied little across the bed at the start of the bioleaching experiment and was on average 8.6%. After 25 days the moisture content had increased in the first two thirds of the bed, but not in the third on the right. The highest moisture content at this stage was in zones below the irrigation point (A, D and G). Hence at the start of the experiment gravitational flow dominated while lateral movement of the liquid was limited. The average moisture content increased as the experiment progressed and was 12.2% at the end of the experiment. The majority of the solution (98% on average) was collected out of ports one to six over the course of the experiment. The most liquid was collected from port 5 which showed that there was some lateral flow of the liquid.

Lateral movement of the liquid increased with increasing depth and the driest zones of the bed at the end of the experiment were in the top right corner (zones B, C and F). The results also showed that the solution distribution was non-uniform across the bed which is evidence that preferential flow paths developed. The liquid flow was demonstrated to affect leaching efficiencies as the majority of the copper extracted from the ore bed was removed from the areas with the higher fluid throughput. The moisture content also affected microbial colonisation of the ore as the lower moisture regions of the bed had very low or zero cell numbers. The majority of the microbial colonies accumulated near and downwards from the irrigation point. Downward migration of microorganisms due to cell detachment was observed too and caused a decrease in the cell numbers at the top of the ore bed (zones A and B) over time. This confirmed that fluid supply has a major effect on cell growth and detachment and can be a contributor to poor colonisation of ore beds.
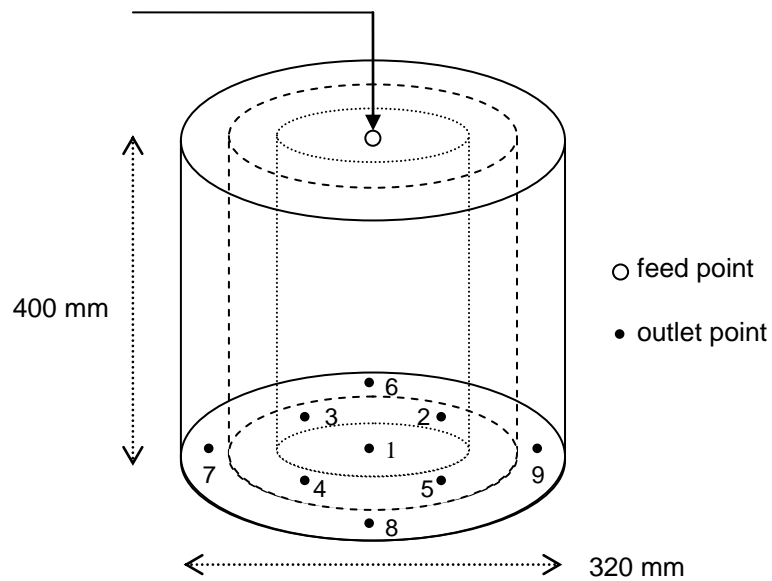
Figure 6.1. Schematic representation of the bucket reactor setup used by van Hille et al. (2010) where there was a central single drip irrigation point at the top and nine outlet ports at the base.
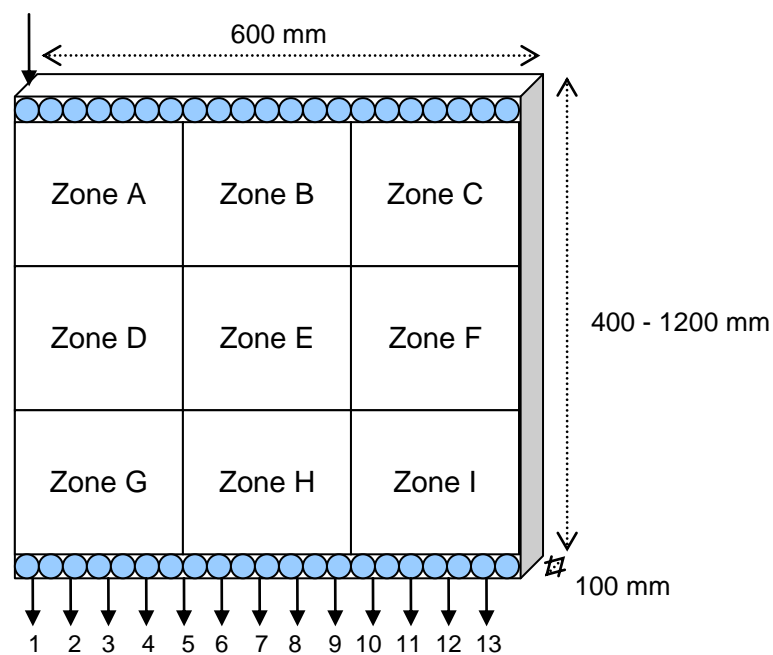

Figure 6.2. Illustration of the box reactor used by Chiume (2011). It was irrigated at the top from the one side and had 13 collection points at the base. Zones of the bed were monitored through multiple sample points that were distributed throughout the bed.

Dixon (2003) modelled the solution flow in a heap from a single point source by solving the Richards' equation, a theoretical equation for unsaturated flow based on Darcy's law, at steady state in 3D axisymmetric coordinates for an isotropic porous medium. The study indicated that not much lateral liquid flow occurs away from the channels of flow after the initial wetting of the ore and that the majority of flow is limited to within a few centimetres of the vertical axis (the irrigation point) despite a significant degree of saturation being achieved thought the entire ore bed. Afewu and Dixon (2008) later developed a more complex model for heap hydrodynamics in drip irrigated systems based on transport parameter estimates from the results of tracer and gravimetric studies on small (100 mm internal diameter) and large (1 m internal diameter) columns. They found that the dispersivity of the liquid increased with an increased irrigation flux within the ranges examined (3 to 30 L m^{-2} h^{-1}).

Literature on liquid distribution from drip emitters in the fields of plant and soil science is abundant as it is an important concern for the design of irrigation systems for optimised water and nutrient supply. It describes that the shape of the wetted volume and the infiltration rate (superficial velocity of the liquid) will depend on many factors including soil hydraulic characteristics (determined primarily by the particle size distribution (PSD)), initial conditions (wetness of the soil), emitter discharge rate and application frequency (Brouwer et al. 1988, Clothier 1984). Solution flow in heaps has been shown to be described best by unsaturated zone hydrology theory, a theory that was originally developed for soils (Decker and Tyler 1999, O'Kane Consultants Inc. 2000), so it would be expected that the critical parameters affecting liquid distribution from a point source in heap leaching and soil science would be the same. The studies by van Hille et al. (2010) and Chiume (2011) do not consider the effect of varying these parameters, operating instead at a single set of conditions, and Afewu and Dixon (2008) only address the question of flow rate to validate their model. Therefore the aim of this study is to use MRI to examine the liquid infiltration into a small packed bed of ore from a single drip irrigation point source with a specific focus on lateral liquid distribution and to test the effect that PSD, flow rate and initial wetness of the ore have on the liquid path.

6.2 Experimental

6.2.1 Sample Preparation

The cell used in the experiments is shown in Figure 6.3. The internal length of the column was 170 mm and the internal diameter was 70 mm. One end of the cell was fixed and one was removable to allow for ore to be packed into the column. The removable end had an o-ring seal to ensure that there was no liquid leakage. The end was additionally secured using brass

screws. A silicon inlet tube, inner diameter of 2 mm, entered the cell at the top of the fixed end. An elbow connector was fitted to the end of the inlet tube so as to direct the flow onto the packed ore. A liquid drainage point was located at the bottom of the cell, also on the fixed end. It had a 5 mm internal diameter to enable ready drainage of the liquid from the cell. A drainage plate with 3 mm diameter holes fitted into the column 10 mm above the base and balanced on shelves on either end. A layer of 10 mm glass beads was packed as an initial layer on the drainage plate. This allowed for a disengagement region and a drainage space below the ore thereby preventing the upward wicking of liquid.
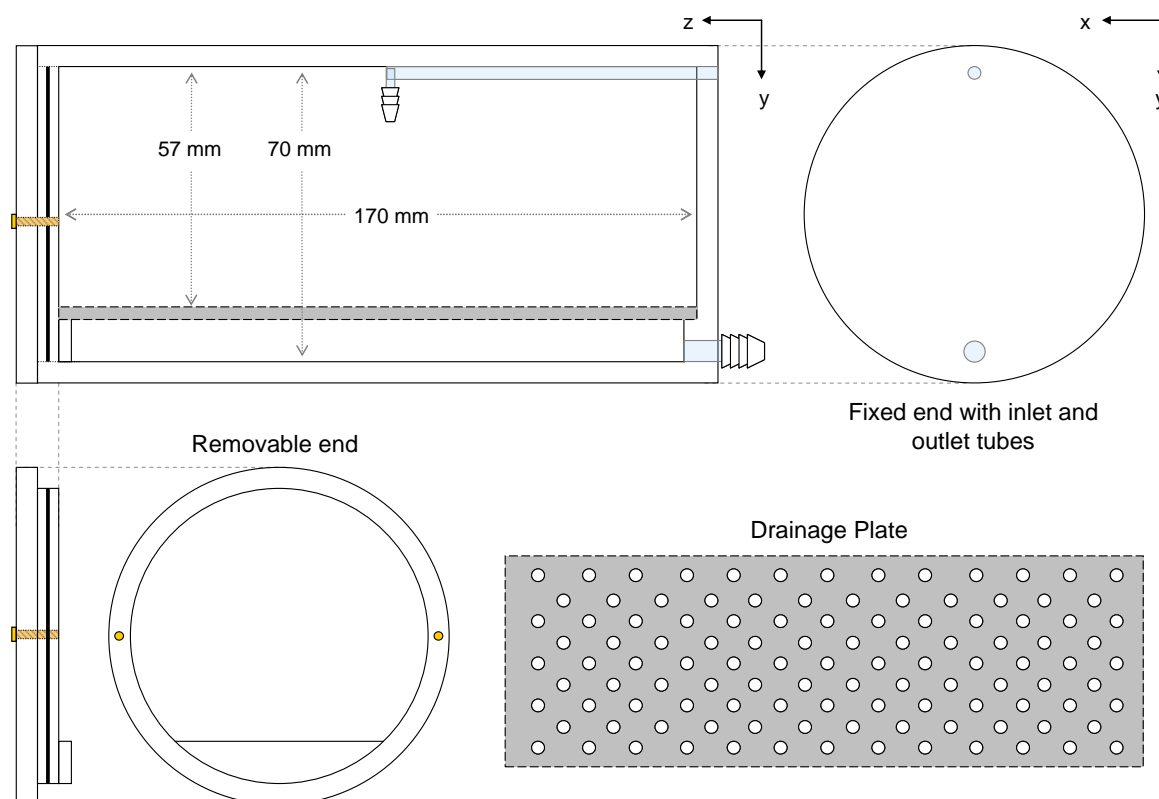

Figure 6.3. Illustration of the drip irrigation cell components.

Escondida Type B ore (2.95% Fe, 0.69% Cu and 2.02% S by weight) was used in the experiments. The full PSD of the ore, as determined by sieving, is given in Table 6.1. The fine ore experiments only included ore less than 2 mm in size while the large ore experiments used only ore particles larger than 9.5 mm. The full PSD was used for the agglomerated ore samples where a water to ore ratio of 50 ml per kg ore was applied. The large and fine ore was packed into the cell dry, but the agglomerated ore was packed in wet. Fresh fine ore packings were used for each flow rate experiment unlike for the other samples because the clays in the fine ore caused the bed to harden if it was dried.

The cell was irrigated with distilled water that had been doped with 0.8 g L^{-1} of GdCl$_3$·6H$_2$O so that it had a T_1 in the region of 30 ms. The doped solution was used because in preliminary tests it was found that the solution was visible in the ore region, but not at the irrigation point if pure water was used in conjunction with the SESPI acquisition technique. In the D$_2$O (heavy water) tracer experiments the feed was switched to D$_2$O (99.9 atom % D) and the disappearance of the signal from the steady state GdCl$_3$ doped liquid system was monitored. The feed solution was pumped using a peristaltic pump which resulted in pulse-like (drip) irrigation. Flow rates of 10, 20, 40 and 80 ml h^{-1} were used in the experiments which are approximately equivalent to between 1 and 10 L m^{-2} h^{-1}.

If the ore was wet, either because it was freshly agglomerated or from a previous irrigation run on the sample, it was dried overnight in an oven at 70°C before the MRI experiments were commenced. This was done to ensure that there was no signal from liquid in the sample before each experiment. The exception to this was in the D$_2$O experiments where in the first run the ore was agglomerated with D$_2$O which does not give off signal. The ore was also not dried for the D$_2$O tracer tests when the feed swapped from the GdCl$_3$ doped solution to D$_2$O once the GdCl$_3$ irrigated system had reached a steady state.

Table 6.1. PSD of the Escondida Type B ore.

Size (mm)	Weight (%)
> 13.2	14.0
9.5 - 13.2	18.4
5.6 - 9.5	20.3
2.0 - 5.6	19.8
0.71 - 2.0	9.1
< 0.71	18.5

6.2.2 MRI Hardware and Imaging Parameters

The imaging was performed on a Bruker AV 85, 2 T horizontal bore spectrometer with a wide bore radio frequency (RF) coil which had an inner diameter of 83 mm. The field of view (FOV) was 80 mm × 80 mm in the x and y directions and 160 mm in the z (along the bore length). The z FOV is longer than the length of the homogeneous imaging region of the coil (closer to 100 mm), but it was chosen to prevent wrap-around artefacts that would affect the image analysis and to allow for the same resolution to be applied in all three directions. The acquisition size was 32×32×64 in the case of a 3D acquisition. This corresponds to a nominal

resolution of 2.5 mm per pixel. A standard SESPI acquisition sequence was used. It utilised a total gradient encoding time (t_p) of 300 μs, a repeat time (*TR*) of 50 ms and an echo time (*TE*) of 750 μs. Four repeat scans were done for phase cycling and eight points were acquired at 5 μs intervals along each echo for signal averaging.

2D projections (x-y and y-z) were acquired of the setup before irrigation was started so as to confirm that the sample was dry or to have a zero map, depending on the experiment. The zero maps were also used to position the cell within the spectrometer bore correctly, with signal from a small piece of Blu-Tack® above the elbow connector enabling accurate positioning. 2D projections were acquired at 4, 15, 30 and 60 minutes intervals once irrigation had started, followed by hourly scans until an approximate steady state had been reached (the flow path was no longer evolving significantly). A 3D image was acquired at this stage.

6.3   Results and Discussion

6.3.1   Large Ore Particle Irrigation

The liquid distribution in a bed of large ore particles is examined using two samples. Figure 6.4 shows a selection of the y-z projections acquired of the first sample irrigated at a rate of 40 ml h^{-1}. The liquid in this experiment only flows to the left of the irrigation point, extending a final 40 mm in this direction, rather than distributing in a symmetrical manner. The liquid is observed to flow rapidly through the ore as drainage already occurs at the 15 minute point. There is also rapid drainage in the case of the second sample, where drainage is recorded at the 4 minute mark. The 2D y-z projections of the second sample irrigated at 40 ml h^{-1} in Figure 6.5 illustrate that the liquid distribution was more symmetrical in this plane than in the case of the first sample, with the liquid extending 30 mm to either side of the irrigation point. However, the central slices from the 3D acquisition in Figure 6.6 show that there is preferential flow to the left of the irrigation point in the x direction.

Drip irrigation of the large ore particle bed is therefore demonstrated to result in channel or macro-pore flow. This is because the bed of large ore particles will have larger pores compared to a smaller or mixed PSD packing and flow will therefore be dominated more by gravitational effects than matric suction, resulting in the rapid drainage of liquid and limited lateral liquid distribution (O'Kane Consultants Inc. 2000). The preferential flow observed in the y-z projections of the first sample and in the x-y central slice of the second sample is because the orientations of the ore particles determine the liquid flow path. This is a clear example of the difficulty of achieving uniform wetting of a heterogeneous ore bed.

The second large ore particle sample was additionally irrigated at flow rates of 20 ml h^{-1} and 80 ml h^{-1}, the 2D y-z projections of which are shown in Figure 6.5. The final extent of the liquid distribution is similar for the three flow rates, though an additional rivulet forms to the far left of the cell in the 80 ml h^{-1} run. The liquid flow pattern in the 80 ml h^{-1} run is also different during the first hour of irrigation with the liquid following a very direct path down through the ore, distributing a maximum of 10 mm either side of the irrigation point compared to 27.5 mm in the 20 ml h^{-1} scan and 25 mm in the 40 ml h^{-1} scan. This demonstrates that changes in liquid flow rate can result in perturbed liquid paths in a large PSD packing, but that there is minimal effect on the lateral distribution of the liquid. Increases in flow rate in a mixed particle size bed are also known to cause a higher fraction of the liquid to flow through macro-pores due to the finer ore packings becoming saturated (O'Kane Consultants Inc. 2000).
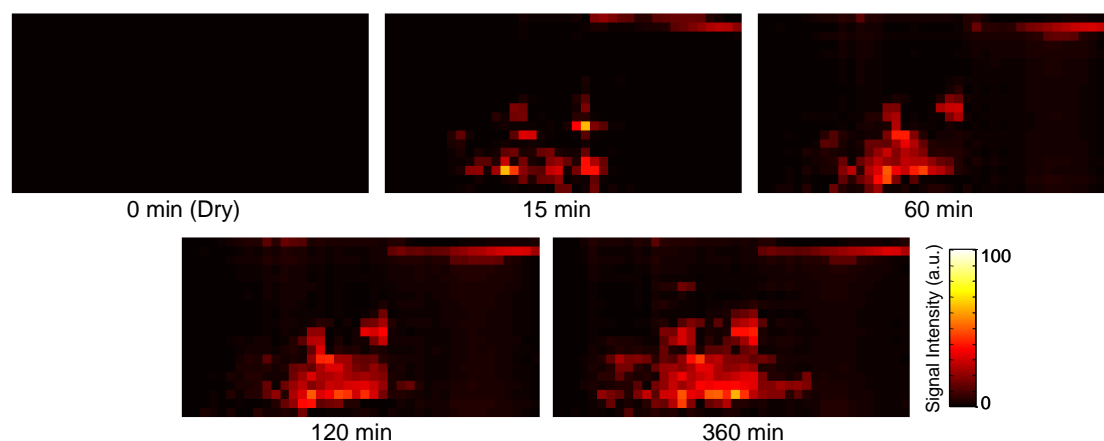

Figure 6.4. 2D y-z projections of the first large ore particle sample irrigated at a rate of 40 ml h^{-1}.
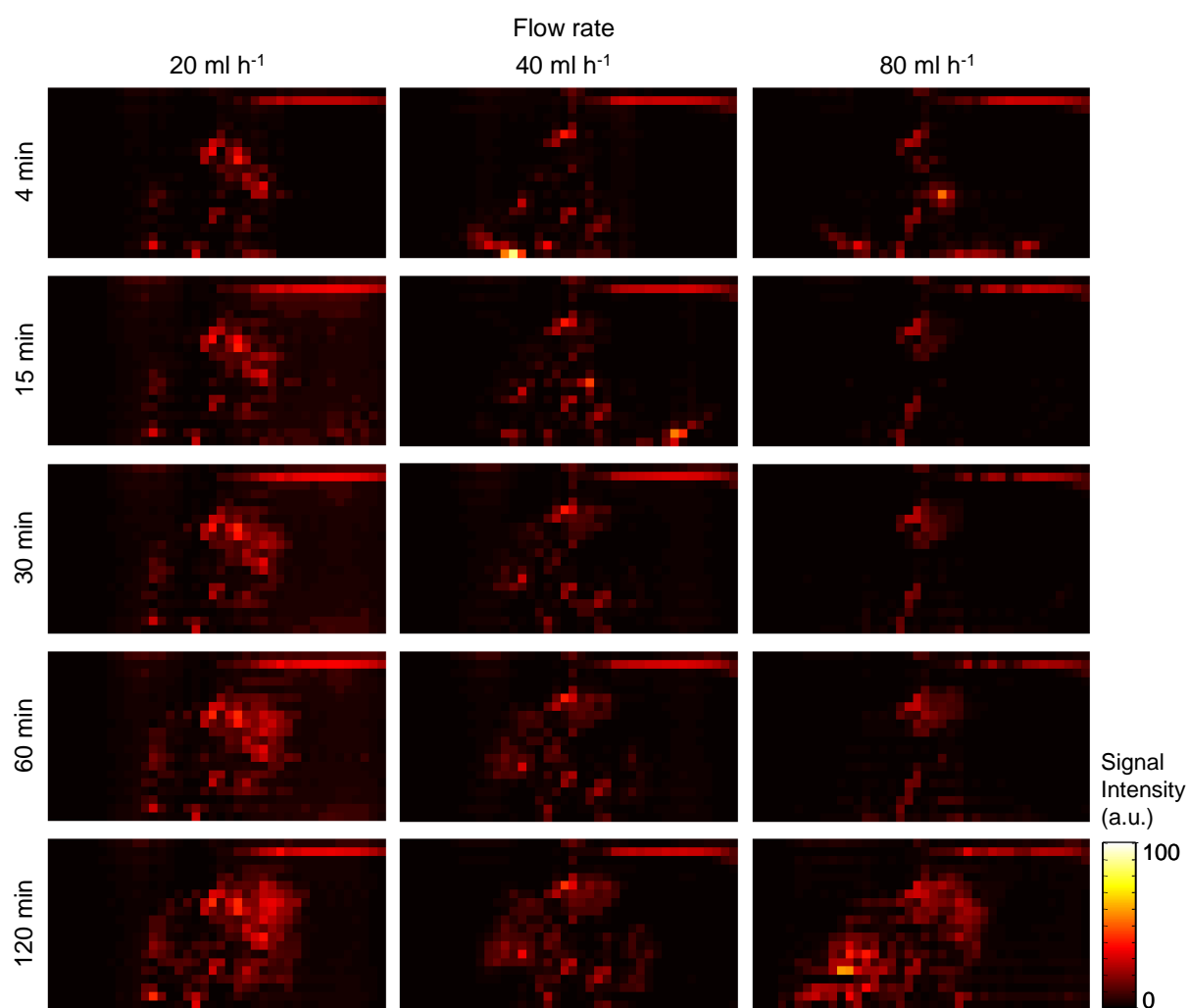
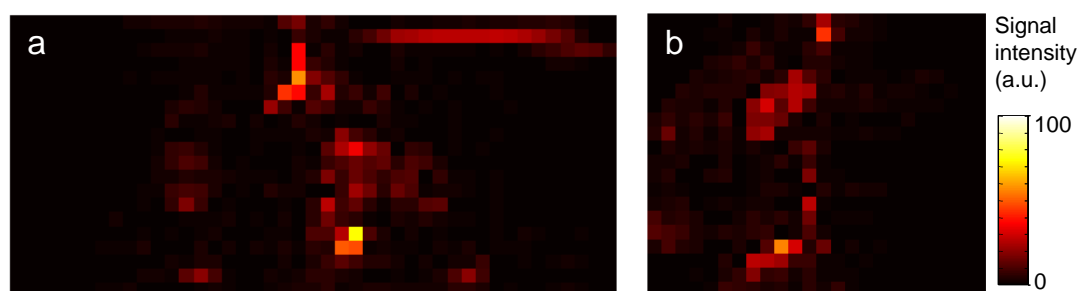Figure 6.5. 2D y-z projections of the second large ore particle sample irrigated at flow rates of 20, 40 and 80 ml h^{-1}.

Figure 6.6. Central (a) y-z and (b) x-y slices from the 3D acquisition of the second large ore particle sample irrigated at 40 ml h^{-1}.

6.3.2   Fine Ore Irrigation

The fine ore in a heap is the opposite extreme in particle size to the large ore particles. Unlike the coarse ore they tend to be more mobile in heaps as they can be carried by the liquid, which may result in issues such as plugging where the fines accumulate. Distinct regions of fines can also form during heap constructing because of segregation of the coarse and fine ores, with the fines accumulating at the top of the heap (Bartlett 1998, O'Kane Consultants Inc. 2000) or in diagonal stratifications along the heap sides (Kappes 2002), thereby creating areas of low permeability in the heap. It is consequently desired to examine the effect of regions of fine ore on the liquid flow.

The fine ore bed was irrigated from an initially dry state at flow rates of 10, 20, 40 and 80 ml h^{-1}, the images of which are shown in Figure 6.8. The different runs are compared by considering the systems when a common volume of liquid had been irrigated. The percentage of the ore bed visible in the MRI acquisitions that contained liquid is presented in Table 6.2 and the percentage of the wetted area found to the right of the irrigation point is given in Table 6.3.

The extent of the wetted area is observed to increase with decreases in the flow rate. The most even distribution of the signal (and hence of the liquid) is in the 10 ml h^{-1} run, with only a single pixel of higher signal intensity located at the drip irrigation point. As time passes, the signal intensity in this run increases relatively uniformly across the bed. In the higher flow rate experiments there is a larger area of intense signal in the region around the irrigation point which is evidence of ponding of the liquid – a saturated region of the bed. The signal then decreases in intensity from the liquid pond area outwards. There is consequently a greater variation in the degree of saturation of the ore in the higher flow rate experiments compared with the 10 ml h^{-1} run. The ponding of the liquid will have been the reason for the decrease in the wetted area with increasing flow rate.

The liquid flow from the irrigation point is very symmetrical in the 10 ml h^{-1} run where the liquid travelled outwards from the irrigation point in a radial manner, flowing horizontally due to capillary forces as well as downwards under gravity to the same degree. The liquid has reached the bottom of the ore packing (37.5 mm below the drip point) by the 120 minute mark. At this time the liquid extends a maximum of 30 mm to the left and 35 mm to the right of the irrigation point. The liquid continues to distribute horizontally through the fine ore and the edges of the imaging region are reached by minute 360 (only the central 100 mm of the 170 mm bed are visible). No liquid drains from the ore until a total of 480 minutes has passed. At this time 80 ml of liquid has been dripped into the ore, hence the whole ore sample is just

over 48% saturated if a standard voidage of 40% is assumed. The initial drainage of liquid is directly below the drip irrigation point, but drainage subsequently occurs along the whole length of the sample. This shows how a layer of fine ore may restrict the downwards flow of liquid in an ore heap at the same time as limiting oxygen supply to deeper regions. In heap leaching practice such plugging of the bed is detrimental (O'Kane Consultants Inc. 2000), but this fact could also prove to be advantageous for acid mine drainage prevention where clays are commonly used as 'sealing layers' (Johnson and Hallberg 2005). Purposefully installed layers of fines could also potentially be used to improve the lateral distribution of the liquid.

The shape of the wetted region in the 20 ml h^{-1} run is slightly different to in the 10 ml h^{-1} experiment, although the liquid distribution is still highly symmetrical. The wetted region in the first 120 minutes extends a few pixels further laterally in the 20 ml h^{-1} run compared to the 10 ml h^{-1} case, but the liquid has not travelled as far in the vertical direction. This behaviour (more lateral and less vertical flow at higher flow rates) is typical of soil irrigation (Bresler 1977, Brouwer et al. 1988).

The symmetry of the wetting worsens considerably as the flow rate is increased to 40 ml h^{-1} and then again to 80 ml h^{-1}. This is because some of the liquid travels across the surface of the fine ore bed in the void space above the ore region before trickling into the ore bed. Lateral solution flow due to ponding of the liquid on the surface of the heaps (where fines are known to segregate in heap construction) is a common heap operation issue – it promotes channel flow in heap leaches which can result in poor uniformity of irrigation (Bartlett 1998). Liquid runoff is also a common issue when irrigating clay soils (Brouwer et al. 1988, Irrigation Direct 2012) and because ore fines are known to contain clays (Bartlett 1998) this behaviour is not unexpected.

Table 6.2. Imaging region occupied by liquid in the y-z projections of the fine ore.

Volume of irrigated liquid (ml)	Liquid filled area (% of imaging region)			
	10 ml h^{-1}	20 ml h^{-1}	40 ml h^{-1}	80 ml h^{-1}
10	33.0	26.7	29.0	-
20	49.5	44.8	43.5	37.3
40	71.2	67.2	64.5	56.7
80	82.0	80.0	78.1	67.7

Table 6.3. Liquid to the right of the irrigation point in the y-z projections of the fine ore.

Volume of irrigated liquid (ml)	Liquid to the right of the irrigation point (%)			
	10 ml h^{-1}	20 ml h^{-1}	40 ml h^{-1}	80 ml h^{-1}
10	43.4	45.0	74.7	-
20	46.1	46.8	71.7	80.4
40	48.5	49.1	66.2	75.0
80	52.6	51.5	55.4	63.8

In the experiments thus far the fine ore had been irrigated from an initially dry state. Therefore a tracer experiment was performed using D_2O (which is MRI inactive) to examine the liquid infiltration into the already wetted ore bed at steady state. The feed to the fine ore sample irrigated with the $GdCl_3$ doped solution at 10 ml h^{-1} was switched after 26 hours to D_2O. The disappearance of signal due to the D_2O infiltration was related to a 'zero map' that was acquired of the system at steady state before the introduction of the D_2O to determine the steady state liquid flow path, as is illustrated in Figure 6.7. The irrigation of the originally dry sample and the subsequent D_2O tracer study images are presented in Figure 6.9.
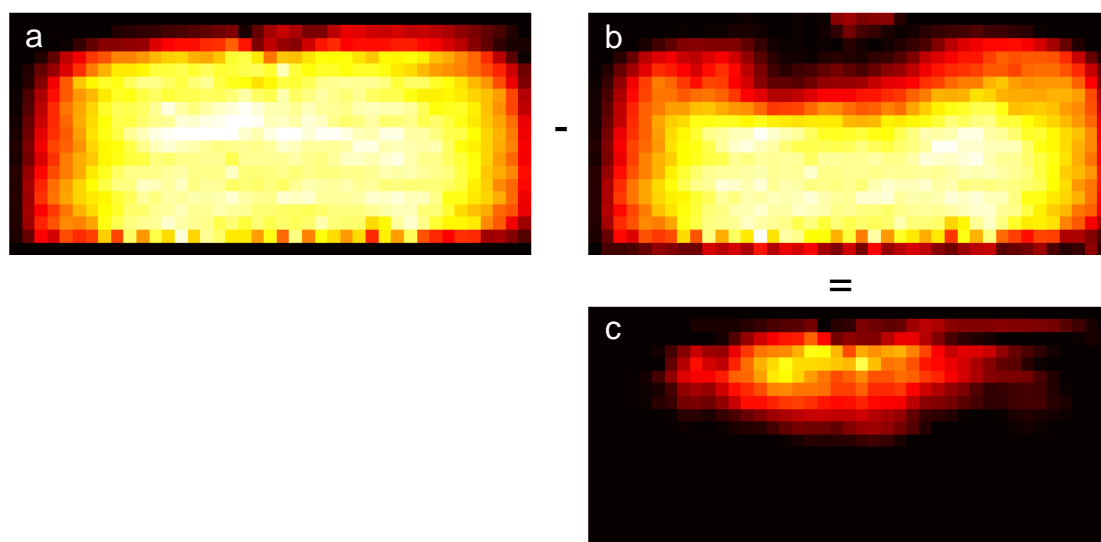

Figure 6.7. The (c) D_2O flow into the bed is determined by relating (a) the zero map before any D_2O is irrigated to (b) the projection from the D_2O experiment.

The liquid in the already wet ore system strongly favours lateral distribution as opposed to downwards flow. The resulting distribution pattern is therefore quite different to the radial distribution of the liquid from the irrigation point in the case of the dry ore irrigation. The preferential lateral movement of the liquid in the wet ore case may be attributed to the

stronger capillary suction of the less saturated fine material located towards the top of the ore bed being more dominant than gravitational effects. This is a standard characteristic of clay soil irrigation (Irrigation Direct 2012). Table 6.4 gives the vertical and horizontal infiltration rate of the liquid into the fine ore. The infiltration rates all decrease with time and level out by around 180 minutes, reaching what is known as the 'terminal' infiltration rate (Withers and Vipond 1974). The preferential lateral movement of the liquid in the wet ore case means that the vertical infiltration rate is slower initially compared to the dry case. This agrees with literature on soil irrigation where the vertical liquid infiltration rate into dry soil, the 'initial' infiltration rate, is reported to be more rapid than the steady state or 'basic' infiltration rate which occurs when the soil is already wet (Brouwer et al. 1988). The basic infiltration rate of the fine ore after the first 15 minutes of irrigation is most similar to that of clay soils which are classified as having basic infiltration rates of between 1 and 5 mm h^{-1} (Brouwer et al. 1988).

The higher signal intensities in the equivalent time images in Figure 6.9 indicate that the liquid is also more concentrated in the wet run. The wetted region of the bed as a percentage of the ore filled imaging region is presented in Table 6.5 for the dry and wet ore cases. The wetted region is less in the wet ore case for the duration of the experiment. The difference between the wetted areas for the two cases also increases with time for the first 240 minutes. The decrease in the difference in the wetted region after this is because the liquid flow has extended out of the imaging region.

Therefore flow through the fine fraction of the ore from a single drip irrigation point has been demonstrated to be strongly dominated by capillary effects in all of the experiments, behaviour which closely mirrors the descriptions of clay soil drip irrigation in the literature.

Table 6.4. Infiltration rates of the liquid for irrigation of the fine ore at 10 ml h^{-1}.

Irrigation period (minutes)	Vertical infiltration rate (mm h^{-1})		Horizontal infiltration rate (mm h^{-1})	
	Dry ore	Wet ore	Dry ore	Wet ore
15	90	50	60	100
30	10	5.0	10	10
60	5.0	2.5	5.0	2.5
120	2.5	2.5	3.8	2.5
180	-	1.7	1.7	0.8
240	-	0.6	1.9	0.0
300	-	1.0	1.0	0.5
360	-	0.4	0.8	-

Table 6.5. Imaging region occupied by liquid in the y-z projections of the fine ore irrigated at 10 ml h^{-1}.

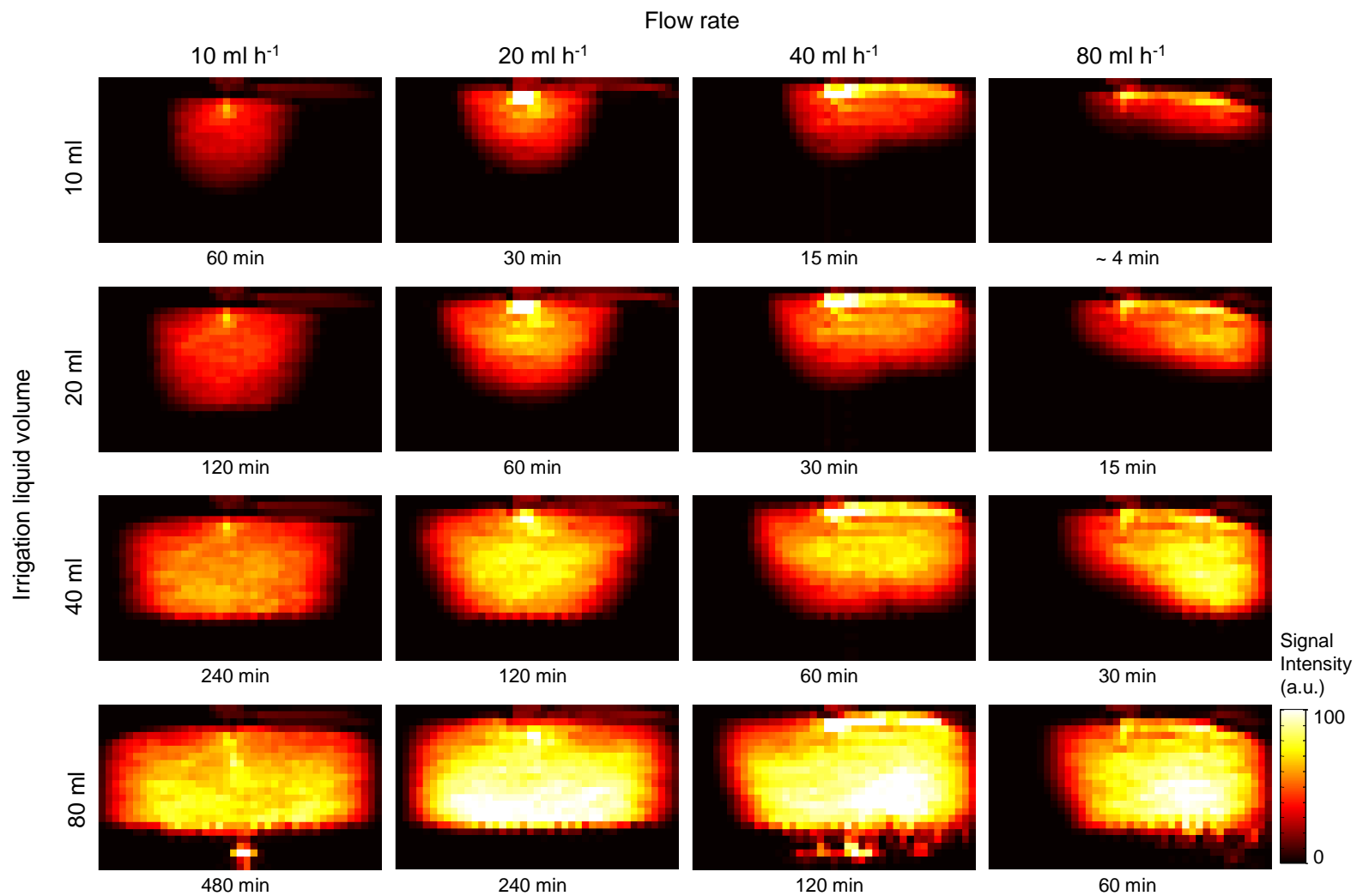| Irrigation period (minutes)	Liquid filled area (% of imaging region)	
	Dry ore	Wet ore
15	12.8	11.0
30	18.7	16.3
60	30.5	24.7
120	47.5	37.8
180	58.7	49.7
240	70.0	59.8
300	77.5	71.0
360	80.8	75.0

Figure 6.8. Comparison of the liquid distribution in the fine ore bed for different flow rates after the same volume of liquid had irrigated. These 2D y-z projections have been cropped to include the drainage region of the cell.
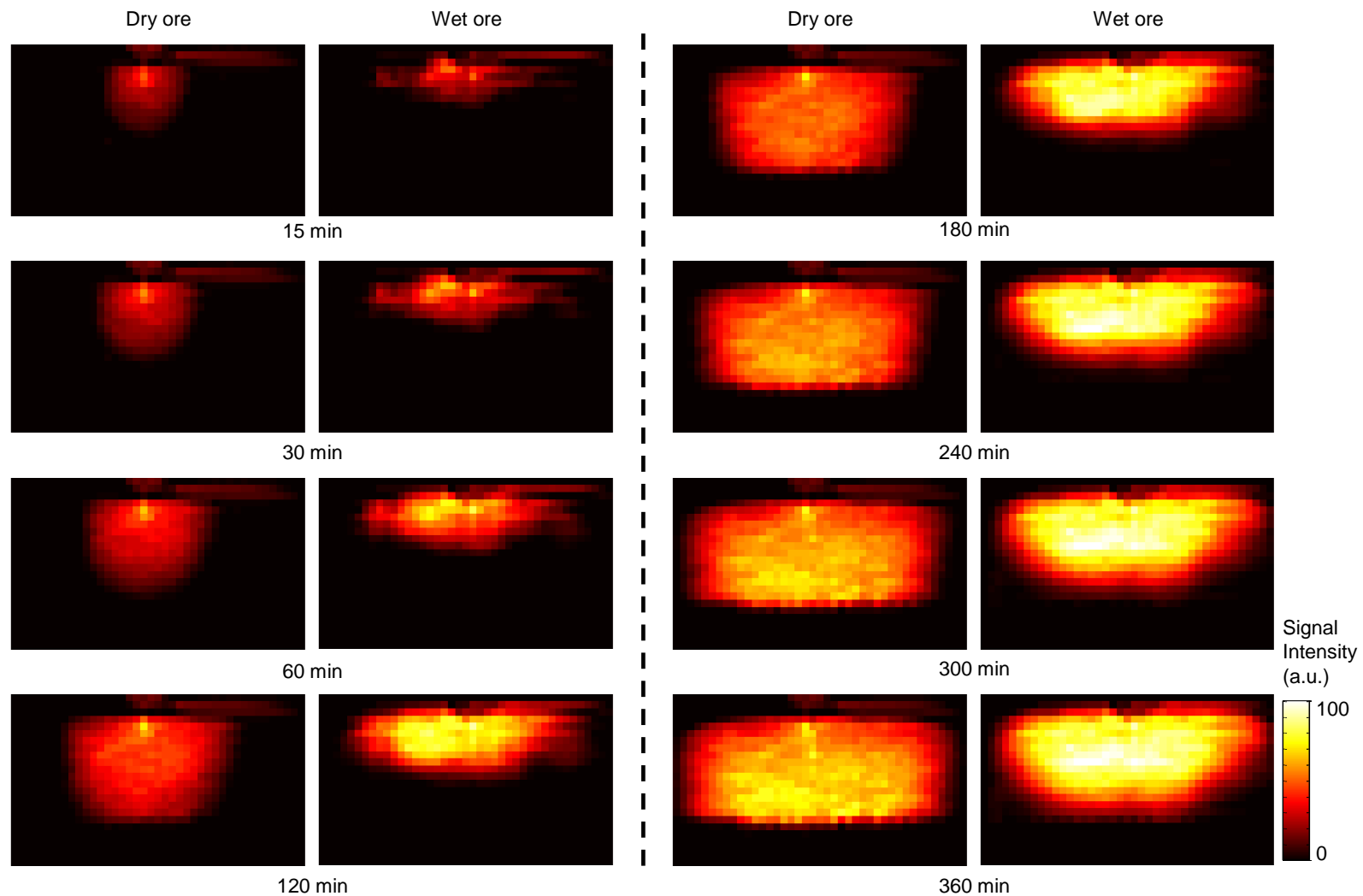
Figure 6.9. Comparison of the liquid distribution in the fine ore bed when the ore was irrigated at a flow rate of 10 ml h^{-1} from a dry initial state and when it was already wet. These 2D y-z projections have been cropped to include the drainage region of the cell.

6.3.3 Agglomerated Ore Irrigation

Now that the liquid flow from a single drip irrigation point had been tested on the two extremes of the ore particle size (very large and fine), it was desired to examine the flow through an agglomerated ore bed.

6.3.3.1 Repeat Irrigation of a Dry Agglomerate Bed

In the first series of experiments a bed of agglomerated ore was drip irrigated at a flow rate of 10 ml h^{-1} from an initially dry state on three occasions (A, B and C). The first run, A, was the first time that the agglomerated ore sample was irrigated following the sample preparation. B and C were subsequent irrigations after drying. Two agglomerated ore samples were tested and the 2D y-z projections for the three irrigation cycles (A, B and C) are presented in Figure 6.10 for the first sample and in Figure 6.12 for the second sample. The images are thresholded at the same level and combined to compare the liquid distributions. The results are shown in Table 6.6 and Figure 6.11 and Figure 6.13.

In the first sample, the horizontal movement of the liquid in run A_1 is as extensive as the downward movement during the first 60 minutes of irrigation. At the 30 minute mark the liquid extends approximately 27.5 mm to the left, 10 mm to the right and 35 mm down from the liquid entry point. This extends to 32.5 mm, 25 mm and 42.5 mm respectively after 60 minutes has passed. This echoes the liquid distribution behaviour in the bed of dry fine ore and indicates that there is strong capillary suction within the agglomerated ore bed, though the vertical infiltration rate is slightly higher. An increase in the infiltration rate with particle size is a common feature of soil irrigation (Brouwer et al. 1988). The horizontal movement of the liquid is also present in runs B_1 and C_1, though there is preferential flow to the right side of the sample rather than to the left. These initial differences do not affect the final liquid distribution, where the entire ore bed is wetted after 180 minutes. However, in a larger sample the liquid distribution differences observed in the first hour between the first and subsequent runs will be expected to extend further into the ore bed.

In the second sample the liquid flow during the first 30 minutes of irrigation is relatively symmetrical in run A_2, with only a slight bias to the right side of the cell. After 30 minutes the liquid has travelled 42.5 mm down from the drip point and a maximum of 22.5 mm and 20 mm to the right and left of the drip point after 30 minutes. The liquid reaches the bottom of the ore at this time and so only changes in the horizontal movement of the liquid are observed from this stage onwards. The downwards flow of the liquid under gravity is therefore more dominant for this sample than the horizontal movement due to capillary suction. This result is

different to the previous sample where the horizontal movement of the liquid in run A_1 is as extensive as the downward movement during the first 60 minutes of irrigation. Such variations between ore samples are expected as the larger ore particles in agglomerated samples introduce a high degree of heterogeneity to the bed. After 30 minutes in runs B_2 and C_2 the liquid has traversed 40 mm down, 12.5 mm right and 25 mm left. Hence the liquid distribution in this case shows a preference towards the left of the drip point. This is more pronounced than in run A_2 which indicates that there is a change in the capillary suction following the initial irrigation cycle. The rate of the downwards flow of the liquid is unaffected from the initial irrigation of the ore.

Therefore the liquid distribution in run A is different to the results of the later runs (B and C) for both samples. In the case of the first sample less than half of the liquid follows the same flow path for the first 30 minutes of irrigation. The effect is less pronounced for the irrigation of the second sample where less than half of the liquid follows the same flow path for the first 15 minutes. By contrast, the liquid flow path in runs B and C are very similar with relatively minor changes in the liquid flow path developing. This is particularly evident in the results of the second sample, where more than three quarters of the liquid follows the same flow path in the latter two runs. The initial differences in the three runs' liquid distributions become insignificant by the 180th minute in both samples at which stage the entire ore bed is wet.

Both ore beds slumped during the first irrigation run: by 12 mm for the first bed and 5 mm for the second bed. No further slumping of the bed occurred in the later runs. This behaviour is common in both lab scale experiments and full scale operation of heaps (Bouffard and Dixon 2001, Lin et al. 2005). Therefore the change in the liquid path following the initial wetting of the sample may be attributed to some of the finer ore particles having shifted during the first irrigation of the ore, thereby causing the liquid to wick into a different part of the ore bed. The movement of fines is a common phenomenon in heap leaching and has been reported to result in areas of lower voidage developing where the fines accumulate towards the base of columns (Lin et al. 2005) as well as plugging of void spaces in some extreme cases (Bartlett 1998). The results consequently illustrate that changes in the structure of the packed ore due to slumping have a substantial effect on the liquid flow.

Table 6.6. Agreement between the images of the agglomerated ore being drip irrigated at 10 ml h^{-1} where A is the first irrigation of the ore and B and C are subsequent irrigation cycles.

Time (minutes)	Sample 1 Agreement (%)			Sample 2 Agreement (%)		
	A_1 vs B_1	A_1 vs C_1	B_1 vs C_1	A_2 vs B_2	A_2 vs C_2	B_2 vs C_2
4	8.8	19.4	44.0	20.3	22.2	76.9
15	36.1	45.6	57.1	45.9	48.9	88.9
30	33.3	39.9	63.9	58.5	64.3	88.4
60	50.3	62.0	73.4	76.3	80.9	92.3
120	75.5	81.7	88.6	85.7	87.4	96.2
180	87.3	89.3	89.9	89.3	86.9	93.3

The wetting of the agglomerated ore is not as symmetric as is observed for the irrigation of the fines at the same flow rate (Table 6.9). This is due to the preferential flow that is caused by the larger ore particles, the effect of which is evident in the previous large ore particle experiments. However, by the 120th minute the liquid has distributed relatively uniformly in all three directions from the drip point and a liquid 'front' has developed on either side of the drip irrigation point. The slope of the front is between 40° and 45° to the vertical and remains so for the remainder of the experiments. An increase in the extent of the lateral movement of the liquid with depth is a result that is also reported by Chiume (2011) in a larger ore bed.
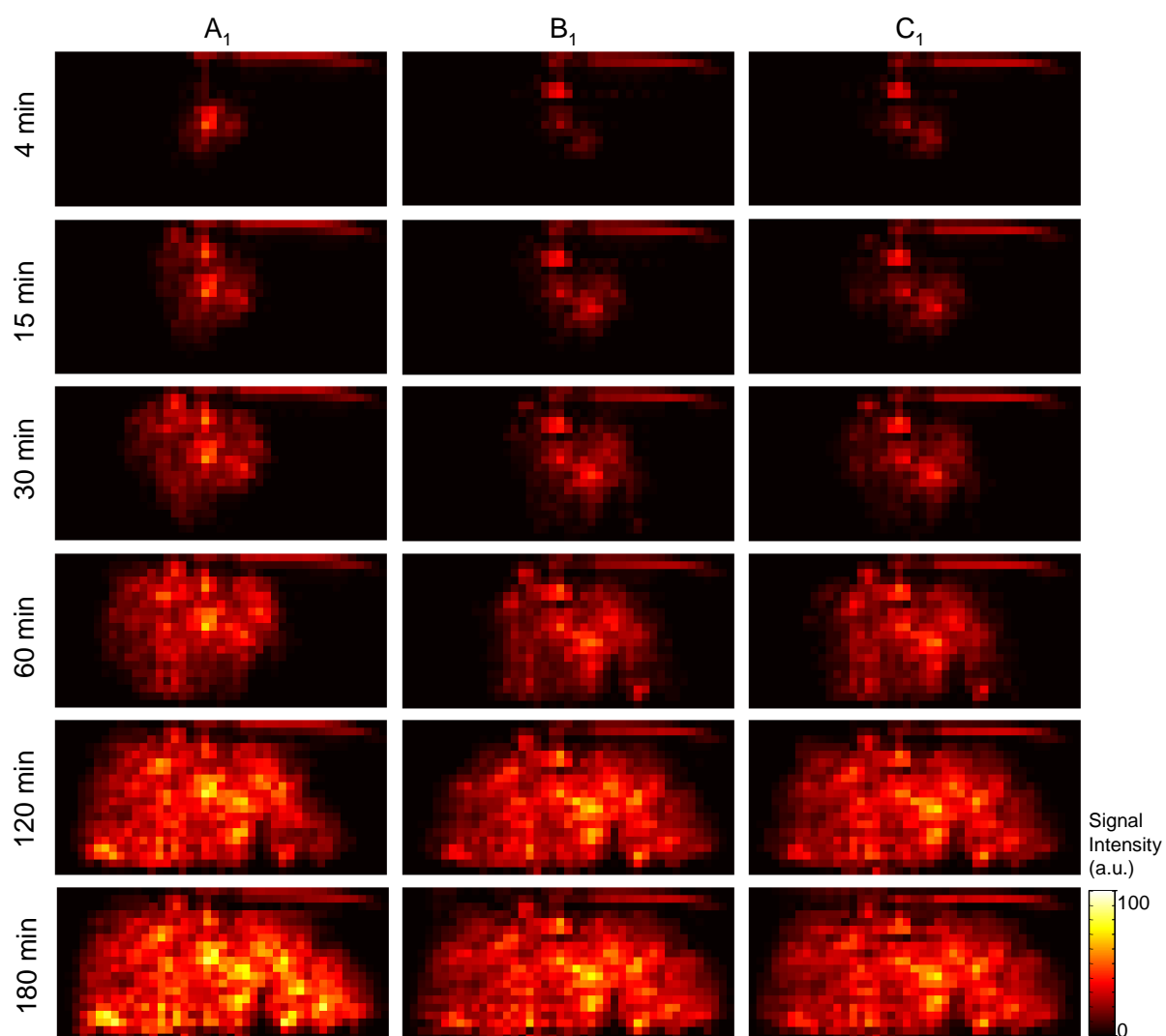
Figure 6.10. 2D y-z projections of the first agglomerated ore sample drip irrigated at a rate of 10 ml h^{-1} where A_1 is the first irrigation of the ore and B_1 and C_1 are later runs that followed the initial irrigation and drying cycle.
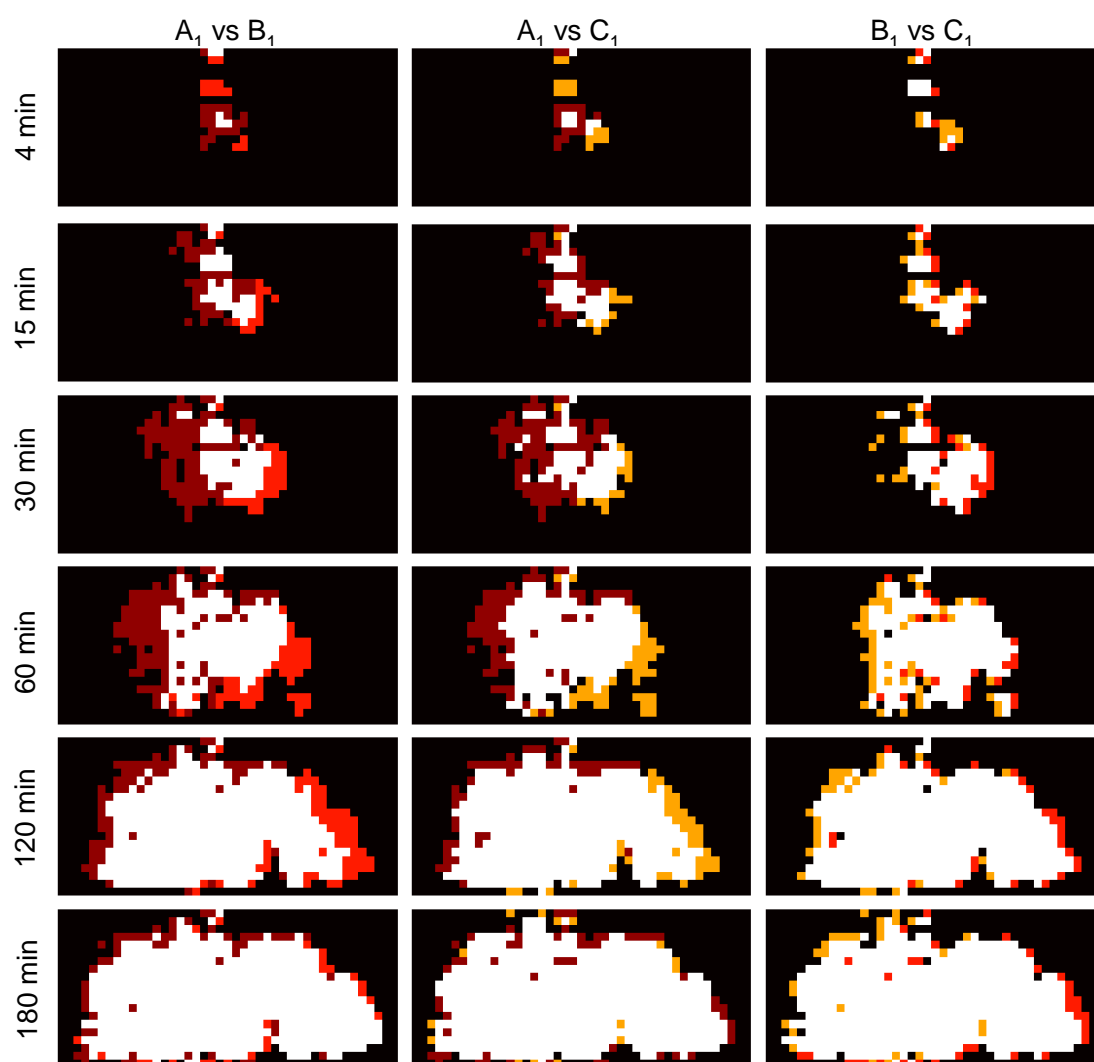
Figure 6.11. Representation of the image agreement (white) of the first ore agglomerated sample drip irrigated at 10 ml h^{-1} where A_1 is the first run and B_1 and C_1 are later runs that followed the initial irrigation and drying cycle. The unmatched pixels are shown in brown (A_1), red (B_1) and yellow (C_1) respectively.
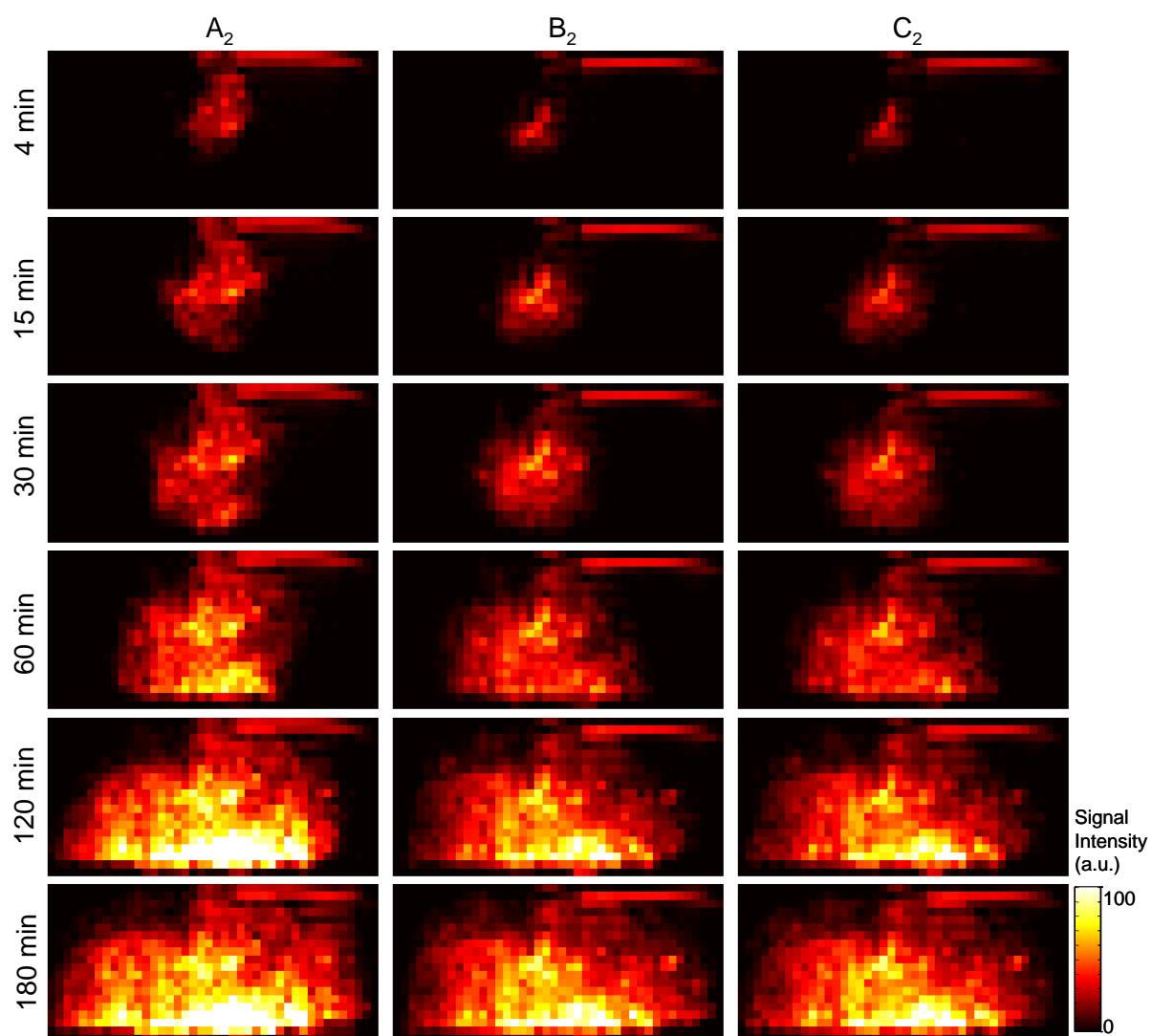
Figure 6.12. 2D y-z projections of the second agglomerated ore sample drip irrigated at a rate of 10 ml h^{-1} where A_2 is the first irrigation of the ore and B_2 and C_2 are later runs that followed the initial irrigation and drying cycle.
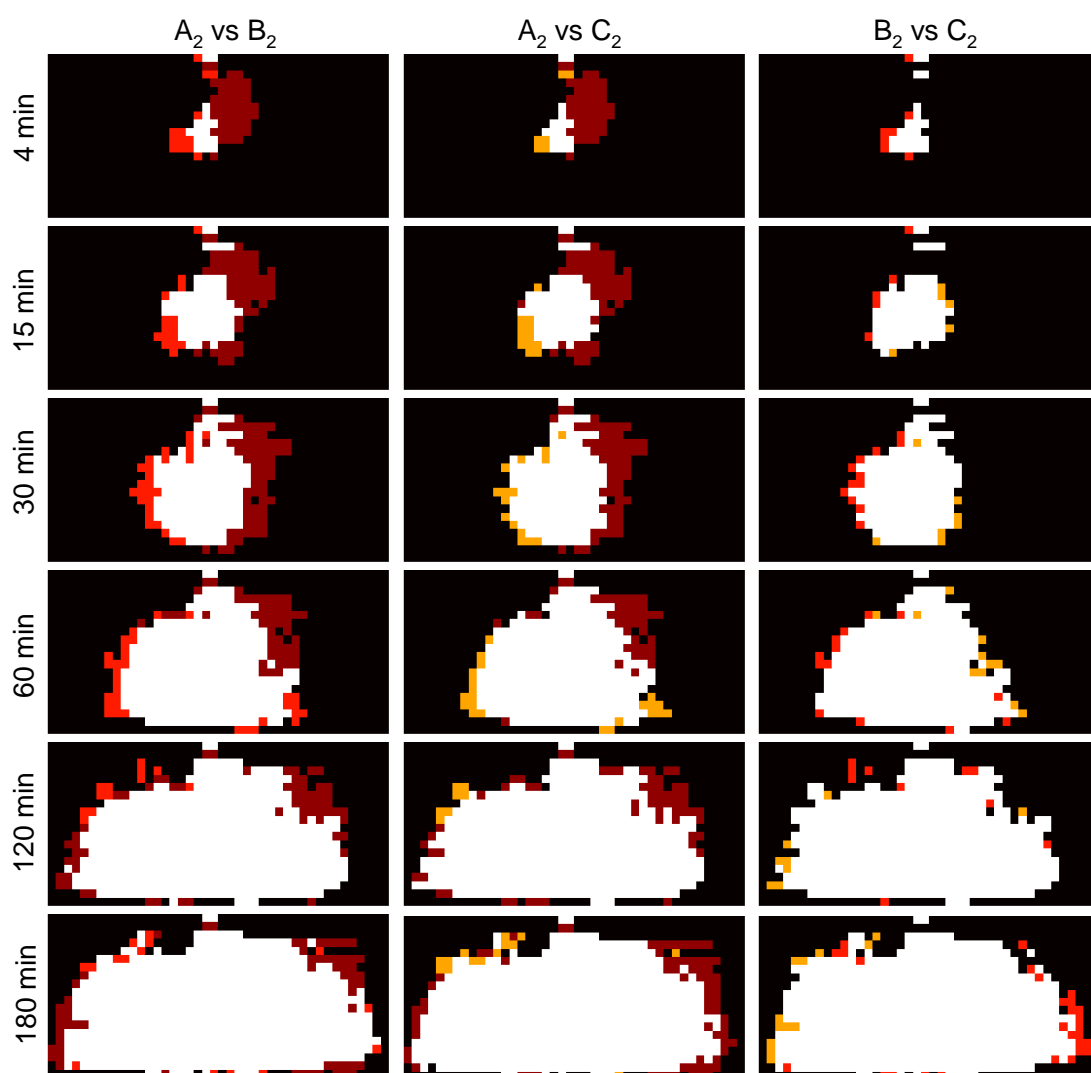
Figure 6.13. Representation of the image agreement (white) of the second agglomerated ore sample drip irrigated at 10 ml h^{-1} where A_2 is the first run and B_2 and C_2 are later runs that followed the initial irrigation and drying cycle. The unmatched pixels are shown in brown (A_2), red (B_2) and yellow (C_2) respectively.

6.3.3.2   Effect of Flow Rate

The samples were irrigated at 20 ml h^{-1} and 40 ml h^{-1} following the 10 ml h^{-1} experiments. The 2D y-z projections at the three flow rates are presented in Figure 6.14 and Figure 6.16. The second 10 ml h^{-1} experiment (B) was used for the comparison as there was minimal variation between runs B and C and the slumping in run A, the initial irrigation of the ore, made this scan less appropriate. The images were thresholded at the same level as the 10 ml h^{-1} images to compare the extent of the liquid distribution given the irrigation of a common volume of liquid to the ore bed. The thresholded images are combined to assess the image agreement as shown in Figure 6.15, Figure 6.17 and Table 6.7.

The image agreement is worst between the 10 and 40 ml h^{-1} runs. The only exception to this trend is when the 10 and 40 ml h^{-1} runs of the second sample are compared after only 10 ml of liquid has been irrigated. In the first sample the best agreement is between the 20 and 40 ml h^{-1} runs, whereas in the second sample the best agreement is between the 10 and 20 ml h^{-1} runs. Therefore while the liquid path does change due to variations in the flow rate, it does not change by the same extent in the two samples studied. The improved agreement between the images with time is due to the system approaching the point when the whole imaging region is wet.

The percentage of the imaging region that contains liquid is presented in Table 6.8. Initially, when only 10 ml of liquid has been irrigated, the liquid occupied region in the first sample increases with flow rate. This trend does not occur in the second sample, where the least extensive wetting is in the 20 ml h^{-1} run. The liquid occupied region decreases with increasing flow rate for both samples when 20 and 40 ml has been irrigated. Figure 6.15 and Figure 6.17 show that this is because the liquid does not extend as far horizontally from the irrigation point at the higher flow rates. This indicates that there is less capillary suction at higher flow rates, an effect that has previously been discussed by O'Kane Consultants Inc. (2000) and is the cause of macro-pore preferential flow. The measurements at the 10 ml stage may deviate from this trend because the liquid flow is not yet sufficiently established. The liquid occupied region is larger in the second sample than in the first sample for all irrigation volumes and flow rates. This will simply be due to variations in the structure of the agglomerated ore bed and the relative location of the finer and larger ore particles in the two samples.
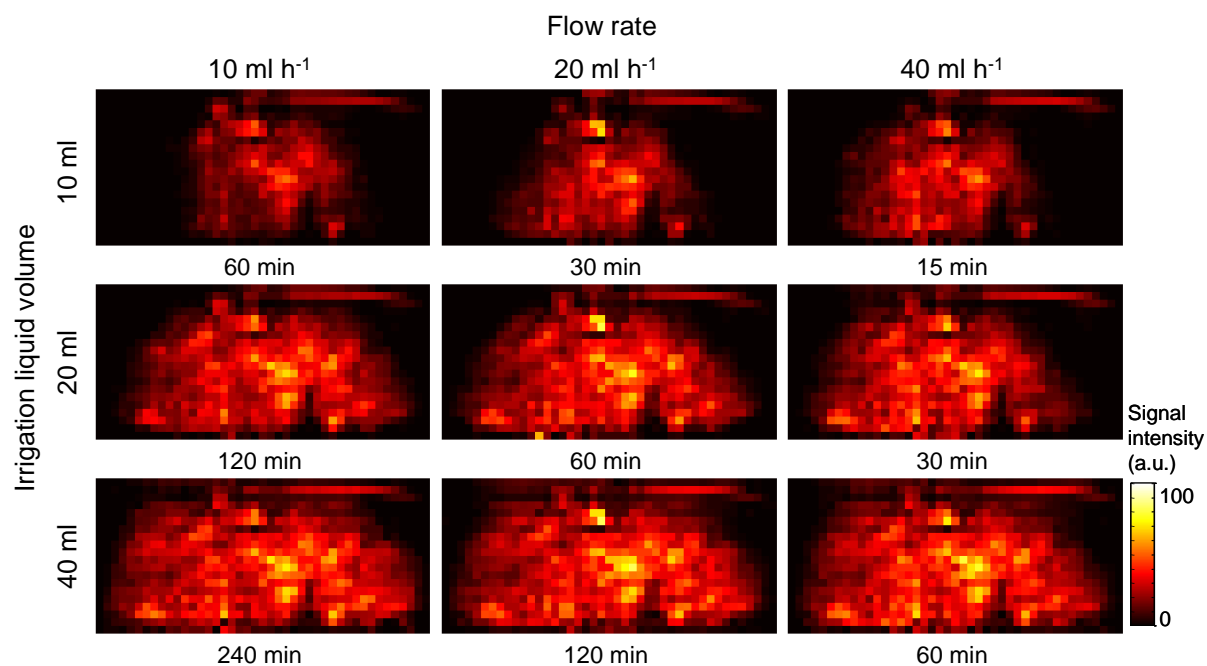
Figure 6.14. Comparison of the liquid distribution in the first agglomerated ore sample for different flow rates after the same volume of liquid has been introduced to the system.

Figure 6.15. Representation of the image agreement of the first agglomerated ore sample after the same volume of liquid has been introduced to the system. White is for the matching pixels while brown is for 10 ml h^{-1}, red is for 20 ml h^{-1} and yellow is for 40 ml h^{-1} unmatched pixels.

Figure 6.16. Comparison of the liquid distribution in the second agglomerated ore sample for different flow rates after the same volume of liquid has been introduced to the system.
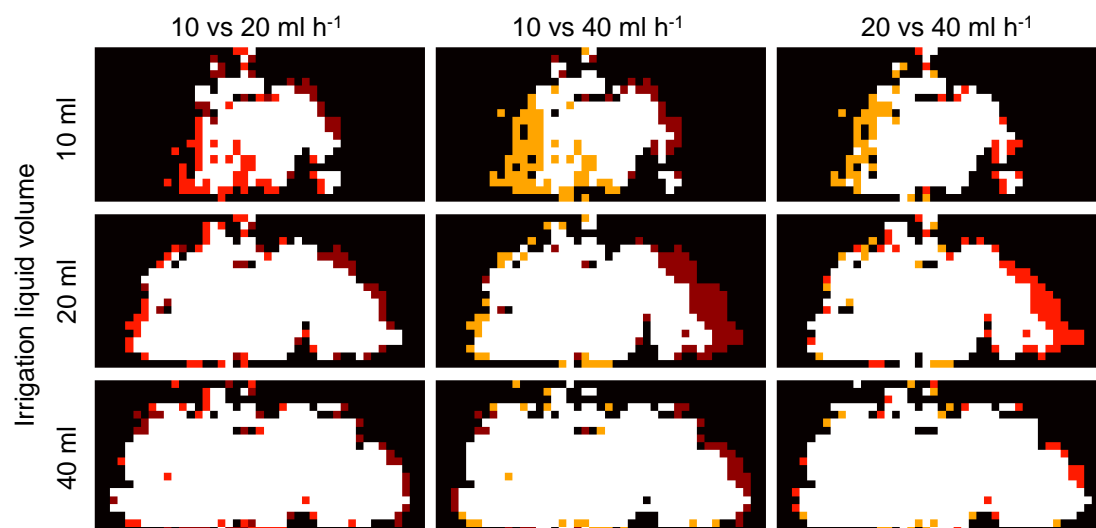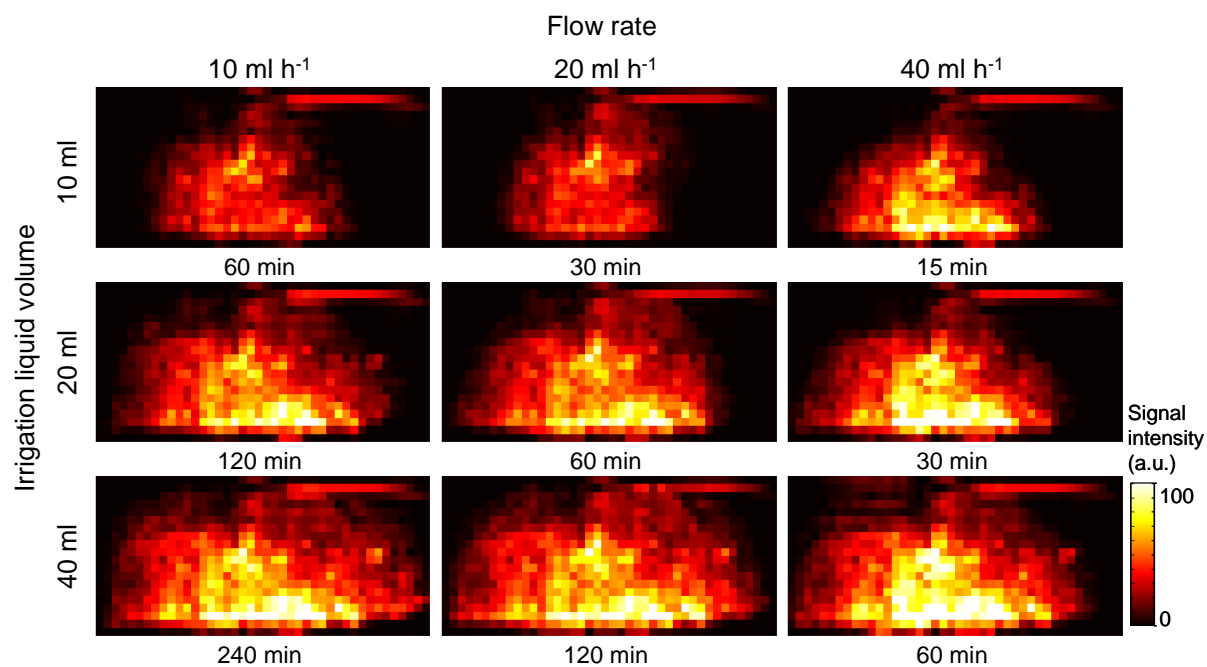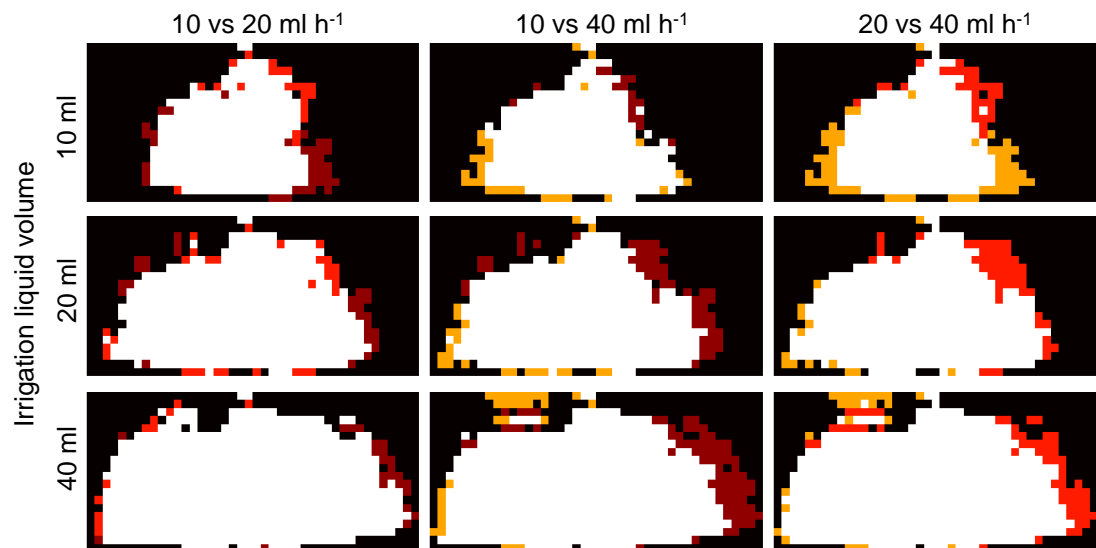

Figure 6.17. Representation of the image agreement of the second agglomerated ore sample after the same volume of liquid has been introduced to the system. White is for the matching pixels while brown is for 10 ml h^{-1}, red is for 20 ml h^{-1} and yellow is for 40 ml h^{-1} unmatched pixels.

Table 6.7. Agreement between the images of the agglomerated ore after the same volume of liquid has been introduced to the system.

	Sample 1 Agreement (%)			Sample 2 Agreement (%)		
Volume of irrigated liquid (ml)	10 vs 20 ml h^{-1}	10 vs 40 ml h^{-1}	20 vs 40 ml h^{-1}	10 vs 20 ml h^{-1}	10 vs 40 ml h^{-1}	20 vs 40 ml h^{-1}
10	70.8	64.7	79.7	82.1	87.1	74.0
20	88.1	80.5	84.6	89.3	83.8	86.8
40	91.8	91.2	94.7	94.4	84.0	87.5

Table 6.8. Imaging region in the y-z projections of the agglomerated ore occupied by liquid.

	Sample 1 liquid filled area (%)			Sample 2 liquid filled area (%)		
Volume of irrigated liquid (ml)	10 ml h^{-1}	20 ml h^{-1}	40 ml h^{-1}	10 ml h^{-1}	20 ml h^{-1}	40 ml h^{-1}
10	30.6	33.8	37.0	44.4	42.4	45.7
20	64.9	64.0	56.9	67.6	66.6	60.7
40	76.9	75.6	74.5	86.2	84.7	77.2

Table 6.9 presents a measure of the symmetry of the flow, expressed as the percentage of the liquid occupied region that is found to the right of the irrigation point. In the first sample the symmetry improves with an increase in flow rate. The liquid distribution in the 40 ml h^{-1} run is close to symmetrical throughout the course of the experiment. The least symmetrical flow is after only 10 ml has been irrigated in the 10 ml h^{-1} run where two thirds of the wetted area is located to the right of the irrigation point. The symmetry improves with time in the 10 and 20 ml h^{-1} runs. In the second sample the liquid distribution is more symmetrical for the 10 and 20 ml h^{-1} runs compared with the results for sample 1. The symmetry improves with increasing flow rate in this sample as well, with the exception of the results when 10 ml has been irrigated. The largest degree of asymmetry occurs in the 10 ml h^{-1} run when 40 ml of liquid has been irrigated.

Unsaturated zone hydrology theory predicts that below a critical liquid throughput rate the matric suction of a finer ore packing will exceed that of a larger ore packing. O'Kane Consultants Inc. (2000) showed how the flow path of liquid through an ore bed segregated into zones of different particle sizes may be altered to favour either the large or fine ore packing by changing the flow rate. Therefore the improvement of the liquid distribution symmetry at higher flow rates may be because the effect of capillary suction due to the finer ore particles is stronger at lower flow rates. This will also account for the increased horizontal

movement of the liquid which is discussed with respect to the image agreement. As the liquid flow rate is increased, the matric suction of the larger voids as a result of the larger ore particles will have increased relative to that of the fine ore, thereby causing the liquid to favour gravitation dominated macro-pore flow.

Table 6.9. Liquid occupied region that is found to the right of the irrigation point in the y-z projections of the agglomerated ore.

Volume of irrigated liquid (ml)	Sample 1 liquid to the right of the irrigation point (%)			Sample 2 liquid to the right of the irrigation point (%)		
	10 ml h^{-1}	20 ml h^{-1}	40 ml h^{-1}	10 ml h^{-1}	20 ml h^{-1}	40 ml h^{-1}
10	67.0	60.7	49.4	51.2	51.1	47.1
20	58.1	54.7	49.1	54.0	53.7	48.2
40	55.7	54.1	53.6	56.0	53.7	49.7

Figure 6.18 shows how the signal magnitude profiles, calculated by summing the signal in the 3D acquisitions, vary as a function of distance from the irrigation point once steady state has been reached. As the echo time (750 μs) is much shorter than the T_2 of the doped water (longer than 20 ms in all the samples tested) the signal magnitude is a suitable indicator of the amount of liquid present. Note that the dips in the profiles (which are particularly evident in sample 1) are due to the existence of large ore particles in these locations.

The profiles show that an increase in the flow rate does not equate to a proportional increase in the liquid retention. This agrees with literature findings (Bouffard and Dixon 2001, Ilankoon and Neethling 2012) and the results from the leaching column experiments that are presented in the previous chapter where flow rate changes only resulted in a small change in the liquid hold-up. Bartlett (1998) explains that the flow rate does not strongly affect the liquid retention while particle size distribution does.

In the centre of the ore bed a higher flow rate results in an increase in the liquid hold-up, with only a few exceptions in sample 1. The amount of liquid retained by the ore bed also decreases as the distance from the irrigation point increases. This is because more of the liquid in the outer regions will have moved there under capillary suction and the retention will consequently be a function of the local ore particle sizes rather than the flow rate of the liquid. Furthermore, as the distance from the irrigation point increases, the differences in the liquid retention at different flow rates decrease. In some regions of the sample (more than 20 mm to the left and 15 mm to the right of the irrigation point in sample 1 and more than 17.5 mm to

the right of the irrigation point in sample 2) there is almost no change in the liquid retention for all of the flow rates. This indicates that though liquid hold-up increases slightly with flow rate, the effect decreases as the distance from the irrigation point increases. This result agrees with the predictions of Dixon (2003). Note that these distances correspond closely to the radius of the column used in the previous chapter (25 mm) which may explain why similar behaviour was not observed then.
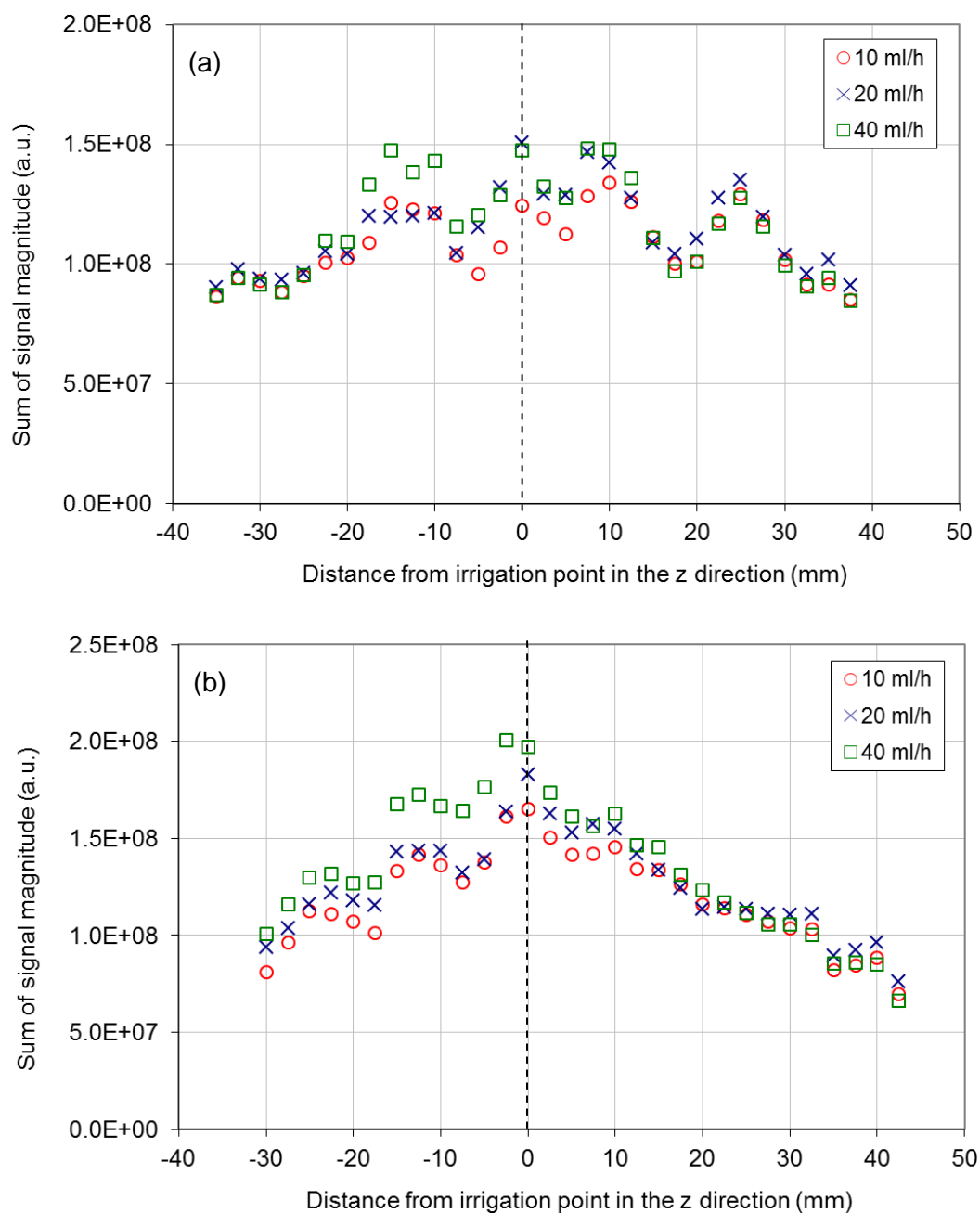

Figure 6.18. The steady state signal magnitude profiles for the three flow rates applied to the (a) first and (b) second agglomerated ore sample.

The amount of liquid that flows in channels versus the liquid that is present in thin rivulets or is held in the pores under capillary suction can be studied by considering the signal magnitude of the individual pixels in the 3D acquisition. The larger channels of liquid flow give off more signal as the volume of liquid per pixel is greater than in other areas. Therefore to analyse the prevalence of the different types of liquid flow/retention at the different flow rates the acquisitions are thresholded at five levels (0.5×10^5, 2×10^5, 4×10^5, 6×10^5 and 8×10^5). 2D slices from the 3D image are shown thresholded at these levels in Figure 6.19. Pixels with signal greater than 8×10^5 are thought to account for the centres of the main channels of liquid flow with the pixels of signal magnitude between 6×10^5 and 8×10^5 forming the rest of the large liquid channels. The lowest value of 0.5×10^5 is the noise level. The summed signal from each signal magnitude range is presented in Figure 6.20. Figure 6.21 and Figure 6.22 illustrate how the signal from each range varies as a function of the distance from the irrigation point in the z direction in sample 1 and sample 2 respectively.
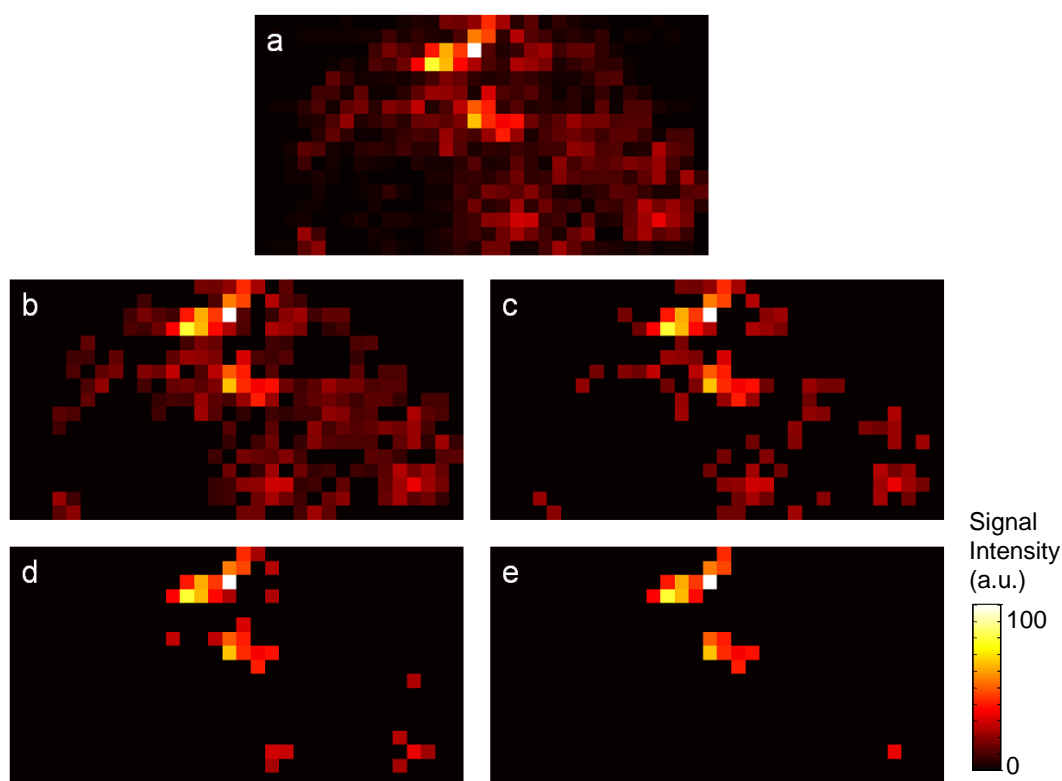

Figure 6.19. Illustration of the threshold levels applied an x-y slice from the 3D acquisition of the 10 ml h^{-1} run where (a) is the original image, (b) is the image thresholded at signal magnitude 2×10^5, (c) at 4×10^5, (d) at 6×10^5 and (e) at 8×10^5.

The most significant change as the flow rate is increased is an increase in the signal from pixels with magnitude greater than $8{\times}10^5$ which indicates that more liquid flows in channels. This effect is more pronounced in sample 2 than in sample 1. In sample 1 there is also an increase in the signal which comes from pixels of signal magnitude between $4{\times}10^5$ and $8{\times}10^5$, though it is less pronounced. The signal between $2{\times}10^5$ and $4{\times}10^5$ decreases in the sample which may be due to some pores increasing their liquid hold-up so that the signal fell into the higher ranges. Changes in the other signal magnitude ranges in sample 2 are relatively minor. In both samples there is almost no change in the amount of signal that comes from pixels of magnitude less than $2{\times}10^5$. This implies that there is little effect on the liquid hold-up by capillary forces in the smaller pores.

The profiles in Figure 6.21 and Figure 6.22 show that the signal from pixels which have signal magnitude less than $8{\times}10^5$ is distributed evenly throughout the sample. Hence non-channel liquid hold-up is relatively uniform across the imaging region. In contrast with this there is considerable variation in the signal from the pixels with magnitude greater than $8{\times}10^5$ along the length of the ore beds. The changes in this signal as the flow rate increases are also focussed in specific areas. This is most noticeable in sample 2 where there is a large increase in this signal in the 25 mm to the left of the irrigation point. These localised changes are biased towards the centre of the column, as is discussed regarding the total liquid signal profiles in Figure 6.18. Therefore the increase in the liquid hold-up with an increase in the liquid flow rate is due to more liquid flowing in channels while there is less of an effect on the amount of liquid retained under capillary suction. Because the flow of larger channels is dominated by gravitational forces, the changes are concentrated in the area below the irrigation point. This agrees with the findings of Bouffard and Dixon (2001) who reported that an increase in the leach solution superficial velocity caused a small increase in the flowing liquid hold-up of the bed, but did not affect the stagnant liquid hold-up.

Table 6.10 and Table 6.11 show what signal magnitude the liquid channel pixels had prior to each increase in flow rate. For each flow rate increase the majority (more than two thirds) of the liquid channel pixels ($>6{\times}10^5$) remain in the same signal magnitude range i.e. the position of these channels remains unchanged. However, the location of some of the existing liquid channels shift when the flow rate is increased as not all the liquid channel pixels remain after each change in flow rate due to changes in the local hydraulic conductivity. New channels are more likely to form in pixels with a higher liquid content and less than 3% of the new channel pixels are previously void or near void of liquid. Therefore increasing the flow rate does not appear to result in improved flow through previously poorly irrigated areas of the ore bed. It is consequently not expected to result in a significant increase in the overall mineral recovery.
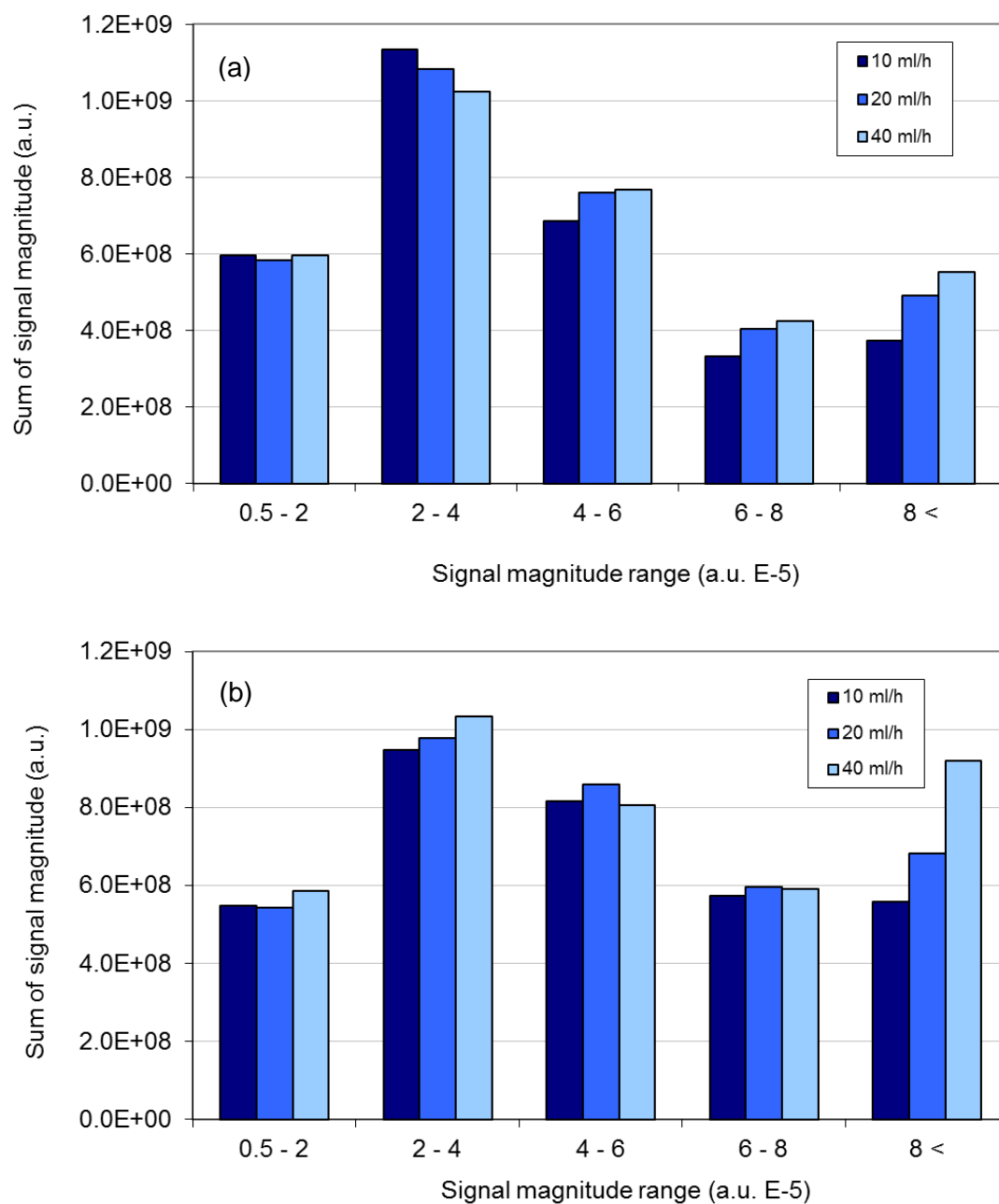
Figure 6.20. Effect of changing the flow rate on the distribution of the liquid in the agglomerated ore beds, where the magnitude of the signal is used as an indicator of channel size for (a) sample 1 and (b) sample 2.
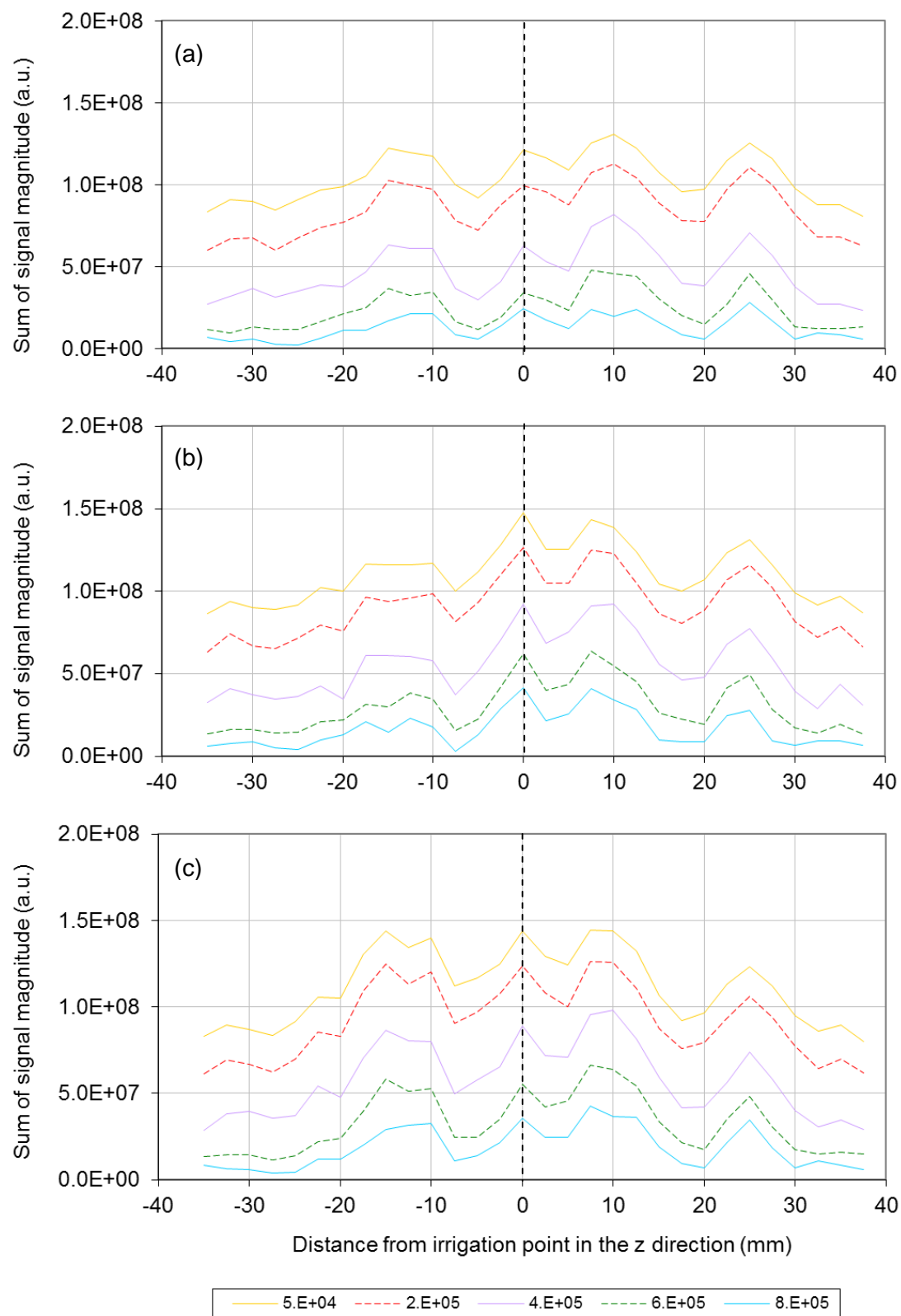
Figure 6.21. Profiles of the signal which have magnitude above a given value for sample 1 of the agglomerated ore irrigated at (a) 10 ml h^{-1}, (b) 20 ml h^{-1} and (c) 40 ml h^{-1}.
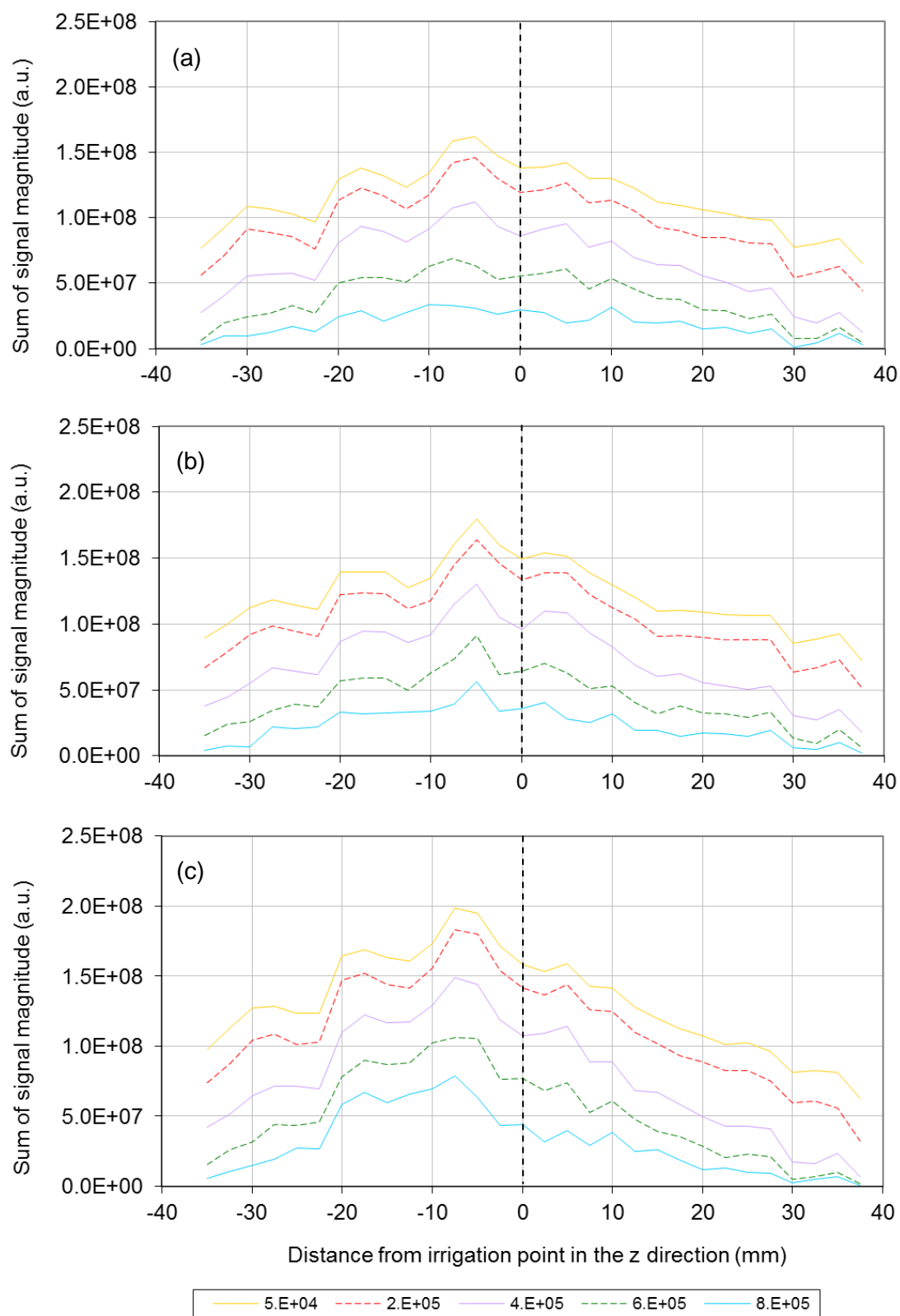
Figure 6.22. Profiles of the signal which have magnitude above a given value for sample 2 of the agglomerated ore irrigated at (a) 10 ml h^{-1}, (b) 20 ml h^{-1} and (c) 40 ml h^{-1}.

Table 6.10. Signal magnitude range that the pixels which contain signal $> 6 \times 10^5$ fell into at the lower flow rate (prior to each increase) for sample 1 of the agglomerated ore, given as a percentage of the total pixels with signal magnitude $> 6 \times 10^5$.

Flow rate	Number of pixels $> 6 \times 10^5$	Signal magnitude before the flow rate increase (% of pixels)			
		$0 - 2 \times 10^5$	$2 \times 10^5 - 4 \times 10^5$	$4 \times 10^5 - 6 \times 10^5$	$> 6 \times 10^5$
10 ml h^{-1}	835	-	-	-	-
20 ml h^{-1}	1032	2.6	16.3	27.9	53.2
40 ml h^{-1}	1113	1.1	10.8	28.7	67.3

Table 6.11. Signal magnitude range that the pixels which contain signal $> 6 \times 10^5$ fell into at the lower flow rate (prior to each increase) for sample 2 of the agglomerated ore, given as a percentage of the total pixels with signal magnitude $> 6 \times 10^5$.

Flow rate	Number of pixels $> 6 \times 10^5$	Signal magnitude before the flow rate increase (% of pixels)			
		$0 - 2 \times 10^5$	$2 \times 10^5 - 4 \times 10^5$	$4 \times 10^5 - 6 \times 10^5$	$> 6 \times 10^5$
10 ml h^{-1}	1371	-	-	-	-
20 ml h^{-1}	1527	1.6	4.4	24.3	69.7
40 ml h^{-1}	1708	1.2	7.4	28.6	74.7

6.3.3.3   D$_2$O Tracer Studies

The degree of wetness of the ore bed had a significant effect on the liquid distribution in the fine ore bed; therefore further experiments were done to investigate if similar behaviour occurred in agglomerated ore systems. This has previously been done on the vertical column, the results of which are presented in Chapter 5, but the small diameter of the column (50 mm) meant that no significant spatial variations in the flow were observed. Figure 6.23 and Figure 6.25 show the 2D y-z projections of a series of three 10 ml h^{-1} drip irrigation experiments performed on two agglomerated ore samples. In the first run, A, the ore had been agglomerated with D$_2$O and was irrigated from an initially wet state with the GdCl$_3$ doped solution. For run B the ore was dried overnight and then irrigated with the GdCl$_3$ doped solution. The sample was irrigated in this manner for a minimum of 24 hours after which the feed solution was swapped to D$_2$O. The disappearance of the MRI signal as the D$_2$O flowed into the ore bed was recorded in run C. Figure 6.24 and Figure 6.26 are overlays of the thresholded images which allow for easier qualitative comparison of the liquid distribution in runs A and C and in runs B and C. The percentages of the imaging region that had been

wetted in each of the runs as time progressed are presented in Table 6.12 while Table 6.13 and Table 6.14 give the approximate vertical and horizontal (maximum) irrigation rates.

In sample 1 there is very close agreement between the liquid distributions in runs B_I and C_I during the first 60 minutes of irrigation. This is because the liquid distribution is dominated by a channel of flow. Such channels can be problematic in heap operation as they cause short circuiting of the liquid (O'Kane Consultants Inc. 2000). This liquid channel is also present in run A_I, but there is more lateral spreading of the liquid at the base of the ore bed than there is in runs B_I and C_I during the first hour. This results in a larger wetted area in run A_I for this period. Run A_I also has both the fastest vertical and horizontal infiltration rates. Similar differences in the liquid distribution were observed in the repeat irrigation of the dry agglomerated ore beds in Section 6.3.3.1, attributed to a shift in the ore particles during the initial irrigation of the ore. The more extensive liquid distribution in run A_I is likely facilitated by an initially more even distribution of fines in the ore bed, a fraction of which were observed to wash out of the cell with the liquid effluent. This will have initially allowed for more lateral wicking of the liquid into the ore bed in run A, which accounts for the faster horizontal infiltration rate. Redistribution of the fines so that they accumulate at the base of heaps or are washed out of ore beds is a known problem in heap operation which may result in regions of reduced permeability (O'Kane Consultants Inc. 2000) and has previously been observed by Lin et al. (2005) using X-ray computed tomography (CT).

If runs B_I and C_I are compared, run C_I has a slightly faster vertical infiltration rate, whilst the lateral distribution of the liquid in the two runs is very similar during the first hour. After this the horizontal infiltration rate of run C_I lags behind run B_I. This is the opposite of what was observed in the fine ore experiments and is typical for soil drip irrigation (Brouwer et al. 1988), where the vertical infiltration rate decreases and the horizontal infiltration rate increases for the wet system relative to the dry sample. This is because at these low flow rates the larger pores in the agglomerated ore will be poor conductors of the liquid compared to the small pores in the fine ore packing, as was demonstrated in the large ore experiments, causing gravitational forces to have a greater influence on the liquid flow. The matric suction of the dry agglomerated ore will be higher than when it is already wet, thereby limiting the amount of liquid that is drawn into the bed by capillary forces in the wet system. The majority of the lateral dispersion of the liquid in run C_I will be through diffusion into the stagnant liquid in the already wet ore instead.

In the case of the second sample, run A_{II} also has the largest wetted area in the first hour of irrigation. In this sample the liquid distribution in run A_{II} has a distinct symmetrical fan shape whose slope is initially 40° to the vertical. This later increases to around 55°. In run B_{II} the

vertical infiltration rate is slower as the liquid instead distributes in a more radial manner, but with a bias to the left of the irrigation point. This is similar to what was observed during the irrigation of the fines. As a result it took 30 minutes for the liquid to reach the base of the ore bed, whereas this occurs within the first 4 minutes of irrigation in runs A_{II} and C_{II}. This will be because the matric suction around the irrigation point is higher than in the first D_2O agglomerated ore sample. The liquid flow in run C_{II} is affected less by these capillary forces and the liquid distribution is more similar to that in run A_{II}, having almost identical vertical and horizontal infiltration rates. However there is a bias to the left side of the ore bed which persists throughout the course of the experiment and is not observed in run A_{II}. This is probably caused by a shift in the fine ore particles during the initial irrigation of the ore, as is proposed to have also occurred in the irrigation of the first sample. The shifting of fines in both of the ore beds results in the slowing and in some instances the limitation of lateral liquid distribution within agglomerated ore. A way of potentially limiting this effect would be the inclusion of a binder such as cement during the agglomeration process (Bouffard 2008).

In order to better describe the type of liquid flow/retention in the ore bed, the pixels in the 3D acquisition of run B, performed after 4 hours of irrigation, were classified according to their signal magnitude using the same methodology as for the different flow rate experiments. The liquid infiltration into the bed in the 3D acquisition of run C was then related to this original classification. Figure 6.27 and Figure 6.28 are profiles which show the contribution of the signal classification ranges along the z axis. The overall liquid distributions are summarised in Table 6.15.

The majority of the liquid in run C, 54.8% and 57.8% respectively, flows preferentially into pixels which have magnitude greater than 6×10^5, previously identified as larger liquid channel pixels. This is around 8% more than these pixels account for in the overall liquid distribution calculated from run B. These pixels are concentrated around the centre of the cell, in the region below the irrigation point, and account for less of the liquid as the lateral distance from the irrigation point increases. Consequently the liquid exchange at the end of run C is highest near to the irrigation point, shown in Figure 6.29. Similar concentration of the liquid flow in the region below the irrigation point is observed in the studies by van Hille et al. (2010) and Chiume (2011) through effluent volume measurements. This result also agrees with the model predictions of Dixon (2003) who found that following the establishment of a wetted system, the majority of the liquid flows into channels, thereby limiting the lateral flow of solution.

The degree of exchange then decreases as the volumetric hold-up (signal magnitude) of the pixels decreases. The least amount of exchange is with the liquid in the pixels which have signal magnitude less than 2×10^5. Only 10.8% and 8.8% of the liquid in the D_2O tracer

experiment flows into these pixels despite 15.4% and 14.4% of the liquid being held in these pixels in samples 1 and 2 respectively. The exchange that does occur is focussed in the central region of the bed, within the 30 mm either side of the irrigation point. These low signal magnitude pixels will most likely contain stagnant liquid held in the intra- and fine inter-particle pores. Therefore any exchange with this liquid is determined by diffusion rather than flow and a longer observation time may be required to see significant exchange with the freshly irrigated liquid in these pixels.

The proportion of the liquid held in the lower intensity pixels increases as the horizontal distance from the irrigation point increases, as can be seen in part (a) of Figure 6.27 and Figure 6.28. For example, the pixels of signal magnitude less than 2×10^5 account for less than 12% of the liquid in the centre of the cell, but more than 50% (maximum of 76%) of the liquid at the edges. Therefore the percentage of the liquid that has been replaced by the end of run C, shown in Figure 6.29, is as low as 2% at the edges of the ore region, much lower than the circa 90% maximum exchange that occurs closer to the irrigation point.

The region of lowest signal intensity is in the top corners of the imaging region in all of the experiments. This is most obvious in runs A and C where there is almost no signal present in these regions. This is because the particle size of the agglomerated ore does not allow for sufficient capillary suction to enable pure horizontal or upward wicking of the liquid when the system is not dry, unlike is seen in the fine ore packing. This is the same result as described by Chiume (2011) on their much larger ore system. Such limited liquid exchange could cause poor local recovery of the mineral in a heap leach because of transport issues, poor microbial colonisation (Chiume 2011), and other problems such as jarosite precipitation caused by high local acid consumption (van Hille et al. 2010). In heap leaching practice drip emitters are placed every 0.5 to 1.5 m (Kappes 2002), hence this issue is expected to be more pronounced in full scale operation than is observed in the 100 mm imaging region of the MRI. This is a major disadvantage of drip irrigation that would not be expected to occur to the same degree if sprinkler irrigation is employed.
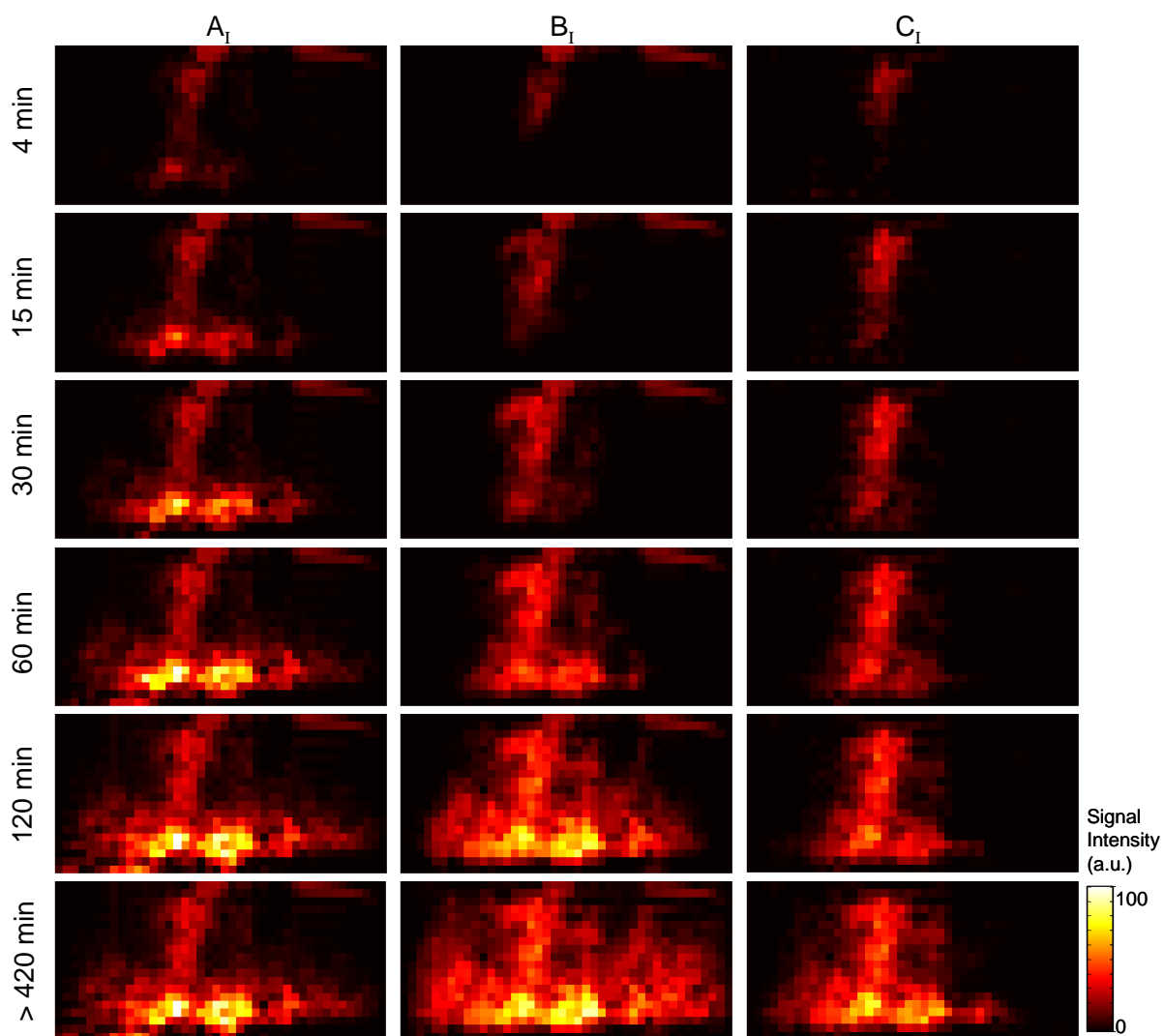
Figure 6.23. 2D y-z projections of the first D_2O agglomerated ore sample drip irrigated at a rate of 10 ml h^{-1}. Run A_I is when the wet D_2O agglomerated ore is irrigated with doped water. For run B_I the ore has been dried overnight and is irrigated with doped water. Run C_I shows where the D_2O liquid flows following a swap in the liquid feed from the doped water solution in run B_I once steady state has been reached.
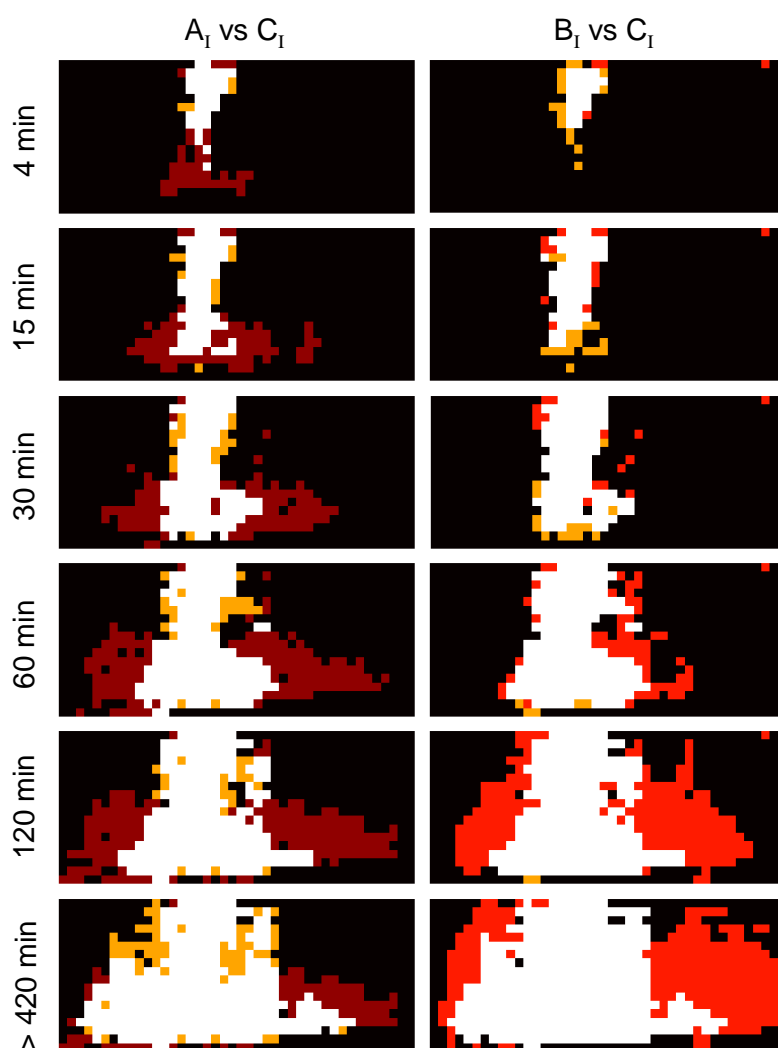
Figure 6.24. Representation of the image agreement (white) of the first D_2O agglomerated ore sample drip irrigated at 10 ml h^{-1}. The unmatched pixels are shown in brown (A_I), red (B_I) and yellow (C_I) respectively.
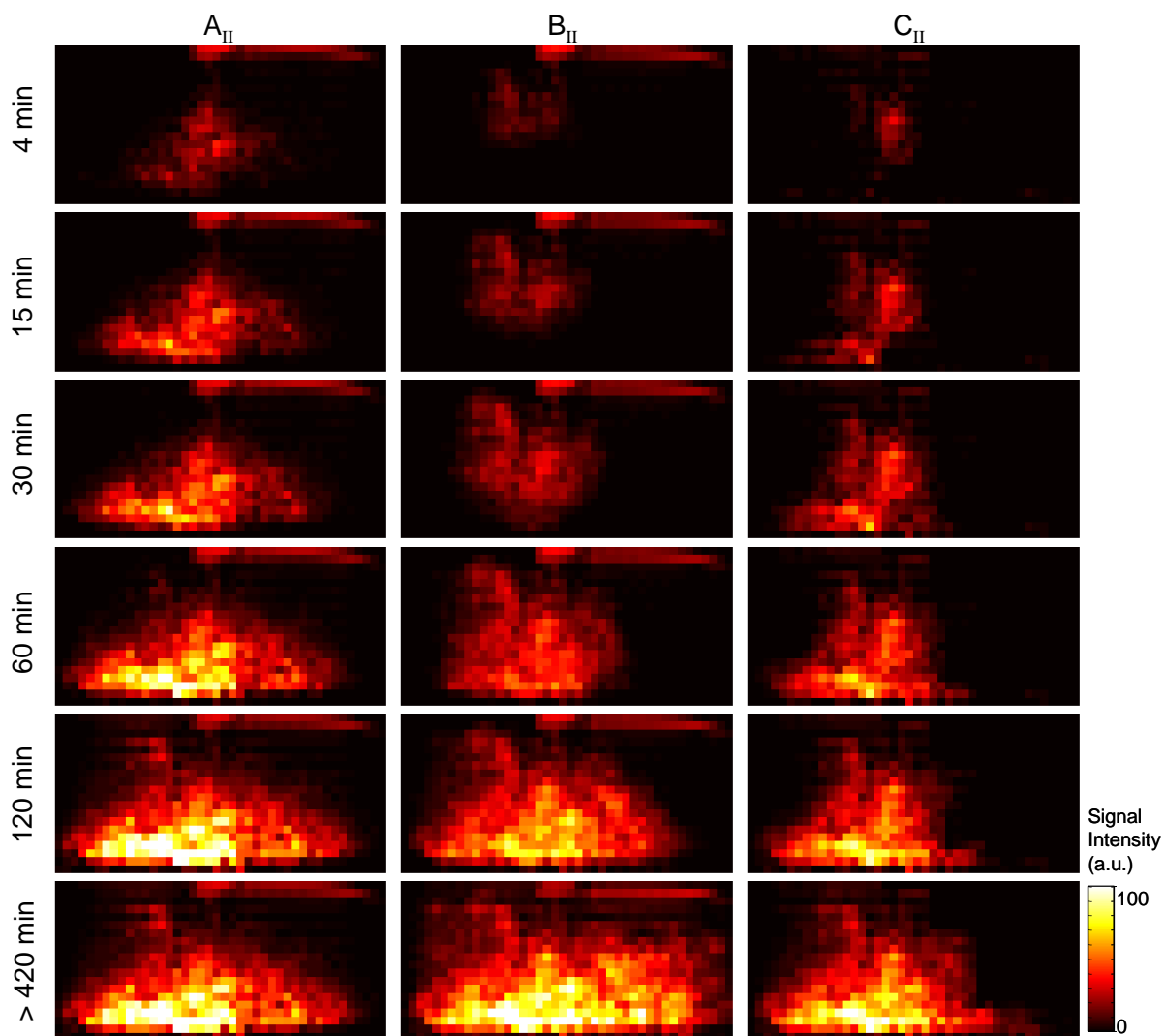
Figure 6.25. 2D y-z projections of the second D_2O agglomerated ore sample drip irrigated at a rate of 10 ml h^{-1}. Run A_{II} is when the wet D_2O agglomerated ore is irrigated with doped water. For run B_{II} the ore has been dried overnight and is irrigated with doped water. Run C_{II} shows where the D_2O liquid flows following a swap in the liquid feed from the doped water solution in run B_{II} once steady state has been reached.
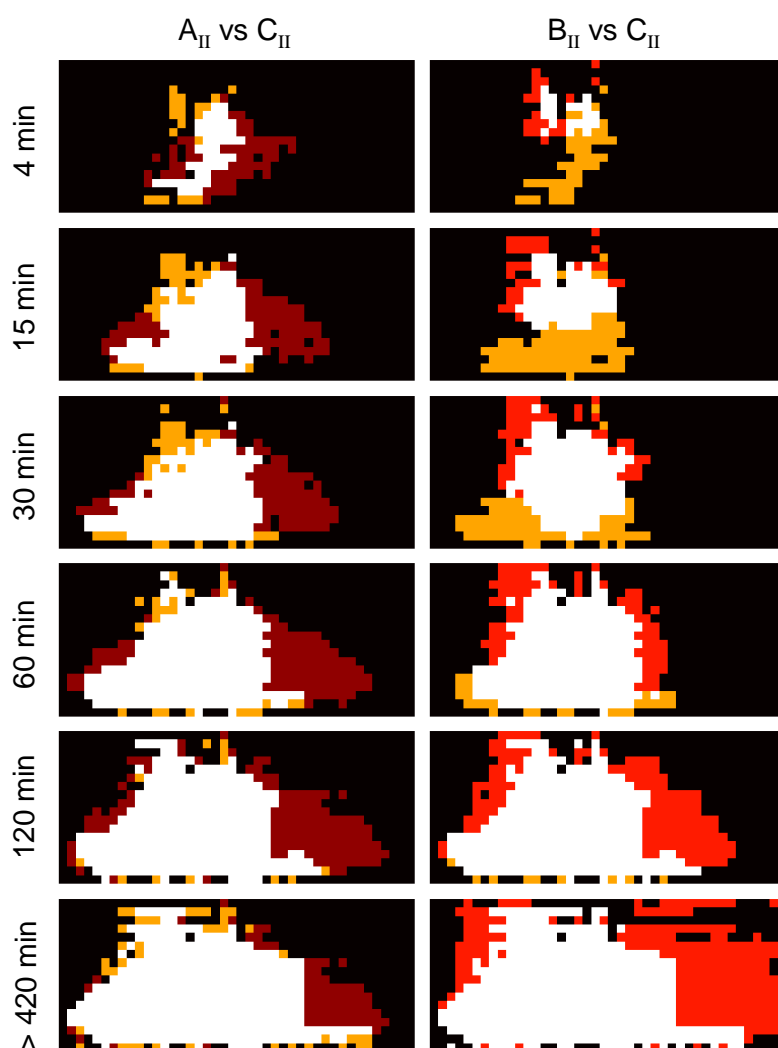
Figure 6.26. Representation of the image agreement (white) of the second D_2O agglomerated ore sample drip irrigated at 10 ml h^{-1}. The unmatched pixels are shown in brown (A_{II}), red (B_{II}) and yellow (C_{II}) respectively.

Table 6.12. Imaging region in 2D y-z projections of the D_2O agglomerated ore that is occupied by liquid.

Time (minutes)	Sample 1 liquid filled area (%)			Sample 2 liquid filled area (%)		
	A_I	B_I	C_I	A_{II}	B_{II}	C_{II}
4	10.4	3.7	4.6	15.9	6.0	5.3
15	20.7	10.2	10.1	31.4	15.3	16.7
30	30.0	18.7	16.7	37.8	27.7	26.6
60	43.8	35.8	26.8	50.0	44.9	33.1
120	52.8	63.5	33.4	59.6	61.9	40.2
> 420	53.2	84.2	50.5	62.0	83.7	52.3

Table 6.13. Sample 1 vertical and maximum horizontal infiltration rate of the liquid for the D_2O agglomerated ore irrigated at 10 ml h^{-1}.

Time (minutes)	Vertical infiltration rate (mm h^{-1})			Horizontal infiltration rate (mm h^{-1})		
	A_I	B_I	C_I	A_I	B_I	C_I
4	563	300	375	225	150	188
15	30	60	50	40	30	20
30	-	-	-	20	25	20
60	-	-	-	15	18	7.5
120	-	-	-	5.0	8.8	5.0

Table 6.14. Sample 2 vertical and maximum horizontal infiltration rate of the liquid for the D_2O agglomerated ore irrigated at 10 ml h^{-1}.

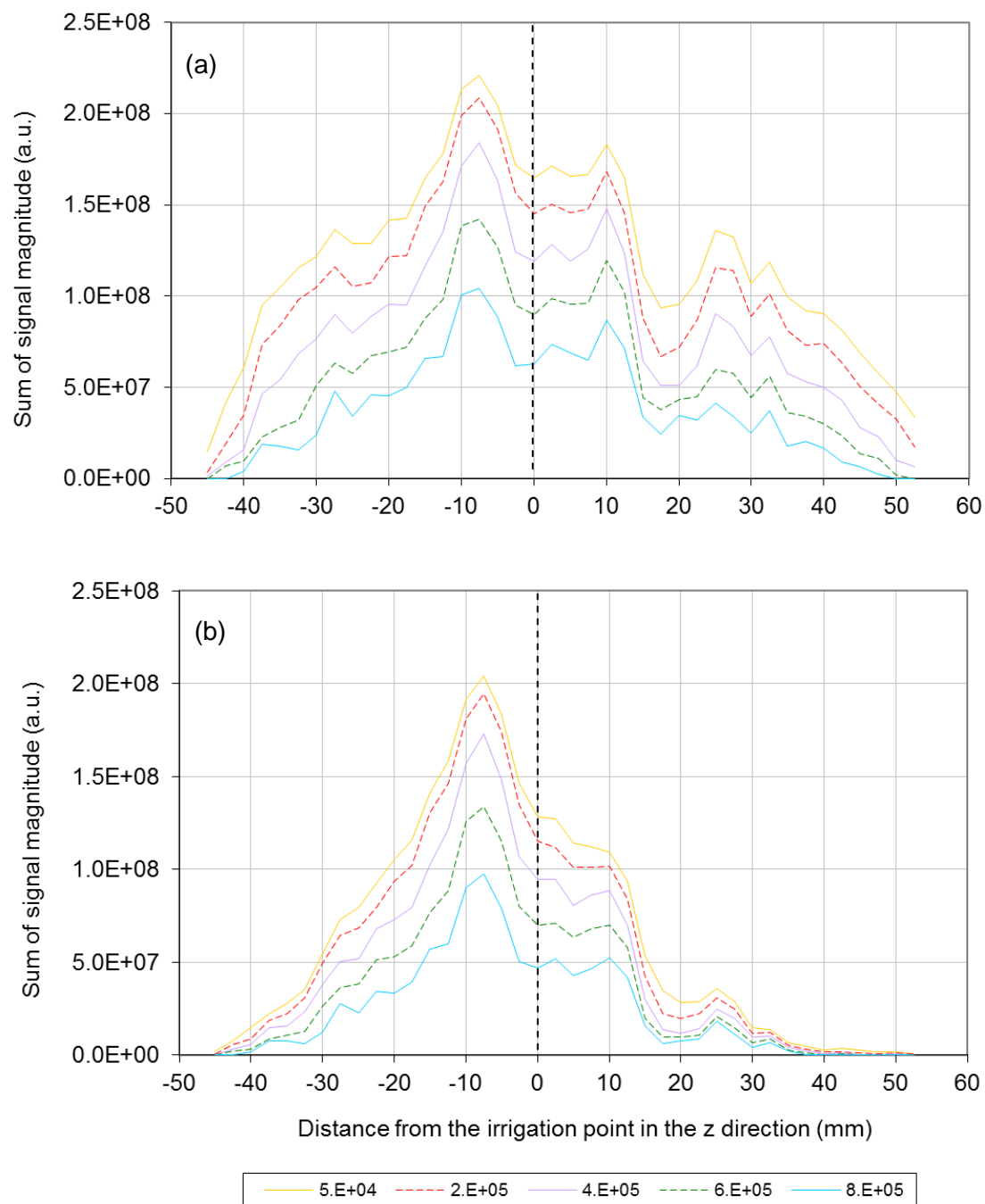| Time (minutes)	Vertical infiltration rate (mm h^{-1})			Horizontal infiltration rate (mm h^{-1})		
	A_{II}	B_{II}	C_{II}	A_{II}	B_{II}	C_{II}
4	638	338	638	375	338	375
15	-	30	-	60	30	50
30	-	20	-	15	15	15
60	-	-	-	10	7.5	7.5
120	-	-	-	3.8	10	3.8

Figure 6.27. The pixels from the 3D acquisition (after four hours) of run B_I on the first D_2O agglomerated ore sample are classified according to their signal magnitude, where (a) shows the profiles of the sum of the signal above given values. The signal from the liquid in run C_I that flows into these pre-classified pixels is presented as profiles in (b).
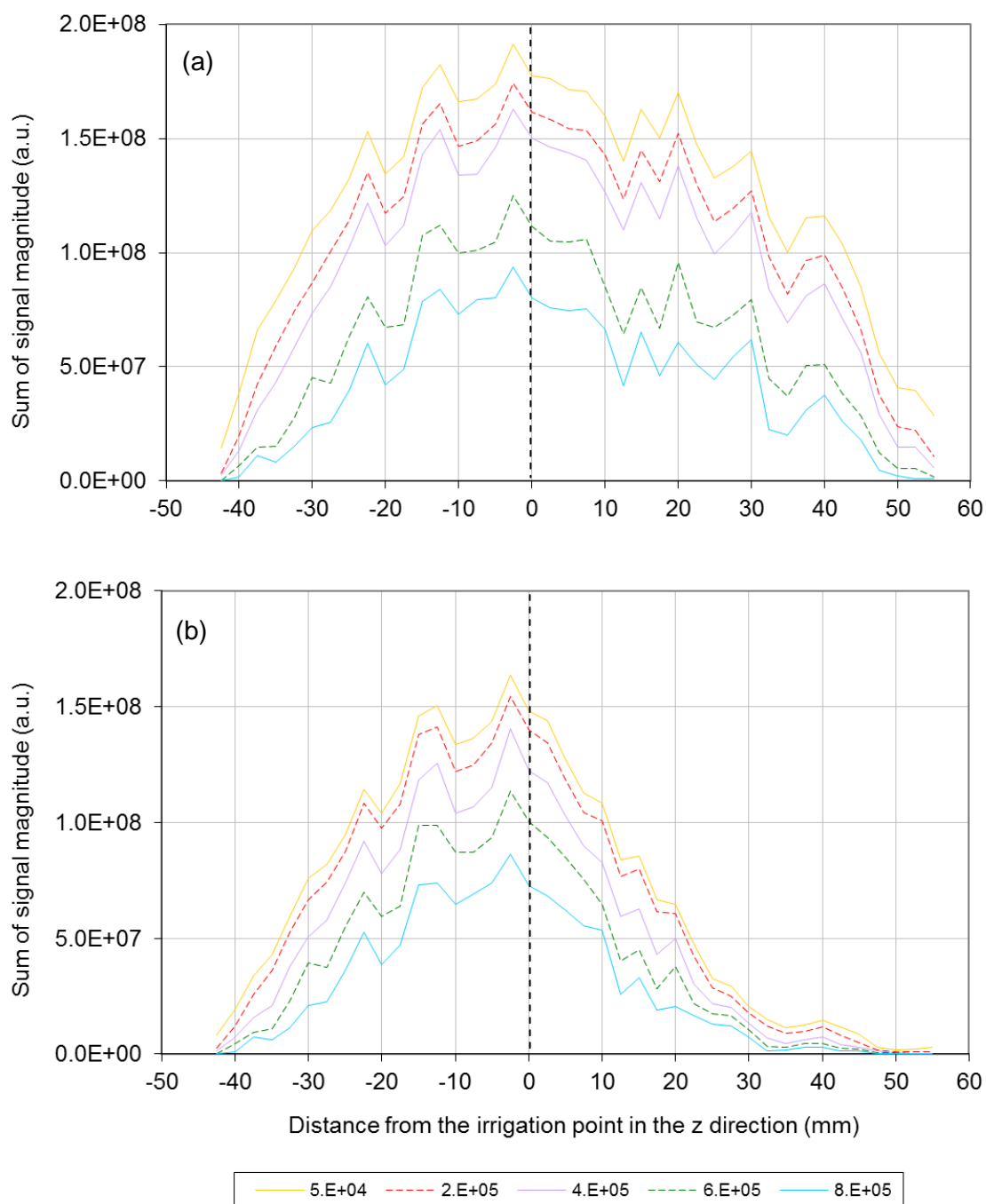
Figure 6.28. The pixels from the 3D acquisition (after four hours) of run B_{II} on the second D_2O agglomerated ore sample are classified according to their signal magnitude, where (a) shows the profiles of the sum of the signal above given values. The signal from the liquid in run C_{II} that flows into these pre-classified pixels is presented as profiles in (b).
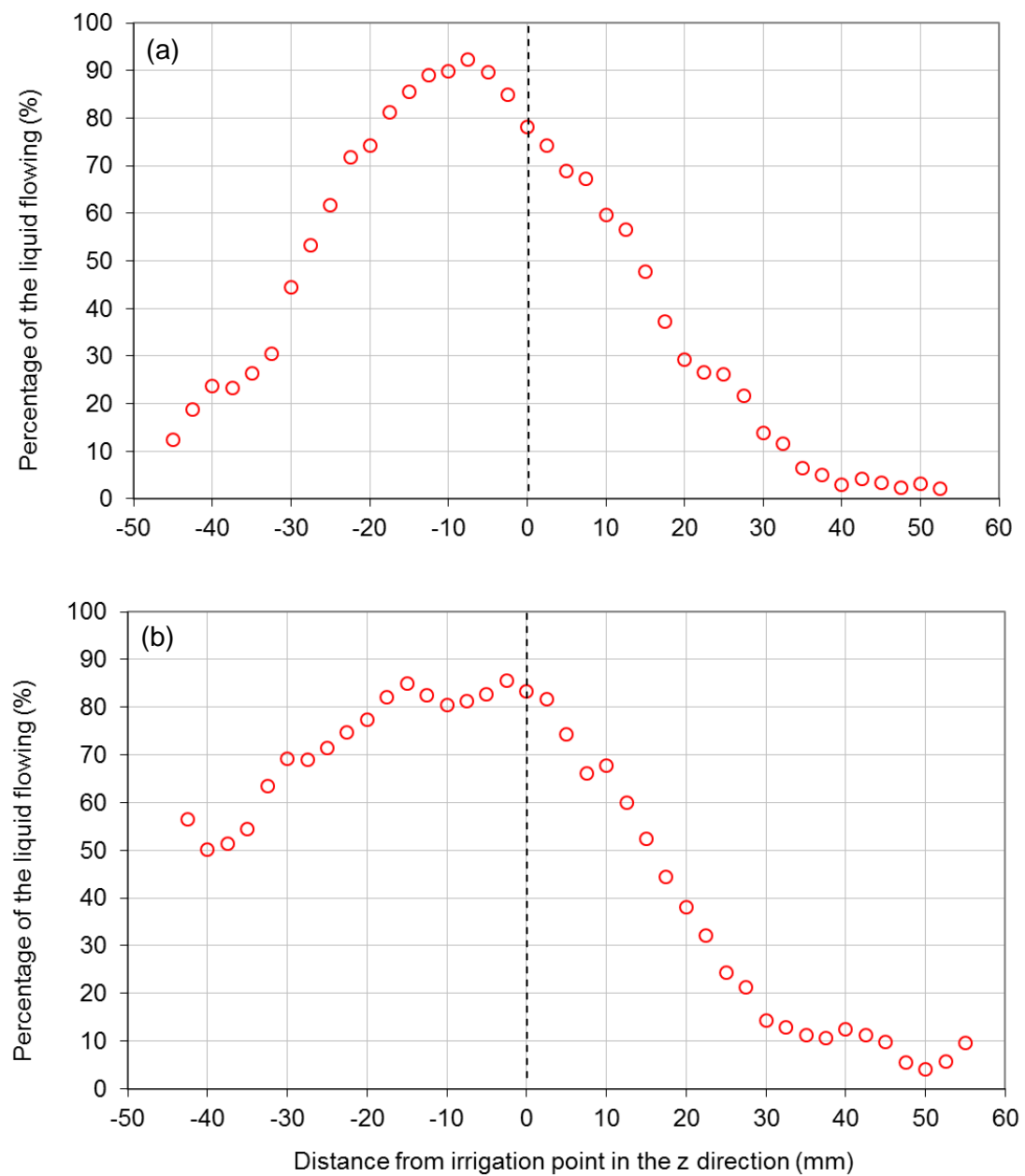
Figure 6.29. Overall percentage of the liquid in (a) sample 1 and (b) sample 2 that is replaced after four hours during run C relative to the steady state of run B.

Table 6.15. Location of the liquid in run C (exchanged liquid) relative to the signal magnitude of the pixels in the 3D acquisition of run B (overall liquid distribution).

Pixel signal magnitude in run B	Sample 1		Sample 2	
	Overall liquid distribution (%)	Exchanged liquid (%)	Overall liquid distribution (%)	Exchanged liquid (%)
$0 - 2\times10^5$	15.4	10.8	14.4	8.8
$2\times10^5 - 4\times10^5$	19.1	16.7	9.7	16.3
$4\times10^5 - 6\times10^5$	18.2	17.7	26.2	17.1
$6\times10^5 - 8\times10^5$	15.5	16.8	15.0	16.2
$> 8\times10^5$	31.9	38.0	34.7	41.6

6.4 Conclusions

Drip irrigation of large ore particles was demonstrated to result in a strong preference for channel or macro-pore flow where the liquid flow was dominated by gravitational effects. This meant that there was relatively limited lateral distribution of the liquid and pronounced preferential flow was observed in both the samples tested. Changes in the flow rate were observed to have limited effect on the flow path, though did result in the formation of new liquid channels in some instances.

The liquid distribution in the fine ore bed was strongly dominated by capillary suction by comparison. Whereas liquid drained almost immediately from the cell in all of the large ore experiments, the fine ore did not start to drain until 80 ml of liquid had been irrigated at which point the ore was almost 50% saturated. The liquid distribution was found to be described well by the heuristics for drip irrigation of clay soils. Low flow rates resulted in highly symmetric radial flow outwards from the drip irrigation point, with the lateral distribution of the liquid increasing with flow rate and wetness of the sample. This symmetry was compromised at high flow rates because the liquid accumulated at the top of the ore bed as liquid runoff. The results confirmed that the accumulation of fines in regions of the bed could plug pores and thereby restrict flow, but also showed how intentionally installed layers of fines in ore heaps could be effective at impeding the downwards liquid flow and oxygen supply to deeper ores which would be advantageous in acid mine drainage prevention.

The liquid distribution in the agglomerated ore beds increased laterally with depth as has been reported previously in the literature. Shifting of the ore particles had a significant effect on the liquid flow path with slumping of the ore bed during an initial irrigation cycle permanently

altering the flow path, which subsequently remained stable. Washing of the fines towards the base or out of the bed resulted in the limitation of the lateral distribution of the leach solution. Following the establishment of a wetted bed, the majority of the freshly irrigated solution entered directly into the established channels of flow. This meant that liquid exchange in the bed was limited to the central region below the irrigation point. The degree of exchange decreased as the volumetric hold-up of the pixels decreased, with the least exchange occurring with the pixels which were presumed to contain stagnant liquid held in pores. Almost no exchange occurred in the areas of lowest liquid content at the top corners of the cell. Doubling of the flow rate from 10 ml h^{-1} to 20 ml h^{-1} to 40 ml h^{-1} only resulted in small increases in the liquid hold-up, limited to the region directly below and adjacent to the drip irrigation point. This was because a higher liquid flow rate caused an increase in the amount of liquid held in channels (pixels of high signal intensity) rather than a change in the amount of liquid held under capillary suction. The lateral distribution of the liquid at higher flow rates was also retarded relative to the slower flow conditions. This meant that changing the flow rate had little effect on the overall liquid distribution and was not successful at perturbing the liquid distribution in a way that would be beneficial to the recovery of previously poorly wetted mineral.

6.5 Nomenclature

Abbreviations

CT   -   computed tomography

FOV   -   field of view

MRI   -   magnetic resonance imaging

PSD   -   particle size distribution

RF   -   radio frequency

SESPI   -   spin echo single point imaging

Symbols

t_p -   phase encode time [s]

T_1 -   spin-lattice relaxation constant [s]

TE -   echo time [s]

TR -   repetition time [s]

6.6 References

Afewu, K. I. and Dixon, D. G. (2008) 'Calibrating a 3D axisymmetric water and solute transport model for heap leaching' in Young, C.A., Taylor, P.R., Anderson, C.G. and Choi, Y., eds., *Hydrometallurgy 2008, Proceedings of the Sixth International Symposium*, Littleton, Colorado: Society for Mining, Metallurgy, and Exploration, Inc., 955-966.

Bartlett, R. W. (1998) *Solution Mining: Leaching and Fluid Recovery of Materials,* 2nd ed.*,* Gordon and Breach Science Publishers.

Bouffard, S. C. (2008) 'Agglomeration for heap leaching: Equipment design, agglomerate quality control, and impact on the heap leach process', *Minerals Engineering*, 21(1), 1115-1125.

Bouffard, S. C. and Dixon, D. G. (2001) 'Investigative study into the hydrodynamics of heap leaching processes', *Metallurgical and Materials Transactions B-Process Metallurgy and Materials Processing Science*, 32(5), 763-776.

Bouffard, S. C. and West-Sells, P. G. (2009) 'Hydrodynamic behavior of heap leach piles: Influence of testing scale and material properties', *Hydrometallurgy*, 98(1-2), 136-142.

Bresler, E. (1977) 'Trickle-drip irrigation: principles and application to soil-water management', *Advances in Agronomy*, 29(3), 343-391.

Brouwer, C., Prins, K., Kay, M. and Heibloem, M. (1988) *Irrigation Water Management: Irrigation Methods, Training Manual Number 5*, Rome, Italy: Food and Agriculture Organization of the United Nations.

Chiume, R. A. (2011) *The impact of irrigation conditions on the spatial development of microbial colonies in bioheaps*, unpublished thesis, University of Cape Town.

Clothier, B. E. (1984) 'Solute travel times during trickle irrigation', *Water Resources Research*, 20(12), 1848-1852.

de Andrade Lima, L. R. P. (2006) 'Liquid axial dispersion and holdup in column leaching', *Minerals Engineering*, 19(1), 37-47.

Decker, D. L. and Tyler, S. W. (1999) 'Hydrodynamics and solute transport in heap leach mining' in Kosich, D. and Miller, G., eds., *Closure, Remediation & Management of Precious Metals Heap Leach Facilities*, Reno, Nevada: University of Nevada.

Dixon, D. G. (2003) 'Heap leach modeling – the current state of the art', in Young, C. A., Alfantazi, A. M., Anderson, C. G., Dreisinger, D. B., Harris, B., James, A., eds., *Hydrometallurgy 2003, Volume 1: Leaching and Solution Percolation*, Warrendale, Pennsylvania: The Minerals, Metals and Materials Society, 289-314.

Ilankoon, I. M. S. K. and Neethling, S. J. (2012) 'Hysteresis in unsaturated flow in packed beds and heaps', *Minerals Engineering*, 35(1), 1-8.

Irrigation Direct (2012) 'Soil types considerations for drip irrigation systems', [online], available: www.irrigationdirect.com/expert-advice/drip-irrigation-tutorials/general-overview/soil-types [accessed 28 November 2012].

Johnson, D. B. and Hallberg, K. B. (2005) 'Acid mine drainage remediation options: a review', *Science of the Total Environment*, 338(1–2), 3-14.

Kappes, D. W. (2002) *Precious Metal Heap Leach Design and Practice,* Reno, Nevada: Kappes, Cassiday & Associates.

Lin, C. L., Miller, J. D. and Garcia, C. (2005) 'Saturated flow characteristics in column leaching as described by LB simulation', *Minerals Engineering*, 18(10), 1045-1051.

O'Kane, M., Barbour, S. L. and Haug, M. D. (1999) *A Framework for improving the ability to understand and predict the performance of heap leach piles,* Phoenix, Arizona: Copper 99 Conference, 409-419.

O'Kane Consultants Inc. (2000) 'Demonstration of the application of unsaturated zone hydrology for heap leaching optimization', *Industrial Research Assistance Program Contract # 332407*, (628-1).

van Hille, R. P., van Zyl, A. W., Spurr, N. R. L. and Harrison, S. T. L. (2010) 'Investigating heap bioleaching: Effect of feed iron concentration on bioleaching performance', *Minerals Engineering*, 23(6), 518-525.

Withers, B. and Vipond, S. (1974) *Irrigation: design and practice*, London: B. T. Batsford Limited.

Wu, A. X., Yin, S. H., Qin, W. Q., Liu, J. S. and Qiu, G. Z. (2009) 'The effect of preferential flow on extraction and surface morphology of copper sulphides during heap leaching', *Hydrometallurgy*, 95(1-2), 76-81.

Wu, A. X., Yin, S. H., Yang, B. H., Wang, J. and Qiu, G. Z. (2007) 'Study on preferential flow in dump leaching of low-grade ores', *Hydrometallurgy*, 87(3-4), 124-132.

Chapter 7 – X-ray CT Study of a Column Leach

This chapter presents a study of a long term ferric leach of low grade copper ore using X-ray computed tomography (CT) imaging. Three sections of an agglomerated ore column were imaged at different stages in the leaching process. The images were used to quantify the changes in the mineral content present in the ore as the leach progressed. The influence of the position of the mineral relative to its distance from the edge of the ore particles, the local voidage and the mineral's position within the column were quantified and related to the local recoveries in order to identify which of these features had the largest influence on mineral recovery.

7.1 Introduction

X-ray CT is a well established technique for the imaging of opaque samples. Though primarily developed and used as a non-destructive medical imaging technique, X-ray CT can also be a useful tool for the study of chemical engineering systems. Already in the field of heap bioleaching it has been used in various studies. On a macro-scale Lin et al. (2005) and Yang et al. (2008) used X-ray CT to study voidage changes that resulted from the slumping of ore beds as was described in the Heap Leaching Theory chapter.

It has also been used on the micro-scale to monitor the structure of ore particles and mineral grains. These micro-scale studies are possible because the mineral grains have a higher X-ray absorbance than the benign, or gangue, rock and so appear as brighter areas in the images. Miller et al. (2003) was able to use this principle to study the effect that the crush size of the ore has on the distribution of exposed versus internal mineral grains. These findings were related to the recoveries that were achieved when the different particle size samples were leached. They proposed that such studies could be used in the future to identify the optimal crush size of the ore with respect to mineral recovery. More recently, Ghorbani et al. (2011a,b) used X-ray CT to study crack and mineral dissemination in sphalerite ore particles. Their porosity measurements compared well with traditional methods which allowed them to conclude that their approach produced accurate results. They also found that X-ray CT was a more robust tool for the measurement of the spatial distribution of surface and interior micro-cracks in large ore particles than physical gas adsorption and porosimetry methods. They subsequently used their method to study the effect of communition (crushing) devices, specifically high pressure grind rolls (HPGR) and conventional cone crushers, on the generation of cracks in the ore. Kodali et al. (2011) performed a similar X-ray CT study which compared HPGR to jaw crusher crushing. Through analysis of the images they

determined that HPGR caused more particle damage which resulted in higher copper recoveries compared to ore of the same particle size that had been prepared using the other technique. Like Miller et al. (2003), they found that grain exposure and consequently mineral recovery decreased with an increase in particle size. Finally, Lin and Garcia (2005) used X-ray CT to study the evolution of specific mineral grains over the course of a 67 day acid leach. They were also able to speciate the minerals within the ore by determining the density and the effective atomic number of the minerals in the ore and comparing the results to that of standard samples.

The aim of this study is to build on the approach of Lin and Garcia (2005) and relate the recovery of mineral in a long term ferric leach of a low grade copper ore sample to both the location of the mineral grains within the ore particles as well as their position within the column.

7.2 Experimental

7.2.1 Ore Column Preparation

The preparation and operation of the column was done collaboratively by Harrison of the Centre for Bioprocess Engineering Research, University of Cape Town and the research team of Cilliers, Department of Earth Sciences and Engineering, Imperial College London. Escondida Type A copper ore (0.67% Cu, 3.03% Fe, 2.29% S, 2.35% K and 9.5% Al by weight) with the particle size distribution (PSD) given in Table 7.1 was agglomerated and packed into a column of internal diameter 23.5 mm. A layer of filter paper followed by mesh was laid between the irrigation point and the ore, as illustrated in Figure 7.1, to ensure that the liquid distribution was uniform across the column width. Ball bearings were attached to the outside of the column for image registration. The column was irrigated with a ferric solution of 5 g l^{-1} Fe^{3+} in 0.1 M H_2SO_4 from the top at a rate of 4 ml h^{-1} (approximately 2.3 L m^{-2} h^{-1}) and operated at ambient temperature for a period of 102 days.

Table 7.1. PSD of the Escondida Type A ore.

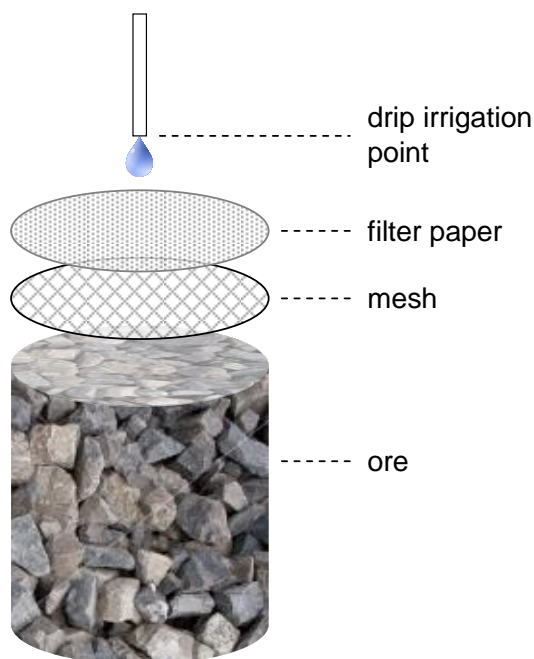| Size (mm)	Weight (%)
> 16.0	6.7
8.00 - 16.0	4.6
5.60 - 8.00	47.5
2.00 - 5.60	9.4
1.18 - 2.00	13.5
0.25 - 1.18	9.9
< 0.25	8.4

Figure 7.1. The column was drip irrigated with a layer of filter paper followed by mesh ensuring the uniform distribution of the liquid.

7.2.2 X-ray CT Imaging

The X-ray CT imaging was performed by the group of Lee at the Department of Materials, Imperial College London on a Pheonix X-ray micro-tomography system. The images were acquired at resolutions of circa 34 μm. Each 3D scan acquired 1015×1015×512 data points and required approximately two hours to run.

The whole column was imaged before leaching was commenced. It was imaged in 11 separate sections of an approximate height of 17.5 mm, from top (1) to bottom (11), because a smaller field of view (FOV) allowed for a finer image resolution. Three sections (2, 6 and 10) were

monitored over the leaching period. The sections were chosen as they were spread out along the length of the column and had a suitable mineral content and distribution, with scans 6 and 10 containing large particles that were of interest. The scans will be henceforth referred to as scans A (2), B (6) and C (10). The column was imaged at 0, 1, 7, 28, 40, 50, 64, 78, 88 and 102 days.

Some scans were omitted from the final analysis due to their poor quality (a lot of noise or poor contrast) or because they were acquired with a significantly different resolution which made an accurate comparison of the images difficult. The columns were taken off stream to be imaged, sometimes for a period of days. This time was not included in the leaching period count.

7.2.3   Image Analysis

The initial image handling was performed in ImageJ, a public domain image processing and analysis program. Only the first 396 of the 512 slices could be loaded due to the memory restrictions of the computer hardware available. The first 40 slices of each data set were discarded as they contained artefacts. Therefore slices 41 to 396 were used for the final image analysis. The images were converted from 32 bit real to 8 bit images with an enhanced contrast. Some of the finer image information would have been lost in this process of resizing, but it was not possible from a computer memory perspective to analyse the files in their original format. The files were read into MATLAB® for the image analysis, where they were handled as uint8 (unsigned 8 bit integer) data sets.

The images were thresholded on 2 levels: the lower level was to define the gangue rock filled area and the upper level was to define the mineral position. The lower threshold level was readily identified and easy to implement. The threshold level for the mineral was more difficult to identify however, despite having the ball bearings' signal magnitude for reference. For this reason, pixels with a signal magnitude one unit more or less than the upper threshold level were included in the analysis as an error measurement. The resulting thresholded images, an example slice of which is shown in Figure 7.2, were used to quantify the voidage in each section of the bed and the mineral content of each slice. A region of interest was defined in this calculation which included everything within the walls of the column to avoid inclusion of any signal from the ball bearings. A morphological thinning algorithm (Baldwin et al. 1996) was used to determine the position of the mineral in the ore relative to the ore surface. An example of a 2D slice from a 3D data set which resulted from this process is shown in Figure 7.2 (c).
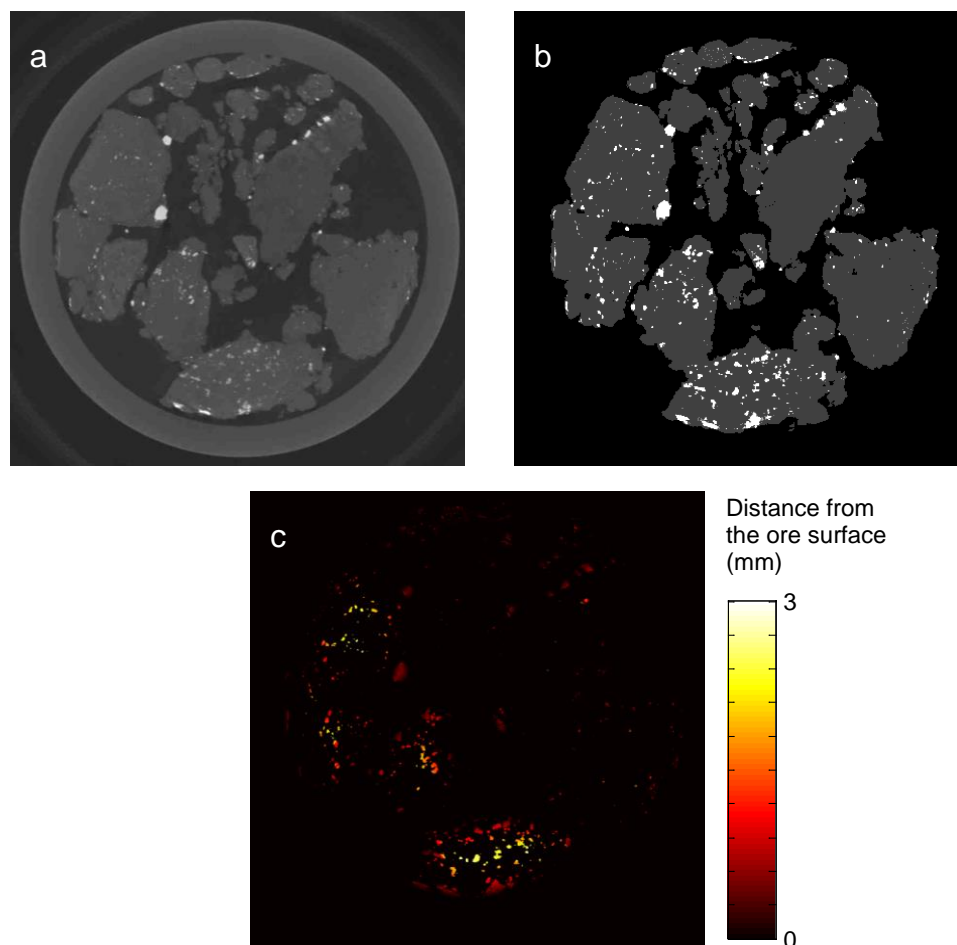
Figure 7.2. (a) Original slice from scan A on day 0 and (b) its thresholded equivalent which shows the position of the mineral (white) and the gangue rock (grey) while excluding information from outside the ore containing region. The result of the 3D morphological thinning to determine the minerals' position in the ore relative to the ore surface is shown in (c).

The pore space was characterised in more detail by considering the individual pore sizes and the pore interconnectivity which was quantified by the pore coordination number. The pore size distribution on day 0 was determined using the morphological thinning algorithm in IDA, an in-house image analysis program. This morphological thinning algorithm and subsequent pore sizing algorithm is described in Baldwin et al. (1996). The steps involved in this process are illustrated in Figure 7.3. A distance map (Figure 7.3 (b)) which classed the void pixels according to their proximity to the solid ore or column walls was calculated initially by only considering those void pixels which shared a face to be connected. When the results of this pore identification procedure were considered, it was evident that single pores were being

split into multiples. Therefore this assumption was causing the pores to not be correctly identified. Diagonally adjacent pixels were therefore considered to be connected too. The resulting pore sizing appeared more reasonable. The coordination number of the pores (the number of pores a given pore is in contact with) was determined as part of this analysis. Pores with a coordination number of zero were excluded in the final analysis as they were deemed not to form part of the interconnected pore network.
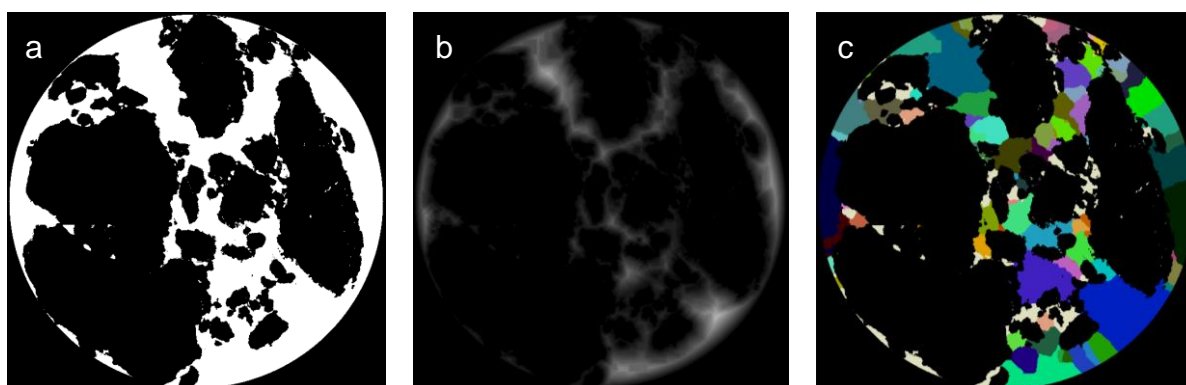
Figure 7.3. The (a) binary gated image of the pore space was used to generate (b) a 3D distance map which was subsequently used to identify (c) the individual pores.

7.3 Results and Discussion

7.3.1 Overall Mineral Recovery

The thresholded images, as illustrated in Figure 7.2, were used to identify the mineral and gangue rock in the sample, the data from which were used to calculate the mineral content and to determine the mineral particles' positions. The mineral particles will have included recoverable metal sulfides (such as pyrite and chalcopyrite) as well as other unrecoverable minerals and dense materials present in the ore. X-ray imaging with a monochromatic source can allow for the identification of the different materials through comparison of the signal magnitude in the images with that of the pure materials (Ghorbani et al. 2011b, Lin and Garcia 2005, Miller et al. 2003). Such calibration was not performed for these experiments and it should be kept in mind that the recoveries discussed in these results have been calculated based on the total mineral content which may include materials that are irrecoverable. For the analysis of the X-ray data it was assumed that there would not have been significant variation in the mineral composition of the ore in the three different regions of the column.

The volumetric mineral content changes over time in the three sections of the column are shown in Figure 7.4. Scans B and C start with similar total mineral volumes, 194 and 209 mm^3 respectively. The lowest initial mineral content is in scan A, at 166 mm^3. The majority of the leaching in the scans occurs within the first 28 days of operation with the leaching rate slowing with time as the more readily recoverable mineral is removed. Far less mineral is recovered in the later leaching period. The overall mineral recovery is 39±2%, 32±3% and 38±4% in scans A, B and C respectively. Two key factors are identified as possible causes of the different recoveries in the three scans: variations in the packed bed structure that would affect the liquid flow path, and the location of the mineral particles within the gangue rock.
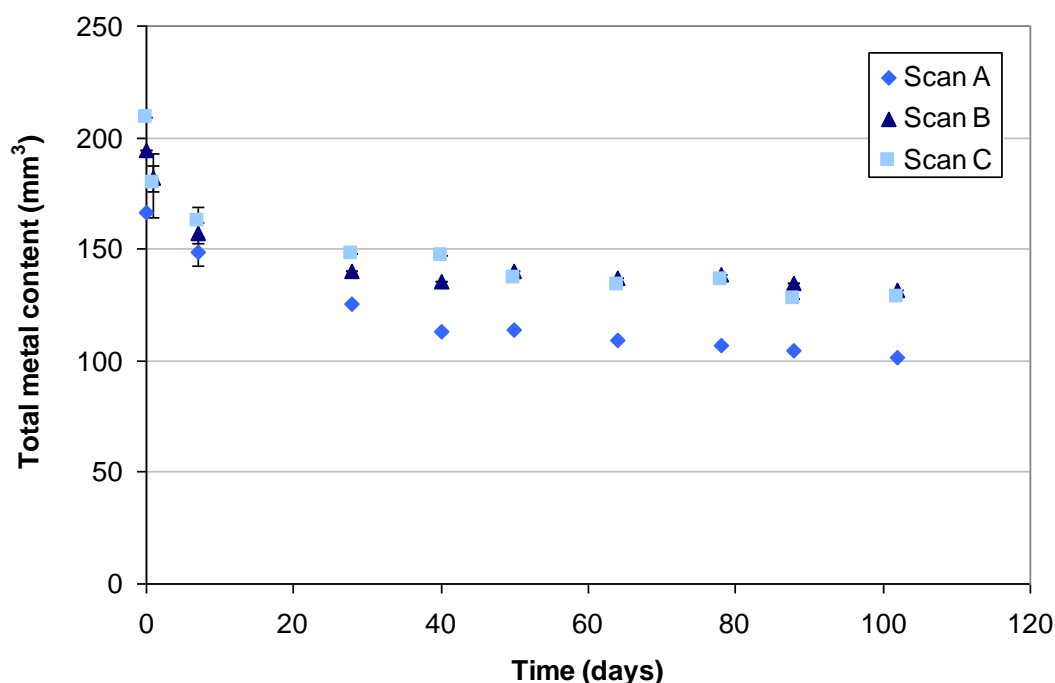

Figure 7.4. Total volumetric mineral content in scan A, B and C as a function of time.

7.3.2   Mineral Position in the Ore

The distributions of the mineral distance from the ore surface are shown in Figure 7.5 for scan A, Figure 7.6 for scan B and Figure 7.7 for scan C. The position of the mineral grains within the ore and the recovery of the mineral as a function of their position are summarised in Table 7.2.

The majority of the mineral particles in the ore on day 0 appear within 0.5 mm of the ore surface in all three sections of the column. Furthermore, a clear peak in the mineral population occurs around a distance from the ore edge of approximately 0.07 mm (or

2 pixels) in all three data sets. In scan A the furthest distance of a mineral particle from the ore surface is 4 mm. There is a longer tail in the mineral position distribution for scan B where some mineral particles are located as far as 7.1 mm from the surface. Similarly, scan C contains mineral a maximum of 6.1 mm from the ore surface. The larger distances in scans B and C fit with the knowledge that these regions of the column contain large particles. These scans also have a larger percentage of the mineral content positioned further than 2 mm from the ore surface. This is in agreement with the study by Miller et al. (2003) who found that the amount of mineral exposed on the ore surface increases with decreasing particle size.

Scans A and C have more mineral located within 1 mm of the ore surface than in scan B (72% and 70% versus 66%) and also have the highest overall recovery. The highest recovery is of the mineral particles that are immediately on the ore surface, where 70%, 73% and 67% of the mineral is leached over the 102 day period in scans A, B and C respectively. The mineral recovery decreases as the distance from the surface increases and there is negligible change in the mineral content located further than 2 mm from the ore surface. The position of the mineral within the ore can therefore be concluded to have a major impact on the mineral recovery, with the overall recovery increasing as the percentage of the mineral within 2 mm of the ore surface increases.

The preferential leaching of surface mineral is expected because the leaching rate of minerals from ore is dependent on the mineral surface area that is able to come into contact with the leaching solution (Petersen 2010). Recent studies have reported that leaching, especially from large particles, occurs only at the surface and subsurface regions on the ore, where subsurface refers to those mineral nodes that are accessible through cracks and pores (Ghorbani et al. 2011a). Mineral particles on or close to the ore surface will be more likely to come into contact with the leaching solution, thereby increasing the chance of their recovery. By the same logic, minerals within the ore particles (not near the surface) will be more difficult to recover as they will be less likely to come into contact with the leaching solution. The slowing overall rate of mineral recovery with time may therefore be attributed to the fast depletion of readily contactable mineral on or near the ore surface.

There is greater variation in the recoveries as the distance from the ore surface increases. This may be because the leaching of mineral further from the surface of the ore has a higher dependence on its surrounding environment, such as whether it is in contact with mineral that is closer to the surface, for example in a seam.

The average distances of the mineral from the surface of the ore in scans A, B and C are illustrated in Figure 7.8. Scans A and C have similar initial average distances, 0.72 mm and

0.76 mm, while scan B has an initial average value of approximately 0.94 mm. Only a small change in the average distance of the mineral from the edge of the solid ore is observed in scan A over the experimental time as those mineral particles further than 2 mm from the ore surface account for a small percentage of the total and the maximum distance is significantly less than for the other two scans. The average value increases with time in scan B and scan C. This is due to the presence of mineral much further than 2 mm from the ore surface than is present in scan A.

Table 7.2. Mineral position and recovery as a function of position in the three scans.

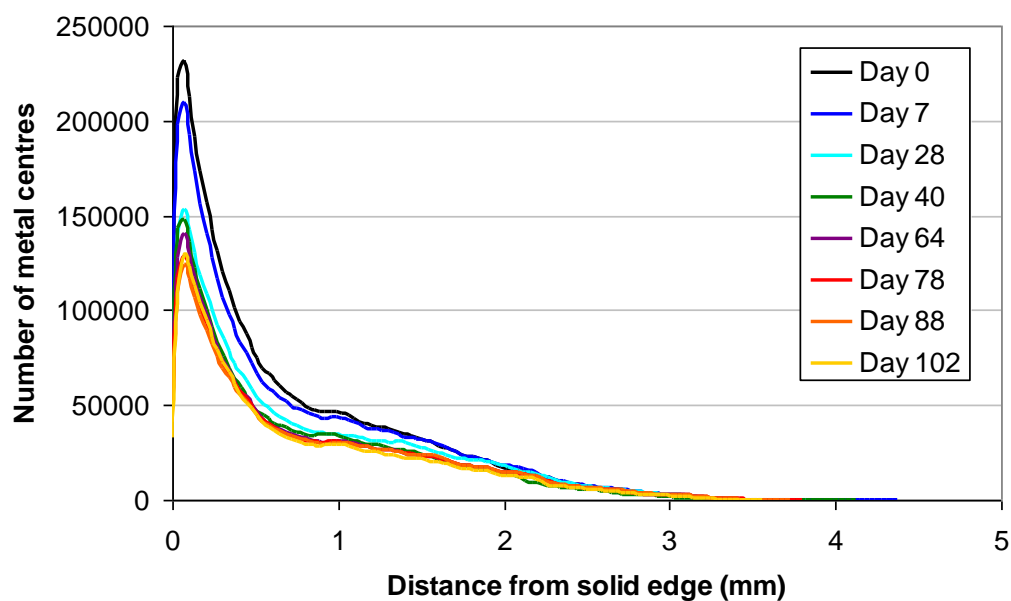|	Scan A	Scan B	Scan C
Mineral position on day 0			
< 1 mm from surface	72%	66%	70%
1 - 2 mm from surface	22%	21%	20%
> 2 mm from surface	6%	13%	10%
Mineral recovery			
Surface	70 ± 1%	73 ± 2%	67 ± 3%
< 1 mm from surface	42 ± 1%	47 ± 2%	53 ± 3%
1 - 2 mm from surface	33 ± 4%	19 ± 2%	24 ± 1%
> 2 mm from surface	< 1%	< 1%	< 1%

Figure 7.5 Change in the distance of mineral particles from the edge of the ore as a function of time in scan A.
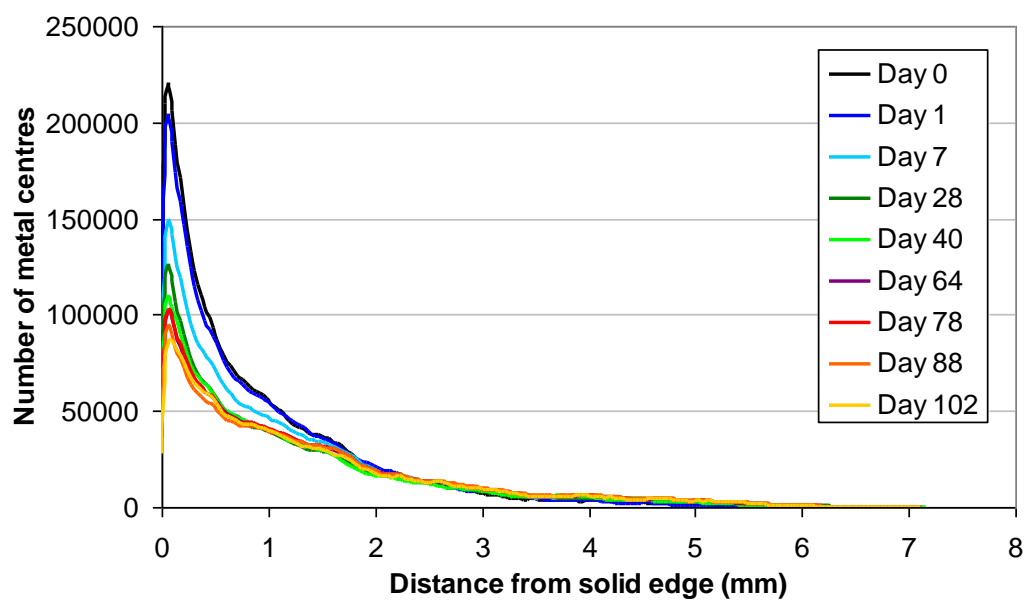

Figure 7.6. Change in the distance of mineral particles from the edge of the ore as a function of time in scan B.
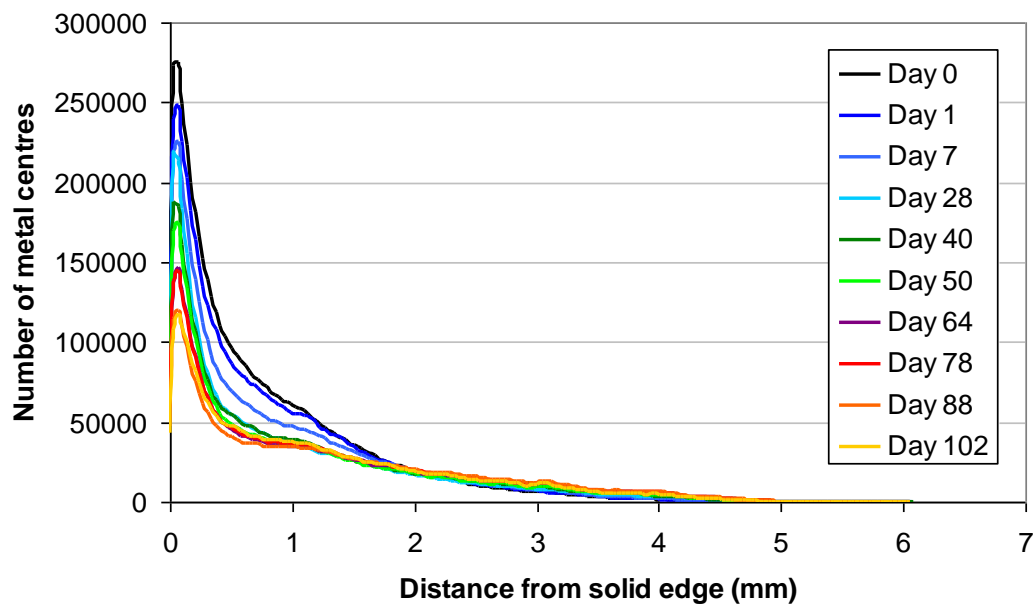
Figure 7.7. Change in the distance of mineral particles from the edge of the ore as a function of time in scan C.
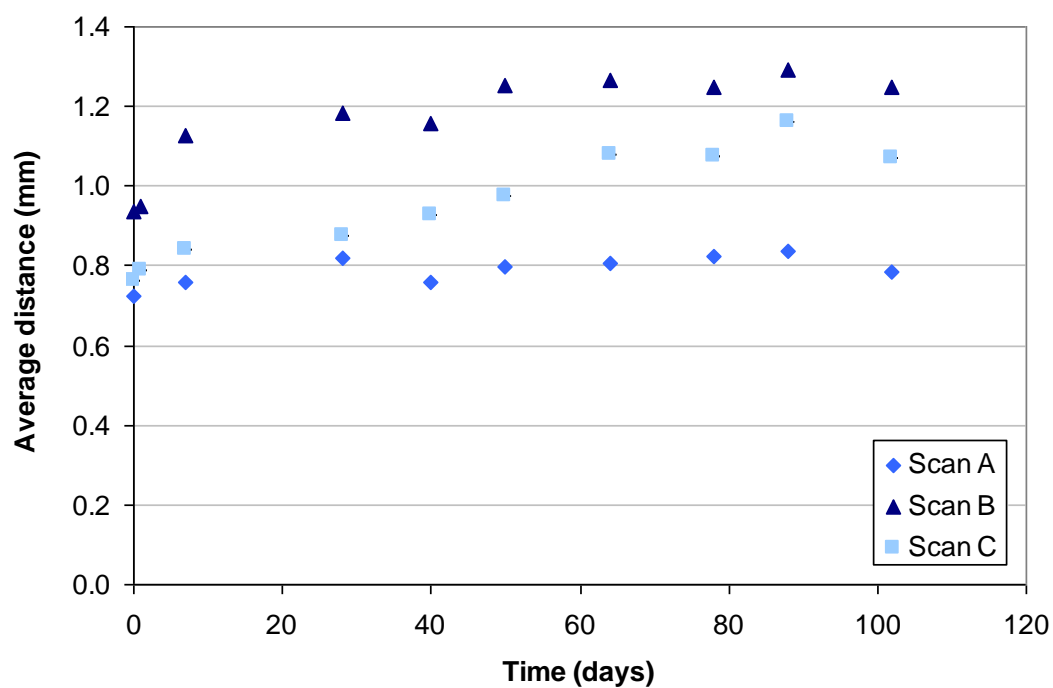

Figure 7.8. Average distance of the mineral particles from the edge of the ore as a function of time in scan A, B and C.

7.3.3   Voidage and Pore Size Distribution

The voidages of the three sections were calculated from the binary gated images to be $35.6\pm0.5\%$, $34.0\pm0.6\%$ and $31.3\pm0.6\%$ respectively. This is slightly lower than has typically been quoted for heap leaching beds where the voidage is typically circa 40% (Bouffard and Dixon 2001, Lin et al. 2005). This deviation from the norm is because the bed was carefully packed to include as many ore particles in the sample as possible. The column is also much smaller than typical beds (to allow for a higher X-ray CT imaging resolution) in which a range of voidages would be expected to be present, including regions of low voidage comparable to this sample.

Knowledge of the pore sizes in a packed bed of ore is important to the characterisation of the bed as it is known to have an impact on the flow path as was illustrated in the preferential flow studies done by O'Kane Consultants Inc. (2000). It is also postulated that the majority of leaching occurs in the stagnant liquid which would be more likely to be present in smaller pore volumes as opposed to larger channels.

The final pore size distributions for the three scans are displayed in two manners in Figure 7.9, Figure 7.10 and Figure 7.11. Graph (a) shows the size distribution as a cumulative percentage of the total volume, whereas graph (b) gives the volume of the pore space occupied by 1 mm^3 ranges (i.e. 0-1 mm^3, 1-2 mm^3, …).

Scans A and B contain fewer pores than scan C (2327 and 1608 versus 3970). 'Micro'-pores of a size less than 1 mm^3 account for 13% and 22% of the pore space in scans A and C respectively. These pores (less than 1 mm^3 in volume) account for 7% of the void space in scan B, a significantly smaller percentage. The contribution of the pore size ranges to the total volume decays in exponential-like manner in scans A and C, with only a few larger pores existing. This is not the case in scan B, where a third of the void space is occupied by pores larger than 40 mm^3. Scan B also contains the largest pores out of the three regions, the largest of which has a volume of 104 mm^3, while the largest pores in scan A and scan C are 88 and 67 mm^3 respectively. Approximately 50% of the pore space is occupied by pores smaller than 9 mm^3 in scan A, 16 mm^3 in scan B and 5 mm^3 scan C.

The coordination number information for the pores is summarised in Figure 7.12 to Figure 7.14. Pores with a coordination number of zero were excluded from the analysis, as they were deemed not to form part of the interconnected pore space that would affect the solution flow and consequently would not impact leaching efficiencies. Those pores with a coordination number of zero only contribute to 0.17%, 0.26% and 0.31% of the total pore space volume so their exclusion from the analysis is not expected to affect the overall trends significantly. The

population distributions are very similar for all three scans and lower coordination numbers are more common. The most common coordination number for a pore is 2.

Larger pores, such as that found in scan B, are expected to result in less liquid retention on the ore surface and between adjacent particles due to less capillary pressure. This may be why the lowest overall mineral recovery is recorded in scan B. However, the mineral position data shows that the leaching of the surface and near-surface mineral in scan B is similar to that in the other scans. It may therefore be concluded that the pore size distribution does not have a significant effect on the recovery of the mineral. This may be because the small diameter of the column results in inadequate solution distribution not being identified or because the solution to ore ratio in the column is higher than would be found in normal operation (Kappes 2002). The effect of pore size distribution on mineral recovery may still become significant in larger samples and in full scale operation.
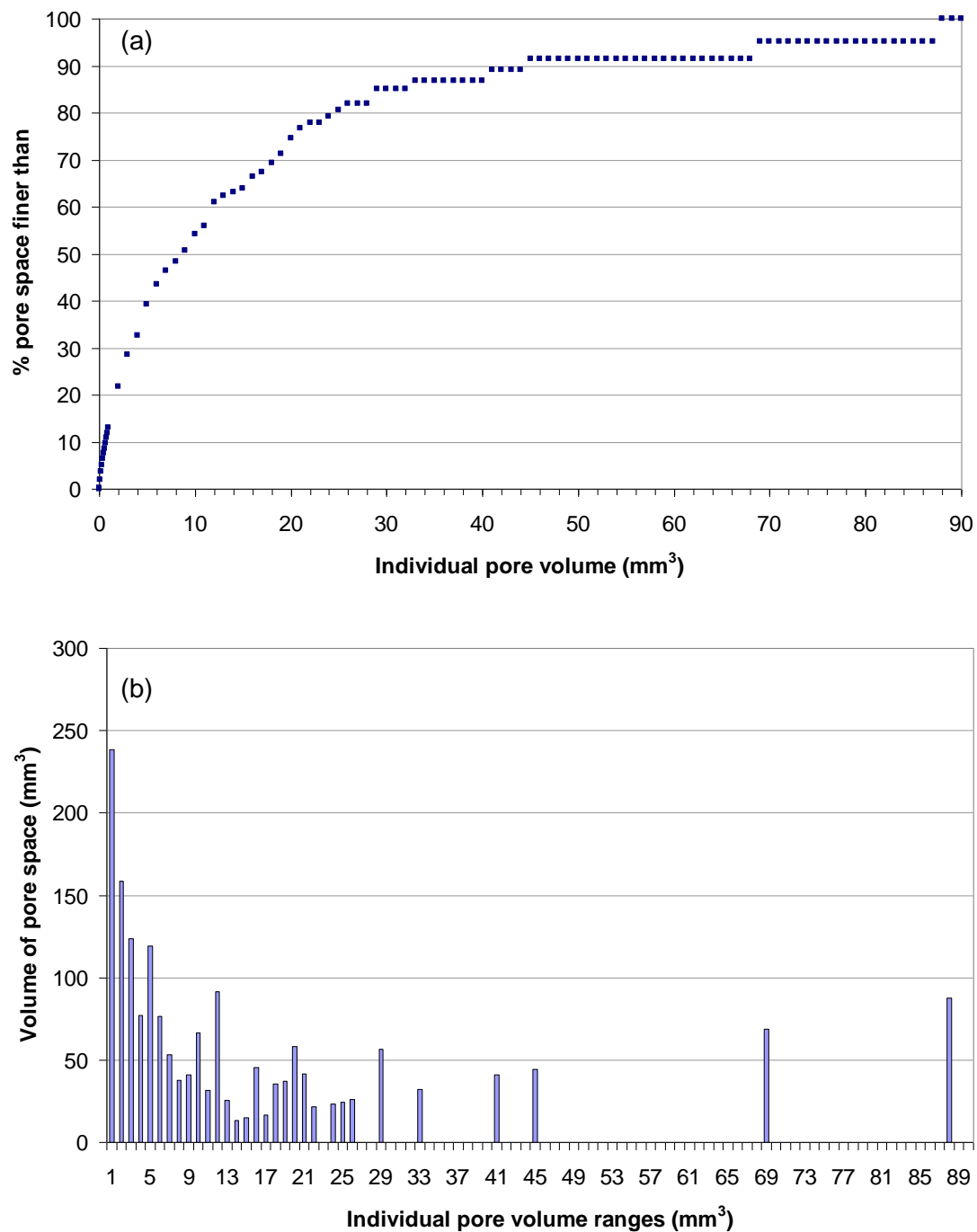
Figure 7.9. Pore size distribution for the pores in scan A where (a) displays the data as a cumulative percentage of the total pore space and (b) gives the volume of the pore space occupied in 1 mm^3 ranges.
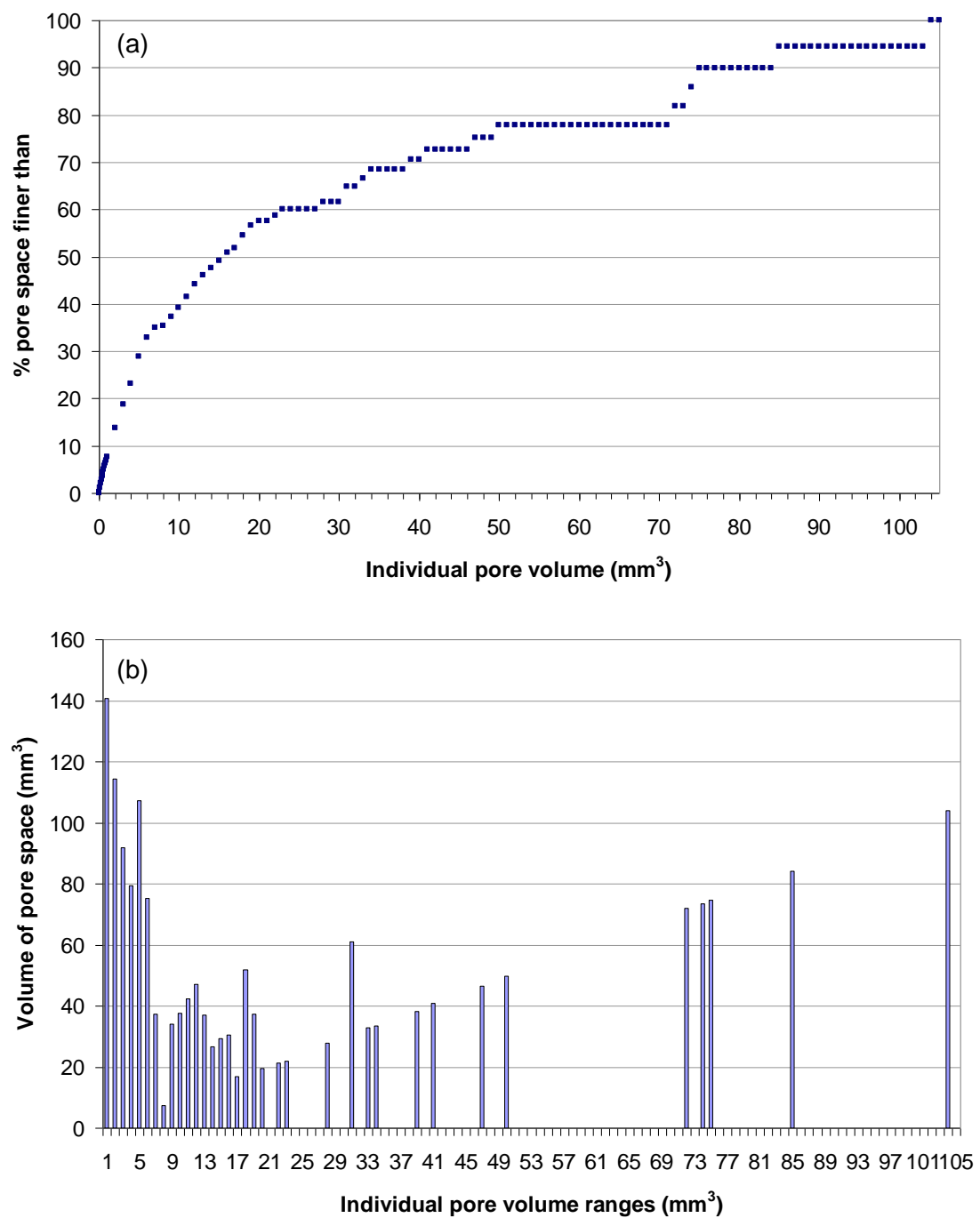
Figure 7.10. Pore size distribution for the pores in scan B where (a) displays the data as a cumulative percentage of the total pore space and (b) gives the volume of the pore space occupied in 1 mm^3 ranges.
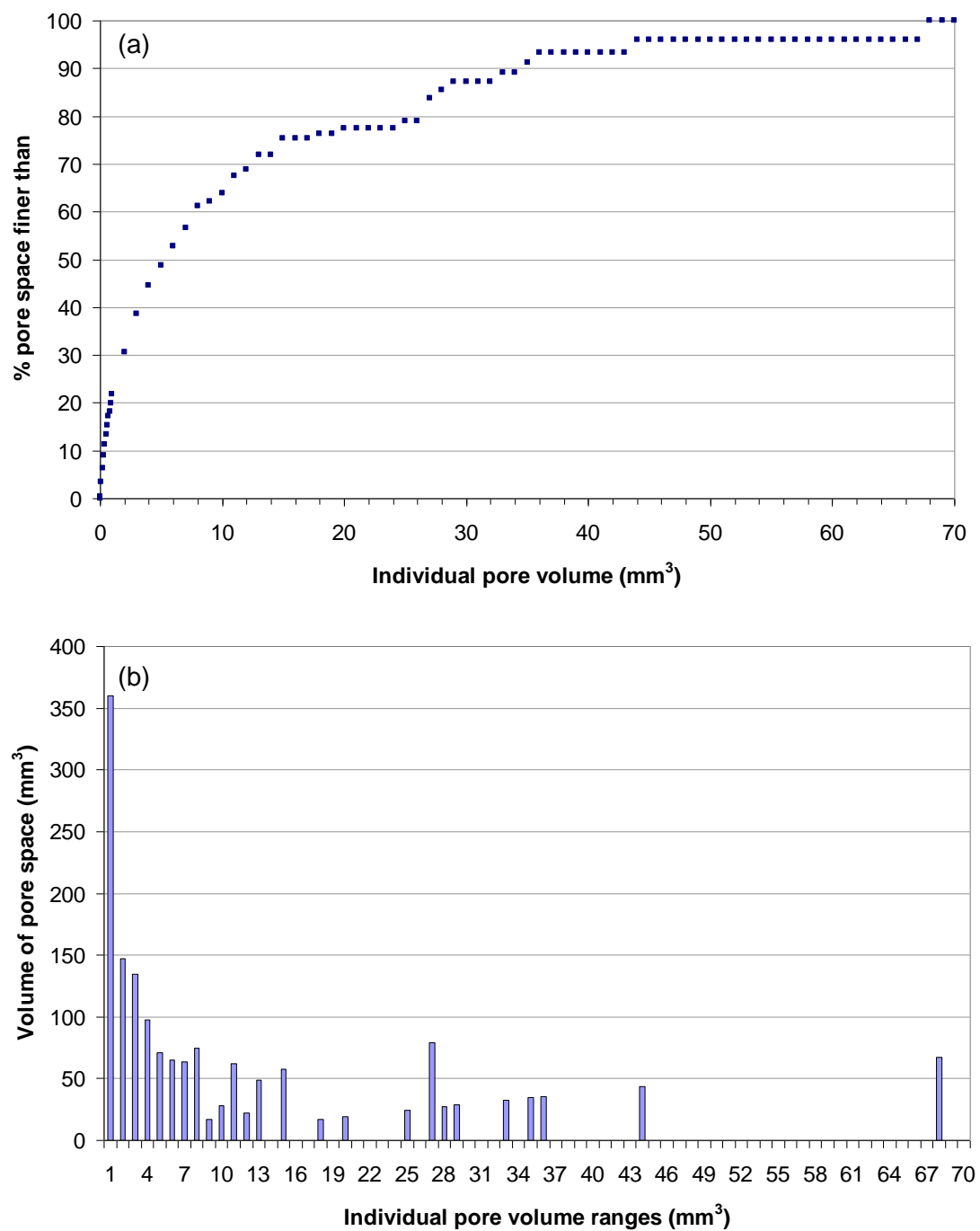
Figure 7.11. Pore size distribution for the pores in scan C where (a) displays the data as a cumulative percentage of the total pore space and (b) gives the volume of the pore space occupied in 1 mm^3 ranges.
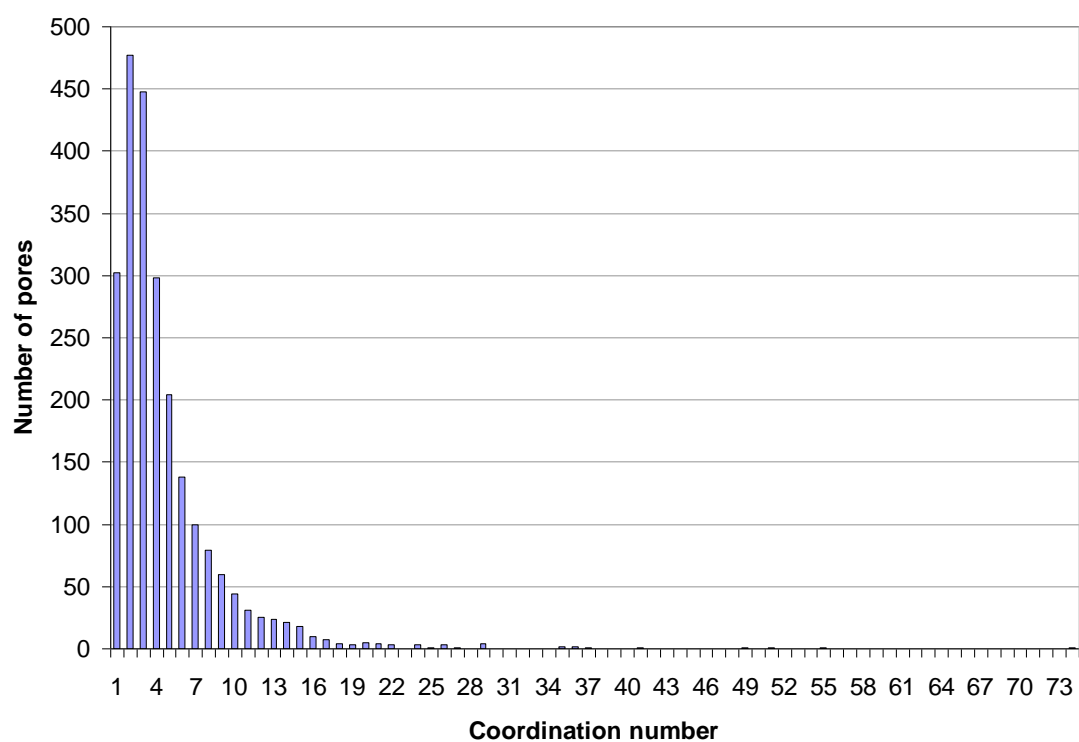
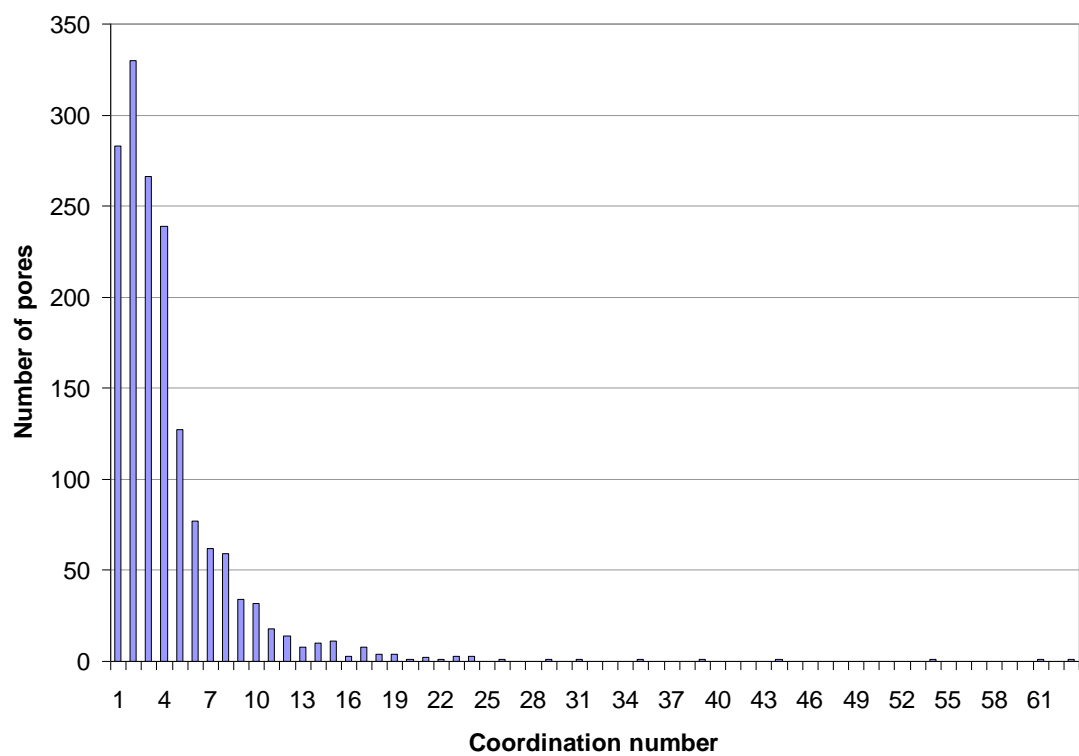Figure 7.12. Coordination number summary for the pores in scan A.

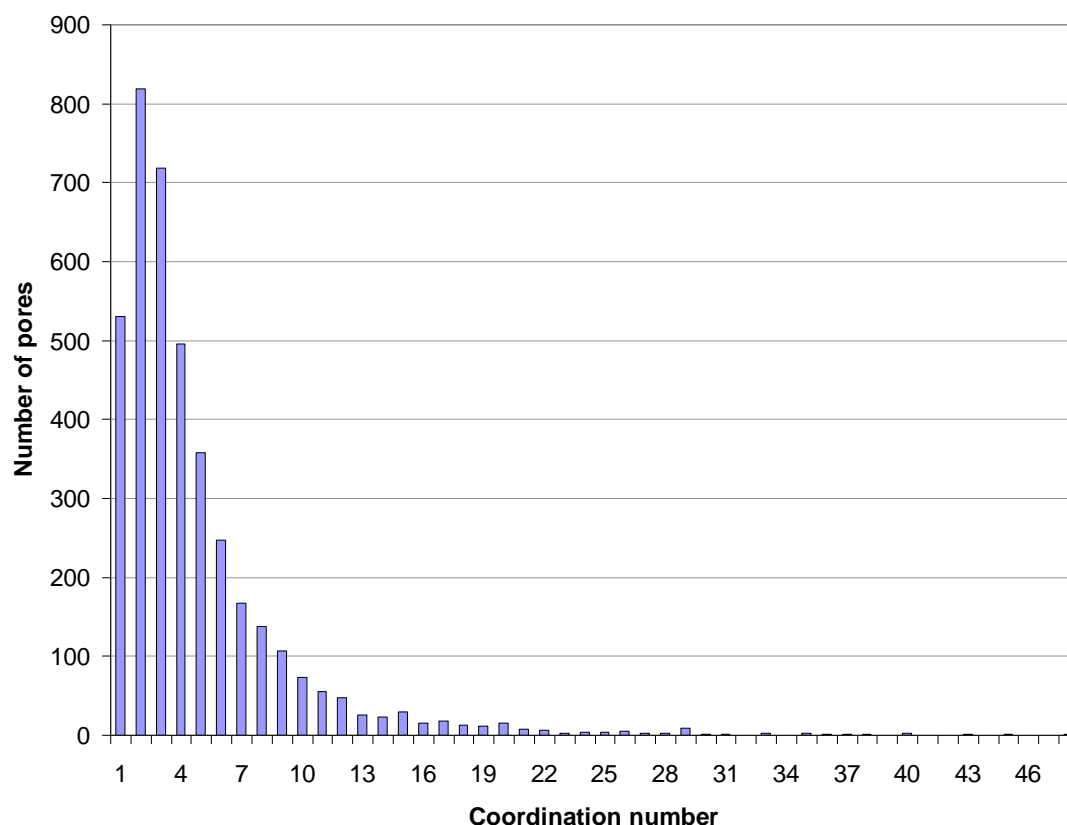Figure 7.13. Coordination number summary for the pores in scan B.

Figure 7.14. Coordination number summary for the pores in scan C.

7.3.4 Effect of Radial Variations

The mineral leaching varies as a function of distance from the centre of the column as is shown in Figure 7.15. The highest recovery in all three scans (50%, 50% and 58% respectively) occurs in the outermost 1.5 mm, by the column wall. The recovery decreases towards the centre of the column until 6.8 mm from the centre within which there is little variation.

The voidage also varies as a function of radial distance from the centre of the column as is shown in Figure 7.16. This is a common characteristic of packed beds as particles must conform to the curvature of the column wall (Benenati and Brosilow 1962). The highest voidage in all three scans is at the wall of the column at 64±8%, 61±6% and 55±9% respectively. The voidage within the central 10.2 mm from the centre is significantly lower, on average less than half the voidage of the outer ring. No clear trend is identifiable in this central region because variations in the voidage will be due to the random orientation of ore particles. In scan B there is a large standard deviation in the central 3.4 mm of the column.

This is due to the large particles known to be present in the centre of this section of the column which will cause areas of very low and very high voidage.

The voidage radial variations therefore follow a similar trend to that of the mineral leaching (decreasing towards the centre of the column). This suggests that the higher voidage at the walls may cause the leaching solution to flow preferentially along the column walls resulting in relatively inefficient leaching in the less irrigated centre of the column. This type of behaviour would be expected in a system with a high flow rate (relative to the particle size distribution), when liquid will preferentially flow through a region of coarser packing (O'Kane Consultants Inc. 2000). Preferential liquid flow along the column walls is supported by visual observation.

Another consideration is the availability of the mineral as a function of the distance from the centre of the ore bed, as this has shown to have a significant effect on the mineral recovery. The original volume of mineral per cubic millimetre is presented as a function of distance from the centre of the column in Figure 7.17. Figure 7.18 shows what fraction of this mineral is within 2 mm of the ore surface as the results in Section 7.3.2 showed that this is the mineral that is recovered. In scans B and C the fraction of mineral within 2 mm of the ore surface decreases towards the centre of the column, with the exception of the central 3.4 mm radius circle in scan C when it increases. This is because of the large particles in these sections of the column whose edges, and so too the mineral within 2 mm of the ore surface, are located nearer to the walls of the column. This trend is complementary to the decrease in recovery from the outside to the centre of the column and suggests that the radial variations in recovery could be because less mineral is accessible for leaching towards the centre of the column. The results from scan A however do not fit this trend, confirming that there are factors other than the proximity of the mineral to the ore surface that contribute to the mineral recovery. Barring the existence of a higher concentration of non-recoverable mineral in the 6.8 mm closest to the centre of scan A (a theory which cannot be tested from the acquired data), the decrease in recovery towards the centre of the column is therefore most likely a combination of the proximity of the mineral to the ore surface and liquid distribution variations due to preferential flow into the areas of higher voidage near the wall of the column.
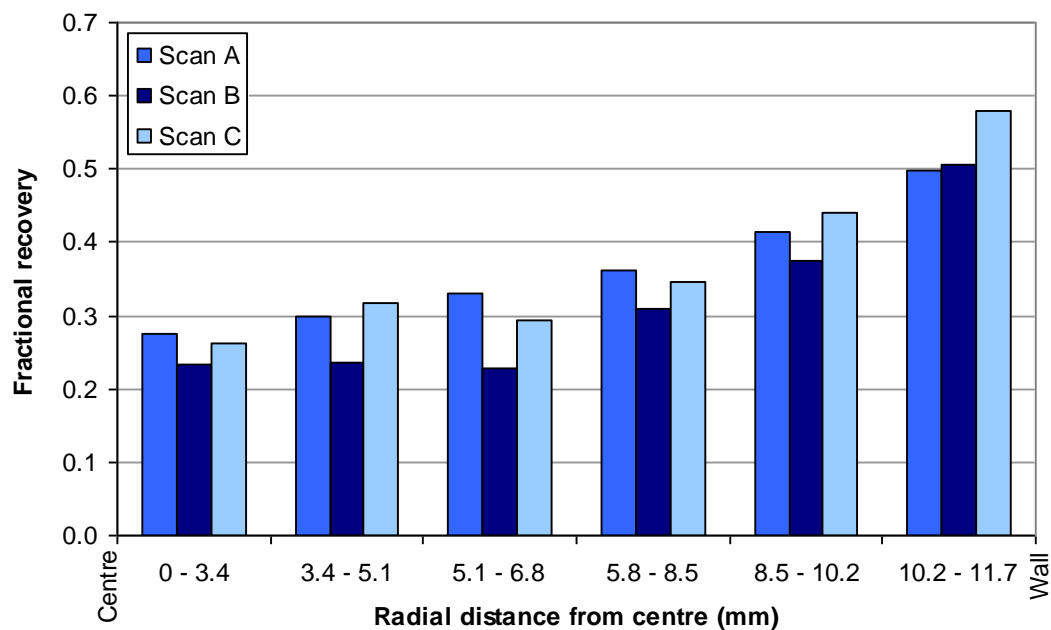
Figure 7.15. Fractional recovery of the mineral after 102 days of leaching as a function of the column radius.

Figure 7.16. Radial variation in the voidage where the error bars show the standard deviation in the voidage along the height of each scan.

Figure 7.17. Volume of mineral per mm^3 as a function of the column radius on day 0.

Figure 7.18. Fraction of the mineral particles less than 2 mm from the ore surface as a function of the column radius on day 0.

7.4 Conclusions
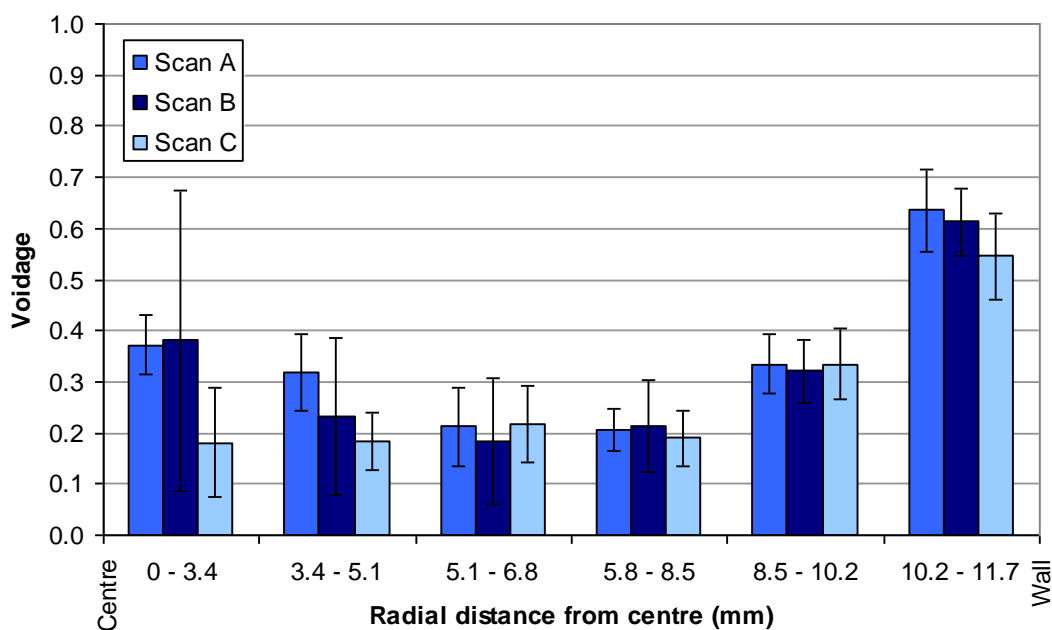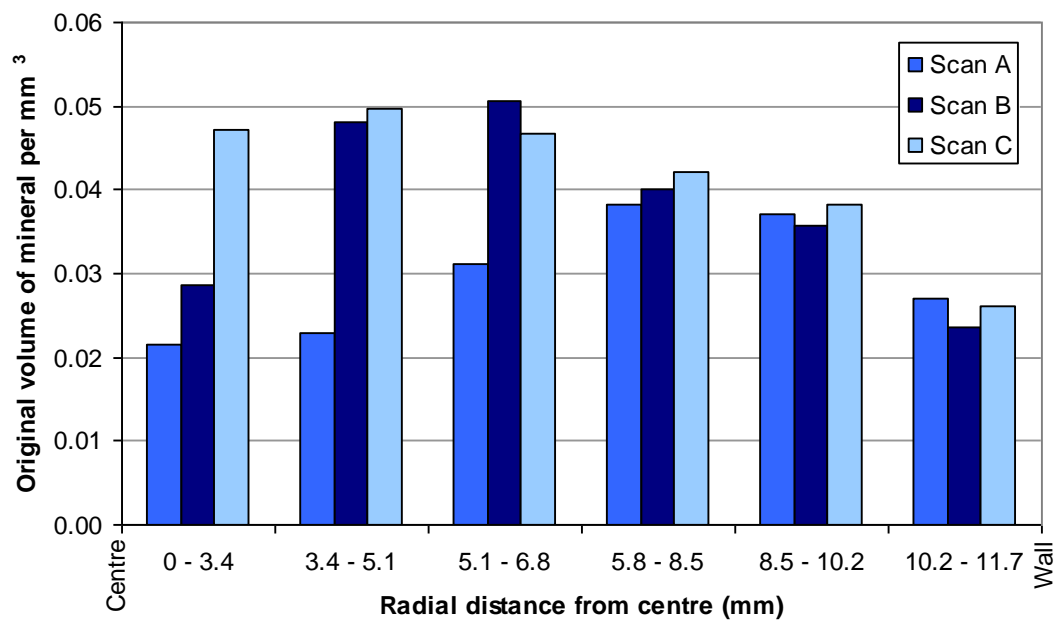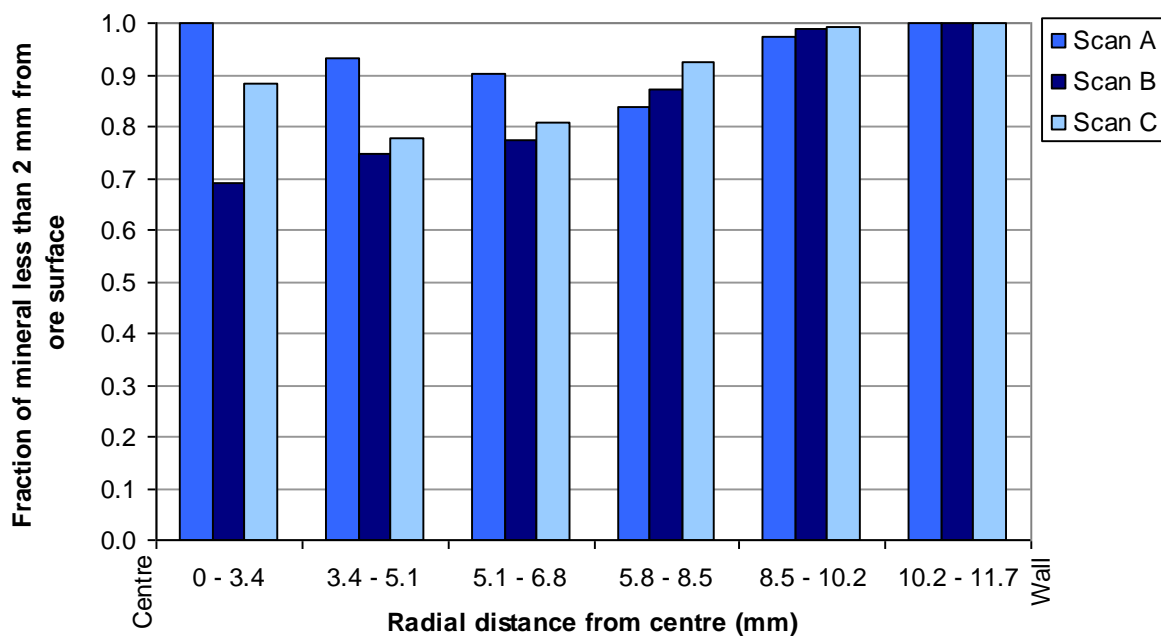
The overall mineral recoveries after 102 days of ferric leaching were found to vary throughout the ore bed, having been calculated from the thresholded images to be 39±2%, 32±3% and 38±4% in scans A, B and C respectively.

The proximity of the mineral particles within the gangue rock to the ore surface was found to have the biggest influence on the mineral recovery. The recovery was highest on the ore surface and decreased as the distance from the surface increased. There was negligible recovery of mineral located further than 2 mm from the ore surface. The recovery varied more between the scans as the distance from the ore surface increased. This is because the recovery of mineral located further from the ore surface has a higher dependence on the surrounding environment, such as whether it is in contact with mineral that is closer to the surface. This result should ultimately inform the optimal preparation of ore (such as crush size) in order to optimise mineral recovery in future leaching operations.

A pore distribution analysis on the three regions uncovered no correlation between the mineral recovery and the pore size. This is likely because the small size of the sample did not allow for significant issues (i.e. channelling) with the leaching solution flow to develop. However, the radial variations in the recovery showed that the proximity of the mineral to the ore surface was not the only phenomenon that affected mineral recovery. In scan A it was found that the recovery decreased towards the centre of the column, while the mineral 2 mm from the ore surface did not follow the same trend. The high recovery at the column wall, an effect that was seen in the other two scans too, was consequently attributed to preferential flow of the leaching solution in the higher voidage regions at the column wall. Therefore variations in pore size (voidage) were found to have some influence on the mineral recovery.

7.5 Nomenclature

Abbreviations

CT   -   computed tomography

FOV   -   field of view

HPGR -   high pressure grind rolls

PSD   -   particle size distribution

7.6 References

Baldwin, C. A., Sederman, A. J., Mantle, M. D., Alexander, P. and Gladden, L. F. (1996) 'Determination and characterization of the structure of a pore space from 3D volume images', *Journal of Colloid and Interface Science,* 181(1), 79-92.

Benenati, R. F. and Brosilow, C. B. (1962) 'Void fraction distribution in beds of spheres', *AIChE Journal,* 8(3), 359-361.

Bouffard, S. C. and Dixon, D. G. (2001) 'Investigative study into the hydrodynamics of heap leaching processes', *Metallurgical and Materials Transactions B-Process Metallurgy and Materials Processing Science,* 32(5), 763-776.

Ghorbani, Y., Becker, M., Mainza, A., Franzidis, J. P. and Petersen, J. (2011a) 'Large particle effects in chemical/biochemical heap leach processes – A review', *Minerals Engineering,* 24(11), 1172-1184.

Ghorbani, Y., Becker, M., Petersen, J., Morar, S. H., Mainza, A. and Franzidis, J. P. (2011b) 'Use of X-ray computed tomography to investigate crack distribution and mineral dissemination in sphalerite ore particles', *Minerals Engineering,* 24(12), 1249-1257.

Kappes, D. W. (2002) *Precious Metal Heap Leach Design and Practice,* Reno, Nevada: Kappes, Cassiday & Associates.

Kodali, P., Dhawan, N., Depci, T., Lin, C. L. and Miller, J. D. (2011) 'Particle damage and exposure analysis in HPGR crushing of selected copper ores for column leaching', *Minerals Engineering,* 24(13), 1478-1487.

Lin, C. L. and Garcia, C. (2005) 'Microscale characterization and analysis of particulate systems via cone-beam X-ray microtomography (XMT)', in Young, C. A., Kellar J.J., Free,

M.L., Drelich, J., King, R.P., ed. *Innovations in Natural Resource Processing - Proceedings of the Jan D. Miller Symposium*, Society for Mining, Metallurgy and Exploration, 421-432.

Lin, C. L., Miller, J. D. and Garcia, C. (2005) 'Saturated flow characteristics in column leaching as described by LB simulation', *Minerals Engineering,* 18(10), 1045-1051.

Miller, J. D., Lin, C. L., Garcia, C. and Arias, H. (2003) 'Ultimate recovery in heap leaching operations as established from mineral exposure analysis by X-ray microtomography', *International Journal of Mineral Processing,* 72(1–4), 331-340.

O'Kane Consultants Inc. (2000) 'Demonstration of the application of unsaturated zone hydrology for heap leaching optimization', *Industrial Research Assistance Program Contract # 332407,* (628-1).

Petersen, J. (2010) 'Modelling of bioleach processes: Connection between science and engineering', *Hydrometallurgy,* 104(3-4), 404-409.

Yang, B. H., Ai-Xiang, W., Jiang, H. C. and Chen, X. S. (2008) 'Evolvement of permeability of ore granular media during heap leaching based on image analysis', *Transactions of Nonferrous Metals Society of China,* 18(2), 426-431.

Chapter 8 – Concluding Remarks and Suggestions for Future Studies

The main conclusions from this thesis are now summarised and, in addition to the information that may also be found at the end of each experimental chapter, suggestions for future work are presented.

8.1 Magnetic Resonance Imaging (MRI) Methods Development

The first aim of this thesis was to identify and develop a MRI acquisition method that would allow for the distortion free imaging of low grade copper ore samples. It was confirmed that traditional frequency encode methods are inappropriate for this application due to the formation of magnetic susceptibility artefacts. As was hypothesised, images acquired using single point imaging (SPI) and spin echo single point imaging (SESPI), both of which are pure phase encode techniques, showed no such distortions because there was no measurement of the time evolution of the MRI signal (Gravina and Cory 1994). This was confirmed through the comparison of the images with equivalent X-ray computed tomography (CT) 3D images which are immune to magnetic susceptibility distortions.

SESPI was found to be the best suited of the two pure phase encode methods for the imaging of the ore systems. This decision was based on the fact that SESPI had the highest signal to noise ratio (SNR), a measure of the image quality, and because the signal magnitude was relatively unaffected by the particle size distribution (PSD) of the ore. With respect to the latter point, the relaxation times of the liquid in saturated ore samples was measured to decrease as the PSD of the sample decreased, a result which is consistent with the fact that a smaller crush size results in more mineral grains being present on the ore surface (Miller et al. 2003). The T_2 times of different PSD samples were all at least one order of magnitude longer than the SESPI echo time, TE, and so the effect of T_2 weighting on the signal was minimal. By contrast, because the T_2^* times of the ore samples were the same order of magnitude as the acquisition time, t_p, the relative attenuation of relaxation times by smaller ore particle sizes caused significant information loss in the SPI acquisitions, especially at higher field strengths where the effect of magnetic susceptibility distortions was greater.

The inherent slowness of SESPI may limit its suitability for future work if transient systems are to be studied. Preliminary under-sampling experiments to reduce acquisition times demonstrated that sorted under-sampling allows for a much reduced acquisition time with minimal loss in accuracy. However, different under-sampling protocols should be considered

in the future specifically as sorted under-sampling requires prior knowledge of the system which may not always be possible. This should include random under-sampling where the distribution of the points is specified. Though compressed sensing (CS) reconstruction of the images was not found to offer an obvious advantage over Fourier transform (FT) methods, the results were not conclusive and it should be investigated further. Shortening SESPI acquisition times by performing multiple echo trains or by employing a smaller tip angle which would necessitate a shorter recovery time should also be explored.

8.2 Hydrology Studies of Ore Beds

8.2.1 Phase Mapping Experiments

Following the identification of a distortion free imaging method, SESPI was used to study the distribution of the gas, liquid and solid phases within a column leach by producing 3D phase maps as has been done in the past (e.g. Sederman and Gladden (2001)). The phase map hold-up and voidage values agreed with literature and gravimetric values which further confirmed the accuracy of the MRI method. The 3D phase maps of the columns allowed for the novel quantification of the liquid film thickness and the interfacial areas between the phases. This analysis revealed a strong preference for surface flow which is consistent with the ore being preferentially water wetting, though significant variations existed between the different columns despite them being prepared in the same manner. This therefore highlighted how important the information obtained using MRI can be with respect to understanding the hydrodynamics in a specific ore bed.

A higher liquid flow rate resulted in an increase in the liquid hold-up, with the vast majority of the newly retained liquid being held in new rivulets rather than the existing rivulets increasing in size. This agrees with the postulations of Ilankoon and Neethling (2012) based on their gravimetric measurements and hydrodynamic models. This caused an increase in the liquid-solid interfacial area which is beneficial to leaching as more of the mineral is contacted by the leaching solution. However, another effect of the increased liquid flow rate was to decrease the gas-liquid interfacial area (per liquid volume) because the liquid film thickness increased on average. This may lead to oxygen mass transfer limitations, thereby restricting the rate of mineral recovery, because of the lengthened diffusion path for the oxygen from the gas through the liquid to the leaching sites at the surface of the ore. Therefore both of these effects need to be considered when deciding on the best flow rate for a given ore sample and further experiments of this type should be considered. These should include the quantification of the mineral leaching and microbial colonisation of the ore, which Chiume et al. (2012)

found to be affected by the flow rate, with faster colonisation occurring at lower flow rates and higher flow rates resulting in more cell detachment and removal. These experiments should be compared to existing heap leaching models which predict mineral recovery which would also serve to determine how well the models of the hydrodynamic behaviour predict the actual liquid distribution and flow as ascertained by the MRI.

Furthermore, the effect of hysteresis, a known phenomenon in ore beds (Ilankoon and Neethling 2012), could be quantified using the MRI phase mapping technique. This is especially important with respect to the flooding of the ore bed for the imaging of the total void space. The effect of the liquid (flow rate, film thickness, distribution, etc.) on the colonisation of the ore by microorganisms in a biotic leach could now be examined using MRI phase mapping in conjunction with traditional microbiology techniques.

The accuracy of the results of future studies could be improved through the acquisition of higher resolution images. This was not possible in this study due to the spectrometer limitations and time restrictions, but could be achieved on more robust machines, through under-sampling or through the application of modified acquisition sequences as has been demonstrated with SPRITE (Balcom et al. 1996).

8.2.2   Tracer Studies

An MRI step tracer study using D_2O was shown to be an accurate descriptor of liquid behaviour through comparison with a standard $NaNO_3$ conductivity tracer experiment (Bouffard and Dixon 2001, Bouffard and West-Sells 2009). The MRI tracer experiment was demonstrated to have the advantage of allowing for the spatial resolution of the tracer flow as opposed to being limited to effluent measurements. However, the column D_2O experiment did not uncover any major variations in the liquid flow behaviour across the column width. This is likely due to the narrowness of the column (50 mm diameter); therefore future experiments should consider larger diameter columns if possible.

D_2O tracer experiments may be used in future studies to identify the position of the stagnant and flowing liquid within an ore column. This will require more rapid acquisition sequences than have been used in this thesis. This could be achieved by pursuing the time reduction techniques that have been discussed previously in Section 8.1. An alternative approach would be to modify the SESPI pulse sequence so that it is slice selective.

8.2.3   Single Point Drip Irrigation

Studies on the drip irrigation of ore from a single point source were effective at demonstrating the extreme differences in the liquid distribution in beds of either exclusively large or fine ore. Liquid distribution in the large ore was dominated by gravitational effects, resulting in a strong preference for channel or macro-pore flow, and thus limited lateral liquid distribution and pronounced preferential flow. By contrast, the fine ore liquid distribution was dominated by capillary suction and the liquid distribution was well described by heuristics for clay soil drip irrigation. Whereas changes in the liquid flow rate did not significantly change the liquid distribution in the large ore, it was observed to have a pronounced effect on the fine ore liquid distribution where higher flow rates caused more lateral liquid distribution and degradation of the wetting symmetry. Such behaviour in the fine ore bed was because liquid accumulated at the top of the ore bed as liquid runoff to a greater degree in the higher flow rate systems. The results hence clearly illustrated the ability of accumulations of fines to plug pores and thereby restrict flow, but also showed how intentionally installed layers of fines in heaps could be advantageous in acid mine drainage prevention by restricting downwards liquid flow and oxygen supply to deeper ores. Alternating layers of fine and agglomerated (conventionally prepared) ore should be tested to further examine the potential of using layers of fines as either liquid distributors or downwards flow retardants. An aspect of fines irrigation that was not considered in this thesis was the effect of drying on the fine ore bed structure. This should be a consideration in future work because caking (hardening) of the sample due to clays and subsequent cracking could have significant effects on the liquid flow.

The full PSD agglomerated ore had a liquid distribution which increased laterally with depth. Slumping of the ore due to shifting of the ore during initial irrigation cycles caused permanent alteration of the liquid flow path which subsequently did not change. This was specifically observed to result in the limitation of lateral liquid distribution because the movement of the fines reduced the capillary suction of the ore bed. The majority of the fresh solution in the established wetted bed was found to enter directly into the existing liquid channels, thereby limiting the short term liquid exchange to the region below the irrigation point. This behaviour was observable in this ore bed due to the larger diameter (100 mm) relative to the previous section's column (50 mm). The exchange with the liquid held in thinner films or in the small pores was slower and the least amount of exchange occurred with the liquid held in the top corners of the ore bed. This shows that liquid exchange was limited more as the role of capillary suction on the liquid retention increased. This observation agrees with the studies of van Hille (2010) and Chiume (2011). Flow rate increases caused the increase in the liquid hold-up in flowing channels, which corresponds to the results of the previous section where

flow rate increases were found to result in the formation of new rivulets. Changing the flow rate consequently had little effect on the liquid distribution beyond the central region of the bed below the irrigation point, so the effects of the flow rate changes on film thickness and liquid-solid interfacial area that were observed in the previous section will have been limited to only a small region of the ore bed. This means that flow rate changes may have little overall effect on the mineral leaching efficiencies.

In future work the effect of binders on the slumping of agglomerated ore and therefore on the liquid distribution in such samples should be examined. This technique could also be used to study liquid behaviour when multiple drip points are installed or when sprinklers are used, though the latter study would require access to a spectrometer with a larger bore diameter.

8.3 X-ray CT Studies of Leaching Systems

The final experimental section of this thesis was concerned with the study of mineral leaching using X-ray CT as the measurement technique. The main factor affecting the mineral recovery in the long term ferric leach was identified to be the proximity of the mineral to the ore particle surface. The recovery was highest on the ore surface and then decreased with distance until the 2 mm mark beyond which no recovery was achieved. This was concluded to be because the recovery of mineral located further from the ore surface has a higher dependence on the surrounding environment, such as whether it is in contact with mineral that is closer to the surface. This result should be kept in mind with respect to the best preparation of ore (such as crush size) in order to optimise mineral recovery in future leaching operations.

The pore size was not found to have any measurable effect on the recovery. This could be because the small size of the sample did not allow for significant issues with the liquid flow (i.e. channelling) to develop. However, higher mineral recoveries at the wall in one section of the column indicate preferential flow in the higher voidage region by the walls did impact the leaching efficiency.

Future studies should consider the identification of the mineral composition in the ore by correlating the signal intensities with standard samples as has been demonstrated previously by Lin and Garcia (2005). This could provide spatially resolved information regarding the selective leaching of certain mineral species under different conditions. X-ray CT studies could also be used to examine the effect of temperature on the leaching efficiencies. The influence of wall effects on the liquid flow could be limited in future experiments by using columns of larger diameter, though this will need to be balanced with resolution requirements.

Finally, combination of the X-ray CT and MRI techniques should be considered so that the gas and liquid distributions can be correlated with the leaching efficiencies. This would need to be performed on an abiotic bed to ensure that the X-ray CT imaging does not influence the leaching. Biotic studies could be considered if X-ray CT imaging was only performed at the start and end of the experiment.

8.4 Nomenclature

Abbreviations

CS   -   compressed sensing

CT   -   computed tomography

FT   -   Fourier transform

MPA   -   multiple point acquisition

MRI   -   magnetic resonance imaging

PSD   -   particle size distribution

SESPI   -   spin echo single point imaging

SNR   -   signal to noise ratio

SPI   -   single point imaging

SPRITE -   single point ramped imaging with T_1-enhancement

Symbols

t_p -   phase encode time [s]

T_2 -   spin-spin relaxation constant [s]

T_2^* -   effective spin-spin relaxation constant [s]

TE -   echo time [s]

8.5 References

Balcom, B. J., MacGregor, R. P., Beyea, S. D., Green, D. P., Armstrong, R. L. and Bremner, T. W. (1996) 'Single-point ramped imaging with T-1 enhancement (SPRITE)', *Journal of Magnetic Resonance Series A,* 123(1), 131-134.

Bouffard, S. C. and Dixon, D. G. (2001) 'Investigative study into the hydrodynamics of heap leaching processes', *Metallurgical and Materials Transactions B-Process Metallurgy and Materials Processing Science,* 32(5), 763-776.

Bouffard, S. C. and West-Sells, P. G. (2009) 'Hydrodynamic behavior of heap leach piles: Influence of testing scale and material properties', *Hydrometallurgy,* 98(1-2), 136-142.

Chiume, R. A. (2011) *The impact of irrigation conditions on the spatial development of microbial colonies in bioheaps*, unpublished thesis, University of Cape Town.

Chiume, R. A., Minnaar, S. H., Ngoma, I. E., Bryan C., G. and Harrison, S. T. L. (2012) 'Microbial colonisation in heaps for mineral bioleaching and the influence of irrigation rate', *Minerals Engineering*, 39(1), 156-164.

Gravina, S. and Cory, D. G. (1994) 'Sensitivity and resolution of constant-time imaging', *Journal of Magnetic Resonance Series B,* 104(1), 53-61.

Ilankoon, I. M. S. K. and Neethling, S. J. (2012) 'Hysteresis in unsaturated flow in packed beds and heaps', *Minerals Engineering,* 35(1), 1-8.

Lin, C. L. and Garcia, C. (2005) 'Microscale characterization and analysis of particulate systems via cone-beam X-ray microtomography (XMT)', in Young, C. A., Kellar J.J., Free, M.L., Drelich, J., King, R.P., ed. *Innovations in Natural Resource Processing - Proceedings of the Jan D. Miller Symposium*, Society for Mining, Metallurgy and Exploration, 421-432.

Miller, J. D., Lin, C. L., Garcia, C. and Arias, H. (2003) 'Ultimate recovery in heap leaching operations as established from mineral exposure analysis by X-ray microtomography', *International Journal of Mineral Processing,* 72(1–4), 331-340.

Sederman, A. J. and Gladden, L. F. (2001) 'Magnetic resonance imaging as a quantitative probe of gas–liquid distribution and wetting efficiency in trickle-bed reactors', *Chemical Engineering Science,* 56(8), 2615-2628.

van Hille, R. P., van Zyl, A. W., Spurr, N. R. L. and Harrison, S. T. L. (2010) 'Investigating heap bioleaching: Effect of feed iron concentration on bioleaching performance', *Minerals Engineering,* 23(6), 518-525.